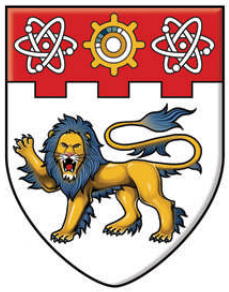

NANYANG TECHNOLOGICAL UNIVERSITY

Hydrothermal Synthesis of Lead Free Piezoelectric Materials

Albertus Denny Handoko

School of Materials Science and Engineering

A thesis submitted to the Nanyang Technological University in partial fulfillment of the requirement for the degree of Doctor of Philosophy

2011

Acknowledgement

I would like to express my heartfelt gratitude to my advisors, Dr. Gregory Goh and Prof. Ma Jan for their guidance and support throughout my PhD studies. I thank Assoc. Prof. Timothy J. White and Dr. Martin K. Schreyer for invaluable advice on crystallography fundamentals, XRD measurement and refinements and report writing during my research.

I am indebted to Dr. Maxim Avdeev and the support staff at Braggs Institute, Australian Nuclear Science and Technology Organization for their approval and help for neutron diffraction experiments and analysis. Dr. Chacko Jacob of Institute of Chemical Engineering Sciences, Singapore, is credited for the solid state NMR measurements and discussions. Supports from the SERC Nanofabrication and Characterisation (SNFC) at IMRE are fully appreciated, including Dr. Debbie Seng and Ms. Doreen Lai for conducting TOF-SIMS measurements and analysis, Ms. June Ong and Mr. Daniel Li for conducting XPS analysis, and Mr. Lim Poh Chong for HRXRD advice and experiments. I also thank Dr. Yao Kui and Ms. Goh Phoi Chin of Institute of Materials Research and Engineering, Singapore, for their assistance with the ferroelectric and laser vibrometry piezoelectric measurement. Mr. Stevin Snellius Pramana is thanked for his help in TEM analysis.

I am grateful to Mr. Tan Chee King for guidance and enlightening discussions. I am also grateful to the technical staffs here at IMRE. Special thanks for friends, colleagues and support staffs at IMRE and NTU MSE without whom I could not make this project successful.

Dedicated to my parents,

who taught me to persevere, be patient, and never lose hope.

and to Kwai Fun,

for making my life complete.

Attempt the end and never stand to doubt; Nothing's so hard, but search will find it out.
Robert Herrick (1591-1674).

Table of Contents

List of Tables and Figures

Tables

Figures

Abstract

PZT, the current leading piezoelectric material, contains 60 wt% lead content in its mass. The continued widespread usage of PZT is unsuitable due to the high content of lead, and therefore significant works on alternative systems possessing high ferro/piezoelectric properties have been initiated. To date, research activities on lead-free piezoelectrics focus on three types of materials: bismuth based perovskites (and also some tungsten-bronze structure), I-V perovskites (e.g. alkali niobates), and II-IV (e.g. barium titanate, $BaTiO_3$) based perovskite. Among the three lead-free material types, the $(Na_xK_{1-x})NbO_3$ (NKN) based I-V perovskite solid solutions have been identified to possess the highest ferro/piezoelectric response and low toxicity level.

This thesis reports successful synthesis of NKN solid solution powder series with compositions around the morphotropic phase boundary (MPB) hydrothermally at 200°C using a simple KOH and NaOH mixture with Nb_2O_5 as a precursor powder. Hydrothermal synthesis route adds the green-synthesis advantage to the already less toxic NKN by enabling growth at low temperatures (≤200°C, way below NKN Curie temperature), in water using simple chemicals and recyclable process.

More significantly, this thesis demonstrates that the NKN solid solutions can be grown epitaxially over a conductive substrate using the same procedure. Thorough structural studies of hydrothermally grown NKN films and powders described in this thesis have shed light on the significant role of lattice trapped –OH related defects to the films' electrical

properties, crucial in devising strategies to remove the defects effectively and improve the ferro/piezoelectric performance.

This thesis envisions to make widespread usage of I-V perovskite based lead-free ferro/piezoelectric materials a step closer to reality and shift the heavy reliance towards the high temperature, energy and labor intensive solid-state based materials synthesis.

List of Publications, Conferences, and Poster Presentations

Journal Publications

1. Handoko, A.D. and G.K.L. Goh, *Hydrothermal Synthesis of Sodium Potassium Niobate Solid Solutions at 200°C.* Green Chemistry, 2010. **12**(4): p. 680-687.
2. Handoko, A.D. and G.K.L. Goh, *Hydrothermal Synthesis of Epitaxial $Na_xK_{(1-x)}NbO_3$ Solid Solution Films.* Thin Solid Films, 2011. **519**: p. 5156-5160.
3. Handoko, A.D. and G.K.L. Goh, *One-dimensional perovskite nanostructures.* Science of Advanced Materials, 2010. **2**: p. 1-18.
4. A. Huang, A.D. Handoko, G.K.L. Goh, P.K. Pallathadka, S. Shannigrahi, *Hydrothermal synthesis of (00l) epitaxial $BiFeO_3$ films on $SrTiO_3$ substrate*, CrystEngComm, 2010. **12**(11): p. 3806-3814.
5. Huang, A., Shannigrahi, S.R., Handoko, A.D. and Tan, H.R., *Stress analysis of (001) preferred oriented $BiFeO_3$ and $Bi(Cr_{0.03}Fe_{0.97})O_3$ films*, Integrated Ferroelectrics: An International Journal, 2009, **113**(1), 9 — 25.
6. Handoko, A.D. and G.K.L. Goh, *Low temperature formation of $(Na_xK_{1-x})NbO_3$ from hydrothermally synthesized $NaNbO_3$.* Materials Research Innovations (Accepted).

Conference Oral Presentations

- Thin Films 2008, Singapore: Handoko, A.D. and G.K.L. Goh, "Hydrothermal synthesis of I:V Perovskite Thin Films – Defects and Properties"

- ICMAT 2009, Singapore: Handoko, A.D. and G.K.L. Goh, "Effects of post-growth treatments on hydrothermally epitaxied $KNbO_3$ thin films"
- Thin Films 2010, Harbin, China: Handoko, A.D. and G.K.L. Goh, "Epitaxial growth of $Na_xK_{1-x}NbO_3$ thin films in water"

Poster Presentations

Handoko, A.D. and G.K.L. Goh, "*Hydrothermal Epitaxy of Lead-free Piezoelectric Films*", presented in the 4th Materials Research Society of Singapore Conference on Advanced Materials, 17-19 March 2010, Singapore (Best poster award judged by panel of senior MRSS members)

Papers in preparation

- Handoko, A.D., G.K.L. Goh, and Chew, R. X., "Ferroelectric and piezoelectrically active $KNbO_3$ thin films synthesized via hydrothermal synthesis" Submitted to CrystEngComm.
- Albertus D. Handoko, H. Q. Le and Gregory K. L. Goh, "Low Temperature Hydrothermal Epitaxy of Oxide Films", to be submitted to Progress in Crystal Growth and Characterization of Materials.
- Handoko, A.D. and G.K.L. Goh, "Hydrothermal Epitaxy of Lead Free $(Na_xK_{1-x})_yLi_{1-y}(Nb_zTa_{1-z})O_3$ Piezoelectrics"

1. Introduction

1.1 Motivation

Lead zirconium titanate (PZT) based ceramics are high-performance piezoelectric materials, extensively used in sensors, actuators and other piezoelectric devices. Their best properties are achieved near the morphotropic phase boundary (MPB) – a discontinuous alteration of crystalline structure found in between the tetragonal and rhombohedral phases due to the chemical substitution of Zr to the Ti sites [1, 2]. At this composition, about 60 percent of PZT weight is made of lead, which is particularly hazardous to the human central nervous system because its ability to bind strongly to proteins [3]. The hazard of lead in PZT is exacerbated by the multiple high-temperature steps (sometimes at temperatures in excess of 1000°C) that are necessary to synthesize PZT with correct composition but unfortunately trigger lead oxide (PbO) volatility [4]. Despite the clear ill-effect of lead toward human and environment, PZT however is still exempt from the Restriction of the Use of Certain Hazardous Substances regulation [5] (RoHS – a law enacted in the Europe Union to limit the amount of hazardous elements in a product) because a similarly high performance material have yet to be demonstrated. It is therefore imperative to continue the search for a suitable lead-free piezoelectric for PZT replacement.

A large portion of the lead-free ferro/piezoelectric materials research focused on the three ceramics system: the

Ever tried. Ever failed. No matter. Try Again. Fail again. Fail better. ***Samuel Beckett (1906-1989)****.*

bismuth based [6-8] (including those with tungsten-bronze structure), niobium based [9-11], and $BaTiO_3$ based [12-14]. Hitherto, the bismuth based piezoelectric ceramics compounds have demonstrated the best properties – some equal or better than PZT [7, 8] – but the bismuth element, being a heavy metal (and highly toxic) itself is not a suitable replacement for lead. Niobate based ceramics, on the other hand, exhibit moderately high piezoelectric performance [15, 16] with a relatively low toxicity level towards humans [17]. Additionally, niobate based ceramics also possess flexible perovskite structures that can accommodate different alloying atoms to form MPBs to further improve their properties. One of the most noteworthy examples are the works done by Saito et al. on $(Na_xK_{1-x})NbO_3$ (NKN) based ceramic compounds [18-20]. NKN can exhibit large electromechanical coupling coefficient comparable to that of soft PZT when doped with different elements like lithium, tantalum and antimony to alter its Curie temperature and form multiple morphotropic phase boundaries (MPB) [18, 19]. Textured growth is also found responsible for NKN's high electromechanical coupling because by texturing to a specific crystallographic direction, most of the piezoelectric responses can be aligned towards the measurement direction (i.e. along the film's out-of-plane) [21].

Until now, bulk niobium based lead-free piezoelectric ceramics (including the NKN based ceramic compounds demonstrated by Saito et al.) are still commonly synthesized by solid-state processing method from their precursors, typically various carbonates and oxides. The main problems with conventional solid-state processing are the reliance to the volatile carbonate precursors and to the surface diffusion/migration reactions among the

precursors, which is why it is necessarily done at high temperatures, to achieve the desired composition. While solid-state processing works well to some other ceramic compounds, in the case of NKN solid-solution process, potassium (as K_2O) starts to volatize at temperatures as low as ≈600°C, leading to severe difficulties in controlling the stoichiometry and ultimately degradation of performance [22-25]. Moreover, conventional solid state synthesis technique requires laborious steps, including pre-mixing, attrition ball milling, calcination, and sintering at high temperature for long hours which consumes large amount of energy [26-28]. Comparatively, a chemical solution synthesis route offers inexpensive processing of NKN with less steps, markedly lower temperature (200°C and below) and possibility of growing epitaxial film over suitable single crystal substrates [29, 30]. Availability of low cost and environmentally friendly process of lead-free ferro/piezoelectric materials will attract the attention of industry.

While simple, non-solid solution perovskite films and powders (e.g. $KNbO_3$ and $NaNbO_3$) have been successfully grown using hydrothermal synthesis route [31, 32], to the author's knowledge there is no thorough report on the understanding of hydrothermally grown I-V solid-solution at or close to the MPB composition. More specifically, there is no report on ferro/piezoelectrically active I-V perovskites grown hydrothermally. We are therefore motivated to direct our research not only to find alternative lead-free ferro/piezoelectric materials to replace PZT and reduce the dependence on lead-based ferro/piezoelectric materials, but also to grow these alternative materials in a more environmentally friendly synthesis routes based on hydrothermal synthesis.

1.2 Specific problem statements

To achieve our main goal of synthesizing lead-free ferro/piezoelectrically active materials hydrothermally, we have identified specific problems with hydrothermally grown I-V perovskites to be addressed in this study:

1. There are no reports on the ferro/piezoelectric properties of hydrothermally synthesized simple (non-solid solution) I-V perovskites. The absence of ferro/piezoelectric properties of even simple (non-solid solution) hydrothermally synthesized I-V perovskites is an indication of unsolved/unoptimized problems during the properties measurements resulting in difficulties of getting decent and reliable results. Our initial guess is that the properties reporting absence may related to the –OH defects generated by incomplete dehydration during hydrothermal growth [33].
2. Previous works on hydrothermally synthesized NKN powders [34, 35] reported failure to obtain compositions at or close to the MPB. Anomalous jump in sodium composition was reported, but no specific understanding why the compositions at/close to the MPB cannot be achieved via hydrothermal synthesis.
3. There are no reports on hydrothermally synthesized I-V solid solution films. Obtaining a dense, textured (or epitaxial) film at the correct composition is also important not only to allow for device integration, but also removing the need for the laborious calcination-sintering steps normally required during bulk processing.

1.3 Objectives and approach

To realize our motivation and tackle the specific problems stated above, we lay out three specific objectives and proposed detailed research plan/approach to reach these objectives. At the same time, the objectives laid construct the main structure of this thesis, and they will be followed and discussed closely in the following order:

1. To grow epitaxial, simple (single ABX_3 component, non-substituted) I-V perovskite film hydrothermally and thoroughly investigate its defect–properties correlation, focusing on the trapped –OH defects.

   While hydrothermal epitaxy of simple perovskites have been previously demonstrated [36, 37], in-depth understanding of defects – properties correlation is yet to be established. To achieve this objective, thorough defect – properties correlation study is proposed, which is especially important in hydrothermally epitaxied film due to possible intrinsic –OH/water related defects due to possible incomplete dehydration during synthesis [33]. Specifically, this part of the study is aimed to confirm the presence and possible locations of lattice trapped –OH, discover effective ways of trapped –OH removal, and its effect towards the electrical performance of hydrothermally synthesized KN films. This study's findings will be useful to develop methods to tackle intrinsic defects present in hydrothermally synthesized films in general; and ultimately to realize ferro/piezoelectrically active hydrothermally synthesized films.

2. To grow I-V perovskite solid-solution powders and investigation of their growth mechanism and structural characterization.

   Hydrothermal synthesis of various single type (non-solid solution) I-V perovskites (e.g. $KNbO_3$, $KTaO_3$, $NaTaO_3$, $LiNbO_3$, and $NaNbO_3$ have been demonstrated [23, 30, 32, 38]. It is known that even though they are within the same structural family, they display different growth characteristics, due to different solubility of the precursors and intermediate states/phases present prior to perovskite formation. A few examples are the different solubilities of sodium and potassium intermediate complexes [39] and different dissolution behavior of niobium and tantalum oxide [40]. Dissimilar behavior of growth and phase stability are foreseen to be main obstacles to growing complex compositions. Efforts to obtain solid solution will involve rigorous trial of different processing parameters and identification of synthesis products. Phase identification will rely on X-ray diffraction techniques, coupled with elemental analyses such as energy dispersive X-ray spectroscopy (EDS) and inductively coupled plasma mass spectroscopy (ICP-MS) for acid digestible compounds. Structural models will be developed using peak fitting and Rietveld refinement software. Structures will be compared and contrasted with those synthesized using high temperature solid-state methods in the literature. Ultimately, this part of the study aims to understand the process of synthesizing (or attempts to synthesize) solid solution NKN hydrothermally.

3. To grow epitaxial I-V perovskite solid-solution films hydrothermally on matching conductive substrate.

   Epitaxial film growth of most niobate based end members had been previously shown [30, 41]. However, there are no reports on any I-V solid solution film grown hydrothermally, possibly linked to the difficulties faced in solid solution powders growth [34, 35]. Processing parameters will be systematically adjusted, using knowledge of end members synthesis paths and compositions obtained from first part of this project. Film properties and characterizations will be thoroughly studied, using HRXRD intended for thin film analysis, AFM to gauge surface roughness of the film, TEM to understand epitaxial relation between substrate and film, also identify defects and relate them to the properties. Results from the electrical characterization, including dielectric testing, ferroelectric and piezoelectric testing will be related to the structural imperfections. Ultimately this section of the study aims to understand the growth of ferro/piezoelectrically active epitaxial solid solution films. Knowledge obtained from the previous study on non-solid-solution film will also be applied to achieve the best properties of solid solution film.

To enable the readers to read this thesis in the right context, some useful background information on the perovskites materials system, hydrothermal synthesis and epitaxy, and general ferroelectric response of materials will be discussed briefly in Chapter 2. Materials synthesis and characterization methods are consolidated in Chapter 43.

2. Literature Review

2.1 Perovskite structure

Perovskites, an important class of ceramic material with general formula of ABX_3, are highly attractive to many commercial and industrial applications today. Perovskites are the most abundant mineral on earth [42] and practically every element of the periodic table (with the exception of the noble gases) can be found in some perovskites or perovskites variant [43]. Perovskites are arguably the most studied inorganic materials due to their interesting electrical, optical and physical properties. A quick search through Web of Science search engine shows that since early 1990s, there are over 1200 papers on the crystal structure and properties of perovskites published each year from a spectrum of research disciplines [44]. The name *"perovskite"* originally refers to the $CaTiO_3$ mineral, a *pseudocubic* crystal named after Count L.A. Perovskii[†]. Now, the word perovskite is used to describe a group of crystals with similar structure to $CaTiO_3$ represented by a general formula of ABX_3: the "A" and "B" represent two types of cations (positively charged ions) and "X" represents the anion (negatively charged ions).

An ideal (*aristotype*) perovskite is cubic, with "A" cations sitting in the large eightfold coordinated site at (0, 0, 0), "B" cations in the

The beginning of knowledge is the discovery of something we do not understand. ***Frank Herbert (1920-1986).***

[†] (1792-1856)

octahedral coordinated site at (½, ½, ½) and "X" anions at equipoint (½, ½, 0) (Figure 1 (a)). The packing of the ions can alternatively be thought as a closely packed face-centered cubic (FCC) array of A and X ions (represented by yellow balls in Figure 1 (b)), as previously suggested by Mitchell [45]. The B ions then occupy a quarter of the octahedral vacant sites in FCC array (represented by a black ball on the center). The rest of the octahedral vacant sites are located on the center of the cube edges, represented by red dotted lines. This visualization is more common in perovskites that have similarly sized "A" cations and "X" anions.

Ideal perovskites are very stable, even at high temperatures, and possess huge dielectric constant that makes $BaTiO_3$ perovskites popular as capacitors during World War II period [46]. The high chemical stability of perovskites is mainly attributed to the strong pairs of B-X coordination that form the structurally rigid BX_6 octahedra. Due to the symmetry however, an ideal perovskites cannot exhibit significant non-linear dielectric properties like ferroelectricity, except when the crystals are physically distorted to induce lowering of the symmetry [47].

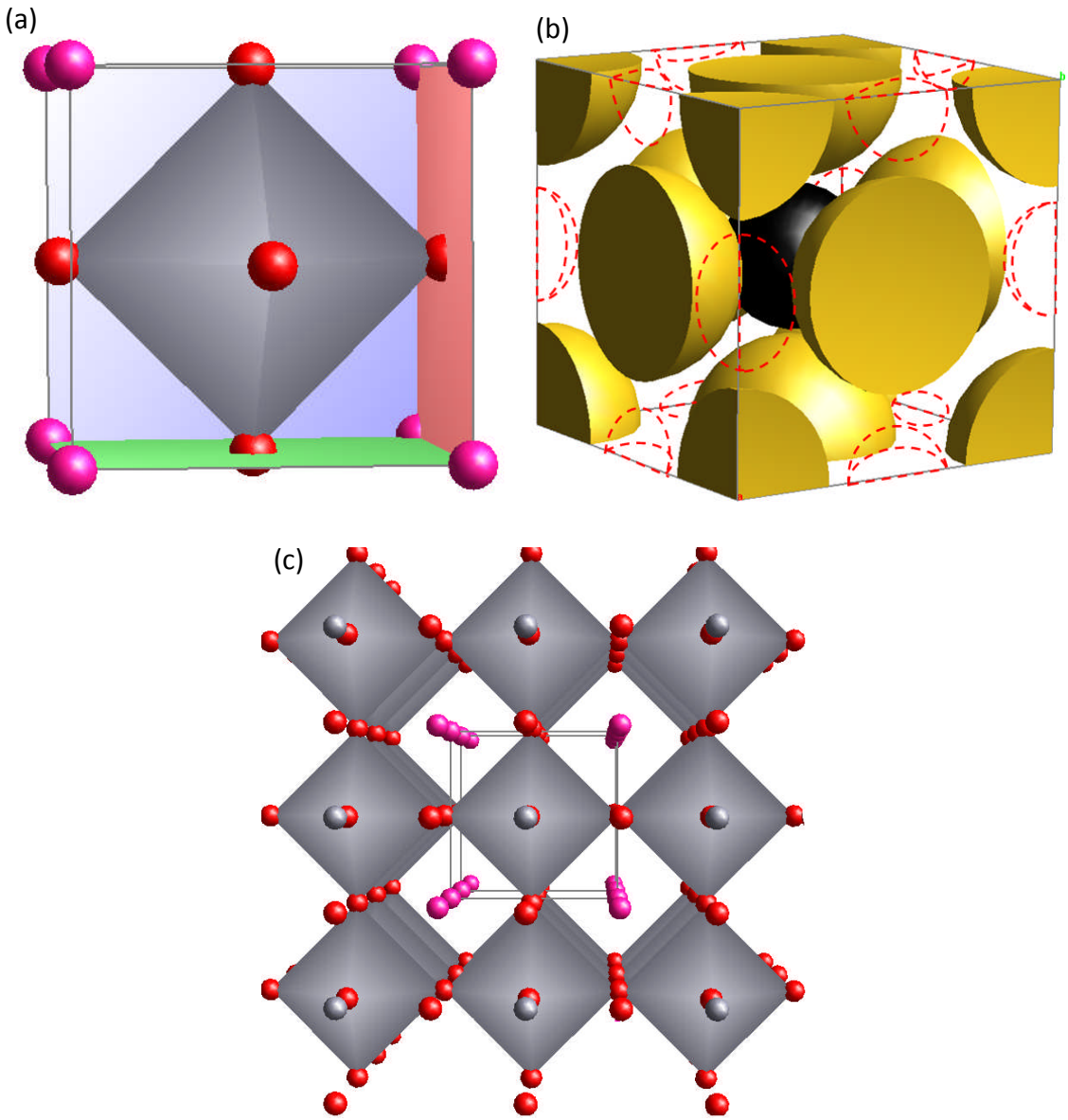

Figure 1: (a) The structure of $SrTiO_3$ (STO), an example of cubic perovskite structure. "B" sites atoms are each bonded with six "X" anions forming a corner-shared BX_6octahedra network. "A" site atoms occupy spaces in between octahedra channels. (b) Alternative views of a cubic perovskite structure, showing an FCC-packed "A" and "X" atoms (yellow balls) with "B" atoms occupying a quarter of the octahedral site in the center (black ball). The rest of the octahedral vacant sites are located on the cube edges, marked with dotted lines. (c) View of several STO unit cells down the [001] direction, showing rows of "A" atoms sitting on a tunnel-like space in between the BX_6 octahedral network.

If we view the perovskite structure array down the [001] axis (Figure 1 (c)), the "A" atoms can be visualized as if they were sitting on the center of tunnel-like space formed by

the 3D network of corner sharing BX_6 octahedra. This tunnel-like space allows the freedom of either accommodating different types of "A" atoms or having them empty i.e. vacancies. Different types of crystal impurity/defects can be responded by slightly tilting the flexible corner-connected BX_6 octahedral frameworks, creating different variations of the ideal perovskite without radically changing the structure (i.e. each BX_6 octahedron is still rigid and corner connected to the other octahedra).

The earliest and possibly the most commonly used measure of perovskite distortion and stability is the "tolerance factor" proposed by Goldschmidt in early 1920s [48]. The Goldschmidt tolerance factor (τ) is defined as:

$$\tau = \frac{r_A + r_X}{\sqrt{2}(r_B + r_X)}$$

where r_A, r_B, and r_X are the ionic radii of A, B, and X ions in the ABX_3 perovskite, respectively. For an ideal (cubic) perovskite, assuming that the bond length is equal to the sum of two ionic radii, the ratio of the bond length of A–O bond to the bond length of B–O bond should be $\sqrt{2}/1$, yielding a τ value of 1.0. Different τ value obtained with different A, B and X ion combinations could predict the formability and degree of perovskite distortion. The larger τ value deviation from 1 the larger the geometric distortion is, up to a point where certain A-B-X ion combinations cannot form perovskite structures because the τ value is outside the range of 0.75 to 1 [49].

However, it has been shown that although Goldschmidt's tolerance factor is a necessary criteria but not sufficient to predict formability, stability and distortion behavior of perovskite structure [50]. Megaw [51] and later Howard and Stokes [52] use group-

theoretical approach on the perovskite system and compiled five possible perovskite variations from the aristotype (ideal) perovskite: (1) distortion in the BX_6 octahedra, (2) displacement of the B-cation (both ferroelectric and antiferroelectric mode), (3) tilting of the BX_6 octahedra, (4) formation of double perovskites ($A_2BB'X_6$) and the related B-site cation orderings: ±1:2 B-site cation ordering (i.e. formation $A_3BB'_2X_9$ perovskites) and ±1:3 B-site cation ordering (i.e. $A_4BB'_3X_{12}$ perovskite). Although the variations are subtle, the resulting crystal structure is significantly altered, such that *eight* different types of modified (imperfect) perovskite other than the aristotype (perfect) can be derived according to the different elements present [42]. Four examples of the modified perovskites model are illustrated in Figure 2.

The subtle variations also greatly affect the perovskite properties, especially on the verge of a phase transformation (either temperature or composition controlled). Lead zirconium titanate ($PbZr_{1-x}Ti_xO_3$, PZT) is a classic example: when the *x* (titanium substitution to zirconium lattice in PZT) approaches 0.48, reaching the composition-controlled phase transformation (more commonly referred to as the morphotropic phase boundary or MPB), it exhibits superior electromechanical performance [53, 54]. In other types perovskite materials, subtle variations in the crystal structure can result in a colossal dielectric material (e.g. $(Ba_{1-x}La_x)(Ti_{1-x}Cr_x)O_3$) [55, 56], a superconductor (e.g. $(La_{2-x}Ba_x)CuO_4$) [57, 58], a photovoltaic and multiferroic material (e.g. $BiFeO_3$) [59], or even thermoelectric generators (e.g. $(Sr_{1-x}Ca_x)_3(Ti_{1-y}Nb_y)_2O_7$) [60]. Other more common (but equally important) applications of perovskites include ferro/piezo/pyro-electric transducer (found in most non-

centrosymmetric perovskites, useful for sensors, actuator and ferroelectric memories) [61], ionic conductor (useful for solid oxide fuel cells – SOFC, e.g. $LaGaO_3$) [62], and a ferromagnet (e.g. $SrFeO_2F$) [63, 64].

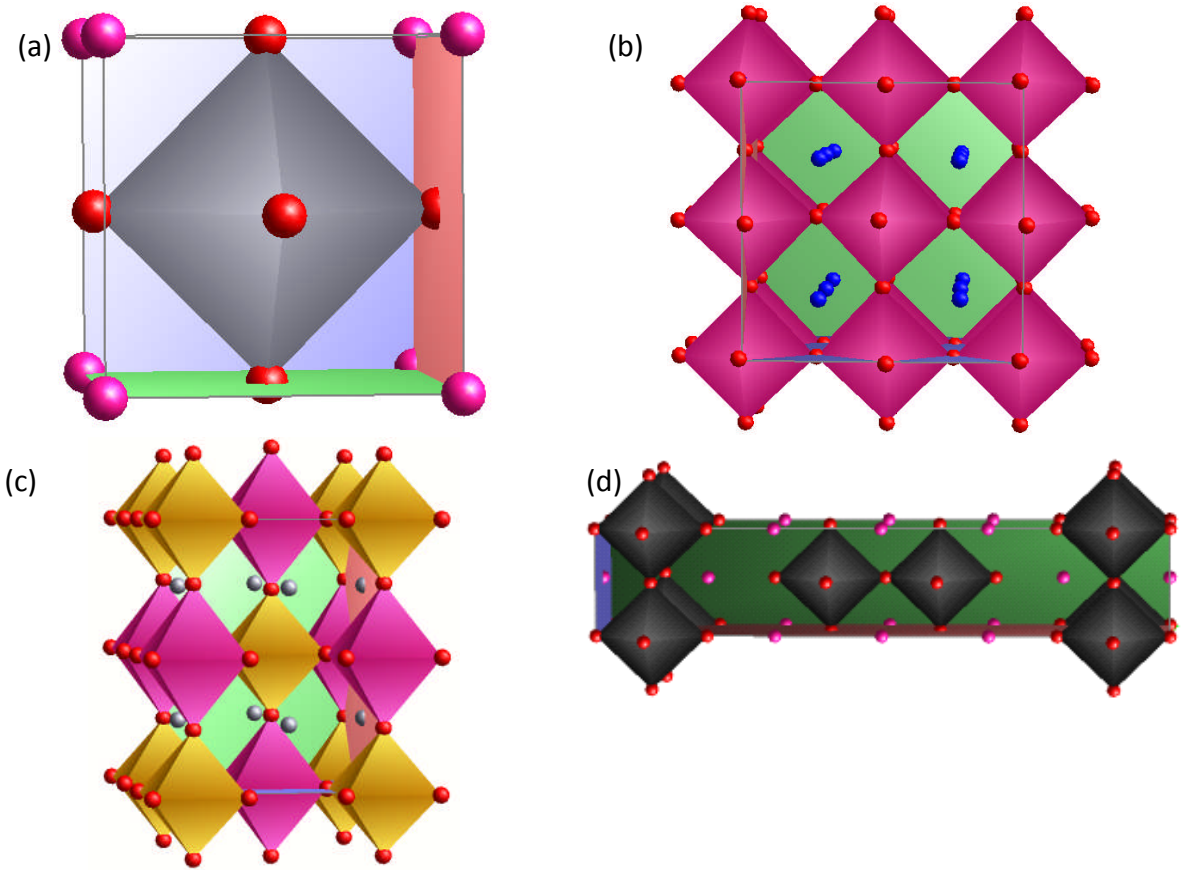

Figure 2: (a) One unit cell of a cubic (P*m* $\bar{3}$*m*) perovskite, for example $SrTiO_3$. The BX_6 units are represented as shaded octahedra ("B" atoms hidden), "A" atoms sit exactly on each corner, and "X" atoms considered lying at the octahedra vertices. (b) One unit cell of monoclinic (P1*m*1) perovskite, for example $Na_xK_{(1-x)}NbO_3$. The "A" sites are located *near* the center of the cubo-octahedral cavity between the BX_6 octahedra. (c) An example of alternating double perovskite with two different B atoms forming alternating BX_6 and $B'X_6$ octahedra along the diagonal. (d) An example of layered perovskite (Ruddleson-Popper) structure. Generated by Topas®.

Most perovskite applications – especially for non-linear optics, ferroelectric and dielectrics – desire single crystal perovskites, because they exhibit better performance (partly because of the single domain properties). However, the usage of the single crystal perovskites is limited due to the high cost and production issues: large and perfect single

crystals are difficult to make because of the high temperature related defects (e.g. cracking during cooling, incongruent melting of the precursors, etc. [65]).

The ability of growing thin film perovskites – particularly a heteroepitaxial perovskite (perovskites film grown over matching substrates that be of slightly different lattice parameters/structures), resolves the cost and production issues and more: it enables the miniaturization and direct integration of electrical components to the substrate level, both reducing power requirement and improving the performance [66]. Many different techniques are available for growing epitaxial perovskite film over matching substrates, but not all can maintain low processing temperature during the epitaxial film growth. Low processing temperature is important because epitaxial perovskites films are prone to thermal related problems like volatization of the elements [67], interlayer diffusions [68], and the formation of interfacial layer [69], which are detrimental to the film properties. In later parts of this thesis it will be demonstrated that hydrothermal synthesis method offers the possibilities of growing dense, epitaxial perovskite films, without the thermal related defects at temperatures of ≤200°C in water.

2.2 Classification of non-ideal perovskite: The Glazer Notation

Some phase transitions in perovskite crystals involve tilting of the octahedral structural units in the crystal, while others can produce a commensurately modulated structure, for example $SrBi_2Ta_2O_9$ (SBT) [70]. SBT was found to be ferroelectric at room temperature and have advantageous over $PbTiO_3$ in terms of excellent fatigue degradation resistance [71].

Glazer [72] had developed an approach to classify perovskites with tilted octahedra by first considering possible tilting patterns then find corresponding subgroups. He expresses the octahedra tilting by the tilt component in pseudo-cubic axes (a, b and c), and later found notations now widely referred as Glazer notation.

The Glazer notation takes the following form: $a^{\#}b^{\#}c^{\#}$. The alphabets "*a, b, c"* refer to the tilting around the [100], [010] and [001] directions (of an ideal perovskite) respectively. The superscript $^{\#}$ takes the value 0, + or – which indicates the tilting directions: "0" indicates that there are no tilts around the particular axis, "+" symbol indicates that tilts of successive octahedra (along the axis) are the same, and "–" symbol indicates that the successive octahedra tilts are in opposite sense. If the tilts are of the same magnitude (or if there is no tilt at all), the alphabet will be repeated, for example $a^0a^0a^0$ indicates that the octahedra are not tilted at any of three axes and they have same magnitude (of zero). Glazer notation will be used to express octahedral tilting in later part of this thesis.

2.3 Ferroelectricity in perovskites

Before going further with the explanation of ferroelectricity, we should first start with a simple illustration of electric field–matter interaction. Figure 3 (a) shows a simple model of an atom, showing a cloud of negatively charged electron field that is bound to the positively charged nucleus. In absence of any disturbance (i.e. equilibrium condition), the sum of the individual electron-nucleus dipole in a single atom will be neutral.

An application of a finite electric field "E" is quickly responded by charged species movements that results in an electron cloud distortion (Figure 3 (b)). Following Coulomb's law of charged matter interaction, the electron cloud distortion results in a complex dipole interaction among itself and with the positively charged nucleus. The sum of all individual interactions can be represented in a simplified single dipole interaction (Figure 3 (c)), separated with a distance "d" and a dipole moment (polarization vector) "M". The net dipole moment will be directly proportional to the externally applied electric field "E" and the material's electronic susceptibility (χ_e), a measure of how easily the material response to the electric field. This phenomenon is termed the *induced electronic polarization*, because it comes from the response electrons bound to an atom under applied field. Consequently, the magnitude of the induced electronic polarization response will vary depending on how much electron in a particular atom (i.e. atomic number) and other factors such as atomic radii, etc.

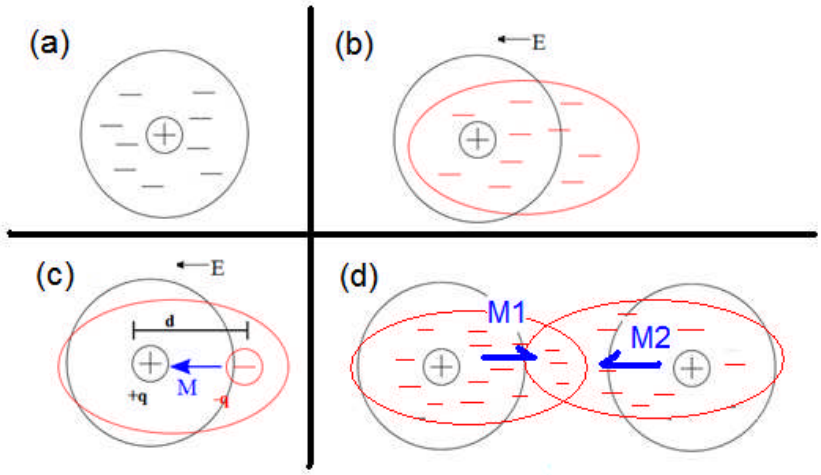

Figure 3: (a-c) Simple atomic model illustrations of electric field induced dipole moment. (d) Two atoms dipole interaction. Adapted from [73].

Similar effect dipole moment can also be obtained by placing an additional atom close enough to the first one such that each other's electron clouds are displaced (Figure 3 (d)). In this case, the same type of atom is placed such that an overlap (sharing) of both atoms' electron cloud occurs, forming a covalent bond. Although the individual dipole moments (M1 and M2) have finite magnitudes, the net dipole moments of these same atoms would be zero because M1 and M2 will be equal but with opposite direction.

The type of atoms placed near the first atom will govern the magnitude of M1 and M2. In the case of two dissimilar atoms placed together, for example Na and Cl, the extremely electronegative Cl atom will attract the electron from Na, forming an ionic bond between the two atoms. In this case, the net dipole moment is non-zero because the magnitudes of M1 and M2 are not equal and thus the Na-Cl bond is said to be polar. In a larger picture, whether or not a material displays a significant net dipole moment (i.e. enough to display a

polar axis) is chiefly determined by the way the atoms are arranged (i.e. the long range order and symmetry).

At room temperature, most of the inorganic crystals is centrosymmetric, that is, a structure class that possesses an inversion center [74]. An example of an imaginary centrosymmetric crystal can be seen in Figure 4 (a). Because of the crystal's symmetry, the individual dipole contributions from different atomic bonds nullify each other, resulting in the absence of a polar axis. Centrosymmetric crystals cannot display a polar axis/net dipole even if the crystal is stressed[*] (Figure 4 (b)). Some other crystals are non-centrosymmetric, but do not have a unique polar axis/net electric dipole moment in the relaxed condition (Figure 4 (c)). This type of crystal is termed *piezoelectric* crystal, which can only display a non permanent polar axis when the crystal is stressed (Figure 4 (d)). If a piezoelectric crystal has many identical unit cells stressed along the same dipole orientation, the dipole strength is altered resulting in surface charges. Similar surface charge generation can also be observed with other types of energy sources, like heat (i.e. pyroelectric crystals) [75].

The third type of crystal, ferroelectric, is more rare and complicated. In addition to the existence of polar axis/electric dipole moment in the relaxed condition (Figure 4 (e)) a key distinguishing feature of a ferroelectric crystal from the rest is the reversibility of the direction of its polar axis/electric dipole moment by the application of an externally applied

[*] Note: There is an exception to this. If the load/field applied is large enough to induce phase transformation to a lower, non-centrosymmetric symmetry, a non-zero net polarization may be observed [84, 85].

electric field. It is therefore a requirement for a ferroelectric material to have two or more stable polar axis directions to switch to. The ability of ferroelectric materials to change and retain the polarized state even after the external field is removed opens the ideas of denser, high capacity ferroelectric based memories [76]. Like in the piezoelectrics case, stressing a ferroelectric crystal disturbs the equilibrium of the net electric dipole moment proportional to the stress applied to the crystal (Figure 4 (f)).

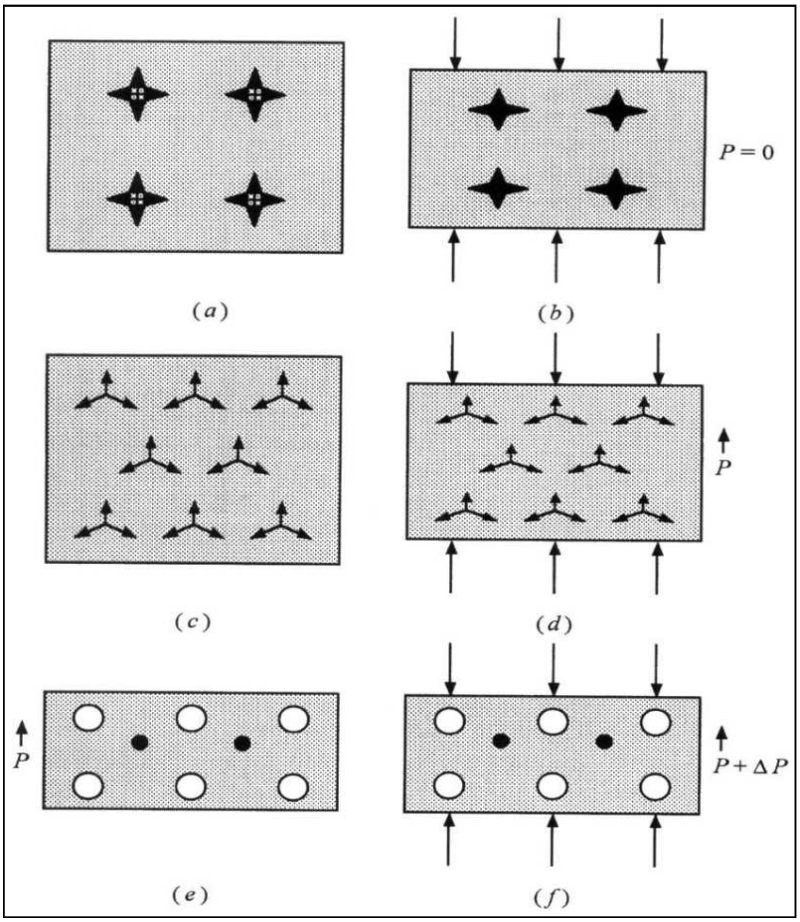

Figure 4: (a) Unstressed centrosymmetric crystal. (b) Stressed centrosymmetric crystal cannot display any net dipole. (c) Unstressed noncentrosymmetric crystal, i.e., piezoelectric. This structure is not ferroelectric because it does not possess a net dipole. (d) Stressed crystal develops a net dipole "P" as shown. (e) Unstressed polar crystal (ferroelectric), with a permanent dipole even in the unstressed state. (f) Stressed ferroelectric crystal varies the dipole moment magnitude by ΔP. Figure taken from [77].

While ferro/piezoelectricity looks straightforward in uniform single crystal unit cells, measuring and understanding ferro/piezoelectric behavior is more complicated in polycrystalline and film samples because of the presence of non-uniformities like grain boundaries, stress/strain in films, crystal defects, etc. There are also complications in measuring the samples' polarization response, which is usually done by measuring the change in a particular crystal's thermodynamic state (e.g. its charge) under a certain stimulus (e.g. change in applied voltage) [78].

Often, the polarization response of a material can be defined as the electronic response due to a "*finite displacement of bound charges of a dielectric in response to an applied electric field, and the orientation of their molecular dipoles*" [77]. The broader definition acknowledges several species that response to the applied stimulus (electric field): space charges, ionic dipoles and the movements (rotations) of bound ionic species.

Early studies of ferroelectricity are phenomenological, based on a Ginzburg-Landau-Devonshire (GLD) thermodynamic theory [79, 80]. The GLD theory has been very successful to predict ferroelectric-related behavior and profile, such as the formation of 180° and 90° *domain walls* during a cubic to tetragonal transition of perovskites such as $BaTiO_3$ and $PbTiO_3$ [81, 82]. Here a ferroelectric "domain" is described as the volume of a crystal that has uniform orientation of its spontaneous polarization (more than one domain can exist within a single crystal) and "domain walls" are therefore the boundaries/regions between different domains.

A single ferroelectric domained crystal is not energetically favorable because of the electrical and mechanical "constraints" imposed to the crystal during the ferroelectric phase transition (usually, from cubic to tetragonal). The electrical constraints are imposed by a depolarizing field that is formed due to surface charges built up on the onset of spontaneous polarization formation. One way to minimize the depolarizing field (other than natural/purpose built conduction of excess polarization charges from the crystal to the atmosphere or grounding mechanisms) is for the crystal to split into domains with oppositely oriented spontaneous polarization (the 180° domains, Figure 5 bottom) such that the net field would be neutralized [83].

Other than the electrical constraints, mechanical constraints can also be imposed to the crystal by the anisotropic change (contraction) of cell parameters when the crystal is cooled through the ferroelectric phase transition. One way to minimize the mechanical stress is for the crystal to rotate the growth direction of the longer axis C_T (almost[†]) perpendicular to the original direction, as shown in Figure 5 (90° domain wall, top). In some cases these 90° ferroelectric domains are visible, for example as twins defect [84].

[†] As shown in the exaggerated illustration in Figure 5, the angle between 90° domains will always be slightly smaller than 90° because the slight difference of longer (C_T) and the two shorter (A_T) axes.

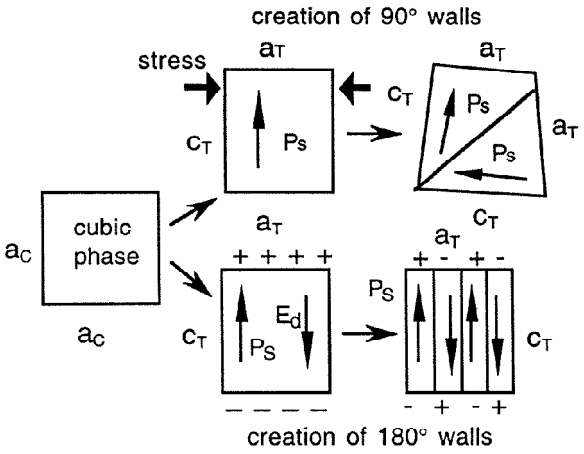

Figure 5: Formation of two different 90° and 180° domain walls in a tetragonal perovskite during the occurrence of a phase transition near T_c.

Reprinted with permission from [83]: Damjanovic, D., Ferroelectric, dielectric and piezoelectric properties of ferroelectric thin films and ceramics. Reports on Progress in Physics, 1998. 61(9): p. 1267. ©1998 IOP Publishing Limited.

It is often suggested that ferroelectric ordering in materials like lead titanate is due to the *freezing* of a polar vibration of the Pb^{2+} ions in the corner of the unit-cell cube against the oxygen octahedron formed by the O^{2-} ions (Figure 6), such that the inversion symmetry of the crystal is broken and ions are displaced such that electrical polarization is formed spontaneously [85]. The frozen polar vibration explanation is rooted in a classical *soft-mode* theory published by Cochran in the early 1960s on the relation between crystal stability and the lattice dynamics (vibration modes) [86, 87].

As a particular crystal undergoes continuous (second order) phase transformation from a more symmetric paraelectric to lower symmetric ferroelectric phase, one of the normal mode frequencies with eigenvector similar to the displacements observed in the ferroelectric phases start to vanish. This phenomena is accompanied by softening of the

mode's force constants due to subtle cancellation of long-range Coulombic forces [76]. The more symmetric paraelectric phase then experiences a "condensation" of the soft optic mode of the atomic vibration, resulting in a spontaneous tetragonal distortion of the structure along one of the cube axes (e.g. [100]) and stabilization of the equivalent soft modes polarized along the other two directions (e.g. [010] and [001]). If we view the "condensation" of the soft optic mode phenomenon from the crystal's lattice perspective, this is actually a cubic to tetragonal phase transition that results in two 'short' axes (relative to the cubic lattice parameter) and one 'long' axis [88]. The lattice distortion therefore, initiates what we observe as permanent dipole (note: that the context of the permanent dipole here is within a single crystal).

Contemporary studies of ferroelectrics based on first-principle calculations suggest that the ferroelectric response is more than just lattice distortions [89-91]. Cohen suggests that the origin of ferroelectricity, observed in the lead titanate system he was studying, is connected to the important hybridization between 3*d* states of the "B" cation and 2*p* states of the "X" anion [90]. Hybridizations between "B" and "X" ions are essential to weaken the short range repulsion (that favors higher symmetry phases) and allow the ferroelectric phase to be stable. The "A" cation also plays an important role in modifying the ferroelectric transition by increasing lattice distortion and hybridizing with the valence states, disturbing B-O interactions.

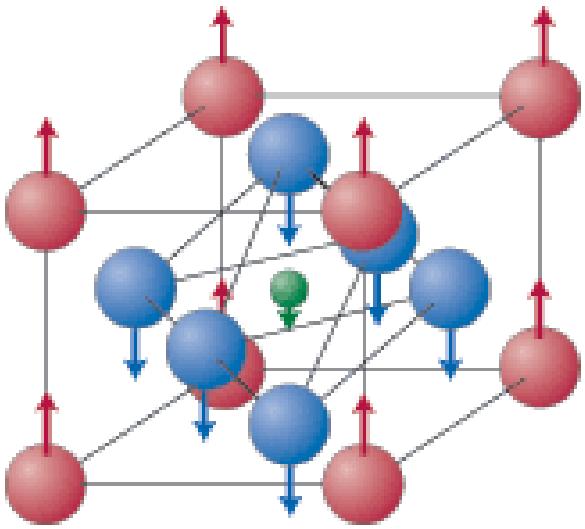

Figure 6: Atomic displacement of the Pb^{2+} (red), Ti^{4+} (green) and O^{2-} (blue) ions leading to the ferroelectric behavior of $PbTiO_3$.

Figure reprinted with permission from Foster, C.M., et al., Anharmonicity of the lowest-frequency A1(TO) phonon in PbTiO3. Physical Review B, 1993. 48(14): p. 10160 [92]. Copyright (1993) by the American Physical Society.

The findings of modern ferroelectric studies highlights that the atomic content is as influential as the structure of a material to the ferroelectric response of a crystal. The research focus was shifted from the temperature-induced ferroelectric transformation (of a single type of material) to a composition controlled phase transformation between two or more types of materials. The combination of two or more material types results in a huge increase in the dielectric/piezoelectric response, especially when the composition is very close to the phase transition boundary, or what is termed morphotropic phase boundary (MPB) as adopted by early chemists/physicists that studies lead-based PZT piezoelectrics [75].

PZT, similar to a single composition $PbTiO_3$ or $KNbO_3$, has a non-polar cubic perovskite structure at high temperature. When it is cooled down, PZT becomes ferroelectric, with two types of possible ferroelectric phase depending on the composition: tetragonal for Ti-rich compositions or rhombohedral for Zr-rich compositions. It has been experimentally shown that PZT display exceptional dielectric and electromechanical response when the composition is at the transition boundary (MPB) between tetragonal and rhombohedral phases [2, 54]. A classical explanation for the exceptional response is the coexistence of tetragonal and rhombohedral phases, increasing the number of possible orientations for the polarization vector, thus facilitating the domains reorientation [75, 93-95]. However, the space groups of the Ti-rich tetragonal and Zr-rich rhombohedral phases (P4*mm* and R3*m*) are *not* symmetry-related, which necessitates first order phase transition at the MPB [96]. However, first order phase transition for PZT at MPB has not been reported [97], and doubts are surfacing whether the rhombohedral-tetragonal phase coexistence is due to compositional or processing related inhomogeneity [98-100].

A recent discovery of new monoclinic PZT phase near MPB composition by Noheda et al. [96, 101, 102] offers a fresh look on the PZT structure, especially those near the MPB composition. It was proposed that the so-called MPB in PZT is actually not a sharp boundary but rather a region containing a distorted monoclinic (C*m*) phase. The newly discovered monoclinic phase fits the role of a bridging/intermediate phase between the tetragonal and rhombohedral phases because of its symmetry relation to both phases (C*m* is a subgroup of both P4*mm* and R3*m*) [101]. Later studies acknowledged the presence of monoclinic phase

in PZT near MPB and propose tetragonal–monoclinic phase coexistence as a possible cause for PZT's high piezoelectric response near MPB composition [103, 104].

Glazer [99] on the other hand suggested there is no strict phase boundary in PZT because both the rhombohedral and tetragonal phases (with the exception of pure $PbZrTiO_3$ and $PbTiO_3$ end members) are actually different monoclinic structures with different degrees of structural disorder. Indeed, contemporary reexamination of of Zr-rich PZT (rhombohedral phase) using high resolution synchrotron reveals that it is actually contains mixture of monoclinic and rhombohedral phase [97, 105]. One of the main difficulties in the experimental approach to this problem is the lack of single crystals of PZT near MPB composition. Glazer's full report on his recent presentation in the 26th European Crystallographic Meeting on single crystal neutron analysis of PZT with x = 0.325 and 0.460 is therefore highly anticipated [106].

Polarization rotation theory [47, 107, 108] quickly surfaced after the monoclinic PZT phase was discovered. Recent studies of classic PZT ferroelectrics reveal that the monoclinic phase(s) may be responsible for the high ferro/piezoelectric response in the MPB system [107, 109]. A unique feature of the monoclinic PZT phase is that their spontaneous polarization is not confined to a definite crystallographic directions, like (001) for tetragonal, (110) for orthorhombic or (111) for rhombohedral, but lies in a symmetry plane with the possibility of its continuous rotation on that plane under the influence of an external electric field [101].

There are other theories on PZT's superior electro-mechanical response near MPB composition, like anomalous softening of tetragonal PZT phase [110], etc. However, as a bottomline, whether it is tetragonal-rhombohdral or tetragonal-monoclinic boundary or continuous transition of different monoclinic phases, all cases have similar effect of increased number of possible polarization vectors that will result in PZT's superior electro-mechanical response [93, 103, 104, 111].

2.4 Materials system: I-V perovskites

2.4.1 $KNbO_3$

Since its discovery in the late 1940's [112], potassium niobate, $KNbO_3$ (then potassium columbate), is fast gaining popularity because of the anomalous dielectric properties, high Curie temperature, and high electromechanical coupling factor it possesses [113]. Today, potassium niobate is still attractive for its excellent nonlinear optical and photorefractive properties [114, 115], finding its way to numerous applications such as second harmonic generator, wave guide, and holographic storage [116].

$KNbO_3$ (KN) has an orthorhombic structure at room temperature (space group A*mm*2, #38) with lattice parameters of *a* = 3.971(1) Å, *b* = 5.697(1) Å, and *c* = 5.723(1) Å [117]. Pure KN is known to have high Curie temperature and electromechanical coupling factor [16, 118, 119] and undergo several phase transformations from cubic to rhombohedral at -40 to 435°C (Figure 7) [120, 121]. Unfortunately, these multiple phase transitions, alongside high temperature related problems like ease of K_2O volatization [122], incongruent melting of its precursors (K_2CO_3 and Nb_2O_5) [123, 124], make growing high quality $KNbO_3$ single crystals or films difficult [65]. Herein lies the opportunity to develop a novel and effective method to grow $KNbO_3$ and related materials at temperatures below the phase transitions.

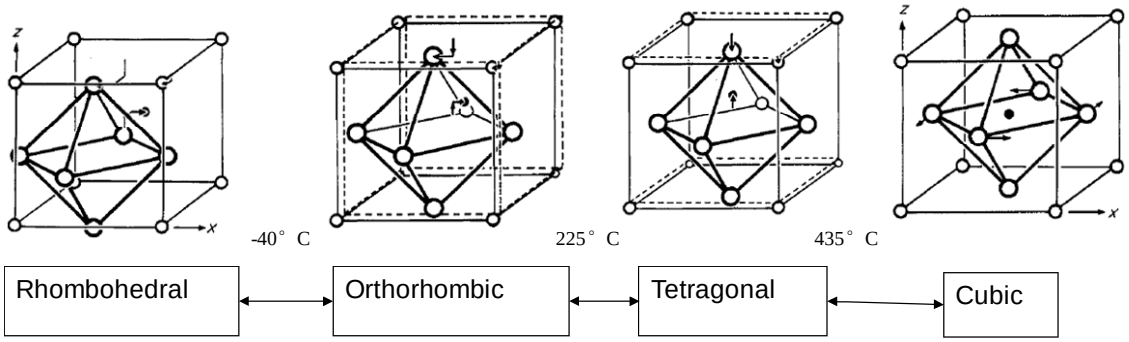

Figure 7: Phase transformations of $KNbO_3$, showing three possible phase transformations of rhombohedral to orthorhombic, orthorhombic to tetragonal and tetragonal to cubic at -40, 225 and 435°C respectively.

Adapted with permissions from [125]: Hewat, A.W., Cubic-tetragonal-orthorhombic-rhombohedral ferroelectric transitions in perovskite potassium niobate: neutron powder profile refinement of the structures. Journal of Physics C: Solid State Physics, 1973. 6(16): p. 2559-2572. ©1973 IOP Publishing Limited.

$KNbO_3$ obtains its net polarization from the displacement of niobium atoms from their centrosymmetric (cubic) sites in the center of mass of oxygen atoms in octahedra down the phase transitions (see illustration in Figure 8). Uneven contraction of the cubic unit cell during the phase transition is accommodated by NbO_6 octahedra tilting to a greater extent rather than distortion, owing to the rigidity of the NbO_6 octahedra. Numerous combinations of concerted tilting of the adjoining NbO_6 octahedra give $KNbO_3$ (or rather any perovskite structure in general) the structural flexibility to accommodate different types of substitution and interstitial atoms that could either result in the amplification or dampening of the net polarization. This opens vast pathways to synthesize different types of complex materials suitable for lead-free piezoelectric compounds.

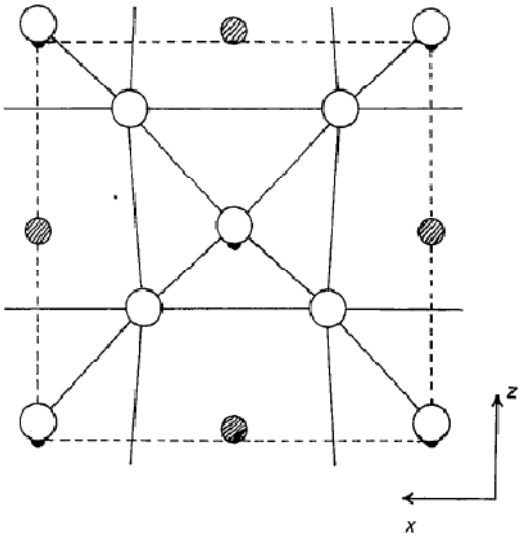

Figure 8: Projection of KN structure seen from (010); showing displacements from aristotype perovksite.

Dashed line outlines unit cell and full lines outline NbO_6 octahedra.

Reproduced with permission of the International Union of Crystallography from reference [126]: Katz, L. and H.D. Megaw, The structure of potassium niobate at room temperature: the solution of a pseudosymmetric structure by Fourier methods. Acta Crystallographica, 1967. 22(5): p. 639-648. ©1967 IUCr Journals (http://journals.iucr.org/)

2.4.2 $NaNbO_3$

$NaNbO_3$ (NN) is anti-ferroelectric at room temperature and because of that it has attracted comparatively less attention than the potassium compound. Compared to $KNbO_3$ (KN), NN exhibits a more complex phase transformations upon cooling below 640°C [28, 127, 128] (see Figure 10, left hand side axis).

Usually, the only way for NN to display ferroelectricity is by doping such that a ferroelectric solid solution with lower symmetry appears. However, it has been reported that pure NN could also display ferro/piezoelectricity when it is in the nanorod (Figure 9) [129] or a very thin film form [130, 131], or when appropriately poled [132]. Although the

reported ferro/piezoelectric constant value was typically small (Figure 9 (c), coercive field (E_c) = 16 kV/cm, remnant polarization (P_r) = 27 μC/cm^2 respectively), the ferroelectricity was stable up to ≈200°C, within the operating temperature of most electronic devices [132].

Similar anti-ferroelectric to ferroelectric transition has also been observed in other perovskite systems like $PbZrO_3$ [131]. The exact cause is not really understood, but it was proposed the formation of a metastable ferroelectric phase due to either external poling [132, 133] or a self-induced interfacial field between the film and substrate when the film dimension is low [130, 131]. The discovery of an anti-ferroelectric to ferroelectric transition in NN and other materials is important because it expands the type of materials that can be used for nonvolatile memory applications.

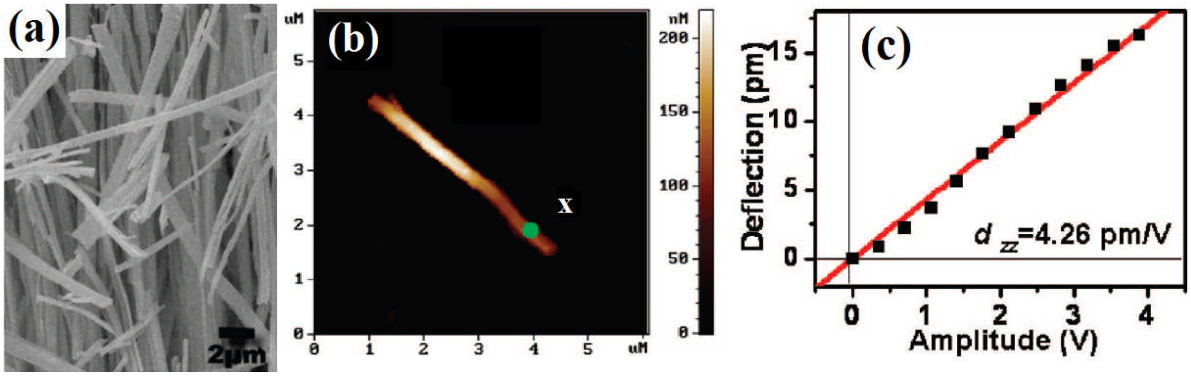

Figure 9: (a) $NaNbO_3$ nanowires obtained from hydrothermal synthesis followed by heat treatment at 400°C. (b) The piezoelectric response of normally antiferroelectric $NaNbO_3$ and the (c) measured piezoresponse at the point X using piezoelectric force microscopy.

Adapted with permission from [129], T.-Y. Ke et al., Sodium Niobate Nanowire and Its Piezoelectricity. The Journal of Physical Chemistry C, 2008. 112(24): p. 8827-8831. © 2008 American Chemical Society.

Another importance of NN is due to its solid solution formation with KN. Although it has been shown that NN is able to form a complete solid solution with KN [39, 134], the peculiarity of its electrical performance is quickly overshadowed by the high performance lead zirconium titanate (PZT) solid solution that was discovered and scrutinized within the same decade [2]. Now the NN-KN (NKN) solid solution has made a re-appearance due to environmental concerns of PZT, and more about NKN can be read in the next section.

2.4.3 $Na_xK_{(1-x)}NbO_3$

Egerton and Dillon [135] are among the first people to report piezoelectric properties of $Na_xK_{(1-x)}NbO_3$ (NKN), since Matthias [112, 113] had first studied its interesting ferroelectric and dielectric properties. Early attempts to synthesize NKN solid solution via high temperature solid-state methods uncovered problems with alkali metal evaporation above 700°C, in particular with the potassium oxide, causing non-stoichiometric products [135-137]. Extensive phase determination of NKN solid solution had established details of its phase diagram (see Figure 10) [128, 138, 139]. Recent renewed interest in this solid solution system have been increasing due to reports of improvements in ferroelectric and piezoelectric properties by additional substitution elements or doping, and urgent redevelopment of lead-free piezoelectric materials [10, 11, 20, 27, 140-144].

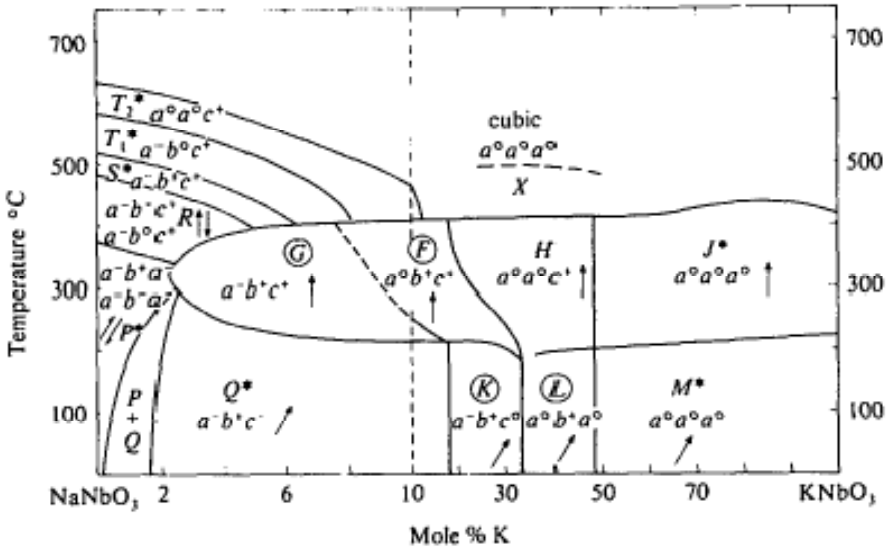

Figure 10: Phase diagram of NKN systems showing temperature and composition effect. To the extreme left is pure $NaNbO_3$ showing complex transformations from 650°C to room temperature. To the extreme right is pure $KNbO_3$ showing cubic-tetragonal-orthorhombic transformations.

Reprinted with permission from [139]: Ahtee, M. and A.W. Hewat, Structural phase transitions in sodium-potassium niobate solid solutions by neutron powder diffraction. Acta Crystallographica Section A, 1978. 34(2): p. 309-317. ©1978 IUCr journals.

More attention is paid to the phase boundary between phase "M" (orthorhombic) and "L" (monoclinic), because NKN starts to show strong ferroelectric properties during these "M" to "L" transformations (more widely referred to as the morphotropic phase boundary (MPB) where phase transformation is composition controlled). When Na substitution of K atoms reaches 51%, it creates anti-parallel cation displacement causing oxygen octahedra in b axis to tilt forming $a^\circ b^+a^\circ$ octahedra tilt system with minimum distortion to the octahedra frame [139]. This increases the sense of polar axis from originally ferroelectric $KNbO_3$ with minimum tilt [15, 51] (illustrated in Figure 11).

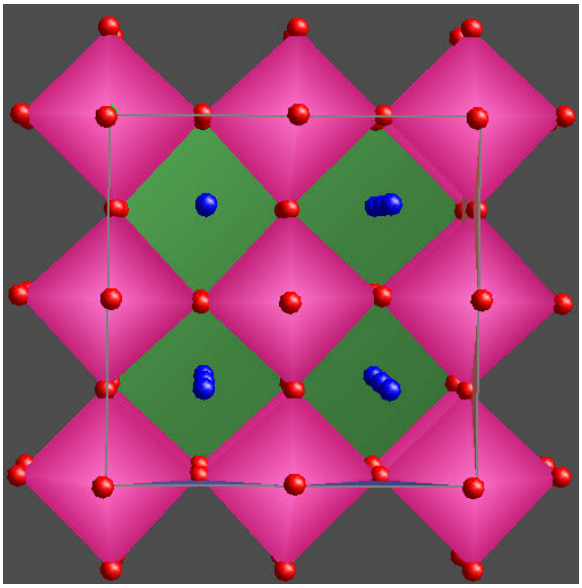

Figure 11: $Na_{0.686}K_{0.314}NbO_3$ structure from XRD data showing octahedra tilting along *b* axis and no tilting in other axes. The tilt system is therefore $a^{\circ}b^{+}a^{\circ}$.

Saito et al. [18, 19] demonstrated that a simple texturing of NKN based compound is able to increase its electric-field-induced strain (d_{33}) to almost double its value when randomly oriented (Figure 12, compare red and blue circles). As a result, a completely lead-free system can be make to display a d_{33} value that is greater than 400 pC/N, comparable to those of soft (donor doped) PZT (Figure 12, black squares for PZT, red circles for NKN-based piezoelectrics). Saito's findings are important in two ways: first, he found out that it is possible to create an additional phase boundaries to the existing ones found in NKN by introducing additional, compatible elements at a right concentration. Second, Saito's findings remind us of the directionality of ferro/piezoelectric properties. Saito highlights that, apart from correct composition, texturing is also equally important in piezoelectric materials. A plethora of renewed research initiatives to investigate possible NKN solid solution with other systems such as $LiNbO_3$, $LiSbO_3$, and $SrTiO_3$ have been triggered by

Saito's finding [9, 10, 145], resulting in not only discoveries in increased ferro/piezoelectric activities but also non-linear optics, wave-guiding [116, 146] and photocatalysis [147].

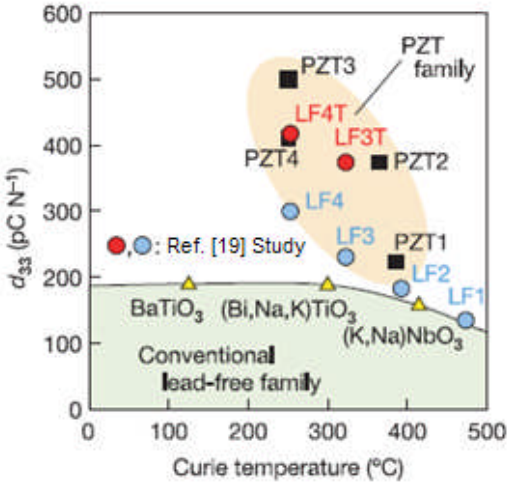

Figure 12: d_{33} value comparison among NKN-LT ceramics as a function of Curie temperature. Triangle points are taken from previously developed lead-free ceramics [136, 137], square points refer to conventional PZT ceramics [54].

Adapted by permission from Macmillan Publishers Ltd.: [19] Lead-free piezoceramics. Nature, 2004. 432(7013): p. 84-87. See footnote‡ for the detailed composition.

2.5 Hydrothermal Synthesis

Hydrothermal synthesis can be defined as a method of materials synthesis from aqueous solutions at temperatures above the boiling point of water, with pressures built up autogenously or with overpressure added, with operations at super critical conditions having been reported [148, 149]. The term hydrothermal was introduced by the British

‡LF1: $[(K_{0.5}Na_{0.5})_{0.94}Li_{0.06}]\ NbO_3$, LF2: $[(K_{0.5}Na_{0.5})_{0.96}Li_{0.04}]\ Nb_{0.9}Ta_{0.1}O_3$, LF3: $[(K_{0.5}Na_{0.5})_{0.97}Li_{0.03}]\ Nb_{0.8}Ta_{0.2}O_3$, LF4: $(K_{0.44}Na_{0.52}Li_{0.04})(Nb_{0.86}Ta_{0.10}Sb_{0.04})O_3$. LF3T and LF4T are textured ceramics of LF3 and LF4, respectively. PZT1: $Pb(Zr_{0.52}Ti_{0.48})O_3$. PZT2: $Pb_{0.988}(Zr_{0.48}Ti_{0.52})_{0.976}Nb_{0.024}O_3$. PZT3: commercially available PZT. PZT4: $[(Pb_{0.85}Ba_{0.15})_{0.9925}La_{0.005}](Zr_{0.52}Ti_{0.48})O_3$. The d_{33} values shown in Figure 12 were measured for specimens poled at 5 kV/mm^2.

Geologist, Sir Roderick Murchison (22 February 1792 – 22 October 1871), to describe the action of water at elevated temperature and pressure in bringing about changes in the earth's crust leading to the formation of various rocks and minerals [150]. Modern hydrothermal syntheses take this concept and carry out crystal growth in glass or steel autoclaves with elaborate seals and safety features, such as those shown in Figure 13, in which the precursor is dissolved in an aqueous solution. One of the first to report modern hydrothermal crystal growth is Schafhalt in 1845 [151] to synthesize microscopic crystals of silica.

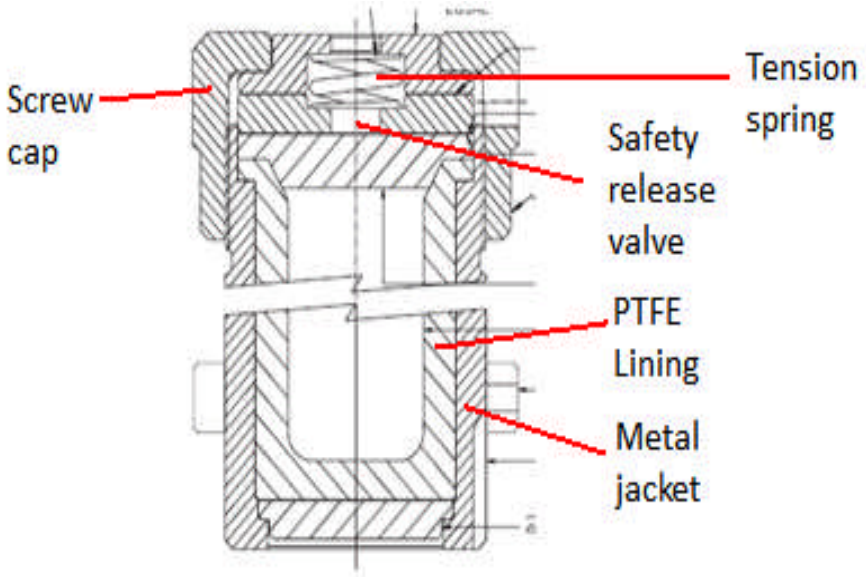

Figure 13: Schematics of Parr® stainless steel autoclave with PTFE inner lining for hydrothermal synthesis and general acid digestion purposes.

Adapted from Parr® 4744 manual [152].

Despite being generally less soluble in water, most modern (purpose built) hydrothermal reactions today use oxide precursor because of their abundance and ease of handling (salts on the other hand are easily soluble in water but are generally more

hygroscopic). This is made possible by the use of mineralizer or complexing agents, usually a strong alkaline solution. The mineralizer can also serve a dual function; during the synthesis of $BaTiO_3$ for example, aqueous $Ba(OH)_2$ acts as both Ba^{2+} ion source and mineralizer, and TiO_2 powder as the Ti^{4+} source.

Hydrothermal synthesis reaction is highly governed by thermodynamics. The progression of a hydrothermal reaction is highly dependent on the reaction condition (e.g. pH, temperature, pressure), which dictates the stability of each species involved in the reaction. Lencka and Riman [153, 154] discovered that simple thermodynamic calculations can be used to predict the most favorable product under hydrothermal condition with certain reaction parameters. An example of the result of such calculation in the hydrothermal growth of $BaTiO_3$ at 90°C in water at different pH values is displayed in Figure 14 (a) where almost 100 mol yield% of $BaTiO_3$ can be obtained using conditions under the shaded region.

One of a few exceptions not included in the thermodynamic calculation is the formation of meta-stable phase(s) before the stable phase is crystallized. One notable example of such a meta-stable phase is the heteropolyniobate crystal, an important polyoxometalate that is useful for drug delivery, catalyst, and nuclear waste storage/processing [155, 156]. These heteropolyniobates can only be formed by restricting the growth time under 20 hours, over which the most favorable perovskite phase precipitates.

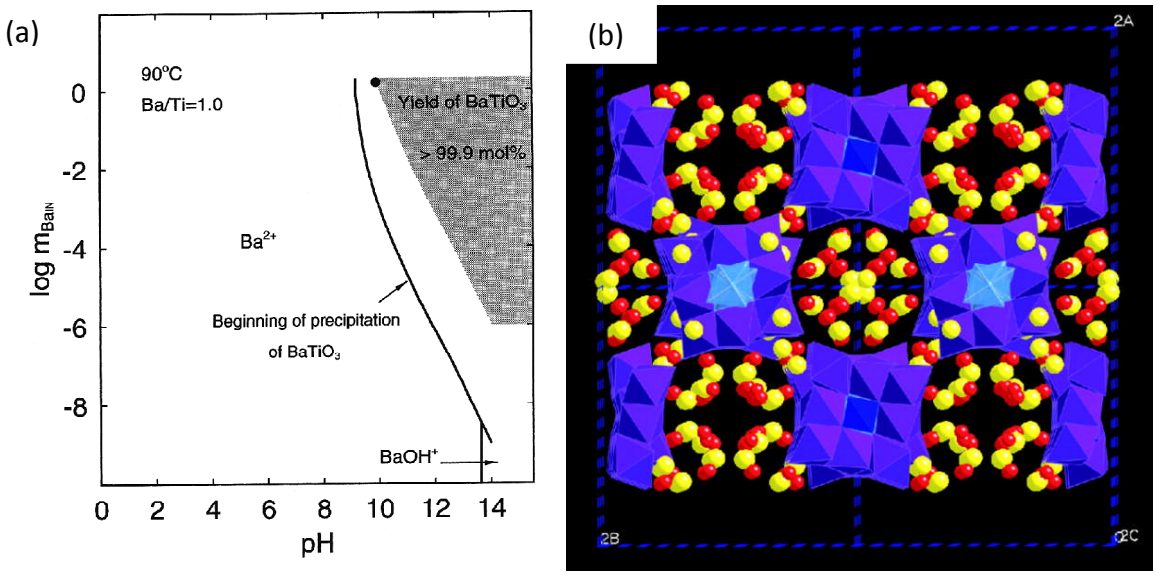

Figure 14: (a) Yield diagram for the hydrothermal synthesis of $BaTiO_3$ from TiO_2 and $Ba(OH)_2$ precursor at 90°C obtained using thermodynamic calculations. (b) Structure of $K_{12}[Ti_2O_2][SiNb_{12}O_{40}]\bullet 16H_2O$ polyoxoniobates viewed down the *c* axis, showing the arrangement of the chains within the *ab* plane. Red spheres are water molecules and yellow spheres are potassium cations.

(a) is taken with permission from reference [157] Eckert, J.O., et al., Kinetics and Mechanisms of Hydrothermal Synthesis of Barium Titanate. Journal of the American Ceramic Society, 1996. 79(11): p. 2929-2939. © (1996) John Wiley & Sons, Inc. (b) is taken from [Nyman, M., et al., A General Synthetic Procedure for Heteropolyniobates. Science, 2002. 297(5583): p. 996-998.]. Reprinted with permission from AAAS.

Reaction kinetics is just as important in hydrothermal synthesis route and need to be considered. In the hydrothermal growth of $BaTiO_3$, TiO_2 is commonly used as a precursor, which is known to have a very low solubility in water (except when it is in the nanoparticle form [158]). There are two different TiO_2 – $BaTiO_3$ transformation mechanisms that were reported. The first $BaTiO_3$ formation mechanism is the in-situ transformation [159], where at the initial stage a continuous layer of $BaTiO_3$ is formed around the TiO_2 surface due to reaction with dissolved Ba^{2+}. Reaction progression mandates barium migration through the BaTiO3 layer until TiO_2 is converted gradually from outside in (Figure 15 (a)).

The second transformation mechanism is the dissolution-reprecipitation reaction that involves multiple reaction steps [160]. In this reaction mechanism, the TiO_2 precursor must first be dissolved, forming hydroxytitanate complex ($Ti(OH)_x^{4-x}$), which could then react with dissolved Ba^{2+} ions to get the final $BaTiO_3$ product. The $BaTiO_3$ will then either precipitate homogeneously in the solution or heterogeneously on the TiO_2 surface (Figure 15 (a)). Intuitively, the reaction rate and mechanisms will change with different choice of precursors, such as the different forms of TiO_2 (anatase, rutile and amorphous gels) that have completely dissolution behavior as reported by Kutty et al. [161].

More recent kinetic studies of hydrothermal growth of $BaTiO_3$ by Eckert et al. [157] however, reveals that both transformation mechanisms may occur during the hydrothermal synthesis of $BaTiO_3$, with the dissolution-reprecipitation dominating at shorter reaction time, and in-situ transformation dominates at longer reaction time. Reaction mechanisms of hydrothermal synthesis of other materials that involve extremely insoluble oxides niobium and tantalum oxides (Nb_2O_5 and Ta_2O_5) has not been studied as much because of the relatively higher requirement of [OH^-] mineralizer concentration (>4M vs. ≈1M in $BaTiO_3$), but the reports of clear precursor solutions during early stages of reactions indicate aggressive leeching of hydroxide mineralizer and dissolution-reprecipitation dominated reaction mechanisms [40, 162].

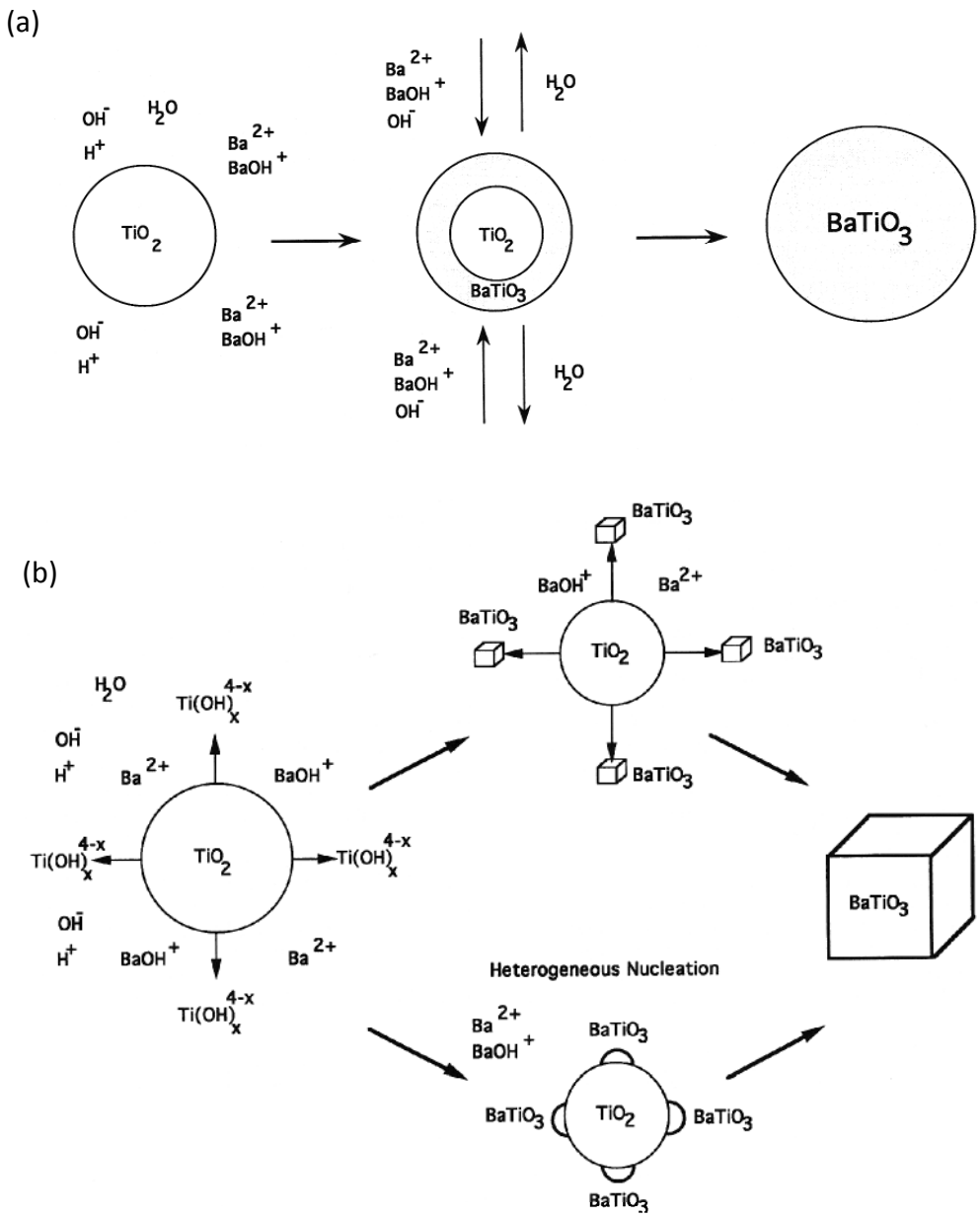

Figure 15: (a) Schematics of the dissolution-reprecipitation and (b) in-situ transformation during the hydrothermal synthesis of $BaTiO_3$ from TiO_2 and $Ba(OH)_2$ precursors.

Reprinted from reference [157] Eckert, J.O., et al., Kinetics and Mechanisms of Hydrothermal Synthesis of Barium Titanate. Journal of the American Ceramic Society, 1996. 79(11): p. 2929-2939. © (1996) John Wiley & Sons, Inc.

2.6 Hydrothermal Epitaxy

Like sol-gel method, hydrothermal epitaxy is categorized as a "chemical solution deposition" method. In this method, the solution is merely a "vehicle" to deliver the precursor(s) to closer to the substrate surface, forming a solid film [29]. The main difference (advantage) of hydrothermal synthesis over sol-gel however, is the absence of a polymeric metalorganic precursor that needs to be removed (pyrolyzed). In hydrothermal epitaxy, the desired film is formed onto the substrate *directly* from the water-based solution. Soluble precursors are transported near the substrate (seed) surface and growth occurs because of heterogeneous nucleation of the soluble precursors following the substrate's crystal structure template.

Hydrothermal synthesis is a proven and cost-effective technique to grow oxide films: it does not involve vacuum systems, makes use of simple and widely available precursors (simple oxides, salts, and hydroxides) and is conducted at lower temperatures than most of other growth methods [29]. Because of the low temperature requirement, hydrothermal synthesis eliminates interfacial reactions (e.g. substrate-film inter diffusion), film cracking and other residual thermal stress related problems that are caused by high processing temperatures in other methods [37].

Hydrothermal synthesis' effectiveness in growing powders and good quality epitaxial films has been demonstrated for a number of materials systems including (but not limited to) lead titanate ($PbTiO_3$) [163], barium titanate ($BaTiO_3$) [164, 165], lead zirconium titanate ($Pb(Zr_{1-x}Ti_x)O_3$) [166] and zinc oxide (ZnO) [167] thin films. Although the thermodynamic

studies shows that the desired phase is stable at much lower [OH^-] molarity [153], the hydrothermal syntheses of these films (except zinc oxide) are still done at relatively high [OH^-] because of the sluggish reaction kinetics at the prescribed [OH^-] from thermodynamic calculations (≥3 days at low [OH^-] vs. 10 to 60 min at higher concentration) [12-14]. Therefore, knowledge of both the thermodynamic and reaction kinetics of the hydrothermal reaction is essential to get a proper control of the epitaxy [168].

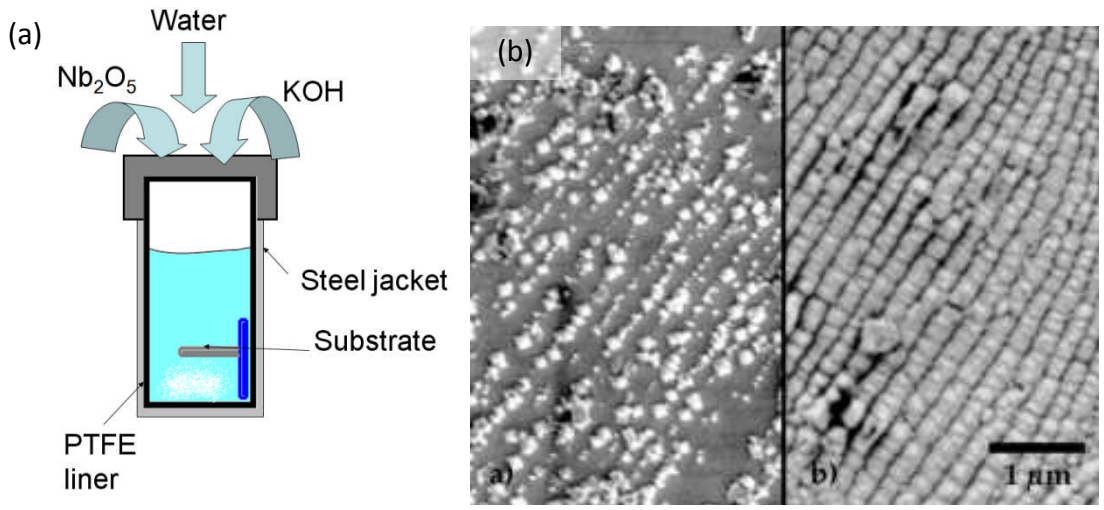

Figure 16: (a) Schematics of hydrothermal epitaxy showing the suspended substrate configuration and (b) SEM micrograph showing initial onset of island nucleation (left) and subsequent growth (right) during hydrothermal epitaxial growth of $BaTiO_3$ thin films.

(b) is reprinted with permission from reference [33]: Lange, F.F. and G.K.L. Goh, Hydrothermal epitaxial growth of perovskite films. Journal of Ceramic Processing Research, 2001. 2(1): p. 4-8.

3. Methods

In this section, various materials synthesis and characterization methods used at different sections of this thesis are described with sufficient detail to enable independent verification, reproduction and/or future development work.

3.1 Synthesis of $KNbO_3$ powder

$KNbO_3$ powders were synthesized hydrothermally using the following method: deionized (DI) water (Millipore) was slowly added and stirred to a beaker, containing appropriate amounts of KOH pellets (>88%, J.T. Baker, Phillipsburg, NJ) to make 6M KOH concentration in 25 ml solution. This clear solution was then transferred to the hydrothermal reactor (4744 PTFE lined reactor, Parr Inst., Moline, IL) containing 1 g Nb_2O_5 powder (99.99%, Aldrich, St. Louis, MO) and then sealed. The sealed hydrothermal reactor was then placed in a programmable convection oven at an optimized condition of 200°C for 2-24 hours. Parameter optimization details of the hydrothermal reaction are not described here but reference can be made to the work of Goh et al. [30, 41].

A scientific or technical study always consists of the following three steps:
1. One decides the objective.
2. One considers the method.
3. One evaluates the method in relation to the objective. ***(Gen'ichi Taguchi 1924-)***

3.2 Synthesis of $KNbO_3$ film

Epitaxial KN perovskite thin films were grown on 10 mm by 5 mm (100) oriented Nb-doped $SrTiO_3$ (Nb:STO) conducting single crystal substrates (MTI Corp., Richmond, CA). The substrates were first cleaned using ultrasonic bath in isopropanol for 5 minutes before being suspended on the same solution described in the KN powder synthesis, polished face down 20 mm above the bottom of the hydrothermal reactor. Deuterium labeled epitaxial KN films were grown using similar setup, but this time the DI water and KOH were replaced with D_2O (99.9%D, Cambridge Isotope Lab., Andover, MA) and KOD (40%, in D_2O, 98% D, Aldrich, St. Louis, MO) respectively in a glove box under argon gas environment. After a preset reaction time the hydrothermal reactor was cooled to touch, the films were removed from the holders, washed repeatedly with distilled water and isopropanol and dried at 60°C for at least an hour before storage in a dry cabinet.

As synthesized KN films were subjected to several post-growth treatments and its combinations. (1) Thermal annealing: as-grown epitaxial KN films were annealed at 400-600°C for 0-3 hours holding time in a box furnace within a closed crucible containing K_2CO_3 powders in order to mitigate K_2O volatility. (2) Oxygen plasma treatment: the as-grown epitaxial KN films were exposed to a reactive ion etcher (Trion Tech., Sunnyvale, FL) working at 200 W with 400 mTorr O_2 pressure for 15 mins.

3.3 Synthesis of $(Na_xK_{1-x})NbO_3$ powder

3.3.1 Direct hydrothermal synthesis of NKN powder

NKN powder was synthesized by reacting 1g of Nb_2O_5 (99.99%, Aldrich, St. Louis, MO) in 25ml of aqueous mixtures of KOH (>88%, J.T. Baker, Phillipsburg, NJ), NaOH (>98%, GCE) and DI water at 200°C for 24 hours in a PTFE lined stainless steel autoclave (Parr Co., Moline, IL). The raw Nb_2O_5 precursor was identified to be a mixture of 91% H-Nb_2O_5 [169] and 9% T-Nb_2O_5 [170]. In all cases, the total [OH^-] was fixed at 6M because it was found to be the optimum concentration for the reaction to complete in 24 hours at 200°C. Fifteen samples with different solid solution composition were synthesized by changing the value of *R* from 0% to 20% where $R = \frac{[NaOH]}{[NaOH]+[KOH]} \times 100\%$ (refer to Table 1 for a list samples). After the reaction was completed, the resulting powder and solution were centrifuged at 3500 rpm for 10 min.

The resulting supernatant was separated and tested for soluble niobate species by gradually replacing the solvent with cold (approx. –21°C) ethanol and/or concentrated (2M) sodium hydroxide solution. The solvent replacement forces intermediate phases to precipitate due to lowered solubility in these solvents [39, 171]. The remaining powder slurry was washed with DI water at room temperature 4-5 times until the pH value was neutral as indicated by a litmus paper. The white powder slurry was then dried at 60°C in air for one day, weighed and stored in a dry box prior to further analysis. To investigate the effects of post growth annealing on the as synthesized powder's phase stability, heat

treatment was carried out in a platinum lined alumina crucible at 800°C for 2 hours with a ramp rate of 10°C/min.

The early stages of NKN phase formation were observed by shortening reaction periods to three hours and below. Six samples with selected *R* values of 10% and 13.3% were prepared to represent the conditions before and after the appearance of second NN phase. The powder slurry, recovered by centrifugation, was then dried at 60 °C in air for one day, weighed and stored in a dry box prior to further analysis.

3.3.2 Synthesis of NKN from hydrothermally grown KN /NN powder

$KNbO_3$ (KN) powder was synthesized by reacting 1g of (previously) hydrothermally synthesized $NaNbO_3$ (NN) with 25ml of 6M aqueous KOH solution (>88%, J.T. Baker, Phillipsburg, NJ) in DI water at 200°C for 1 - 27 hours in a PTFE lined stainless steel autoclave (Parr Co., Moline, IL).

Conversely, $NaNbO_3$ (NN) powder was synthesized using the same method, but this time with 1g of (previously) hydrothermally synthesized $KNbO_3$ in 25ml of 6M aqueous NaOH solution (>98%, Merck) for 0.5 - 3 hours. The $KNbO_3$ (orthorhombic, spacegroup: A*mm2*, *a* = 3.9891(1) Å, *b* = 5.6941(2) Å, *c* = 5.7100(2) Å) and $NaNbO_3$ (orthorhombic, spacegroup: Pbcm, *a* =5.5138(1) Å, *b* = 5.5673(1) Å, *c* = 15.5507(2) Å) precursors were prepared following steps described in Goh et al. [32].

Conversion to a $Na_xK_{1-x}NbO_3$ solid solution was achieved by heating powder mixtures to 800°C at 5°C/minutes and followed by natural cooling. This was done in a tube furnace at 8 Torr of flowing air (mixture of 20% oxygen and 80% nitrogen).

3.4 Hydrothermal epitaxial growth of NKN film

Epitaxial NKN perovskite thin films were grown on 10 by 5 mm (100) oriented Nb-doped $SrTiO_3$ (Nb:STO) conducting single crystal substrates (mixed batches from MTI Corp., Richmond, CA and KMT). The substrates were first cleaned using ultrasonic bath in isopropanol for 5 minutes before being suspended face down 20 mm above the bottom of a 4744 PTFE lined stainless steel hydrothermal reactor (Parr Inst., Moline, IL).

In a separate beaker containing appropriate amounts of KOH (>88%, J.T. Baker, Phillipsburg, NJ) and NaOH (>98%, GCE Chemicals) pellets, deionized water was slowly added and stirred to form 25 ml of 6M total [OH^-] solution before transferring the solution into the hydrothermal reactor containing 1 g Nb_2O_5 (99.99%, Aldrich, St. Louis, MO). The stirring step is essential to ensure that all the hydroxide pellets are dissolved. The hydrothermal reactor was then put into a convection oven at 200°C for 8 hours (NKN) and 130°C for 24 hours (NKN-LT). The raw Nb_2O_5 precursor was identified by XRD to be a mixture of 91% H-Nb_2O_5 [169] and 9% T-Nb_2O_5 [170]. Control of the final Na/K and Ta/Nb ratio in the film was achieved by varying the $\frac{[NaOH]}{([NaOH]+[KOH])}$ (the *R* ratio) and

$\frac{[Ta_2O_5]}{([Nb_2O_5]+[Ta_2O_5])}$ (the *T* ratio) from 0 to 20%. 0.1 - 0.5 g of Ethylene Diamine Tetraacetic Acid (EDTA, 99.8%, Sigma Aldrich, St. Louis, MO) was added to the 25 ml solution to retard the formation of unwanted phase.

3.5 Materials Characterization

3.5.1 Powder and film morphology examination

Microstructures of the hydrothermally grown thin films and powders were examined with a JSM6700F field emission scanning electron microscope (FESEM) operating at these conditions: 5 kV accelerating voltage, 10 μA probe current, 8 mm stage height, 20 aperture, and 0° stage tilt. Thickness measurements for the films were estimated using a surface profilometer (KLA Tencor) and confirmed with cross sectional view using FESEM.

3.5.2 Powder and film elemental analysis

Energy dispersive X-ray spectroscopy (EDS) elemental analysis was done using an OXFORD EDS system attached to a JEOL-5600 thermionic emission scanning electron microscope (SEM) on uncoated powder. Point analysis mode was chosen to standardize probe width, and live time was preset to 100 seconds to obtain statistically meaningful data.

Depth-resolved elemental analysis of hydrothermally grown thin films were done using a TOF-SIMS IV time-of-flight secondary ion mass spectrometer (ION-TOF GmbH, Münster,

Germany) equipped with 25keV Ga gun for analysis, covering an approx. 100x100μm^2 film surface area.

3.5.3 Film and powder x-ray diffraction analysis

Preliminary X-ray diffraction scan of films or powder were conducted using a Bruker® D8 Discover Diffractometer due to its ability to collect wide 2θ range within minutes with its Xe gas-filled HI-STAR area detector.

High resolution gonio (θ-2θ scan) X-ray diffraction, pole figure and rocking curve measurements were done on a PANalytical X'Pert PRO High Resolution X-ray Diffractometer fitted with hybrid four-bounce Ge(220) monochromator with mirror and automatic attenuator to yield Cu-*k*α radiation, operated at 40 kV accelerating voltage, 40 mA current. The goniometer is a half-circle Eulerian cradle with motorized sample stage enables sample tilts of +/- 90°, in-plane rotation of 360°, in-plane X and Y translations of 100 mm, and vertical Z displacement of 11 mm. 1° receiving slit was used for all measurements.

3.5.4 Powder X-ray diffraction

Powder phase content was analyzed by a Philips Multi Purpose Diffractometer with Copper (nickel filtered) radiation at 40 kV and 40 mA, 0.02° step size, 50 seconds per step, and 2θ range from 10 - 150°.

3.5.5 XRD refinement strategies

XRD data analysis and compilation was carried out using the Bruker® TOPAS 3 (main) and Fullprof (secondary) platforms run in the fundamental parameters mode with known instrument parameters.

Rietveld structure refinements of the NKN phases were carefully done based on the series of works by Ahtee and Hewat [138, 139]. The main assumption taken was that the corner-linked NbO_6 octahedra are only distorted to a minor extent – therefore they are treated as rigid units. This assumption was first established by Megaw in her work concerning niobate perovskites [15], and later validated by Glazer in 1972 [72].

The choice of space groups used in the refinements were made in accordance to the NKN phase diagram first constructed by Tennery and Hang [28]. An orthorhombic (*Amm2,* #38, two formula units per cell) space group was used until the phase boundary (MPB) was detected, after which the space group was replaced by P*1m1* (#6, eight formula units per cell). The refinable parameters were progressively released from the most stable parameters (e.g., unit cell parameters) to the least stable (e.g. the atomic occupancy). Once the refinement has converged, normally within 3-4 refinement cycles with, the cell parameter results from each sample were tabulated. Although the atomic displacements result in a reduction in the symmetry to monoclinic, a *pseudocubic* unit cell (Figure 37, shaded cube) can be used for the simplicity and convenience of comparing the cell parameters across the different phases with slight deviation from the ideal (cubic)

structure. The refinement results were therefore converted to pseudocubic unit cell to enable a one-to-one comparison across the MPB.

The refinement consistency was checked by comparing the sodium/potassium occupancy refinement results with the EDS data and the unit cell parameter data with the values obtained from the electron diffraction patterns from TEM. A secondary check of Vegard's law validity within one phase was done by plotting the NKN refined cell volume against sodium occupancy in the NKN phase (*"x"*) and comparing it to the reference data from Ahtee and Hewat [128, 139].

To analyze the intermediate phase, an alternative refinement strategy using a combination of Pawley intensity fitting method [172] and Le Bail intensity extraction function combination [173] (referred to as the whole powder pattern decomposition - WPPD – method [174]) was used. A preliminary qualitative analysis was done by manually matching the reflections of the raw XRD data with thirteen variants of possible intermediate phase found in hydrothermal reactions involving sodium, potassium and niobium oxides [32, 39, 171, 175, 176], and the closest was found to be the sodium hexaniobate, $Na_7HNb_6O_{19}{\cdot}14H_2O$. The initial guess of the unit cell parameters for the WPPD method was taken from the closest matching reference.

To get an approximate weight percentage of the intermediate phase, a Rietveld structure refinement of the powder was done by inserting the refined cell parameters of

the hexaniobate phase obtained via the WPPD method and the atomic parameters of the sodium hexaniobate taken from the closest matching reference ($Na_7HNb_6O_{19}\cdot 14H_2O$) [176]. Structure refinement for other compounds were done according to the previous works on $KNbO_3$ [117], $NaNbO_3$ [177], $KTaO_3$ [178], $LiNbO_3$ [179], Nb_2O_5 [169, 170], and Ta_2O_5 [180] obtained using the ICSD Database for WWW [181]. The actual and maximum niobium and/or tantalum species yield of all samples were compared to ensure all of the niobium and/or tantalum species was precipitated. Details of the refinement codes and atomic positions used in the refinement can be referred to in Table 1, Table 2 and Figure 17 respectively.

Table 1: TOPAS Refinement codes for A*mm2.*

Site	Np	x	y	z	Atom	Occ.	Beq.
Nb1	4	@	=0	=0	Nb+5	Fix	!BNb
K1	2	=1/2	=0	@	K+1	occ	!BK
					Na+1	=(1-occ)	=BK
O1	2	=1/2	=0	@	O-2	Fix	!BO
O2	4	=0	@	@	O-2	Fix	=BO

Table 2: Refinement codes for P*1m1*.

Site	Np	x	y	z	Atom	Occ.	Beq.
Na1	1	xk1	=0	zk1	Na+1	a	!Na
					K+1	=1-a	=Na
Na2	1	=1/2-zk1	=0	=1-xk1	Na+1	=a	=Na
					K+1	=1-a	=Na
Na3	1	=xk1	=1/2	=zk1	Na+1	=a	=Na
					K+1	=1-a	=Na
Na4	1	=xk1	=1/2	=1-xk1	Na+1	=a	=Na
					K+1	=1-a	=Na
Na5	1	=1/2+xk1	=0	=1/2+zk1	Na+1	=a	=Na
					K+1	=1-a	=Na
Na6	1	=1-zk1	=0	=1/2-xk1	Na+1	=a	=Na
					K+1	=1-a	=Na
Na7	1	=1/2+xk1	=1/2	=1/2+zk1	Na+1	=a	=Na

					K+1	=1-a	=Na
Na8	1	=1/2+xk1	=1/2	=1/2-xk1	Na+1	=a	=Na
					K+1	=1-a	=Na
Nb1	2	xn1	yn1	=-xn1	Nb+5	Fix	!Nb
Nb2	2	=xn1	=yn1	=1/2-xn1	Nb+5	Fix	=Nb
Nb3	2	=1/2+xn1	=yn1	=1/2-xn1	Nb+5	Fix	=Nb
Nb4	2	=1/2+xn1	=yn1	=1-xn1	Nb+5	Fix	=Nb
O1	1	x1	=0	zo1	O-2	Fix	!o
O2	1	=-x1	=0	=1/2-zo1	O-2	Fix	=o
O3	1	=-x1	=1/2	=-zo1	O-2	Fix	=o
O4	1	=x1	=1/2	=1/2+zo1	O-2	Fix	=o
O5	2	x2	=1/4+zo1	=1/4	O-2	Fix	=o
O6	2	=1/4	=1/4+zo1	=-x2	O-2	Fix	=o
O7	2	=-x2	=1/4-zo1	=3/4	O-2	Fix	=o
O8	2	=1/4	=1/4-x1	=1/2+x2	O-2	Fix	=o
O9	1	=1/2+x1	=0	=1/2+zo1	O-2	Fix	=o
O10	1	=1/2-x1	=0	=-zo1	O-2	Fix	=o
O11	1	=1/2-x1	=1/2	=1/2-zo1	O-2	Fix	=o
O12	1	=1/2+x1	=1/2	=1+zo1	O-2	Fix	=o
O13	2	=1/2+x2	=1/4+zo1	=3/4	O-2	Fix	=o
O14	2	=3/4	=1/4+x1	=1/2-x2	O-2	Fix	=o
O15	2	=1/2-x2	=1/4-zo1	=1/4	O-2	Fix	=o
O16	2	=3/4	=1/4-x1	=-x2	O-2	Fix	=o

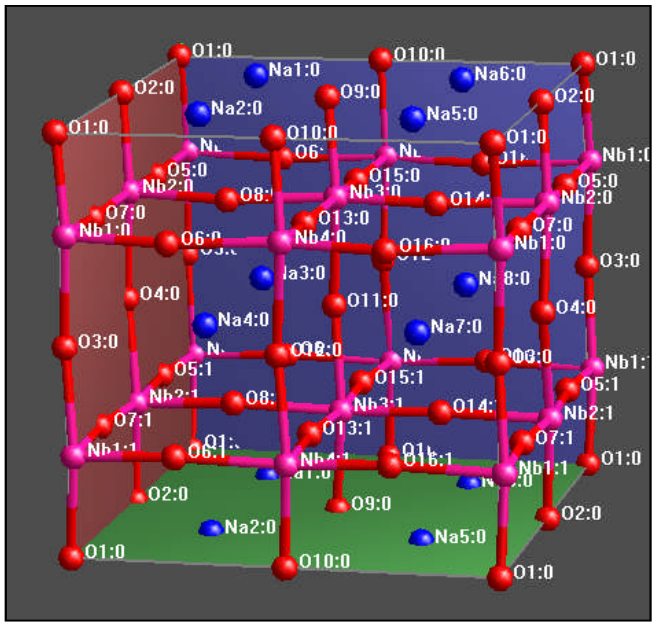

Figure 17: Graphical representative of atoms in one unit cell of NKN (P1*m*1). Here "A" sites are represented by Na atoms. The numbers after the atom name represents sites in refinement code.

3.5.6 Film electrical measurements

For the investigation of electrical and ferroelectric properties of hydrothermally grown films, circular gold electrode patterns were masked onto the film surface, setting up a parallel plate capacitor configuration with the conducting oxide substrate as the bottom electrode.

Dielectric properties up to 100 kHz were evaluated with a HP4194A impedance analyzer fitted with a micro-probe station. Dielectric constant values were calculated using the parallel plate configuration from obtained capacitance and film thickness values.

Leakage current measurements were determined from I-V testing using the same capacitor structure and gold electrodes with a pico-ammeter (HP4140B) that also serves as a DC voltage source.

Ferroelectric response was measured by Radiant Technologies ferroelectric tester using a hysteresis set program. Piezoelectric response was measured by a laser scanning vibrometer (PolyTech GmbH, OFV-056 scanning head and OFV-3001-SF6 vibrometer controller), on the assumption of linear displacement-voltage relationship according to reference [182, 183].

3.5.7 FTIR analysis of powder and films

FTIR analysis was performed on a Perkin Elmer Spectrum 2000 spectrometer with a resolution of $1cm^{-1}$ in transmission mode. Powders were diluted to about 3 wt% in KBr and dried at 60°C for at least one day to remove excess surface water prior to measurement. Each infrared spectrum collected from 400 to 4000 cm^{-1} was an average of 16 measurements.

3.5.8 Thermogravimetric analysis of powders

A simultaneous thermal gravitational analysis (TGA) - differential scanning calorimetry (DSC) was conducted with a SDT2960 (TA Instruments) machine at a 5 °C/min under a 100 ml/min

nitrogen gas flow. Prior to analysis, the powders were dried at 60 °C for at least one day to remove excess surface water.

3.5.9 BET analysis of powders

27 points absorption-desorption BET was done on Quantochrome Nova 1000 Series (Boynton Beach, FL) with N_2 gas adsorbate at liquid N_2 temperature. The correlation coefficients were above 99.7% for each measurement.

3.5.10 Solid state NMR analysis of powders

Solid state NMR spectra were obtained at room temperature on a Bruker AVANCE 400WB spectrometer using a BBO MAS probe, using 4 mm ZrO_2 rotors and spun at 5 kHz. ^2H MAS NMR spectra were recorded at a Larmor frequency of 61.42 MHz with a 6 µs pulse, 3 s recycle time and 64 scans. The reference deuterium signal was obtained from $CDCl_3$ standard reference.

3.5.11 Neutron diffraction of powders

Neutron diffraction data of the $KNbO_3$ powders were collected on the high resolution powder diffractometer (HRPD, Echidna) beamline at high flux Australian reactor (HIFAR) operated by the Australian Nuclear Science and Technology Organisation (ANSTO). Approximately 1.5 g of the $KNbO_3$ was loaded into a 12 mm vanadium can that was rotated

during data collection. The diffraction data were accumulated at ambient temperature using a neutron wavelength of 1.3 Å from 2.75 to 163.95° 2θ in 0.05° steps.

3.5.12 Refinement of the neutron diffraction data

The Rietveld refinement method [184] was used to analyze the raw neutron data to quantifiable lattice, atomic, thermal and shape parameters using FullProf.2k software version 4.80 [185]. The refinement starting point was taken from a previous KN structure determination by Shuaeva and Antipin [117] (space group A*mm2*, #38). Electron density maps were calculated using fourier transformation of the observed and difference intensity plot, performed by GFourier program [186] embedded in the FullProf program [185]. Detailed neutron data treatment is embedded in section 4.2.3.

4. Investigation and Correlation of Ferroelectric Properties of Hydrothermal Epitaxy of $KNbO_3$ Films to the Defects

4.1 Introduction

I:V perovskites has been re-emerging as alternatives to the much established lead based electronic ceramic materials due to environmental concerns of lead. $KNbO_3$ (KN) for example, is known to possess excellent nonlinear optical and photorefractive properties [114, 115, 187], high dielectric constant and ferro/piezoelectric properties [22, 113, 119] due to its spontaneous polarization developed during the structural transitions upon cooling [113, 125, 188].

Although single crystal KN exhibits the best ferro/piezoelectric properties, epitaxial KN films grown on matching single crystal substrates are more attractive; not only because of the difficulties and high cost in growing large single crystal KN but also the potential to achieve smaller, cheaper and better performing ferro/piezoelectric devices. Currently, methods for growing heteroepitaxial $KNbO_3$ thin films, such as pulsed laser deposition, metal-organic chemical vapor deposition, ion-beam sputtering, and sol–gel processing, require processing temperatures in excess of 700°C. The high processing temperature is especially detrimental for achieving a high quality epitaxial KN films because problems like interfacial reactions and cracking due to

To understand is to perceive patterns. ***Sir Isaiah Berlin (1909-1997).***

residual thermal stresses will likely to surface [37, 41]. Additionally, there are two KN phase transitions exist at moderate temperatures (cubic-tetragonal transition near 435°C and tetragonal-orthorhombic near 225°C [65]) that will prohibit the formation of high quality, single-domain film if the epitaxy growth is done above these transition temperatures [37].

On the other hand, hydrothermal epitaxy offers low temperature growth (≤200°C) using mild solution based chemistry that neither requires sophisticated vacuum systems nor toxic metallorganic precursors [29]. Moreover, hydrothermal synthesis has been proven to be flexible and effective in growing vast arrays of high quality heteroepitaxial films, including $PbTiO_3$ [163], $BaTiO_3$ (BT) [164, 165], $Pb(Zr,Ti)O_3$ [166] and ZnO [189] using a variety of substrates.

While much of the growth mechanisms and microstructural evolution of hydrothermally epitaxied KN and its growth parameters has been elucidated [30, 32, 41, 190, 191], to the best of our knowledge none reports its ferroelectric properties. This reporting absence may be connected to the known degradation of electrical properties (dielectric properties in particular) of the as-synthesized hydrothermal epitaxial films that are possibly caused by proton related defects [165, 191]. Protons, in forms of lattice bound OH^- or water groups, can be incorporated in hydrothermally synthesized KN film due to incomplete de-hydroxylation of the hydrated $K_xNb_yO_{(3-z)}(OH)_z \bullet n(H_2O)$ during synthesis [32, 163]. To redress the hydroxyl defects caused problems in hydrothermally synthesized films, several studies were dedicated to explore the different film post-growth treatments, including heat [192],

ozone [191], and oxygen plasma treatments [165, 193], and their positive effects in improving the electrical properties of hydrothermally synthesized films has been reported. However, clear linkage between various post growth treatments and the possible mechanisms of (hydroxyl related) defects removal involved are yet to be established. This chapter is therefore aimed to uncover the link between various post-growth treatments, possible removal of proton related defects, and the resulting improvement of ferroelectric properties of hydrothermally synthesized KN. The best combination of post-growth treatments that resulted in a quadruple improvement of as-grown KN's ferroelectric properties has been singled out and will be discussed in detail.

4.2 Proton Incorporation in Hydrothermally Synthesized $KNbO_3$

Before proceeding with the analysis of electrical and structural studies of epitaxial $KNbO_3$ films, we shall dedicate this section to establish the case of proton incorporation in hydrothermally synthesized KN and identify the possible locations of protons in the KN lattice. The findings of this section will be important not only for the materials system investigated in this study, but also for hydrothermally synthesized materials in general as they share the intimate contact with water during synthesis.

In this section, it will be pointed out that the combination of indirect (e.g. refined cell volume comparison and TGA) and direct techniques (such as solid state NMR and neutron diffraction) can be used as positive identification of lattice trapped –OH/water. Note that the experiments were done on as-synthesized and treated KN powders instead of films due

to lack of material volume in KN film and the fact that the contribution of STO substrates underneath the film is significant and should be avoided.

4.2.1 Indirect proton incorporation determination methods

One of the most widely used methods to probe incorporated –OH/water is by comparing the weight loss of a sample after heat treatment at different temperatures using a thermogravimetric analysis (TGA). This method is therefore indirect, because it is based on assumption that the change in the sample weight is solely due to the removal of the originally incorporated –OH/water (during synthesis) after a certain post-growth treatment.

While it is difficult to completely avoid water adsorption in KN powders, it is possible to minimize the effect of weight loss originated from KN powder's water uptake by combining the TGA measurements with cell parameter study at selected heat treatment temperature points (cell parameter data obtained from the refinement of XRD data). The combined TGA and cell parameter study however, still neglects the fact that adsorbed water can subsequently migrate to KN lattice and change its parameters [194, 195].

The KN powder's weight loss record from the TGA measurement (Figure 18, bottom line) are typical of hydrothermally synthesized powder [196], which has several weight loss regions that can be attributed to the evaporation of water or water-related defects. The surface water is the first to go (labeled surface water), with recorded weight loss of 0.4% after heating the KN powders up to 120°C. The second part (labeled region 1) represents

the evaporation of physisorbed water, indicated by a sharp endothermic DSC peak. The third and fourth weight loss region (labeled region 2 and region 3) occur at a medium temperature range of 200 to 580°C, and have a less distinct boundary and discernable DSC peaks. These are the characteristics of chemisorbed or lattice trapped –OH removal, a slow, diffusion controlled process that may involve removal of oxygen in KN structure.

The KN powder's weight is more or less stable until the fifth region starts at about 850°C where a small endothermic peak can be attributed to a known temperature range for the evaporation (volatization) of K_2O [197]. Assuming that the lattice trapped proton is annealed out as H_2O within Region 3 and the formula weight of KN is close to 180 g/mol after annealing at 580°C, the amount of trapped proton in the KN lattice can be estimated to be about 2.57 mol% by the following calculation:

Table 3: Estimation of –OH fraction in KN from TGA data

Temperature (°C)	*Powder weight (g)*	*Content*	*Formula weight*	*No. of mol*
380	30.6509	KN and H	x	30.6509/x
580	30.6115	KN	180	0.170064
Weight loss (Region 3)	0.0394	H_2O	18	0.002189
Approx. H amount				2.57 mol%

Next, we follow up the DSC-TGA findings by taking the XRD data of KN powders treated at 300, 600 and 900°C to represent the conditions at Region 2, 3, and beyond the suspected K_2O volatility point. To minimize excessive re-absorption of water, the powders are heat treated just before taking their respective XRD patterns for subsequent quantitative analysis.

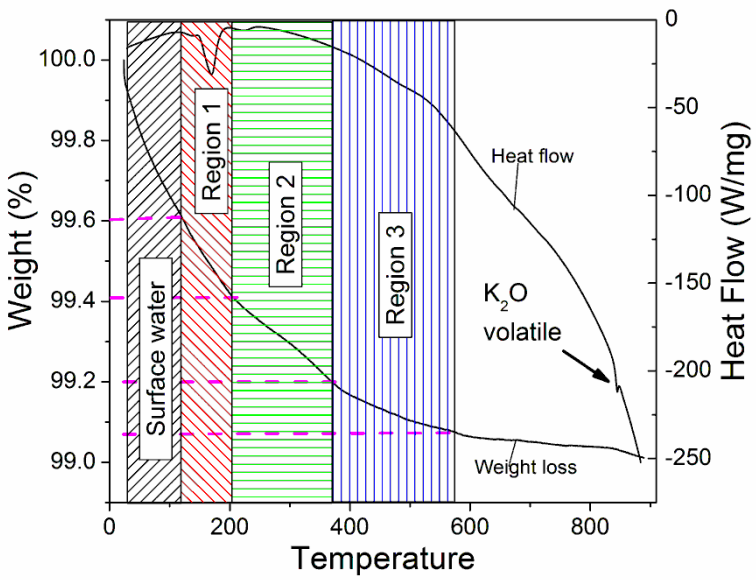

Figure 18: Simultaneous DSC-TGA measurement done on hydrothermally synthesized $KNbO_3$ powder. Top (right scale bar) and bottom lines (right scale bar) represent heat flow data and percentage weight loss respectively. Broken magenta lines are guide to the eye.

The refined cell parameter data of as-grown, heat treated and bulk (Table 4) show several findings that support the hypothesis drawn from DSC-TGA data. First, comparing the refined cell volume information of as-synthesized KN and the reference data synthesized via solid state method [117], hydrothermally synthesized KN has an approx. 0.19$Å^3$ (0.15%) larger cell volume. Assuming insignificant amount of trapped –OH/water content in the bulk KN lattice grown by solid-state method, the 0.19 $Å^3$ cell volume dilation affirms the considerable presence of trapped –OH/water in hydrothermally synthesized powders. Second, the heat treatment at 300°C barely changes the as-synthesized KN powders' cell volume. This indicates that the weight loss recorded up to the Region 2 is mainly caused by the evaporation of physiosorbed water, whose removal will not alter the KN's lattice

parameters. Third, the KN cell parameter value returns close to the bulk reference value after the heat treatment at 600°C (i.e. just above Region 3). As no elemental constituent of KN is expected to volatize at 600°C [197], the change in KN cell parameter must have been caused by evaporation of lattice trapped –OH.

Heat treatment at higher temperature (900°C) appears to be excessive and unnecessary. Apart from the endothermic peak observed in DSC-TGA measurement (Figure 18), the doubling of crystallite size (obtained from a pseudo-Voigt approximation from the XRD data refinement) and contraction of KN cell parameters *below* the bulk reference values (Table 4) after heat treatments at 900°C indicate rapid diffusion and possible K_2O volatility.

Based on the observations from simultaneous DSC-TGA data and powder XRD measurements, it is suggested that an effective post-growth heat treatments to remove trapped water or –OH in hydrothermally synthesized KN should be done in between the Region 3 and 850°C, to prevent possible loss of K_2O.

Table 4: Refined cell parameters of $KNbO_3$. Numbers in brackets represent standard deviation.

	a	*b*	*c*	Vol. (Å^3)	Crystallite size (nm)
As-synthesized	3.9856(1)	5.6946(1)	5.7130(1)	129.66(1)	107(3)
Bulk (ref. [117])	3.971(1)	5.697(1)	5.723(1)	129.47	not recorded
After 300°C for 3H	3.9867(1)	5.6936(3)	5.7110(2)	129.63(1)	134(2)
After 600°C for 3H	3.9874(1)	5.6914(2)	5.7056(2)	129.48(1)	154(4)
After 900°C for 3H	3.9730(1)	5.6947(2)	5.7203(2)	129.42(1)	213(2)

4.2.2 Solid state ^{2}H NMR of hydrothermally synthesized KN

The combination of DSC-TGA and refined cell parameter data can only suggest the existence of –OH related defects empirically. In this section, solid state NMR equipment is utilized to directly probe the presence of lattice trapped –OH/water. Previous ^{1}H solid state NMR experiments have discovered several ^{1}H shifts on KN and NN powders [32]. However, the bulk contribution of ^{1}H solid state NMR signal may be interfered by the higher signals of –OH/water species residing on the surface, and the finding may be inaccurate. In this study, the problem of surface ^{1}H contribution is averted by conducting ^{2}H solid state NMR (instead of ^{1}H) on deuterated KN powders. To achieve complete deuteration, the KN powders were synthesized in ≈99.9% D environment by replacing water (H_2O) and KOH with heavy water (D_2O) and KOD respectively, while keeping the total (estimated) [OH^-] at similar levels with [OD^-]. Once the reaction is completed, –OD/D_2O species residing on the powder surface is expected to be instantly exchanged by H that is 6,600 times more abundant than D in the atmosphere [198], and therefore eliminating any possible ^{2}H surface contribution.

Unlike a wide ^{2}H MAS linewidth observed in a hydrous clinohumite silica, attributed to the dynamic hopping between its four distinct hydrogen/deuterium sites [199], ^{2}H MAS linewidth of the deuterated KN powder display a sharp with a chemical shift of approx. 8.02 ppm (Figure 19 (a)). The singular and sharp ^{2}H MAS linewidth suggests ordered attachment of deuterium to specific sites in hydrothermally grown KN as –OD and not surface adsorbed deuterium, which makes further investigation like neutron diffraction viable.

The chemical shift in ^{1}H or ^{2}H NMR is related to the local electron density near the deuterium nuclei, which can be predicted from the average hydrogen bond strength, neighboring O–O bond distances and electronegativity of the anions [200]. Several ^{1}H or ^{2}H MAS NMR study done on $KTaO_3$ (KT) and $PbTiO_3$ perovskites also indicate a singular, sharp profile of ^{1}H or ^{2}H linewidth [163, 190], with a smaller chemical shift of 5.47 ppm in KT. As another comparison, ^{2}H MAS NMR measurement of deuterated, hydrothermally grown NN powder was also done in this study, showing a smaller 7.79 ppm chemical shift (Figure 19 (b)). As KN, KT and NN have similar atomic arrangements, the similar chemical shift values indicate that the lattice trapped proton/deuterium may attach to similar sites. The slightly smaller chemical shift detected in hydrothermally grown NN and KT compared to KN may be due to the slightly more electronegative Nb anion (than Ta) and longer average bond distances of O – O in KN, thus a stronger O…H bond and increased chemical shift.

It should be noted that the surface ^{2}H peak is absent because, as expected, any surface deuterium left on the powder will be quickly exchanged with proton. Another set of ^{2}H MAS NMR data of non-deuterated, hydrothermally grown KN presented in Figure 19 (c) shows a blank spectrum, confirming that the observed ^{2}H chemical shift was due to the presence of lattice trapped deuterium.

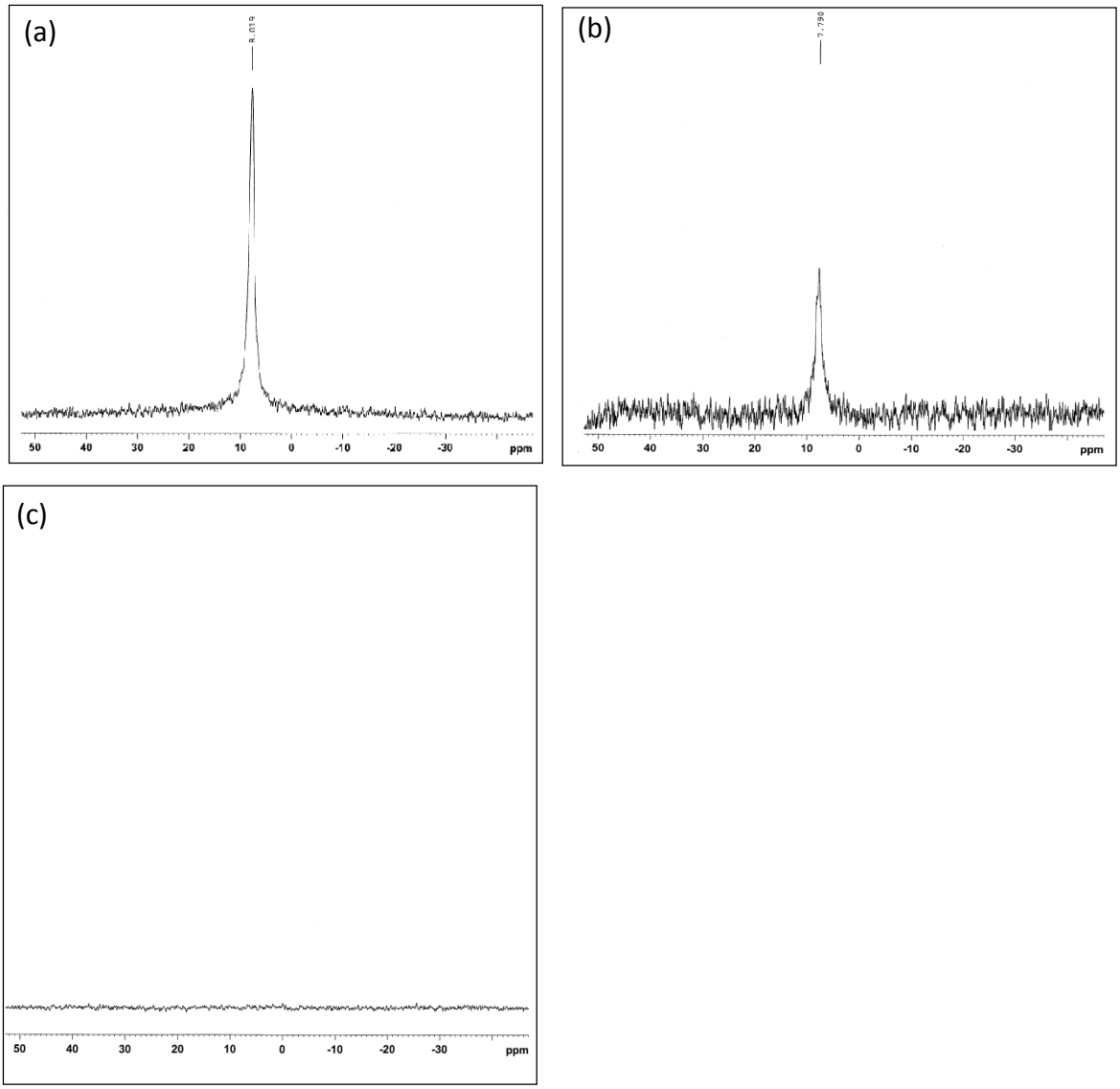

Figure 19: Rotor-synchronized ^{2}H solid state NMR data taken from as-synthesized (a) KN and (b) NN powders synthesized in a deuterium environment using KOD and D_2O. (c) KN powder grown in a normal synthesis environment using KOH and H_2O.

4.2.3 Neutron diffraction experiments

With a confirmed presence of trapped and possibly ordered –OD/OH defects, further analysis to determine probable locations of –OD using neutron diffraction can then be justified. The strategy employed to process the neutron diffraction data is to first generate

the nuclear density difference map, obtained by subtracting forward Fourier transformation of the observed and calculated (refined) neutron diffraction data, and then compare the different nuclear density maps between the as-synthesized and those treated at 600°C.

The optimum heat treatment temperature was chosen according to the DSC-TGA data (Figure 18, just above Region 3), where we hypothesized that most of the lattice trapped water had been evolved out. Figure 20 (a) illustrates the refined neutron diffraction data of as-synthesized, deuterated sample taken at room temperature. The observed data fits well with the calculated intensities based on an orthorhombic KN model, as indicated by the low R factor of 4.398. The Fulprof.2k refinement program [185] allows the neutron scattering densities to be extracted from the Rietveld refinement result, which are then fed to GFourier program [186] that runs the fast-fourier transform algorithm to generate a nuclear density map. Figure 20 (b-c) displays the calculated and observed nuclear density map at x = 0, which are not useful on their own because they look almost exactly similar to each other.

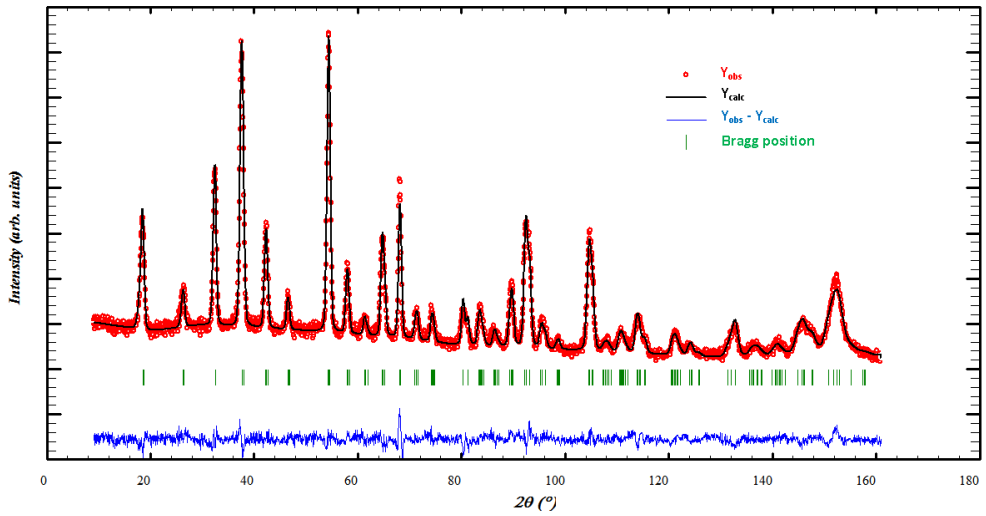

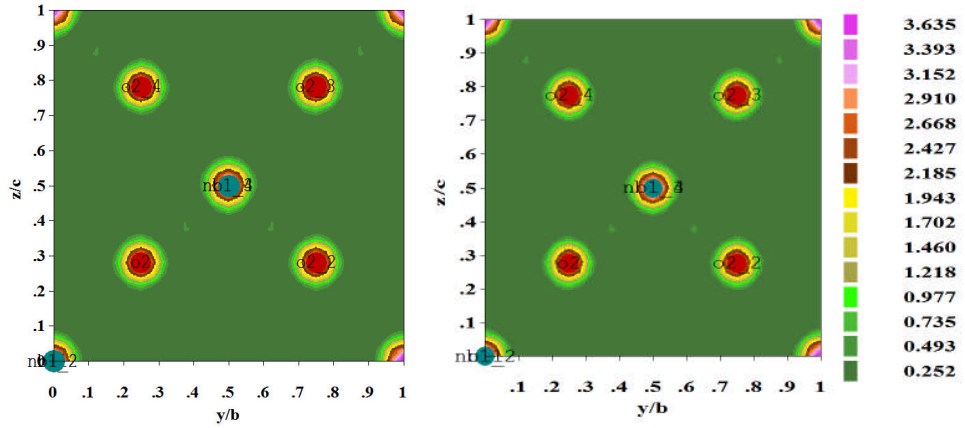

Figure 20: (a) Refined neutron diffraction data of as-synthesized, deuterated $KNbO_3$ sample showing the observed (red circles), calculated (superimposed black lines) and difference plot (bottom blue line). Vertical green lines indicate the possible Bragg peaks generated from the space group. Nuclear density maps calculated from the (b) calculated and (c) observed plot obtained from the neutron diffraction data of the deuterated as-synthesized KN powder

The important information lies in the difference plot (i.e. subtraction of observed plot from the calculated plot) shown Figure 21 (a) (note: the negative differences are ignored because deuterium scattering factor is positive).The nuclear density difference plot shown in Figure 21 (a) indicate presence of nuclear density pockets near the O2 positions that have not been accounted for during the refinement.

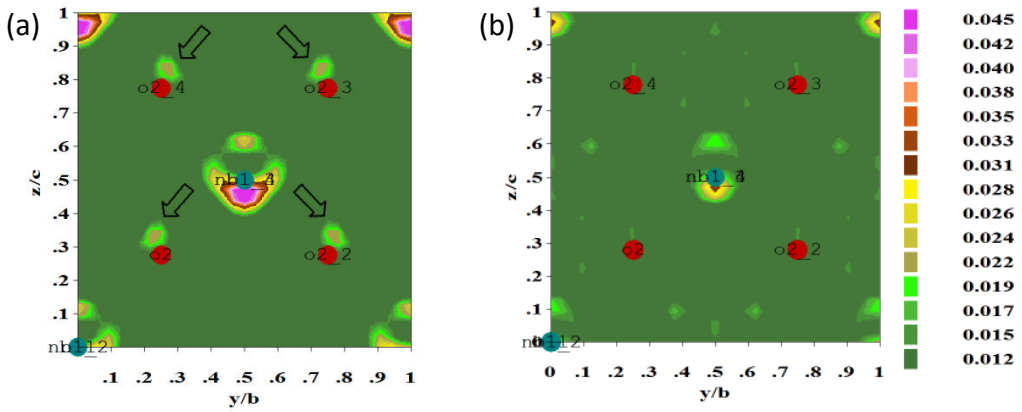

Figure 21: Nuclear density difference plot of (a) as-synthesized and (b) heat treated $KNbO_3$. Pockets of unaccounted positive nuclear densities near (0, 0.224, 0.325; arrows) indicate possible deuterium locations.

When the same refinement routine was implemented to the heat treated sample (at 600°C), we found that the pockets of positive nuclear densities were absent (Figure 21 (b)). Considering the size, the positive nuclear density difference of the pockets, and the fact that they disappeared after heat treatment at 600°C, we are convinced that they represent the most probable locations of deuterium atoms inside KN lattice.

Consistent with the findings from DSC-TGA, and refined cell volume data obtained from XRD measurements, the cell volume data obtained from neutron diffraction also indicate KN cell volume contraction after heat treatment at 600°C (Table 5). How exactly the hydrogen/deuterium atom is removed and the effect to the KN lattice however, is still unknown at this point. What is commonly believed is that the removal of lattice trapped hydrogen (deuterium) likely involves a dehydration reaction [163, 191]:

$$2(OH_O^{\bullet}) \rightarrow H_2O_{(g)} + V_O^{\bullet\bullet} + O_O$$

This means that the removal of –OH related defects via simple heat treatment will necessarily create (new) oxygen vacancy sites. We then released the oxygen occupancy on both XRD and neutron diffraction data, and found an indication of increased oxygen vacancies, particularly in O1 sites from the XRD data (Table 5). The preference of creating oxygen vacancies on the O1 sites may be due to the longer Nb – O1 bond distances (≈2.006(1) Å) compared to the Nb – O2 (≈1.91(4) Å), which makes removal of oxygen at those sites relatively easier.

Table 5: Cell volume and selected occupancy data from refined XRD and neutron data (data from TOPAS)

	Cell Volume data		Occupancy (XRD)		Occupancy (Neutron)		
	XRD	Neutron	O1	O2	O1	O2	D
As grown	129.445(3)	129.83(2)	1.03(2)	0.98(1)	1.10(2)	0.98(1)	0.08 (1)
600°C	129.38 (1)	129.69(1)	0.87(1)	0.95(1)	1.08(2)	0.96(1)	-

To generate a 3D model for visualization, we repeated the refinement using a second program (Bruker TOPAS® 3) by inserting the possible deuterium atom near (0, 0.224, 0.325) found from the nuclear density map. Again the calculated data fits the observed data easily with a recorded R-Bragg of 1.675 (Figure 22, R-Bragg without the addition of deuterium atoms is 1.828). The resulting 3D atomic model can be viewed in Figure 23, with the deuterium atoms occupy the black spheres approx. 8% of the time (based on the occupancy refinement, Table 5). Considering that there are 6 total oxygen positions (2 O1 and 4 O2) in each orthorhombic $KNbO_3$ unit cell (containing 2 formula units per cell), it works out that there are approx. 2.67 mol of hydrogen for every 100 mol of KN. This finding is slightly larger than the estimation obtained by DSC-TGA measurement, indicating that some protons may have been annealed out before Region 3.

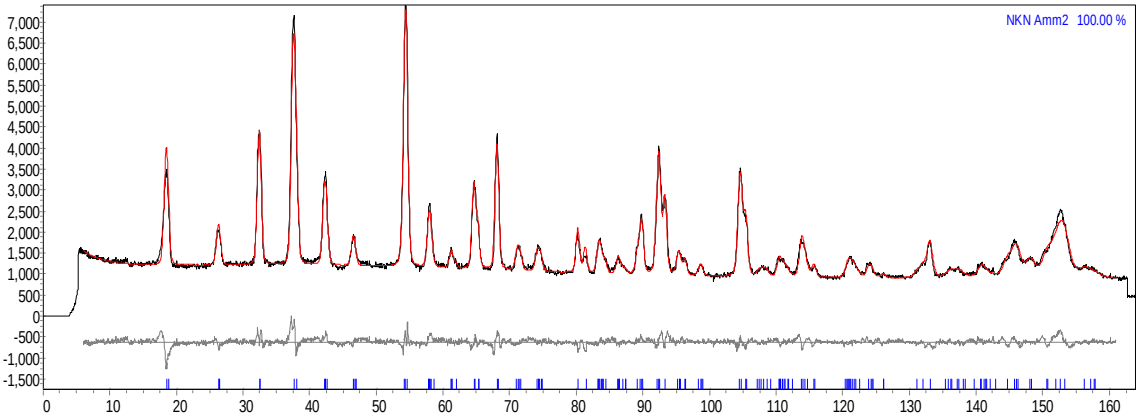

Figure 22: Neutron data fitting with Topas® showing the observed (black line), calculated (superimposed red line) and difference plot (grey line, below). The vertical blue lines on the bottom represent possible reflections generated from the space group number.

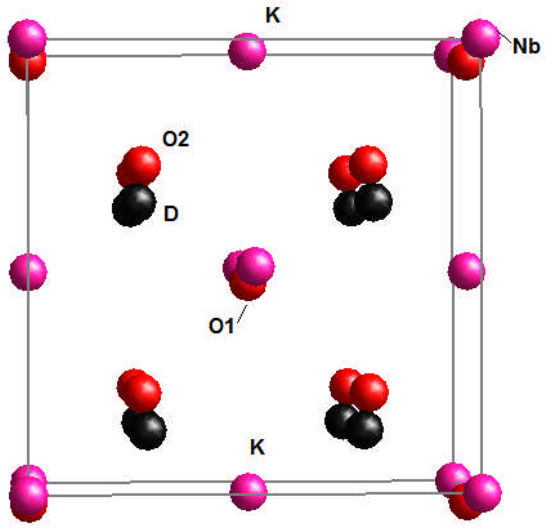

Figure 23: 3D model of $KNbO_3$ looking down the c axis showing the possible location of deuterium atoms adjacent to the O2 positions. Generated using Topas®.

4.3 Hydrothermal growth and characterization of $KNbO_3$ films

4.3.1 As-grown KN films

After establishing the presence of lattice trapped –OH (or –OD) and learnt that it can be removed at 600°C, in this section we move forward to synthesize and characterize epitaxial KN films. The findings from the lattice trapped –OH studies will be linked and/or verified with the electrical characterization of epitaxial KN films.

Phase identification of the hydrothermally grown KN film after 24 hours at 200°C and its epitaxial relationship with Nb:STO substrate are established via XRD and EDS measurements. The average of K/Nb ratio in 8 randomly selected points was found to be approx. 0.97. No other elements were detected by EDS analysis. The slight K/Nb ratio deviation from unity may be caused by due to potassium cation vacancies created to compensate the charge imbalance caused by trapped –OH in KN lattice [32, 190] or due the volatization of potassium during measurement (a thermionic emission SEM was used).

Fast gonio (θ-2θ) XRD survey scan of the as-grown KN film using Panalytical HRXRD (Figure 28 (a)) shows only (0*l*) KN out-of-plane reflections, an indication of epitaxial growth. An off-axis scan pair of $(100)_{o\text{-}KN}$ and $(001)_{STO}$ (Figure 28 (b)[§]) confirms the in-plane ordering

[§] It has been made sure that STO (110) and KN (002) are distinguishable (not overlapped) in the off-axis 2θ scan. See appendix C for details.

between KN film and the STO substrate. The epitaxial relationship between hydrothermally epitaxied KN and Nb:STO substrate is therefore described as:

$$(011)_{o\text{-}KN}/(001)_{pc\text{-}KN} \parallel (100)_{STO},\ [100]_{o\text{-}KN}/[100]_{pc\text{-}KN} \parallel [001]_{STO}$$

Here the subscripts "o" and "pc" refer to the orthorhombic and pseudocubic plane/direction of the $KNbO_3$ respectively while subscript "STO" refers to the plane/direction of the cubic STO. As seen in the schematics of $KNbO_3$ epitaxy over STO substrate in Figure 25, the pseudocubic unit cell is calculated (estimated) to be as follows:

$$a_{pc} \cong a_o ; b_{pc} \cong \sqrt{2} b_o ;\ c_{pc} \cong \sqrt{2} c_o$$

Note that in $(011)_{o\text{-}KNO}/(001)_{pc} \parallel (100)_{STO}$ configuration, the lengths of the a_{pc} and either one of the b_{pc} or c_{pc} that lies on the $(011)_{STO}$ plane are not equal, with an average lattice mismatch of approx. 2.6% [201-203] (see the illustration in Figure 25).

The average full width half-maximum (FWHM) value of as-grown KN film's rocking curve/ω-scan (obtained by pseudo-Voigt curve fitting, Figure 24 (b)) is relatively large at 0.6 – 0.7° when compared to the STO substrate (0.022°). In an epitaxial film, large out-of-plane rocking curve FWHM values usually indicate significant out-of-plane tilt due to film-substrate mismatch [204]. It should also be noted that epitaxial film displaying out-of-plane orientation variation (tilt) is not exclusive to hydrothermally epitaxied KN. For example, a pulsed laser deposition (PLD) epitaxied KN films have also reported to display a typical FWHM values of ≈0.2-0.3° [201].

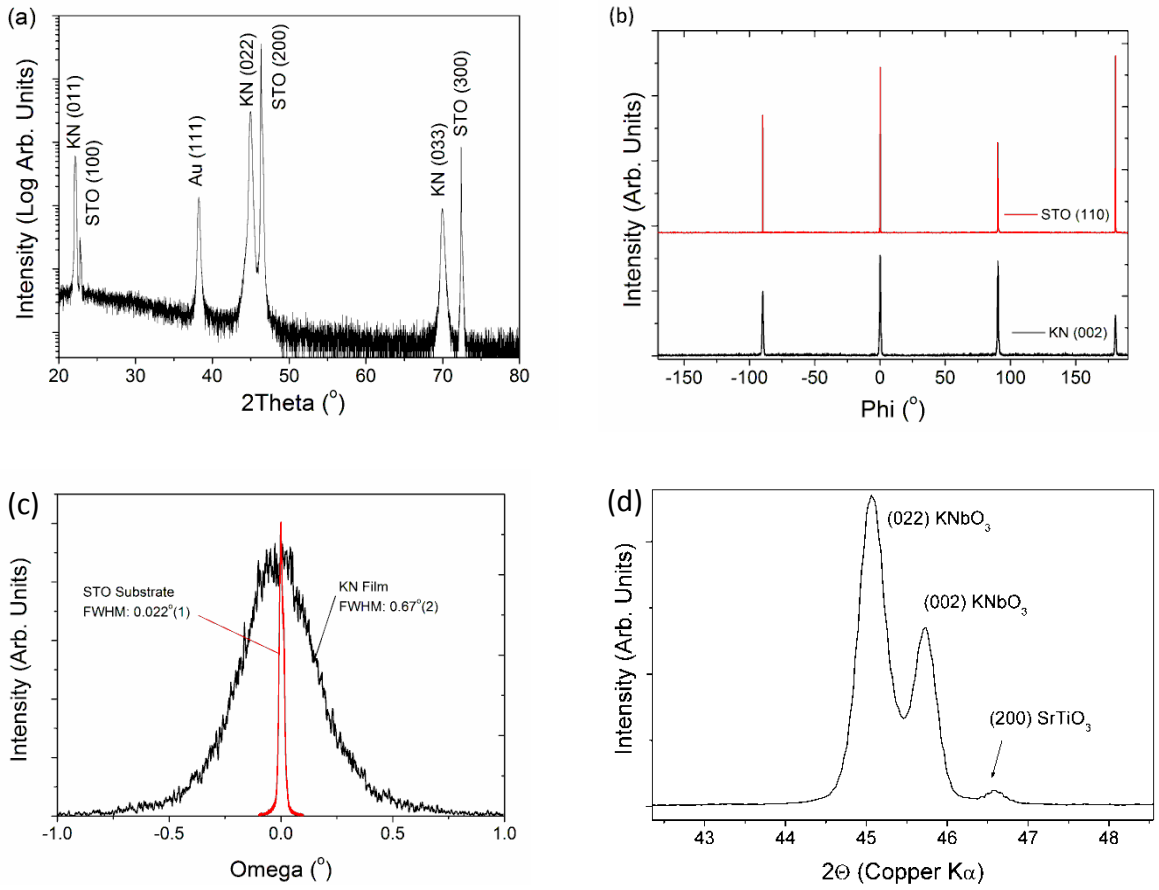

Figure 24: (a) Fast scanning GADDS XRD gonio scan showing (011) out-of-plane orientation of as-synthesized KN film; (b) Off-axis phi (ϕ) scan of STO (110) and KN (002) taken at psi (ψ) angle of 45° showing the in-plane four-fold symmetry of both substrate and film and the cube-on-cube epitaxial relationship; (c) Comparison of KN (022) and STO (200) substrate peaks' omega (ω) scan (rocking curve), showing the significant tilt (out-of-plane variation) characteristics of the as-grown KN films. Bracketed numbers represent statistical errors. (d) HRXRD scan of hydrothermally synthesized KN around STO (200) showing two out-of-plane orientations of (022) and (002) at 15M KOH.

Until now, we have only discussed the $(011)_{o\text{-}KN}/(001)_{pc\text{-}KN} \| (100)_{STO}$, $[100]_{o\text{-}KN}/[100]_{pc\text{-}KN} \| [001]_{STO}$ epitaxial orientation because this is the more commonly observed epitaxial relationship between KN films and STO substrates because of the lower average lattice mismatch. However, it is not the *only* possible configuration. Hydrothermally epitaxied KN film on STO could also display a second type epitaxial relationship of $(100)_{o\text{-}}$

$_{KNO}/(100)_{pc} \| (100)_{STO}$, $[001]_{o\text{-}KNO}/[001]_{pc} \| [001]_{STO}$ (mismatch approx. 3.4%, see Figure 25 on the left part).

This second type of epitaxial relationship was observed when the KOH mineralizer concentration was increased to 15 M (Figure 24 (d)). It is proposed that the increased KOH concentration creates an extremely basic precursor solution, which pushes the solution quickly to supersaturation. One way to relieve the supersaturated solution is for the film to quickly precipitate, causing even the second orientation with a higher film-substrate mismatch to grow. The second epitaxial relationship however, appears to be unstable and will gradually be converted to the first orientation with less mismatch ($(011)_{o\text{-}KN}/(001)_{pc\text{-}KN} \| (100)_{STO}$, $[100]_{o\text{-}KN}/[100]_{pc\text{-}KN} \| [001]_{STO}$) via successive dissolution – reprecipitation reactions when kept in reaction for longer time [30, 37, 205].

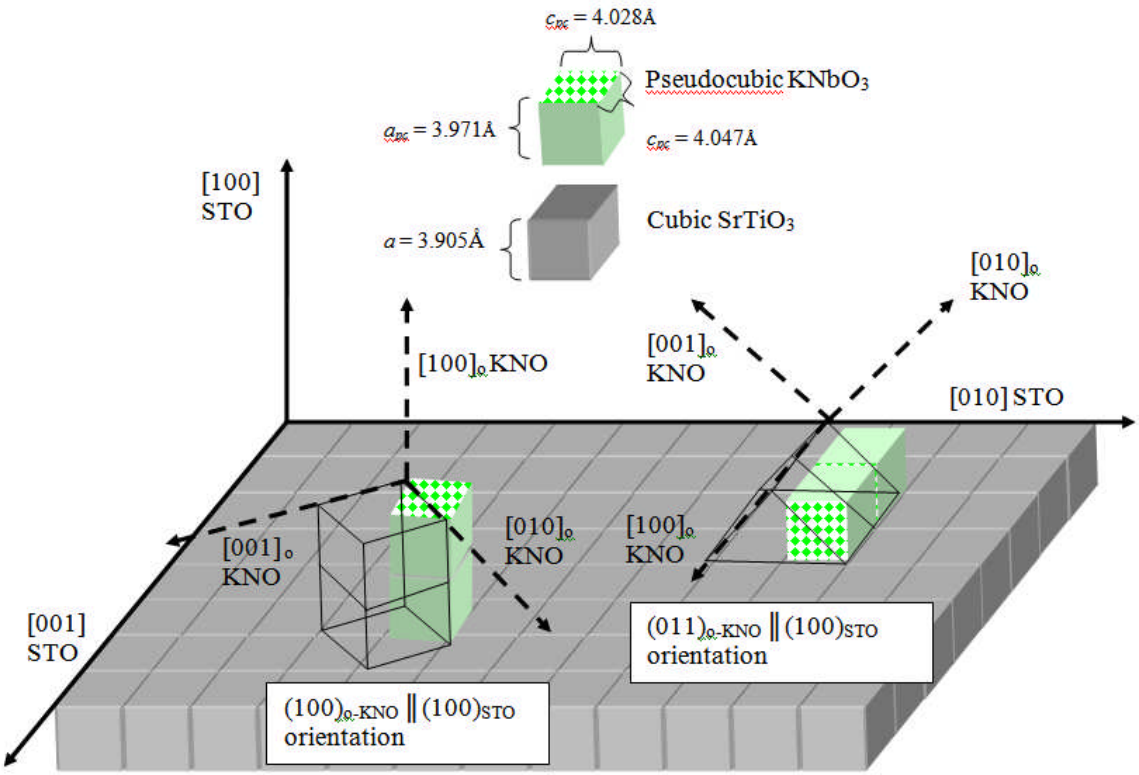

Figure 25: A schematic of possible $KNbO_3$ epitaxial growth over a single crystal $SrTiO_3$ substrate (grey blocks), showing two possible out-of-plane epitaxial orientations of $KNbO_3$ on $SrTiO_3$. The subscript "$_o$" indicates the orthorhombic lattice of $KNbO_3$ (shown in wireframes). The pseudocubic $KNbO_3$ unit cells are represented by green colored blocks.

The evolution of hydrothermally epitaxied KN film morphology with reaction time can be seen in Figure 26. It was noticed that the films gradually become denser and thicker as the reaction period was increased from 2 to 24 hours. Longer growth times were not explored because KN film growth has slowed down significantly after 24 hours (Figure 26 (f)). Films grown for 2 hours are typically not coalesced (as indicated by the high density of open pores, Figure 26 (a)). Attempts to deposit metal contacts on top of uncoalesced films would create a short-circuit path directly to the substrate therefore prohibiting electrical measurements of the film. Higher FESEM magnification (Figure 26 (e)) indicates that even

coalesced films grown for longer time consist of individual islands with uneven/jagged edges. The observation of the uneven individual islands is consistent with the island growth mode known to operate in hydrothermally grown films [29]. It is proposed that the uneven and slightly misoriented islands are the likely contributor to the broad FWHM in XRD data (Figure 24 (c)) and they will unavoidably reduce the overall film density due to the large number of (small angle) grain boundaries in between the islands.

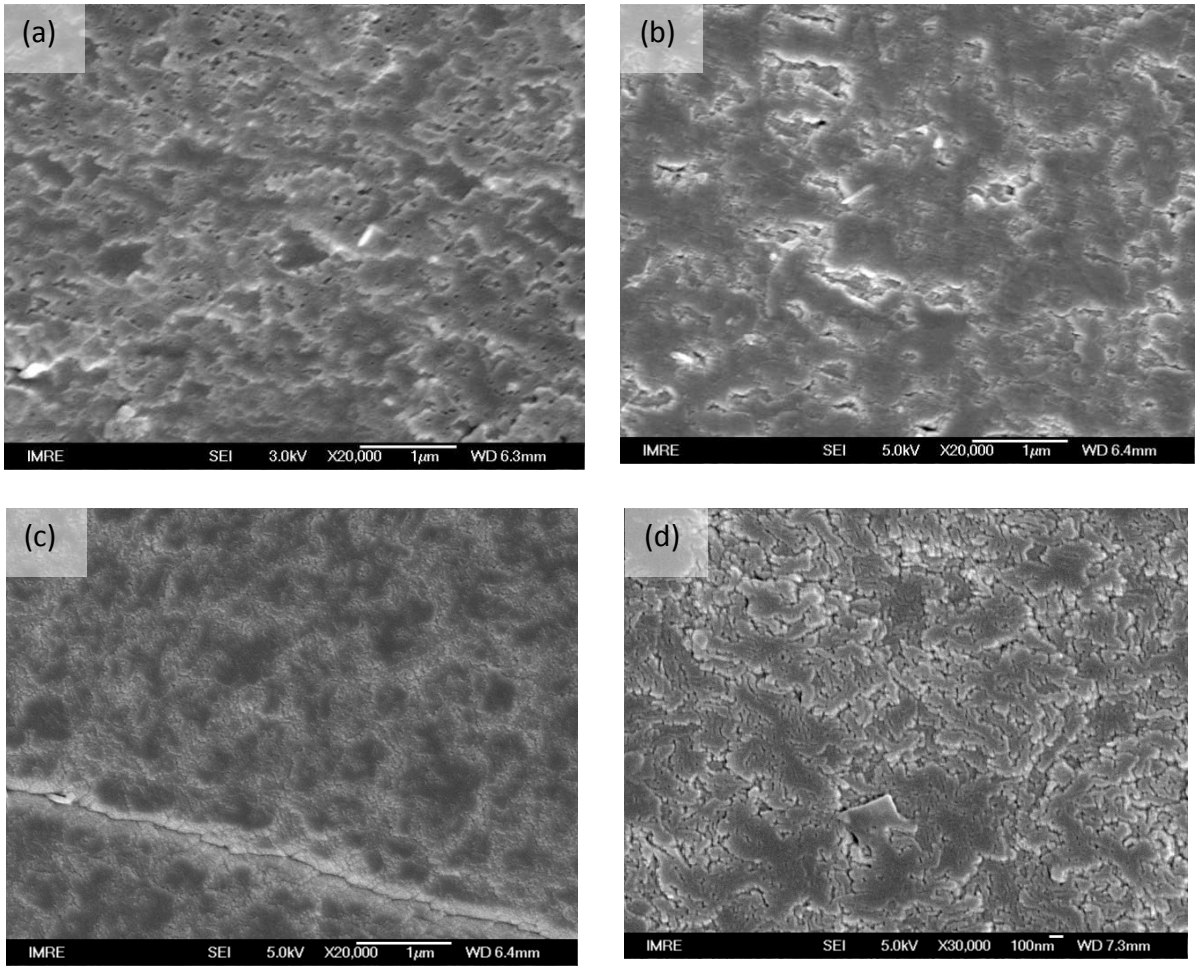

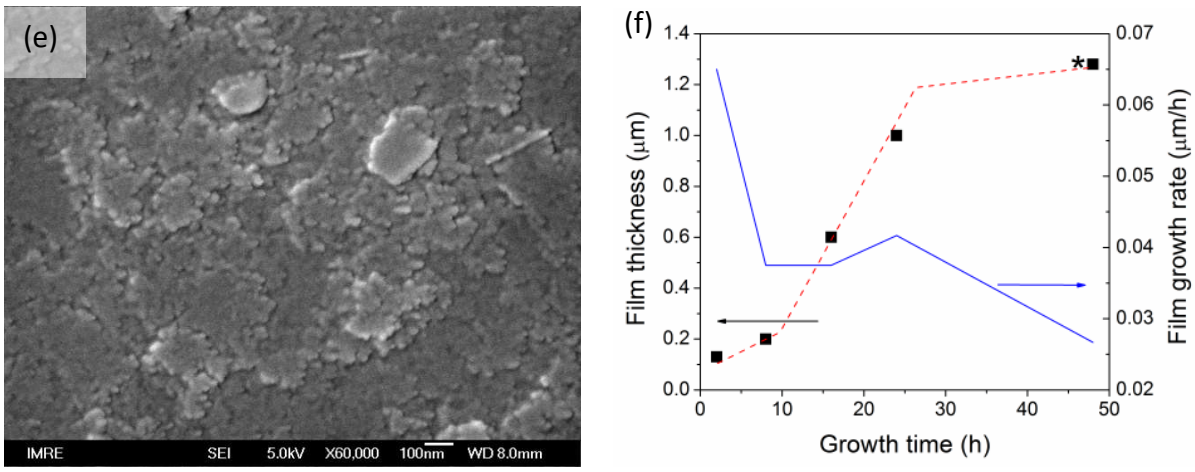

Figure 26: As synthesized KN film's surface morphology (left) and thickness (right) at different reaction times of (a) 2, (b) 8, (c) 16, and (d) 24 hours. (e) A higher magnification view of the same film shown in (d). (f) The average KN film thickness vs. growth time plot of as-grown KN film (filled black squares, left y axis) and the film growth rate (blue line, right y axis). The broken red line is a guide for the eye. *Data for 48H is taken from reference [37].

Electrical properties testing results of as-synthesized KN films at different reaction times are described in Figure 27. First, it was found that the dielectric constant values of all three as-synthesized films (at approx. 100 kHz, Figure 27 (a)) were lower than the bulk (single crystal) KN [114] but consistent with previously reported values for hydrothermally epitaxied KN [191]. All films also show unusually large frequency dispersion (dependency) and excessive dielectric loss, especially at frequencies below 100 kHz (Figure 27 (b)). Typically, the cause of a large frequency dispersion behavior at frequencies below 100 kHz is usually attributed to a combination of two main contributors: the relaxation (response) of space charge polarization from mobile charge carriers such as oxygen or cation vacancies [206, 207]; and the Maxwell–Wagner type interfacial polarization due to the presence of small angle grain boundary and other inhomogeneities in the film lattice [208]. In hydrothermally synthesized films, the combination of intimate interaction between the precursor and water and incomplete dehydration results in a unique trapped –OH defect type that could, by itself,

become or generate secondary mobile charge carriers to maintain the structural charge balance (e.g. by creating cation vacancies) [32, 163, 191]. As a consequence, all three as-synthesized KN films perform poorly in ferroelectric testing (Figure 27 (c)). The already low ferroelectric performance is exacerbated by the film's high (DC) leakage current (Figure 27 (d)), prohibiting the application of higher electric field to reach saturation. No significant properties – film thickness trend can be found among the three as-synthesized KN films, but the 24 hours growth was selected to grow additional batches of films for further analysis due to its consistent film thickness and coalescence.

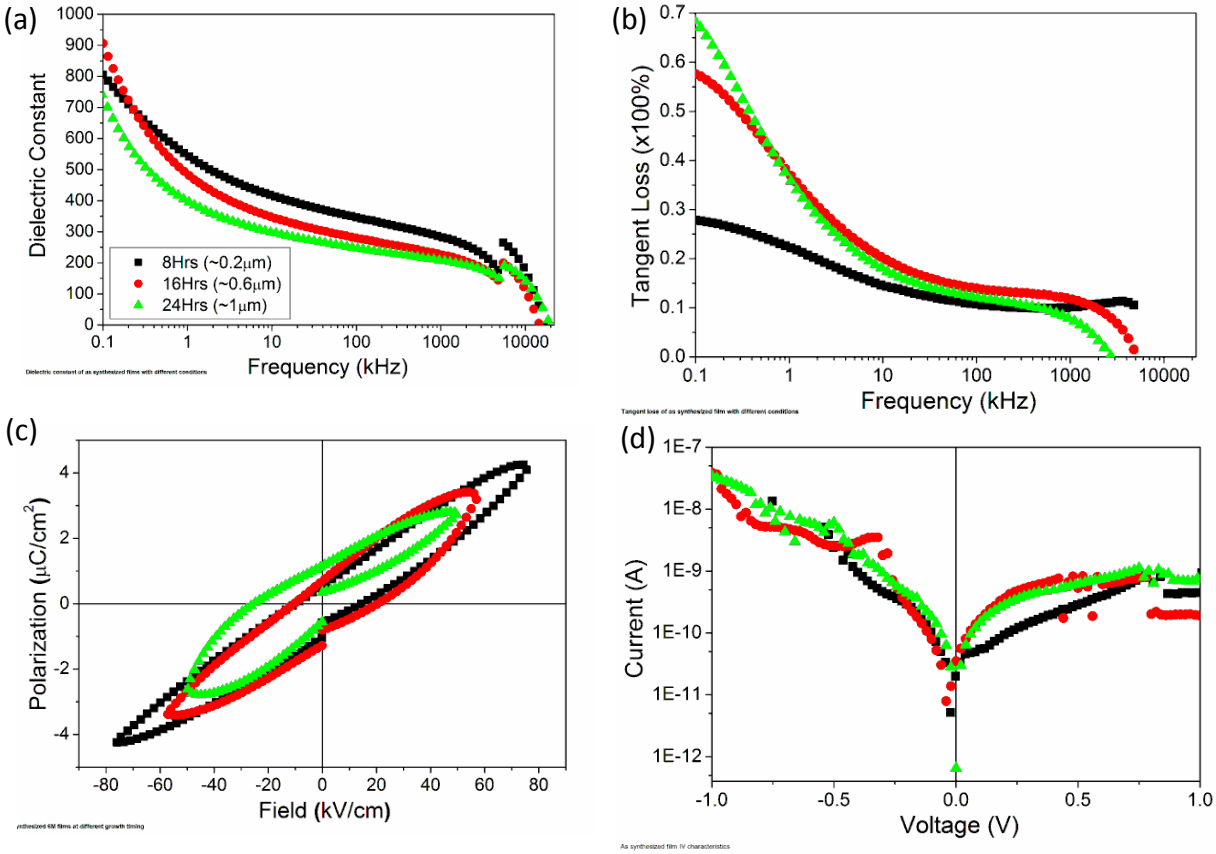

Figure 27: Electrical properties of as-synthesized KN showing the: (a) dielectric constant; (b) dielectric loss; (c) ferroelectric response and (d) I-V DC current loss. Only coalesced KN films were tested.

4.3.2 Post-growth treatments of epitaxial KN films

As the as-grown KN films display excessive frequency dispersion in the dielectric constant and high loss values, post-growth treatments are necessary if hydrothermally synthesized KN films are to be used as a lead-free ferroelectric device. The treatments (or combination of treatments) need to be able to combat two major problems in the as-synthesized KN films: (1) presence of intra-granular [209, 210] and inter-granular porosities and; (2) presence of trapped –OH defects that could become/generate mobile charge carriers. Heat treatments are a natural choice to remove porosities within a material and remove excess water / trapped –OH.

As a start, we know from earlier section on proton incorporation studies (Figure 18) the heat treatment needs to be done at 600°C or higher temperature to effectively remove the incorporated –OH. We are also interested in the oxygen plasma treatments because they have also been reported to remove –OH defects and improve electrical performance of hydrothermally synthesized films [191, 193]. However, there are no detailed studies on the how these treatments improve the film's electrical properties – in term of structural or morphological changes.

This section is therefore aimed to explore heat and oxygen plasma treatments and their combinations in different sequences. The treated films' structure and morphology will be examined and compared, focusing on whether the treatment schemes promote unwanted phases or significantly alter the film's crystal structure. Ultimately, a treatment combination

with specific parameters and sequence that achieves marked performance improvement of hydrothermally synthesized KN films will be proposed and deliberated.

4.3.2.1 Heat treatment of KN films

Figure 28 displays the HRXRD gonio (θ-2θ scan) and rocking curves of KN films before and after various post growth treatments. It was noticed that the $(022)_o$ KN peak position shifted to higher 2θ after the heat treatment but barely change after oxygen plasma treatment (Figure 28 (a)). The peak shift after heat treatment is significant, translating to approx. 0.33% contraction in the out of plane cell parameter.

With reference to the experiments done on KN powders (Section 4.2), the KN film will also contain lattice trapped –OH. The trapped –OH expands the KN powder's cell volume slightly compared to those synthesized via solid state method (see Table 4). It was expected that the heat treated film to show a smaller out-of-plane lattice parameter due to removal of –OH similar to what has been observed in heat treated KN powders. Plasma treatment on the other hand, did not change the film out-of-plane lattice parameters significantly, indicating that it might not remove trapped –OH/water as intended.

It was also found that the KN film's rocking curve became sharper after the heat treatment (Figure 28 (b), red trace). The reduction of the film rocking curve FWHM indicates that the heat treatment process has also improved the film's crystallinity, possibly due to (sub-) grain growth and partial removal of low angle grain boundaries.

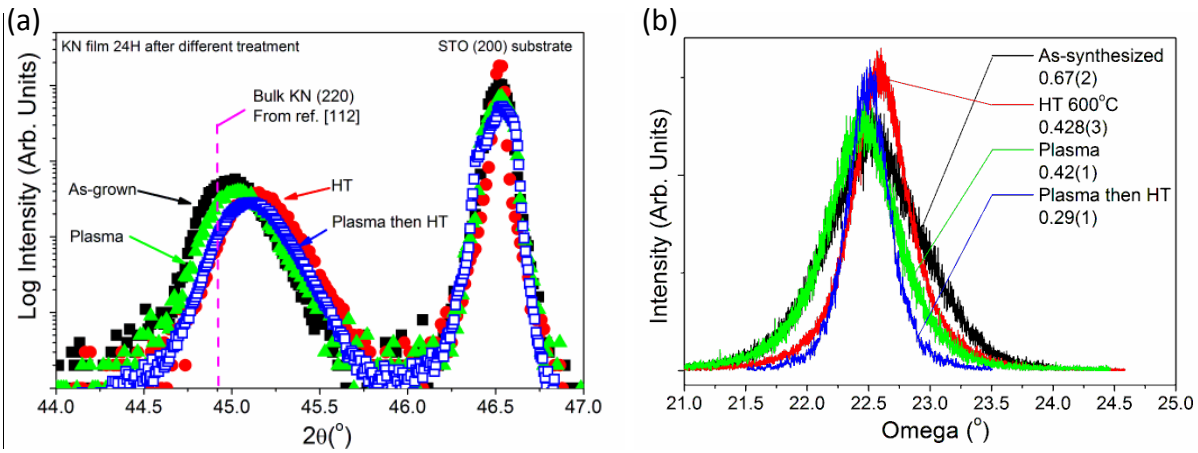

Figure 28: HRXRD data showing (a) θ-2θ scan around KN (022) peak and (b) rocking curve scan of the KN (022) peak before and after various treatments. Values shown in (b) represents FWHM (standard deviation in parentheses) values derived from the individual peak's fitting against a Voigt function. As a comparison, a single crystal STO substrate has a typical FWHM value of 0.02.

After noticing appreciable changes in the out-of-plane lattice parameters, film-substrate epitaxial relationship and improved film epitaxial quality after various post-growth treatments, the next step forward is therefore to conduct systematic studies on the treatments' effect towards the film. In this section, we will focus on post-growth heat treatments of KN films and examine how the treatments affect film morphology, thickness, density, and –OH incorporation in KN lattice.

As the effect of heat treatment should be an incremental, time-dependent one, a time-resolved heat treatment experiment was conducted at a lower heat treatment temperature of 400°C so that the densification/water removal effect can be observed. It is found that heat treatment gradually reduces the film's thickness with increasing heat treatment holding time, down to approx. 1 µm after 3 hours (Figure 29). As indicated by AFM measurements (

Table 6), heat treatment also reduces the film's average surface roughness, from a typical value of 24 nm for an as-synthesized film down to approx. 13 nm for films heat treated for 3 hours at 400°C. The reduction of surface roughness is expected, because as the film densifies under heat treatment, the gaps in between KN islands (i.e. intergranular porosities) close up (compare Figure 29 (d) and (f)).

An interesting phenomenon cropped up after the second hour of heat treatment. A large number of new pores that did not exist previously suddenly surface on (inside the boundary of) the island (Figure 29 (g-h), some of them are marked with red circles) and disappear after longer heat treatment period (Figure 29 (i-j)). As these pores did not exist previously on the as-synthesized KN surface (note: all the samples were cut from the same piece), they should originate from within the KN islands/grains. Similar observations have also been seen in hydrothermally synthesized $BaTiO_3$ powders [209, 210]. While it is recognized that hydrothermally synthesized powders or films contain point defects to compensate for –OH incorporation [163, 166, 168], only recently it is pointed out that these point defects can actually congregate and form pockets of intragranular porosities, and finally macropores [209].

In the case of hydrothermally grown $BaTiO_3$, the intragranular porosities start to become visible under TEM (i.e. migrate and join together to form larger pores of 10 – 50 nm in diameter) after annealing at a temperature as low as 400°C, approx. 1/3 of its melting temperature (T_m) [209, 210]. In our case, the annealing temperature of 400°C should be

sufficient for a similar intragranular porosities migration to take place in the KN film (1/3 of KN T_m is approx. 360°C). It is therefore proposed that the new pores observed during heat treatments at 400°C act as indicators that the intragranular porosities in hydrothermally epitaxied KN grains being annealed out. The removal of the pores after prolonged and/or increased heat treatment temperature can therefore be connected to the continuation of annealing and grain growth process (note the larger grain/island size in Figure 29 (j) and (l)).

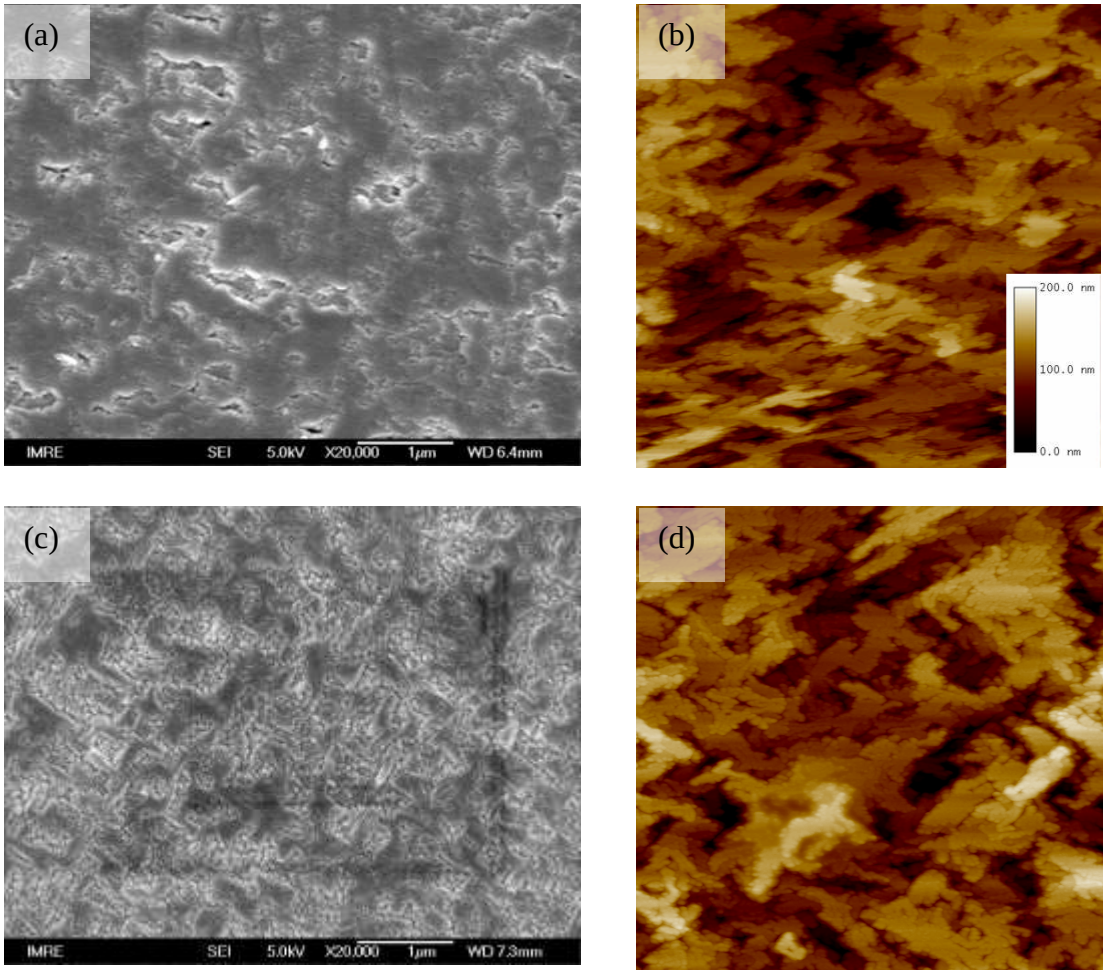

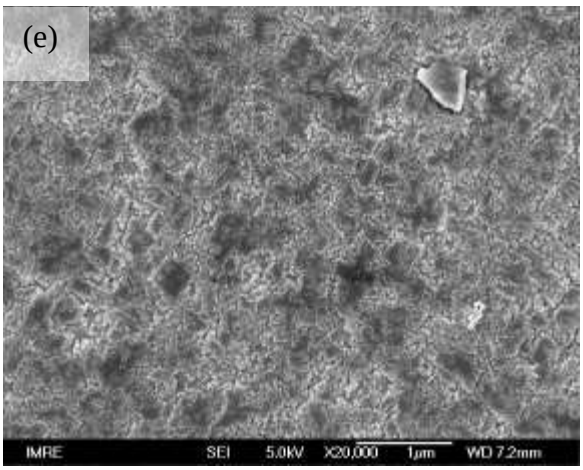
(e)
IMRE SEI 5.0kV X20,000 1μm WD 7.2mm

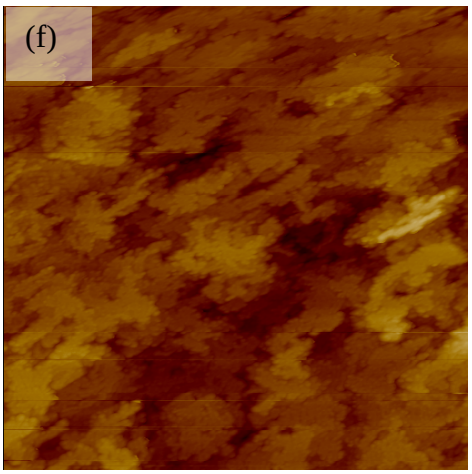
(f)

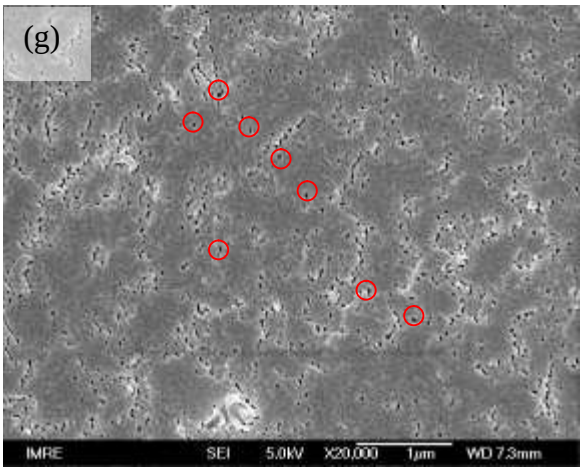
(g)
IMRE SEI 5.0kV X20,000 1μm WD 7.3mm

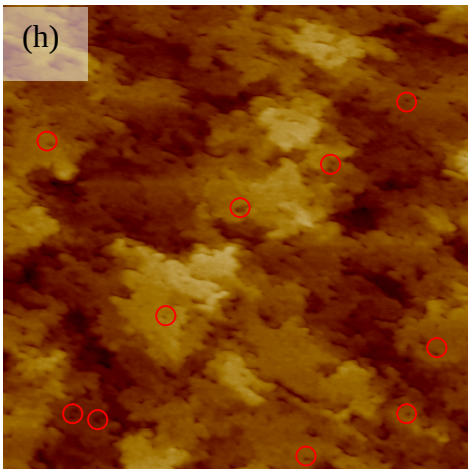
(h)

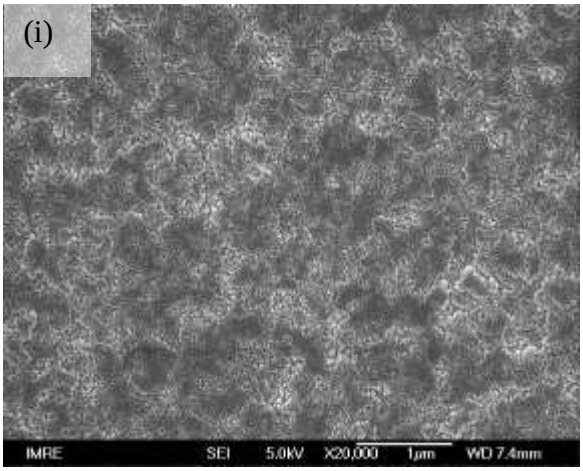
(i)
IMRE SEI 5.0kV X20,000 1μm WD 7.4mm

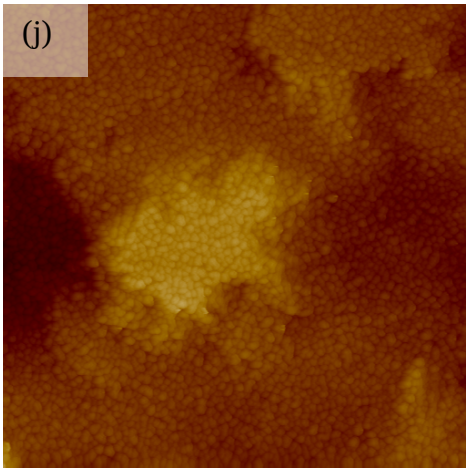
(j)

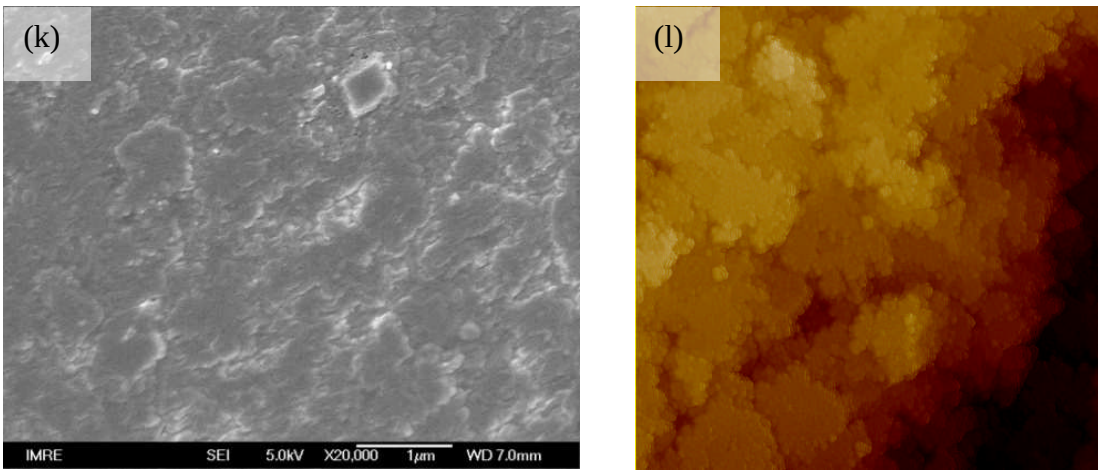

Figure 29: Morphology of KN film as seen from FESEM and AFM analysis before and after heat treatment at 400°C: (a-b) as-synthesized, (c-d) 0 hour holding time, (e-f) 1 hour, (g-h) 2 hours, (i-j) 3 hours. Figure (k-l) displays the morphology after treatment at optimum parameters of 600°C for 3 hours. The AFM scan area is 3x3μm^2, saved with the same scale as (b). Red circles shown in (g) and (h) highlight examples new pores formed from accumulated intra-granular porosities being annealed out.

Table 6: Tabulated NKN film average roughness and range obtained from AFM. Film thickness data is obtained from cross-sectional FESEM

	Average roughness (nm)	Average thickness (μm)
As synthesized	23.66	1.22
HT 400°C 0H	20.71	1.25
HT 400°C 1H	15.82	1.19
HT 400°C 2H	12.47	1.09
HT 400°C 3H	13.03	1.06
HT 600°C 3H	16.50	0.97

The post-growth treated KN films were also examined using SIMS; in particular to observe the evolution of the films' deuterium depth profiles with respect to different post-growth treatments. Deuterium is used to determine, for sure, whether the post-growth treatments could completely remove –OH (OD) from KN lattice. Comparing the deuterium depth profile before (filled black squares) and after optimum heat treatment setting at

600°C 3 hours (filled red circles) in Figure 30 (c), we are convinced that the optimum heat treatment setting has removed –OH completely. Oxygen is the other element that we are interested to look at, because from the findings of earlier proton incorporation study (section 4.2); –OH removal via dehydration reaction should necessarily form oxygen vacancies. Unfortunately, the oxygen depth profile shown in Figure 30 (d) failed to pick up significant difference between as-synthesized (filled black square) and heat treated samples (filled red circles). The oxygen plasma part in Figure 30 will be discussed in the next section.

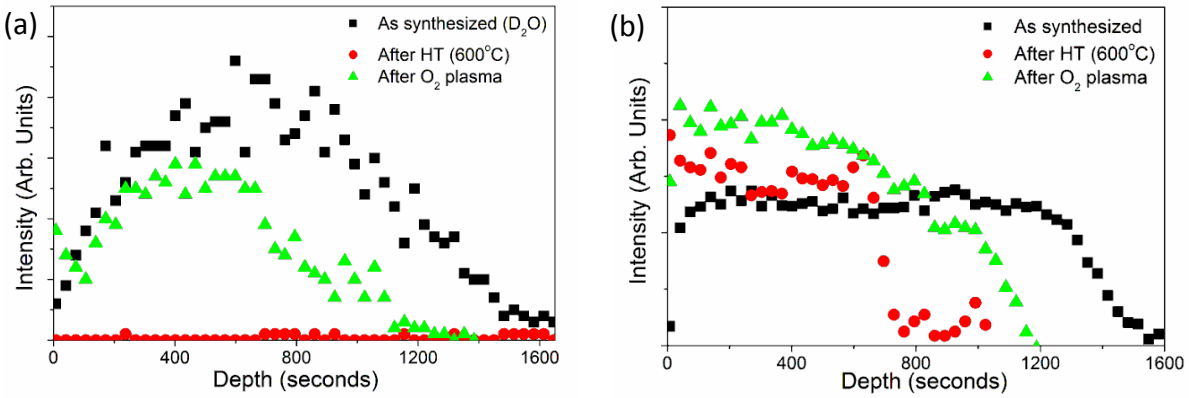

Figure 30: TOF-SIMS data showing (a) deuterium and (b) oxygen depth profiles of KN films after different post-growth treatments.

4.3.2.2 O_2 plasma treatments of KN films

The other post-growth treatment, O_2 plasma treatment, is a unique process that makes use of ionized oxygen gas that reacts primarily with organic substances and useful for the dry etching of photoresists [211]. The beneficial use of reactive O_2 plasma treatments have been demonstrated in improving the electrical performance of hydrothermally synthesized $BaTiO_3$ films [165, 193]. How exactly the O_2 plasma treatment improves the film's properties

however, is not fully understood. We had initial guesses that interactions between O_2 plasma and KN films (or oxide film in general) and their effects should only be constricted near the surface. However, as the experiments go along, we learnt that this post-growth technique has a further reaching effect towards the concentration of oxygen in the films.

As we have guessed, O_2 plasma treatment, being originally designed as a top-down dry etcher, bombards the KN film surface such that the change in the film morphology can be observed after just 5 minutes of treatment (Figure 31 (c-d)). As the O_2 plasma treatment time is increased, the KN film surface gradually become smooth (average roughness drops from 24nm to about 12nm after 15 minutes of O_2 plasma, Table 7) and featureless (Figure 31 (g-h)). The films thicknesses have also reduced slightly after the treatment, from 1.22 µm to approx. 1.08 µm after 15 minutes of plasma treatment. When the plasma treatment period is increased further to 20 minutes however, gaping "potholes" of approx. 100-250nm diameter start to form all over the film surface (Figure 31 (i-j)). At the same time, it is noted that the average film roughness after 20 minutes of O_2 plasma treatment climbs slightly, to approx. 14 nm, followed by a drastic reduction of film thickness to just under 0.7 µm.

The appearance of "potholes" and significant reduction in film thickness indicate rapid etching of the KN film, which is unexpected because oxides are generally quite resistant towards oxygen plasma etching [212]. A recent publication [213] suggests that in addition to O^- ions, oxygen plasma treatment may also generate reactive $\bullet O_2^-$ and $\bullet OH$ radicals from the absorbed water/hydroxyl within the materials treated. Some oxides (ZnO in the paper's

example) are more susceptible to reactive $\bullet O_2^-$ and •OH radicals, which is shown by the unusually rapid etching rate after a certain treatment period. It is possible that similar phenomenon is occurring during KN film O_2 plasma treatment because like KN is prone to chemical attack by –OH (refer to section 5.2 of this thesis). At this point, we conclude that apart from the purported improvement in plasma treated film [191, 193]; O_2 plasma treatment actually does incremental damage towards KN film with treatment time, more severely than previously thought, and it should be done under 20 minutes with the current setting.

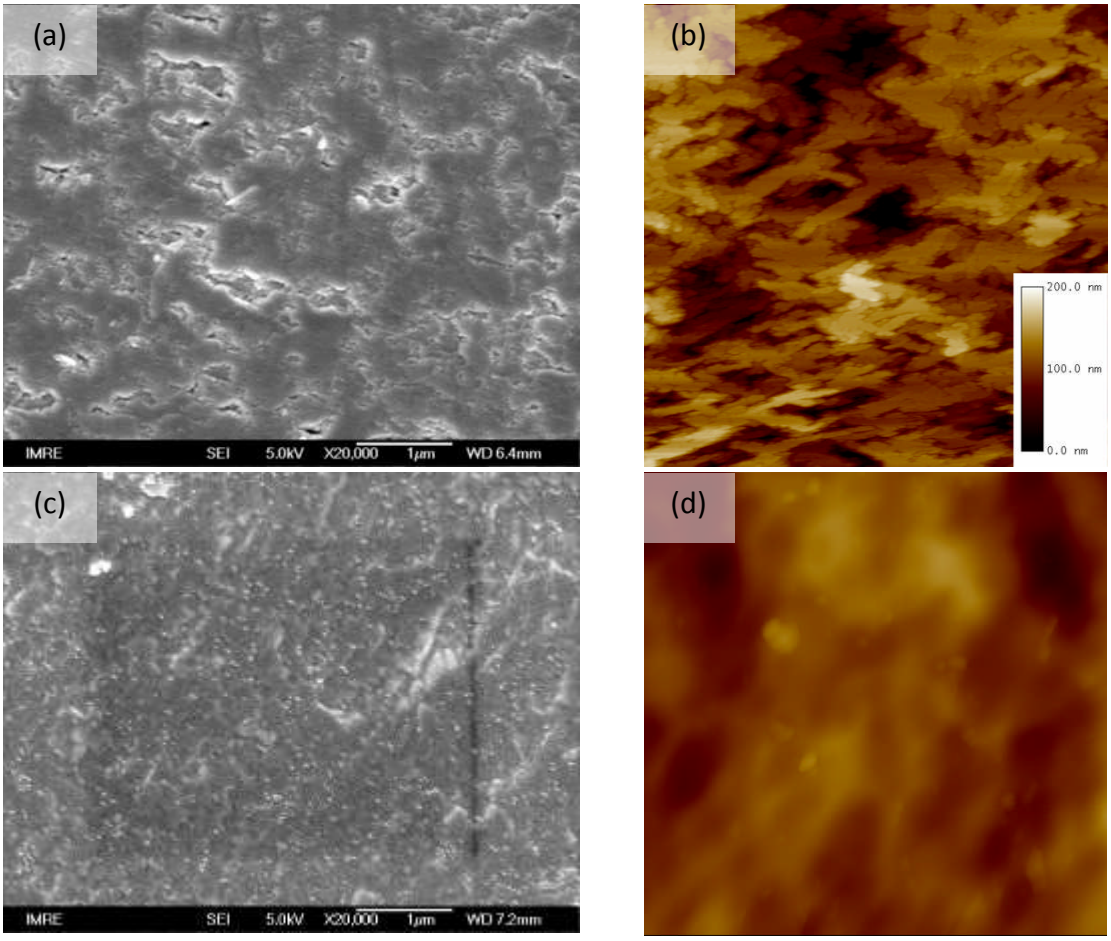

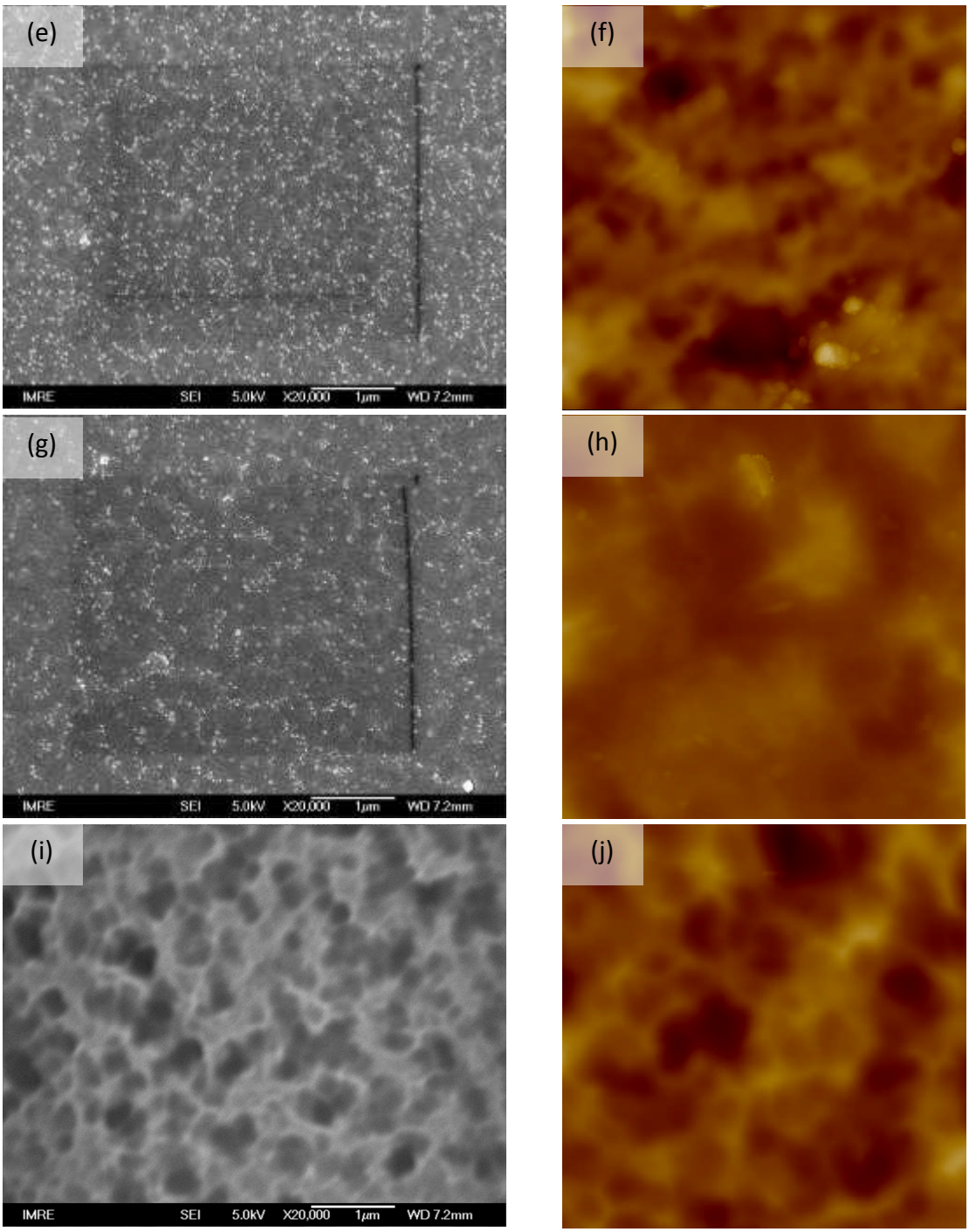
(e)
IMRE SEI 5.0kV X20,000 1μm WD 7.2mm
(f)
(g)
IMRE SEI 5.0kV X20,000 1μm WD 7.2mm
(h)
(i)
IMRE SEI 5.0kV X20,000 1μm WD 7.2mm
(j)

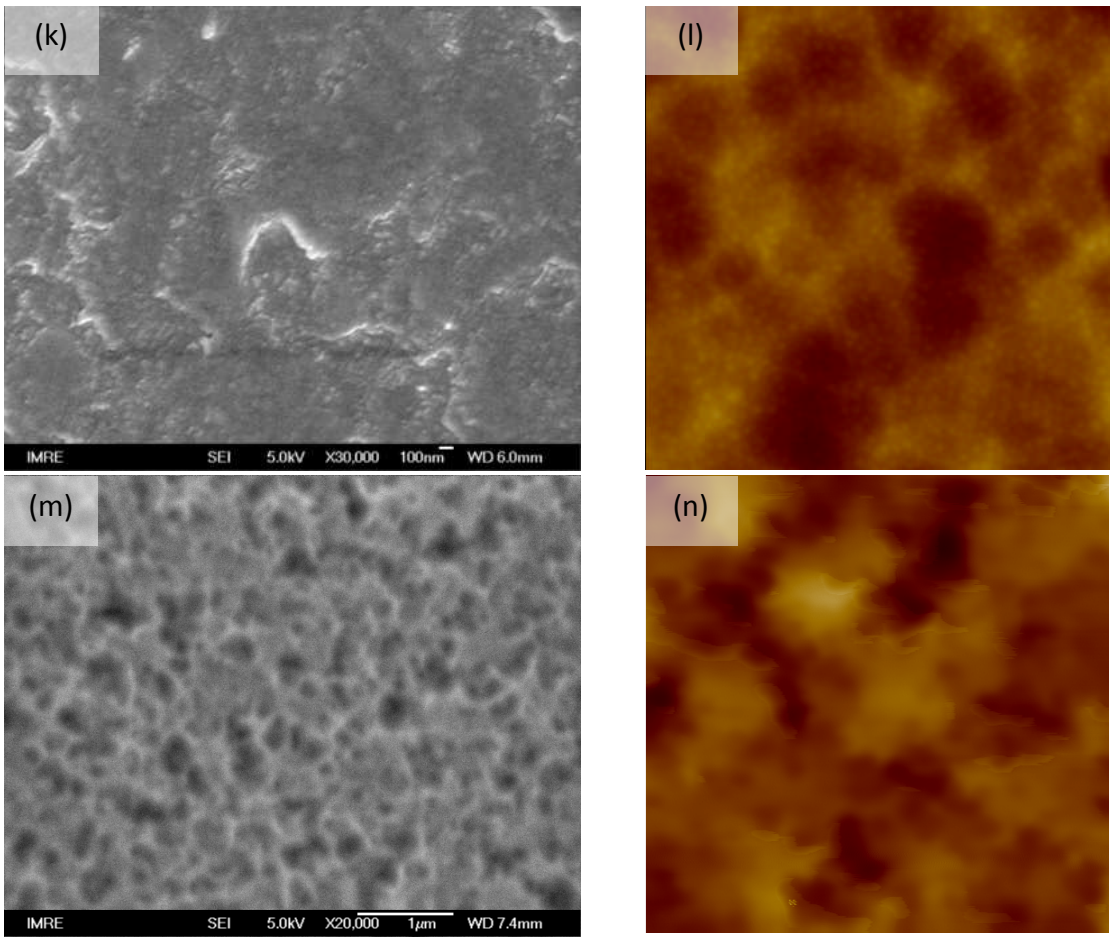

Figure 31: Morphology of (a-b) as grown KN films and after various treatments: after O_2 plasma treatment for (c-d) 5 minutes, (e-f) 10 minutes, (g-h) 15 minutes and (i-j) 20 minutes. Combined treatments with (k-l) 15 minutes O_2 plasma followed by heat treatment at 600°C for 3 hours and (m-n) heat treatment 600°C for 3 hours followed by 15 minutes O_2 plasma. The AFM scan area is 3x3μm^2 saved with the same scale as (b).

Table 7: Tabulated average roughness and range of plasma treated NKN films' obtained from AFM scan. Film average thicknesses are obtained from cross-sectional FESEM data.

Samples	Ave. roughness (nm)	Ave. Thickness (μm)
As synthesized	23.66	1.22
Plasma 5 min	18.70	1.32
Plasma 10 min	13.03	1.25
Plasma 15 min	11.96	1.08
Plasma 20 min	13.79	0.69
Plasma 15min + HT 600°C 3H	9.70	1.05
HT 600°C 3H + Plasma 15min	11.98	0.96

Suspecting some damage to the plasma treated film, we checked the plasma treated (for 15 minutes) film's rocking curve (Figure 28 (b), green line), and found that the FWHM is lower than as-synthesized KN. The lower FWHM value suggests that the tilt in epitaxial KN is not uniform throughout the film but increases with thickness. Therefore, removal of the film outer layers after plasma treatment not only smoothen the film surface but also reduce the average tilt (FWHM).

Next, we did a quick check on using TOF-SIMS analysis, particularly to determine whether O_2 plasma treatment is effective to remove trapped –OH. As with the case of heat treated sample, we used deuterium in place of hydrogen to be sure that the signal does not come from the atmosphere. TOF-SIMS deuterium depth profile results shown in Figure 30 (c) revealed that O_2 plasma treatment (green triangles) does *not* remove significant amount of deuterium. This finding rebuffs previous postulations of possibilities of –OH removal via O_2 plasma treatments [165, 193].

What is more interesting however, comes from the study of oxygen depth profile. We found hints of oxygen enrichment of the KN film after O_2 plasma treatment (Figure 30 (d), green triangles), shown in the increased oxygen depth profile. While it is known that dry etching methods could damage the film surface and create a "confused" (amorphous) layer made of fragments of the film material and part of the gas or radicals created during the etching process [214, 215], not much is known about O_2 plasma, as it is not widely used (and researched) in electronic/semiconductor materials industry. One of a few studies on O_2

plasma on tin oxide films also report the presence of an amorphous oxygen-rich layer that grows from top to bottom as the O_2 plasma treatment period is increased [216]. Judging from the surface morphology and oxygen depth profile, it is proposed that a similar oxygen-rich amorphous layer may have been formed on the KN film during O_2 plasma treatment.

4.3.2.3 Combined treatments of KN films

As we learnt that individual treatments are not effective on their own (e.g. O_2 plasma does not remove –OH while heat treatment removes –OH but necessarily leaves oxygen vacancies behind), we decided to combine both treatments together to get the best ferro/piezoelectric performance out of the KN film. Two combinations with different sequences are available, i.e. heat treatment followed by O_2 plasma and vice versa. We hypothesize that the presence of oxygen-rich layer may help to compensate oxygen vacancies left behind by the heat treatment and similarly, heat treatment may be able to remove the amorphous layer left behind by the O_2 plasma treatment. Therefore the best heat treatment combination of the two should be O_2 plasma treatment followed by heat treatment, because O_2 plasma leaves behind a damaged amorphous layer (Figure 31 (m-n)).

When the plasma treated film (15 minutes) was subjected to heat treatment at 600°C for 3 hours, the film becomes visibly denser (Figure 31 (k-l)) with a very low average surface roughness value of 9.7nm (Table 7). It is also noticed that numerous small (20-50nm), rounded islands were found on the film surface, a sign of recrystallization. HRXRD analysis of the film treated with O_2 plasma followed by heat treatment retained the slight $(022)_{o\text{-}KN}$

peak shift towards higher 2θ observed in heat treated only film due to –OH removal (Figure 28 (a)). O_2 plasma followed by heat treatment combination also gives the best rocking-curve FWHM value of 0.29(1)° (Figure 28 (b)), indicating even lesser out-of-plane tilts due to removal of the more misaligned top layer followed by subsequent film densification/grain growth.

4.3.3 Properties of treated KN films

In this section, we examine the electrical properties of the treated KN films to understand the impact of various post-growth treatments towards the KN film properties. Electrical results of the as-synthesized KN film grown for 24 hours at 200°C is inserted as a reference but as we focused on the treated KN films' properties in this section, discussions regarding as-synthesized film can be referred to in section 4.3.1 and will not be repeated here. An additional KN sample heat treated at 200°C just before electrical measurement is introduced here to represent as-synthesized sample with minimum amount of surface absorbed water[**].

The main purpose of introducing the new sample heat treated at 200°C is to differentiate surface and bulk contributions of the enhancement (or degradation) of the properties. A good example can be seen in the dielectric measurement (Figure 32), where

[**] While heat treatment at 200°C eliminates surface absorbed water (including the inter-granular porosity surface), it is not enough to remove the lattice bound hydroxyls (see Figure 18 on section 4.2.1).

by comparing the as-synthesized samples (filled black squares) and those heat treated at 200°C (filled green triangles) we can deduce that the tangent loss values (b) is more affected by the surface contribution (of absorbed water) compared to the dielectric constant (a). In a similar manner, one can deduce that the effect of O_2 plasma (empty blue squares symbol) is slightly more complicated that just removal of surface water, because while the tangent loss characteristics is similar to the samples treated at 200°C (Figure 32 (b)), the net dielectric constant also drops after O_2 plasma (Figure 32 (a)). We believe that the drop of the net dielectric constant is the manifestation of a thin amorphous layer that formed during O_2 plasma treatment discussed earlier in section 4.3.2.2. This is because when an amorphous layer with a low dielectric constant is stacked on top of (i.e. in series with) the epitaxial KN film, the net dielectric constant of the film will be pulled down as a consequence. The tangent loss is still very large after O_2 plasma treatment because as pointed out in Figure 30 (c), O_2 plasma treatment does not remove significant amount of trapped –OH.

Heat treated films on the other hand, display a superior dielectric constant and very low tangent loss (filled red circles). The cause is proposed to the film densification and complete removal of trapped –OH, as discussed in section 4.3.2.1. The combination treatment of O_2 plasma followed by heat treatment also displays a decent dielectric constant value with even lower tangent loss (empty magenta triangle symbols). This finding is consistent with a high quality recrystallized film observed in the film surface (Figure 31 (k-l)) and a possibility of compensated oxygen vacancies from the recrystallized oxygen rich layer.

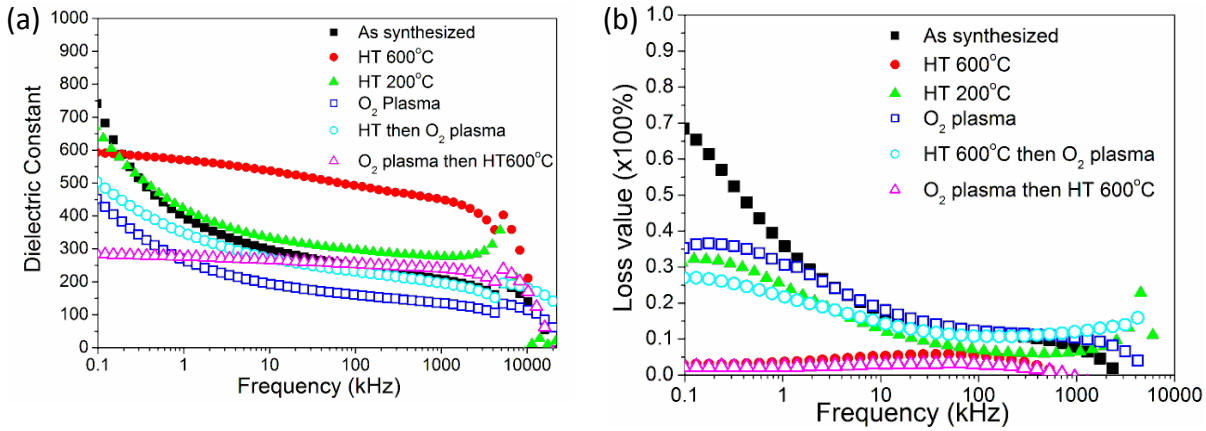

Figure 32: (a) Dielectric constant and (b) Tangent loss of hydrothermally epitaxied KN films after various treatments.

Next, we test the leakage current characteristics of the film with and without heat treatment using I-V measurement system (Figure 33). At low field, the as-grown KN film (filled black squares) showed a linear log I vs. log E plot with slope close to 1, corresponding to the Ohm's law region where majority of the charge carriers are thermally generated. An inflection region was observed around 10kV/cm field, where the leakage current began to increase rapidly with just a slight increase in the field (slope ≈4). Phan et al. [217] denotes this region as the trap controlled region (also known as the Poole-Frankel conduction region) where injected carriers dominate over thermally generated carriers. The large amount of injected carriers can quickly fill various trap levels (e.g. cation/anion vacancies, -OH, etc.) to saturation, and any excess injected carriers will be transferred freely to the conduction band, manifesting as a huge slope in log I vs. log E plot.

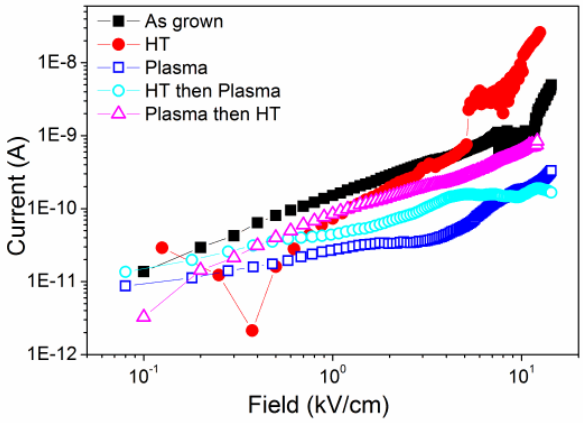

Figure 33: Positive bias side of I-V characteristics measurements of films with different treatments.

The problem of proton hopping/tunneling related conduction mechanism is especially prominent in hydrothermally grown perovskites [218, 219]. Studies on hydrothermally synthesized $BaTiO_3$ perovskite highlights that the amount of trapped –OH is very significant, such that the cubic structure is stabilized at room temperature instead of tetragonal [220]. Presence of "A" cation vacancies, necessary to compensate the charge imbalance caused by lattice trapped –OH, is shown to exacerbate the already high leakage current in hydrothermally grown $BaTiO_3$ [165, 220]. As the defect formation mechanism is similar in hydrothermally grown KN, potassium cation vacancies formation and the related leakage current mechanisms should be expected in the as-grown samples. There is also surface conduction problem in hydrothermally grown film. Increased surface conduction occurs because of significant amount of adsorbed water/–OH on film surface and grain boundaries (or low-angle grain boundaries in mosaic epitaxial film) that can contribute as low resistance leakage paths [221-223].

Plasma treated sample (Figure 33, filled green triangle symbol) displayed a significantly lower leakage current characteristics compared to the as-grown sample. It maintained the slope between at around 0.5 that increases slightly to 1.5 at around 3 kV/cm field. Dry etching/plasma treatment is widely used in the semiconductor processing and known to amorphize the exposed material. The coverage and depth of the amorphous layer depends on the processing time/power used during plasma treatment [215]. It is believed that the low leakage current observed in plasma treated sample was also due to the formation of an amorphous layer on the film surface. An amorphous material is known to have higher resistivity compared to the crystalline counterpart due to high defect density that acts as carrier traps/recombination centers (also true for insulators during the carrier injection process) [224, 225].

Current injection density in metal-insulator-metal configuration is proportional to the applied field (V/d) and concentration of shallow donor (represented by is a scale factor that reduces current density due to carrier trapping in the insulator, θ), and inversely proportional to the thickness (d), as described in the following equation [226]:

$$J \propto c\varepsilon\mu\theta\frac{V^2}{d^3}$$

where c is a constant, ε is the dielectric constant, μ is the carrier mobility. Presence of amorphous layer is analogous to having large concentration of shallow donor which reduces the current density during the carrier injection process in insulators.

What happened to the heat treated samples however, is not so straightforward to be explained. It has been shown that heat treated film has the highest dielectric constant

(Figure 32, filled red circles), but then it was also observed to have worse leakage current properties than the as-grown sample (Figure 33, filled circles), with higher initial slope of ≈1.5 and earlier inflection point to carrier injection at ≈8kv/cm where the slope increases further to around 5. Section 4.2 describes that heat treatment done at sufficient temperature and time can remove lattice trapped water/-OH via dehydration process. It is also expected that heat treated samples should contain significantly lower adsorbed –OH/water on the surface and (low angle) grain boundaries and porosities. We have also seen in Figure 29 that heat treatment removes inter-granular porosities, possibly caused by point defects accumulation and annihilation, joined up together to form inter-granular porosity that eventually diffuses to the surface during sufficient heat treatment [210, 221].

However there are at least two negative effects induced by heat treatment process. First, for each oxygen vacancy created during lattice trapped –OH removal, a positively charged (acceptor) trap. Presence of oxygen vacancies in heat treated KN powder has been deliberated in section 4.2.3 and independently confirmed using photoluminescence measurements on hydrothermally grown $BaTiO_3$ [227]. Second, the newly formed oxygen vacancies need to be charge-balanced by either the release of two extra electrons (to the conduction band) per oxygen vacancy created because the neighboring K and Nb cations would be under-bonded, or the creation of K vacancies if the heat treatment temperature is sufficient for K ion migration. Both scenarios of oxygen vacancies charge balance would result in an increased leakage current.

While it may be argued that oxygen vacancies are deep level defects that should not contribute significantly to room temperature I-V measurements, recent literatures suggest that there are at least two different deep-level defect conduction mechanisms that need to be considered. First, heat treatment in air below the oxidation temperature also gives the possibility of O^- chemisorption on the grain boundary/interface that contributes to the non linear conduction due to formation of Schottky barrier between the grains [228]. Second, Hickmott et al. [226] offers a fresh idea of deep level traps creating an intermediate band in the insulator (Figure 34) that is able to bridge the metal-insulator contact, therefore displaying ohmic conduction characteristics at room temperature. Third, as the lattice trapped –OH removal process is likely to involve diffusion of H^+ to the film surface, more oxygen vacancies would pile up near the film surface rather than the bulk at the end of heat treatment, resulting in large oxygen vacancy concentration gradient. Non-uniform distribution of oxygen defects are known to cause high leakage current in perovskite ceramics, observed in studies conducted under applied bias or heat [229, 230].

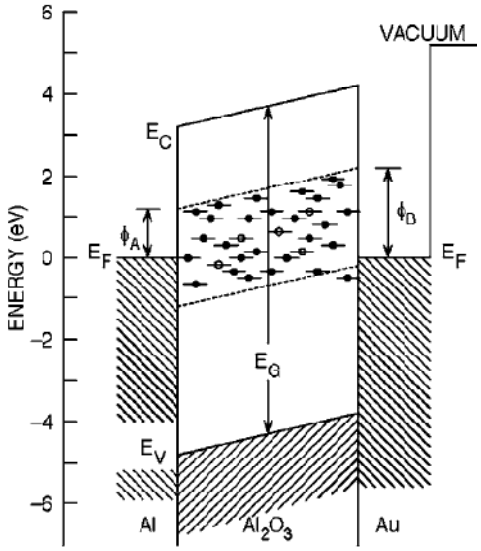

Figure 34: Schematic energy-band diagram for metal-insulator-metal diode, showing an impurity band between 2 and 4 eV below the conduction band.

Reprinted with permission from [226]: Hickmott, T.W., Formation of Ohmic contacts: A breakdown mechanism in metal-insulator-metal structures. Journal of Applied Physics, 2006. 100(8): p. 083712-7. Copyright 2006, American Institute of Physics

As a bottom line, it is believed that the leakage current response of heat treated sample reflects the net effect of the opposing process. Despite inevitable creation of oxygen vacancies, –OH removal via heat treatment will still result in a net improvement KN film's dielectric properties because oxygen vacancies are more localized compared to hydroxyl related defects (i.e. the activation energy for long range proton diffusion is only ≈ 0.15–0.4 eV [231, 232] vs. 1 eV for oxygen vacancies diffusion [233]) and therefore could contribute to KN's dielectric response at higher frequencies. As a trade off however, the newly created oxygen vacancies and the charge compensation mechanisms will contribute to one or several conduction mechanisms described above [228, 234].

The ferroelectric and piezoelectric properties of hydrothermally epitaxied KN film were subsequently tested to observe the effect of various heat treatments sequences. The ferroelectric response of the as-synthesized KN films is low (Figure 35, filled squares, P_{max} ≈2.5 μC/cm^2 and Pr almost negligible at 1 μC/cm^2); expectedly because of the high loss and leakage current displayed on previous electrical tests that prevented the application of higher external field. Heat treated film also performs poorly in ferroelectric testing, with a measured P_{max} of only around 6 μC/cm^2 (filled circles), because the same leakage current problem prevents the application of a higher field.

Samples treated with a combined O_2 plasma followed by heat treatments (empty circles) performs the best among all the samples, displaying the highest P_{max} and P_r values at about 30 μC/cm^2 and 12.5 μC/cm^2 respectively (Figure 35 (b)). The high performance is summarized due to oxygen-compensated removal of –OH hydroxyls, dense, and highly epitaxial film after the O_2 plasma-heat treatment combination.

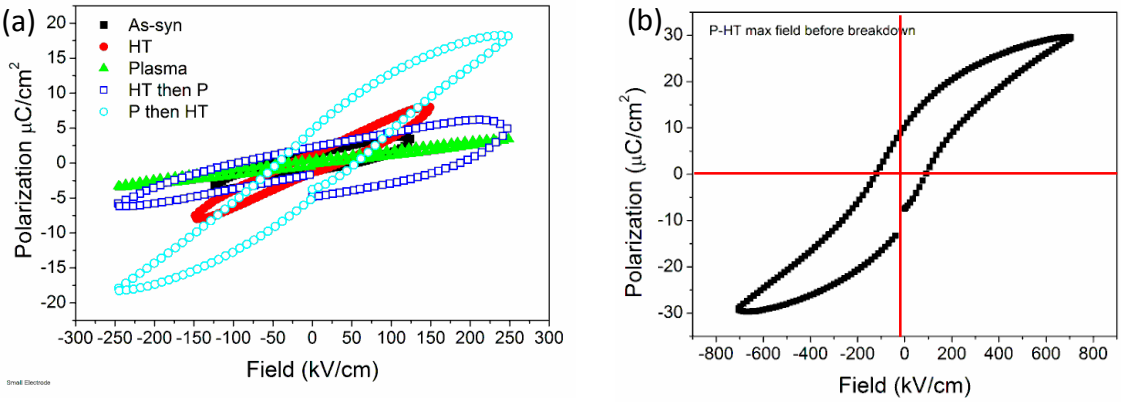

Figure 35: The ferroelectric properties of (a) as grown and treated KN film and (b) maximum polarization response of the film treated with O_2 plasma followed by heat treatment just before breakdown

The best performing film in ferroelectric testing (i.e. the film treated with a combined O_2 plasma then heat treatment) were then taken to a laser scanning vibrometer to test its piezoelectric response. Laser scanning vibrometry simultaneously scan both KN films under the electrode (biased) and the unbiased substrate, therefore giving a more accurate measurement of film displacement [182]. It should be noted that the films measured are under in-plane constraint by the substrate and linear displacement-voltage relation is assumed, resulting in underestimation of the actual d_{33} value.

Although the measured displacement signal is rather noisy (shown by the vibrating baseline level), the piezoelectric response of the sample can still be clearly seen and the d_{33} value was estimated to be about 6 pm/V based on the 1 V net voltage applied to the sample.

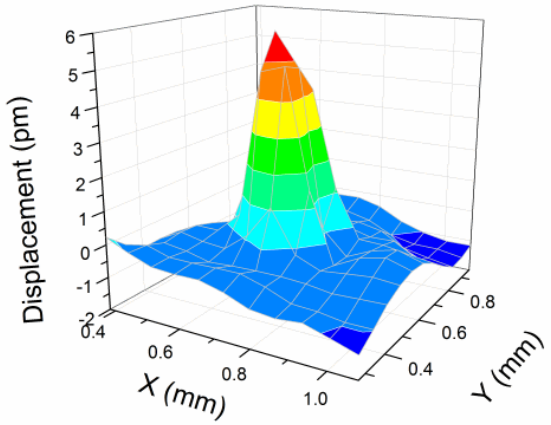

Figure 36: Displacement data from laser scanning vibrometry measurement for heat treated KN sample taken at 1V AC peak to peak voltage, 1.5kHz.

4.4 Summary

We have established the case of proton incorporation in hydrothermally synthesized $KNbO_3$ lattice with aid of indirect DSC-TGA measurements and direct solid-state NMR and neutron diffraction experiments on a deuterated sample. The possible locations of trapped –OH (OD) are probed by comparing the nuclear density maps of as-grown (deuterated) and heat treated KN powders. The possible locations of trapped –OH (OD) are determined to be adjacent to the oxygen atoms on O2 sites around (0, 0.28, 0.27) of an orthorhombic $KNbO_3$ unit cell, with an occupancy rate of approx. 8% of the total O2 sites.

It was also found that a post-growth heat treatment at 600°C is sufficient and necessary to remove the trapped –OH. At the same time however, we observe increased oxygen vacancies on heat treated samples, affirming earlier assumptions of –OH removal via dehydration reaction.

We have also investigated the electrical properties of hydrothermally epitaxied $KNbO_3$ films over $Nb:SrTiO_3$ substrate. It is clear that as-grown films' properties were inferior due to presence inter-granular porosity shown in the film morphology and trapped –OH in the KN lattice shown in the SIMS depth profiles. Heat treatment is a natural choice to remove these lattice-bound hydroxyls. From the KN film experiment, it was found that the heat treatment needs to be done at 600°C for 3 hours to remove trapped –OH (OD) in the film and in particular to increase the film density by removing intergranular porosities.

However, despite the clear hydroxyl removal and film densification effects, it was found that heat treatment alone is actually detrimental to the film's ferroelectric response. This is because the hydroxyl removal process via dehydration reaction necessitates new oxygen vacancies formation. The increased concentration of oxygen vacancies in the heat treated film is reflected in the high leakage current, which in turn prohibits the application of sufficiently high electrical field during ferroelectric measurement tests.

It was also found, contrary to the belief that O_2 plasma treatment improves various hydrothermally grown films' electrical properties by removing lattice trapped –OH, it does not remove significant amount of lattice-trapped –OH in our study. Instead, O_2 plasma treatment introduces oxygen-rich amorphous layer the film surface that alters the film's electrical properties. The amorphous layer on the surface results in a reduction of the film's leakage current but at the same time reduces its polarizability due to increased ionic mobility in amorphous KN.

Finally, by combining the two treatments in a specific sequence (O_2 plasma treatments first, followed by heat treatment – *not* vice versa) we can bring out the best ferroelectric and piezoelectric properties of the film. The good ferro/piezoelectric properties results from a combined effect of lattice bound hydroxyl removal, smooth surface layer for good electrical contact and reduced intergranular porosities.

5. *Hydrothermal Synthesis of $Na_xK_{(1-x)}NbO_3$ Solid solution powders*

5.1 Direct Synthesis of NKN Powders from Oxide Precursor

5.1.1 Introduction

Sodium potassium niobate – a sodium-substituted potassium niobate with a chemical formula of $(Na_xK_{1-x})NbO_3$ (NKN) – is a suitable candidate to replace PZT because, similar to PZT, NKN undergoes a morphotropic phase transition from orthorhombic (A*mm2*, Figure 37, dotted lines) to monoclinic (P*1m1*, Figure 37) when the sodium gradually replaces ≈50% of the potassium sites [28, 119]. To compare and contrast the lattice parameters across different phase boundaries, expressing the lattice parameters in an empirical *pseudocubic* unit cell (Figure 37, shaded cube) is useful and widely used in the perovskite systems [235].

At the morphotropic phase transition composition, a material is able to accommodate large atomic displacements [53], which, depending on the symmetry, may allow the polarization alignment that result in a very high electromechanical coupling [107]. Indeed the same polarization alignment phenomenon near the morphotropic phase boundary (MPB) may be responsible for the sharp increase of the dielectric/piezoelectric performance of NKN at the composition near the MPB [119, 135]. The

A little simplification would be the first step toward rational living, I think. ***Eleanor Roosevelt (1884-1962).***

piezoelectric performance of NKN can still be improved by introducing other elements in the solid solution, like lithium and antimony, to get other morphotrophic transformations that results in increased Curie temperature and piezoelectric properties comparable to a soft (donor-doped) PZT [19].

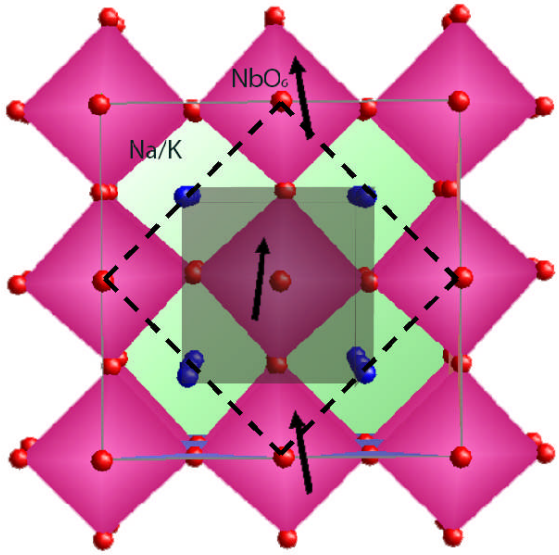

Figure 37: One monoclinic unit cell of $(Na_{0.57}K_{0.43})NbO_3$ (P*1m1*, eight formula units per cell, ≈504 Å^3) showing tilted NbO_6 octahedra due to the sodium substitution of potassium (arrows indicate octahedra tilting directions). The dotted lines on the center represents the approximation of one orthorhombic unit cell (A*mm2*, two formula units per cell, ≈125 Å^3), while the shaded cube on the left hand corner shows the approximation of one *pseudocubic* unit cell containing only one formula unit per cell, ≈63 Å^3.

Sodium potassium niobate is presently synthesized by conventional solid-state processes from potassium and sodium carbonate precursors at temperatures beyond 1000°C [141]. The high temperatures required during the solid-state process are problematic because potassium oxide starts to volatize at 900°C [124], leading to non-stoichiometry [122], lowered density [26] and ultimately, a degradation in the performance [144]. The solid-state

process also requires over 80 hours worth of laborious and high energy steps [236] including pre-mixing, attrition ball milling, calcination, and sintering. In contrast to the solid state process, hydrothermal synthesis does not only ease the process requirements to 200°C for 24 hours [35] but also adds the ability of growing an epitaxial film over a suitable single crystal substrate [30, 36].

While both pure potassium niobate ($KNbO_3$) and sodium niobate ($NaNbO_3$) powders have been successfully synthesized using hydrothermal synthesis at low temperatures [32], it appears that the formation of the NKN solid solution via hydrothermal synthesis is not so straightforward. In an earlier attempt to synthesize the NKN solid solution via hydrothermal synthesis, Sun and co-workers [35] found that there was a big jump in the sodium occupancy from 24% to 89%. The abrupt increase in the sodium fraction prevented the formation of an NKN solid solution with the desired composition near the MPB – crucial for achieving its best properties. This report shows that sodium ions can be incorporated gradually into the NKN solid solution and for the first time NKN solid solutions with compositions near the MPB is achievable through the hydrothermal synthesis method, clearly demonstrating the efficacy of the hydrothermal method in simplifying the current solid state process.

5.1.2 Results and Discussion

The hydrothermal synthesis reaction of NKN completes within 24 hours, indicated by the high (≥97 wt%) NKN powder yield and the negative results from both the cold ethanol and

the sodium hydroxide tests. Phase identification by X-ray diffraction (Figure 38, only selected samples are shown for clarity) shows that the samples are made up entirely of perovskite phases and that the NKN reflections are moving towards higher 2θ with increasing *R* values. These movements are indicative of a lattice contraction and that the smaller sodium atoms are successfully incorporated inside the potassium niobate (KN) lattice. It is also observed that for *R* values above 11.7%, a secondary phase identified as $NaNbO_3$ (NN) appears.

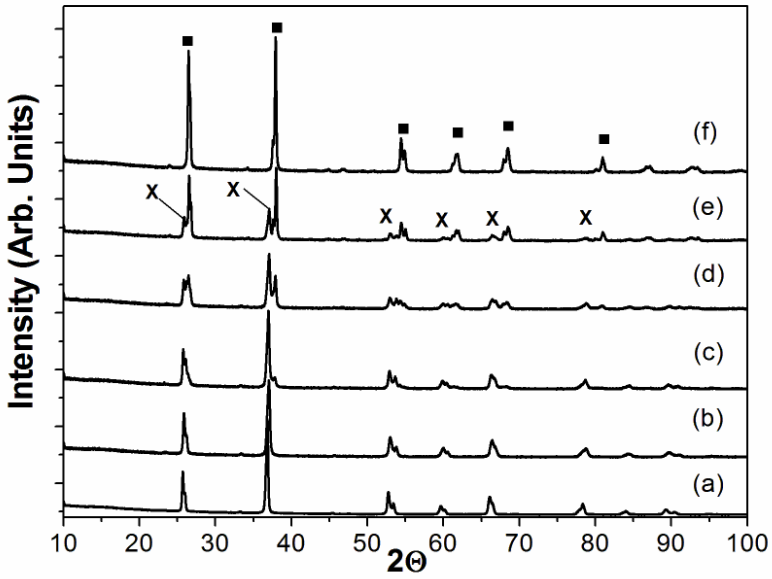

Figure 38: X-ray diffraction of hydrothermally synthesized perovskite powders at 200°C and 24 hours for *R* values of (a) 0%, (b) 11.7%, (c) 13.3%, (d) 15%, (e) 18.3%, and (f) 100% showing the presence of NKN (crosses) and NN (filled squares).

Instead of analyzing the X-ray diffraction data using a peak indexing and visualization method [237, 238], the Rietveld structure refinement method [184] is chosen for three reasons: (1) The Rietveld structure refinement is able to quantitatively analyze the X-ray

diffraction data. The subtle movements of the X-ray diffraction data can be converted to accurate cell parameters, atomic positions, occupancies and thermal parameters. (2) Possibilities for ambiguity due to the presence of the second NN phase introduced by manual indexing are significantly reduced. (3) Increases in cell volume due to proton incorporation [32] in the NKN lattice complicates manual tracking of peak movements. In Figure 39 we can visually observe that the Rietveld refinement (run on the XRD data taken from R = 15% sample) is able to separate and obtain a good fit of the NKN and NN phase, indicated by the minimal difference (observed – calculated) plot shown on the bottom curve. We therefore can expect good refined numerical data for further quantitative analysis.

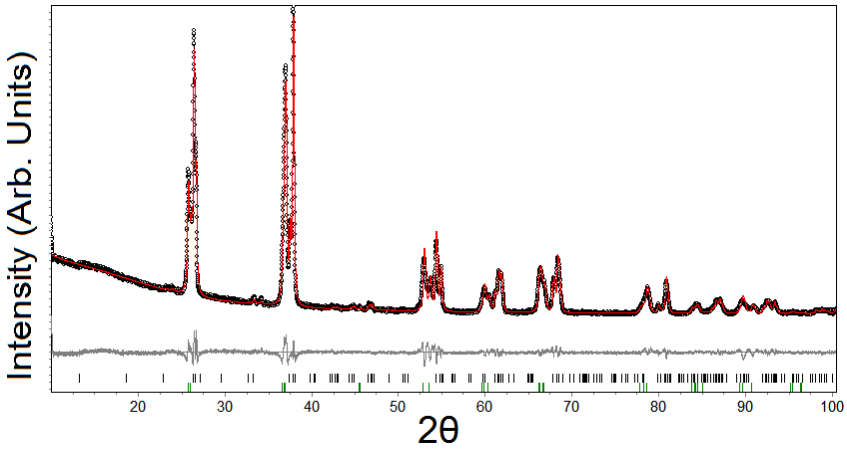

Figure 39: Rietveld refinement of the X-ray diffraction profile of mixed NKN and NN powders precipitated at 200°C showing experimental data (points), calculated (solid line), and the difference curve (bottom curve).

Table 8 contains the entire list of samples with different R ratios, their refinement result and estimated sodium content (represented by *x*) from various determination methods. In this table, unlike manual searching and matching of the XRD spectra that is commonly

found in other works [237, 238], we can confirm the sodium-potassium solid solution in the NKN formed by hydrothermal synthesis and quantify the change in unit cell parameters, as well as *x*, with changing R ratio.

Table 8: List of samples with different R-ratios and the respective XRD data refinement results. Estimated errors are in brackets. Some data in this table, like the sodium content, will be discussed later in the text and will be referred to appropriately.

R (%)	NN 2nd phase (%)	Lattice Parameters			NKN Pseudo cubic vol (Å^3)	Sodium content (*x*)			NKN Phase
		a	b	c		Occupancy refinement	EDS	From volume	
0.0	**0**	4.0263(1)	3.9891(2)	4.0376(2)	64.849	0	0	0	M
1.7	**0**	4.0227(1)	3.9838(2)	4.0359(2)	64.677	0.073(9)	0.0264	0.058	M
3.3	**0**	4.0215(1)	3.9820(1)	4.0357(1)	64.626	0.100(7)	0.0384	0.076	M
5.0	**0**	4.0215(1)	3.9774(2)	4.0353(2)	64.545	0.097(8)	0.0767	0.103	M
6.7	**0**	4.0167(1)	3.9746(2)	4.0320(1)	64.358	0.162(5)	0.1041	0.149	M
8.3	**0**	4.0177(1)	3.9753(2)	4.0320(2)	64.396	0.17(1)	0.1239	0.153	M
10.0	**0**	4.0165(1)	3.9726(1)	4.0331(1)	64.352	0.228(6)	0.161	0.168	M
11.7	**0**	4.0132(1)	3.9729(2)	4.0283(2)	64.228	0.238(7)	0.2143	0.210	M
13.3	**18.7**	4.0134(1)	3.9706(2)	4.0295(2)	64.211	0.245(8)	*	0.216	M
14.2	**47.4**	4.0115(1)	3.9695(2)	4.0285(2)	64.149	0.28(1)	*	0.237	M
15.0	**52.3**	4.0101(1)	3.9701(1)	4.0267(2)	64.112	0.298(8)	*	0.250	M
15.8	**70.6**	4.0098(1)	3.9686(1)	4.0279(3)	64.056	*	*	0.269	M
16.7	**67.4**	4.0036(2)	3.9702(3)	4.0208(6)	63.89	*	*	0.325	M
18.3	**76.6**	3.9982(8)	3.9614(5)	4.0197(9)	63.636	*	*	0.411	M
20	**93.1**	3.938(5)	3.937(6)	4.036(3)	62.873	*	*	0.719	L

The * symbol represents the unavailability of reliable data due to presence of the $NaNbO_3$ second phase.

Rather than evaluating individual unit cell parameters, an assessment of the unit cell volume is more sensitive and appropriate in detecting the structural changes caused by an atomic substitution [239]. Therefore, the cell volume together with *x* values determined by Rietveld refinement and EDS elemental analysis (note: only available for samples with 0% NN 2nd phase) are plotted together in Figure 40 (a). Here, we could observe gradual contraction of the NKN cell volume (filled squares) followed by a corresponding increase of

the sodium occupancy refinement (filled triangles), *x*, in the NKN phase. Around an *R* value of 13.3%, the precipitated powder is no longer single phase NKN but is a mixture of NKN and NN; with the sodium occupancy in the NKN phase still increasing. EDS analysis of the single phase region agrees well with sodium occupancy values obtained from Rietveld refinement.

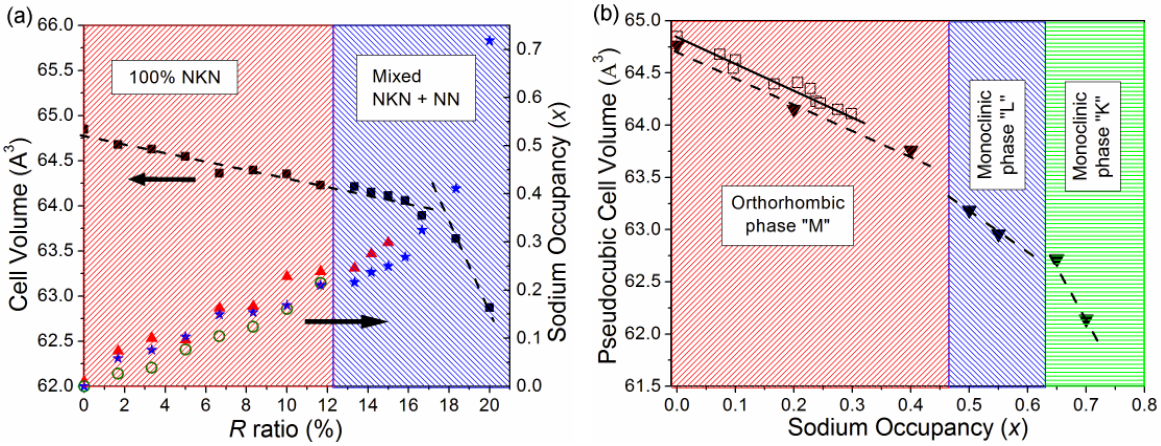

Figure 40: (a) Plot of refined cell volume (filled squares) and sodium content (*x*) obtained from occupancy refinement (filled triangles), EDS (open circles) and cell volume (stars) against *R*. (b) Plot of cell volume vs. sodium content (by refinement) of the as synthesized single phase NKN powder (open squares) and the reference data (filled inverted triangles) [128].

The morphotropic phase boundary between the orthorhombic 'M' phase NKN and the monoclinic 'L' phase occurs around an *R* value of 18.3% when a change in the rate of cell volume decrease (change in gradient in Figure 40(a)) is detected. Unfortunately, the corresponding change in the rate of increase of sodium occupancy as determined from the occupancy refinement cannot be observed around the MPB because from an *R* value of 15.8%, around 70wt% of the precipitated powder consists of sodium niobate. This makes it difficult to determine the sodium fraction in the minority NKN portion from the occupancy

refinement since the diffracted intensities of the minor phase are overshadowed by the majority NN phase.

Alternatively, sodium occupancy can be determined from the cell volume, but only after it is determined that cell volumes (determined from the 2θ values) vary with sodium occupancy (determined from diffracted intensities) according to Vegard's law. This is done by plotting the as-synthesized NKN cell volumes against the *x* values determined from the occupancy refinement, together with the reference data taken from Ahtee and Hewat [128]. As shown in Figure 40 (b), two things are noticed. First, it is confirmed that the variation of cell volume with sodium occupancy for the NKN solid solution obeys Vegard's law [240]. Second, it is noticed that the cell volumes of the as synthesized NKN powders are consistently ≈0.1Å^3 larger than the reference data. This lattice expansion has been observed previously for hydrothermally synthesized perovskite powders and is due to proton and/or water incorporation in the lattice [190, 220]. It is important that this lattice expansion be taken into account during extraction of the sodium fraction from the respective cell volumes since the lattice expansion would make it seem that lattice contraction on replacement of potassium with sodium is less. The sodium occupancy values extracted from the cell volumes is represented in Table 1 ("from vol." column) and Figure 40(a) (filled star symbols) and agree well with EDS and occupancy refinement values. More importantly, the change in the rate of increase in sodium occupancy also occurs in the region indicated earlier by cell volume data to be the MPB. In addition, it shows that NKN can by hydrothermally synthesized with compositions around the MPB.

Examinations of the *R* = 10% sample's morphology using FESEM (Figure 41 (a)) revealed that the synthesized NKN powders was cuboids-shaped with slightly rounded edges, with an average edge-to-edge distance of 200-400 nm. The TEM micrograph and its selected area diffraction pattern shown in Figure 41 (b-c) confirmed that each powder is a single crystal with an estimated *pseudocubic* unit cell of *a*: 3.978 Å.

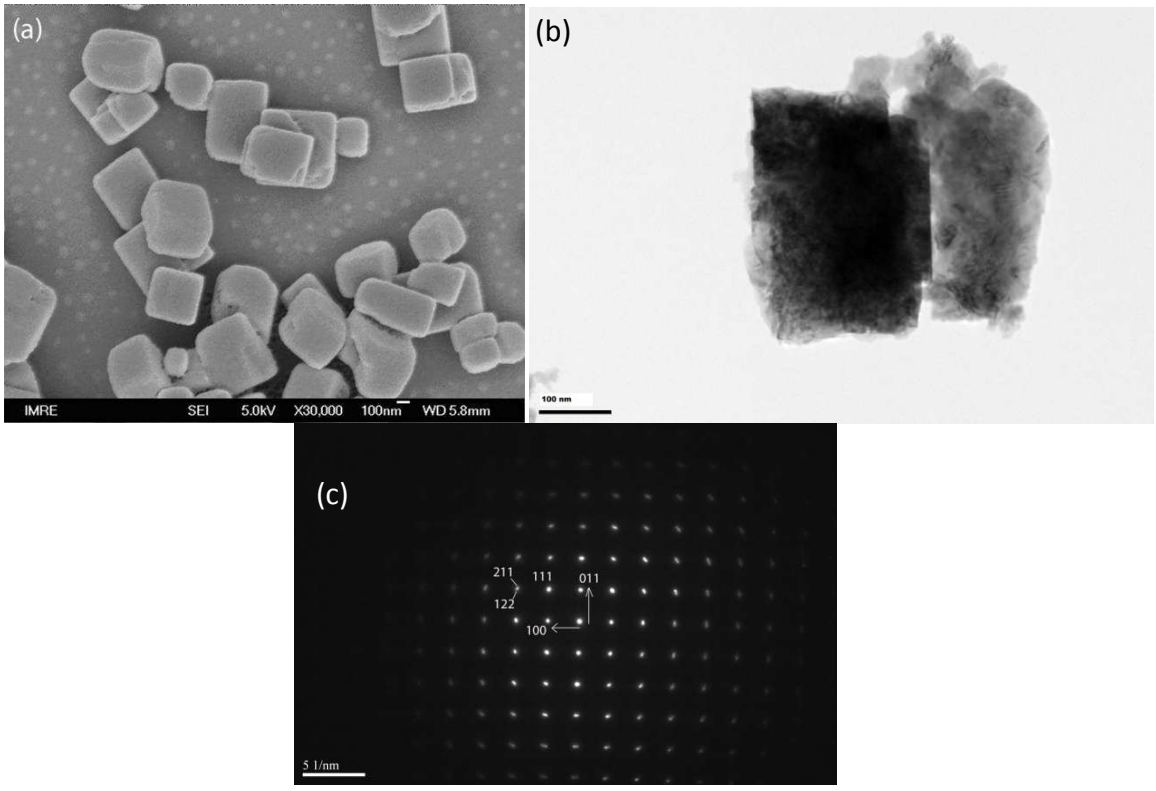

Figure 41: Cube like morphology of as-synthesized NKN powder with "R" ratio of 10% as determined by (a) FESEM and (b) TEM. (c) Selected area electron diffraction of the left crystal shown in (b) along its [0 $\bar{1}$ 1] axis, indicating an orthorhombic single crystal phase.

5.1.3 The Intermediate Hexaniobate Phase

The appearance of a second sodium niobate (NN) phase during hydrothermal synthesis of NKN places some limits on the applicability of the hydrothermal method (e.g. a polymer nanocomposite cannot be made with NKN powders with compositions near the MPB). To

understand the reason for the formation of the second phase, the early stages of NKN synthesis were studied by shortening the reaction period to three hours and lower. Syntheses are chosen using *R* values of 10% and 13.3% as these represent the conditions that yield the pure NKN powder and mixed NKN and NN powders respectively.

As shown in Figure 42, X-ray diffraction reveals that after 1 hour, the precipitated powder consists of the starting Nb_2O_5 and a hexaniobate phase (only the diffractogram for the 10% sample is shown, as it is similar to the 13.3% sample). At 2 hours, the same two phases are still present but for the *R* value of 13.3%, the NN phase is also present in the powder. Finally at 3 hours, only the perovskite phases are present i.e. NKN for the 10% sample and NKN and NN for the 13.3% sample. A manual search and match identified the hexaniobate phase as sodium hexaniobate, $Na_7HNb_6O_{19}\bullet 14H_2O$ [176]. It has been observed in the hydrothermal synthesis of KN that an intermediate hexaniobate phase can precipitate when the solution was left for long period of time [32] or mixed with cold ethanol [171] before the formation of the perovskite phase occurred. In the case of NN, the precipitation of intermediate phase occurs more readily [39] and therefore different types of intermediate phases have been studied and reported [171, 241, 242].

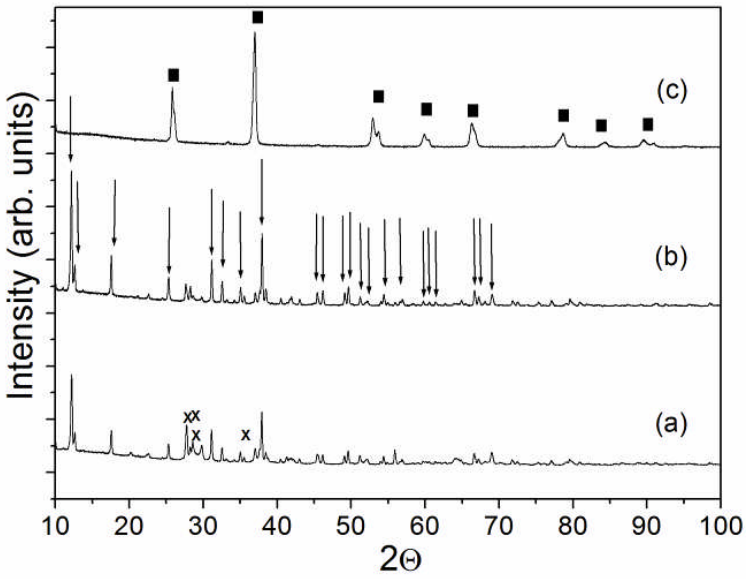

Figure 42: X-ray diffraction spectra of powders after synthesis for (a) 1 hour, (b) 2 hours, and (c) 3 hours for the 10% sample showing transformation of Nb_2O_5 (crosses) to NKN (filled squares) and the presence of an intermediate hexaniobate phase (arrows).

Corresponding scanning electron microscopy of the 10% sample showed that powder morphologies varied in line with changes previously revealed by XRD. As shown in Figure 43 b and c from 1 to 2 hours, Nb_2O_5 powder particles give way to large dodecahedra-shaped hexaniobate particles. Finally, as indicated by XRD, the familiar cube-shaped particles of the perovskite phase are attained at 3 hours (Figure 43 (d)). It is not surprising to find large hexaniobate particles being replaced by sub-micron perovskite particles since a dissolution-reprecipitation process is required to form the perovskite phase. This is because the intermediate hexaniobate is composed largely of edge-sharing NbO_6 octahedra [32] (the lack of corner-sharing NbO_6 octahedra in the intermediate phase was also proven with the absence of light absorption near 300nm, as described by Zhu et al. [242]), while the perovskite phase is composed of a 3D network of corner sharing NbO_6 octahedra.

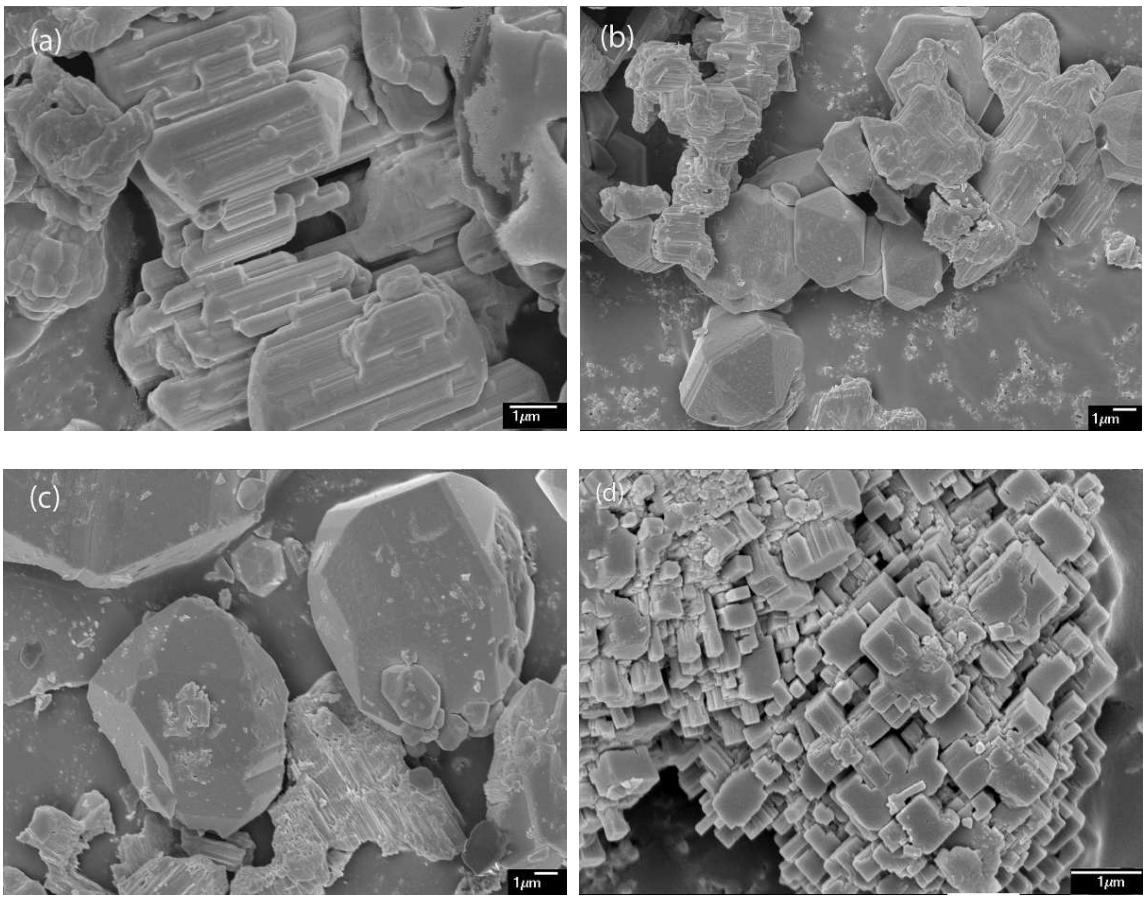

Figure 43: Electron micrographs showing the phase and morphology evolution of (a) Nb_2O_5 precursor and after reaction for (b) 1 hour, (c) 2 hours and (d) 3 hours of synthesis for a *R* = 10% sample.

The Whole Powder Pattern Decomposition (WPPD) refinement method is then applied to the X-ray diffraction data to get the unit cell information. The space group and unit cell information of the $Na_7HNb_6O_{19}•14H_2O$ obtained from the manual search and match method (P*mnn*, #58, *a* = 10.072, *b* = 12.148, *c* = 12.722, two formula units per cell) is taken as a starting point to represent the intermediate hexaniobate phase in the WPPD refinement. Other known phases such as NKN and Nb_2O_5 are also inserted in the refinement to calculate their weight percentage in the powder. The WPPD refinements that are run using only one type of hexaniobate phase quickly converged with R-Bragg values below one,

an indication of very good fits. Any attempts to include more than one phase of hexaniobate in one powder diffraction data leads to convergence failure or *hkl* phase redundancy. This is a strong indication that there is only one hexaniobate phase in each sample. The results of phase composition information and cell volume data obtained from the WPPD method are tabulated in Table 9.

Table 9: WPPD refinement data of samples with *R* = 10% and 13.3%.

	R = 10.00%						*R* = 13.33%					
Time (h)	Hexa cell vol. (Å^3)	Na from EDS (%)	Phase composition (wt%)				Hexa cell vol. (Å^3)	Na from EDS (%)	Phase composition (wt%)			
			Hexa	Nb_2O_5	NN	NKN			Hexa	Nb_2O_5	NN	NKN
1	1560.07	0.321	45.25	54.75	0	0	1565.16	0.455	92.8	4.68	0	2.52
2	1559.72	0.344	90.6	9.4	0	0	1567.52	N.A.	76.44	2.37	18.16	3.03
3	N.A.	NA	0	0	0	100	NA	N.A.	0	0	13.28	86.72
24	N.A.	NA	0	0	0	100	NA	N.A.	0	0	18.98	81.02

It is noticed that the cell volumes of the hexaniobate phases for both the 10 and 13.3% samples (≈1560Å^3 and ≈1565Å^3 respectively) fall in between known cell volumes of sodium (1556.60Å^3) [176] and potassium hexaniobate (1583.75Å^3) [243]. This indicates that the intermediate hexaniobate phase formed was not $Na_7HNb_6O_{19}•14H_2O$ but a mixed hexaniobate, ($Na_yK_{(8-y)}Nb_6O_8•nH_2O$). Since the 13.3% sample has a greater amount of sodium precursor (NaOH), it is counter-intuitive to find that the mixed hexaniobate for the 13.3% sample had a lower amount of sodium (as inferred by its larger cell volume that is closer to potassium hexaniobate), especially since the sodium occupancy in the final NKN powder formed for both samples is higher for the 13.3% sample. Therefore, energy

dispersive X-ray spectroscopy (EDS) was carried out on samples without significant amounts of NN and/or NKN to verify this observation. These results are also found in Table 9.

As expected, EDS analysis indicates that the 13.3% hexaniobate has more sodium than the 10% hexaniobate (34% and 46% sodium for the 10% and 13.3% hexaniobate samples respectively). It is believed that the mixed hexaniobate from the 13.3% sample had a larger cell volume than the 10% sample (thus initially suggesting that the 13.3% sample had lower sodium content) because of greater proton incorporation in the lattice - both in the form of hydroxyl groups (H attaches to one of the O positions) and water molecules.

To verify this, both FTIR and TGA experiments were carried out. Figure 44(a) shows normalized FTIR spectra taken from samples with majority hexaniobate phases (2 and 1 hour for 10% and 13.3% samples respectively). The spectra reveal the signature bands related to O-H stretching (3250 cm^{-1}) and H_2O bending (1600 cm^{-1}) modes [171, 175]; confirming the large presence of incorporated water/hydroxyl in the lattice; and signature bands in the 400–1000 cm^{-1} range - similar to previous works on sodium hexaniobate and are related to the Nb-O vibrational modes [171, 175, 244]. Comparing the normalized FTIR data, the larger (inverted) area under the curve for R = 13.3% samples compared to the R = 10% indicates that the former has more water/hydroxyl incorporation in the lattice. Presence of incorporated water/hydroxyl (instead of surface water) is confirmed by the TGA experiment (Figure 44(b)). The weight loss data reveals significant weight losses from 135-300°C range – commonly attributed to interlayer or lattice trapped water/hydroxyl removal

[245], and it is also observed that the weight loss is greater for the mixed hexaniobate of the 13.3% sample compared to the 10% sample. Although the difference in the weight loss data may arise due to different hexaniobate phase percentage (refer to Table 9), the findings from TGA and FTIR suggest that the larger cell volume of mixed hexaniobate for the 13.3% sample is due to greater amount of water/hydroxyl incorporation.

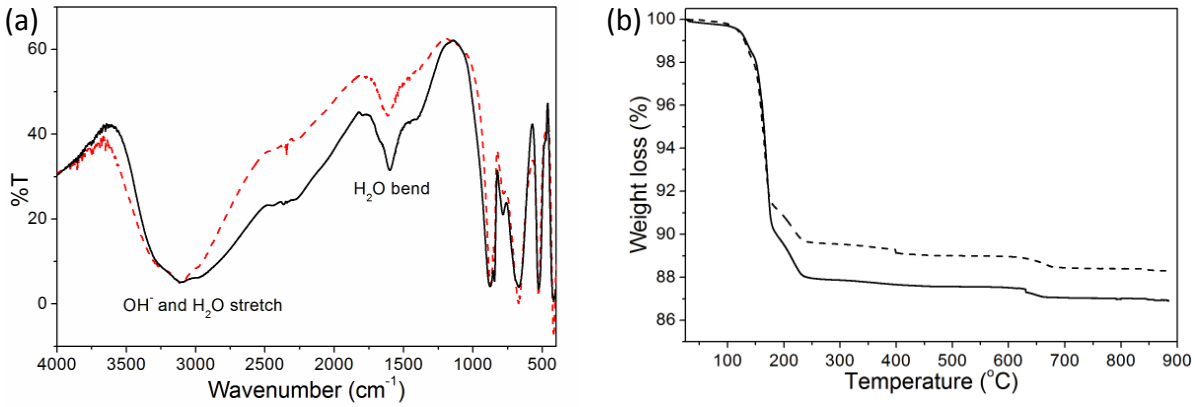

Figure 44: (a) Normalized FTIR (transmission mode) and (b) TGA data of NKN powder samples synthesized at different R ratios of 10% (dashed line) and 13.3% (solid line).

Turning our attention back to Table 9, it is observed that only after the first hour, the phase compositions of the 2 samples are significantly different. For the 13.3% sample, less than 5 wt% of the Nb_2O_5 precursor is still present compared to >50 wt% for the 10% sample. This indicates that the Nb_2O_5 precursor is dissolved at a much faster rate for the 13.3% sample, much faster than what had been reported previously using only KOH solution with similar concentration [40]. Consequently, the intermediate hexaniobate ions for the 13.3% sample are formed more rapidly than for the 10% sample and the system is quickly pushed to supersaturation; evident in the very high amount of hexaniobate powder that precipitated

for the 13.3% sample (>90 wt%). In order to relieve the supersaturation, the more stable perovskite phases are formed. In the case of the 10% sample, only the NKN perovskite phase is formed. In the case of the 13.3% sample, both NN and NKN phases formed and it is believed that precipitation of the NN phase helps to relieve the supersaturation of the system faster. Also, it is NN and not KN that forms as the second phase as NN is reported to form faster than KN [32].

The large amount of the hexaniobate ions precipitated in concentrated KOH solution (an *R* value of 13.3% contains >5M KOH) at 200°C however, was not expected, because the (potassium) hexaniobates are known to be soluble in these conditions [32, 40]. On the other hand, when NaOH is used in place of KOH as mineralizer, the (sodium) hexaniobate is much less soluble [32, 39]. Although sodium and potassium have the same ionic charge, sodium is slightly more electronegative and has a smaller ionic radius than potassium. This means a sodium-bonded atom pair will be shorter (i.e. stronger) and less polar compared to potassium-bonded atom pair. As a result, a lot of sodium salts, including sodium hexaniobate [39] are less soluble than the potassium salt. Therefore, it can be said that although sodium ions increase the solubility of the precursor Nb_2O_5 powder (note that the total OH concentration is the same for all samples), they decrease the solubility of the hexaniobate ion. More detailed understanding of how sodium affects the solubilities of these species appears to be the key to synthesizing single phase NKN powders spanning the MPB.

5.2 Hydrothermal Synthesis of NKN Powders from Perovskite Precursors

5.2.1 Introduction

In this part we attempted an alternative method of synthesizing $(Na_xK_{1-x})NbO_3$ particles by hydrothermal treatment of $KNbO_3$ (as precursor powder) in NaOH solution or $NaNbO_3$ in KOH solution. We expected an intercalation reaction to occur between the sodium and potassium ions to ultimately form $(Na_xK_{1-x})NbO_3$ solid solution in the hydrothermal treatment process but this did not take place. Instead, mixtures of $KNbO_3$ and $NaNbO_3$ powders of smaller particle sizes were formed and could be annealed faster at lower temperatures to form $(Na_xK_{1-x})NbO_3$ powder close to the morphotropic phase boundary.

5.2.2 Results and Discussion

Two XRD data sets showing a series of samples synthesized for different reaction periods (only selected timings are presented for clarity) elucidates the hydrothermal treatment process from $NaNbO_3$ precursor in KOH (Figure 45 (a)) and from $KNbO_3$ precursor in NaOH (Figure 45 (b)). From the preliminary XRD peak position search and matching process, it was apparent that the expected conversion from either $NaNbO_3$ and $KNbO_3$ precursor to $(Na_xK_{1-x})NbO_3$ did not happen since peak positions for the perovskite phases matched either that of $NaNbO_3$ or $KNbO_3$ only. Instead, the conjugate perovskite phase (that is, $KNbO_3$ phase from $NaNbO_3$ precursor and vice versa) appeared in the middle of each reaction – after 10 hours when using the $NaNbO_3$ precursor and after 1.2 hours when using the $KNbO_3$ precursor.

It was also observed that the reaction starting with $NaNbO_3$ in KOH solution was sluggish, requiring more than 20 hours for the $NaNbO_3$ powders to convert completely to the $KNbO_3$ conjugate phase. In comparison, reactions starting with $KNbO_3$ powders in NaOH formed $NaNbO_3$ in less than 2 hours. The other main difference was the presence of an intermediate phase, sodium hexaniobate, (marked with "x" in Figure 45 (b)) which can only be seen during conversion from $KNbO_3$ to $NaNbO_3$. Since the hexaniobate is commonly seen as an intermediate phase before the formation of the perovskite phase, this suggests that instead of an intercalation reaction, the reaction proceeded from $KNbO_3$ to sodium hexaniobate and then finally $NaNbO_3$. Thus, when starting from $NaNbO_3$, the conversion would be from $NaNbO_3$ to potassium hexaniobate and then $KNbO_3$. This would then explain the absence of any intermediate phase in the XRD spectra as potassium hexaniobate is much more soluble than its sodium counterpart and would still be in solution. [32, 190]

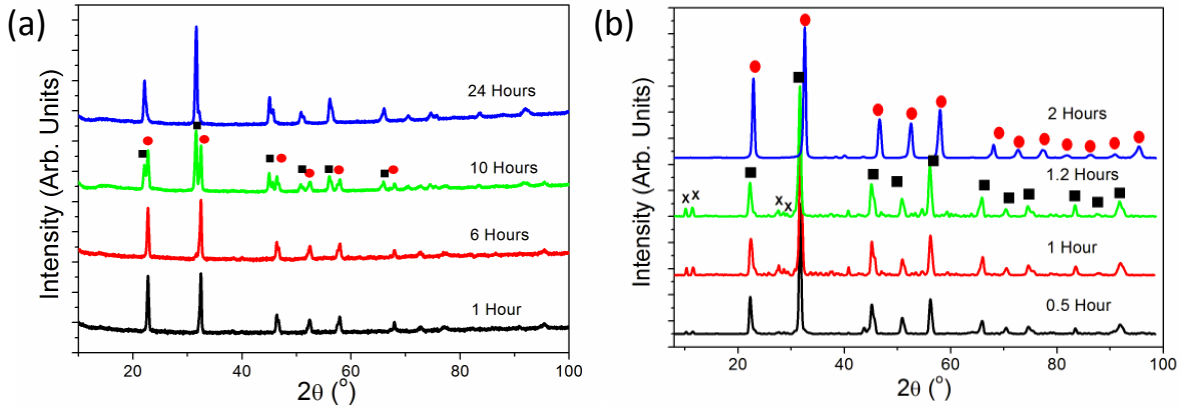

Figure 45: XRD data of selected samples from (a) $NaNbO_3$ to $Na_xK_{1-x}NbO_3$ ("NN to NKN") and (b) $KNbO_3$ to $Na_xK_{1-x}NbO_3$ (KN to NKN) conversion. Symbols: x = hexaniobates, ■ = $Na_xK_{1-x}NbO_3$, ●● $NaNbO_3$.

The faster conversion of the $KNbO_3$ precursor in NaOH to $NaNbO_3$ as compared to the reverse reaction can also be seen in the powder yield graphs in Figure 46. For full conversion of $NaNbO_3$ to $KNbO_3$ (Figure 46 (a)), the yield should be 1.08 since $KNbO_3$ has a higher formula weight than $NaNbO_3$. Immediately it is clear that full conversion to $KNbO_3$ only happens after 24 hours. It is also clear that upon dissolution of $NaNbO_3$ after only 1 hour, the soluble intermediate potassium hexaniobate phase is already present and explains why the ratio is less than 1.

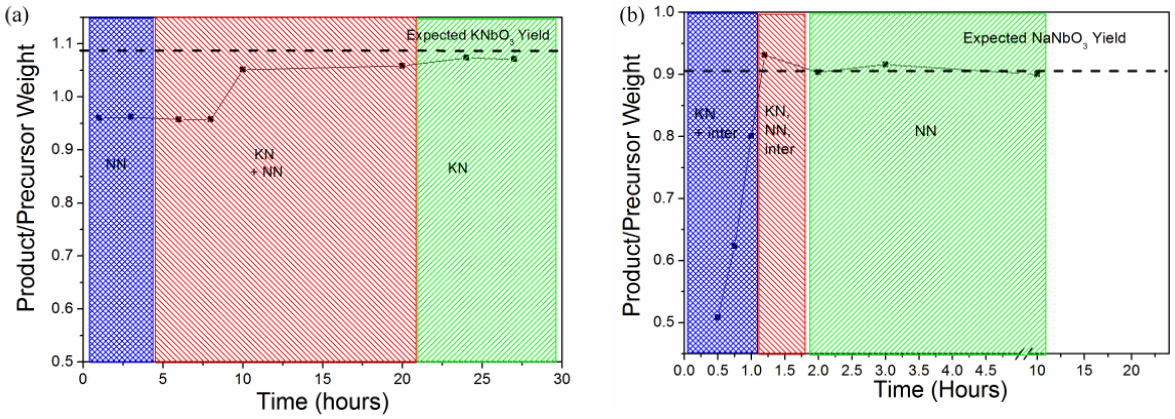

Figure 46: Powder yield curve of (a) $NaNbO_3$ to $Na_xK_{1-x}NbO_3$ ("NN to NKN") and (b) $KNbO_3$ to $Na_xK_{1-x}NbO_3$ (KN to NKN) conversion. Note the time scale difference for (a) and (b).

For full conversion of $KNbO_3$ to $NaNbO_3$, the yield should be 0.92 and Figure 46 (b) clearly shows the faster kinetics of this conversion. Unlike the $NaNbO_3$ to $KNbO_3$ conversion, major weight loss is observed at short reaction times while at the same time sodium hexaniobate was detected by XRD. Since the molecular weight of sodium hexaniobate is higher than $NaNbO_3$ and also has very low solubility, the only explanation for the drastic weight loss is the presence of potassium hexaniobate. Therefore, for the $KNbO_3$ to $NaNbO_3$ conversion,

$KNbO_3$ first dissolves due to the formation of potassium hexaniobate which is converted to sodium hexaniobate and then finally to $NaNbO_3$.

To confirm that no intercalation occurred in the midst of the $NaNbO_3$ to $KNbO_3$ reaction (intercalation for niobate perovskites have been reported even at room temperature [246]), the Rietveld refinement method was employed to reduce and refine the XRD data of powders obtained during the hydrothermal treatment of $NaNbO_3$ in KOH to look for any measureable change in unit cell parameters and volume as substitution of Na^+ with K^+ will result in lattice expansion. The refined lattice parameters of $KNbO_3$ and $NaNbO_3$ are tabulated in Table 10.

Table 10: Refined $NaNbO_3$ and $Na_xK_{1-x}NbO_3$ cell parameters of "NN to NKN" hydrothermal conversion samples with 1-27 hours reaction time.

Time (hrs)	Phase content (%)		NN cell parameter				NKN cell parameter				*Rwp*
	NN	NKN	*a*	*b*	*c*	Vol.	*A*	*b*	*c*	Vol.	
1	100	0	5.5139(4)	5.5661(4)	15.555(1)	477.40	n.a.	n.a.	n.a.	n.a.	0.67
3	100	0	5.5159(4)	5.5671(5)	15.556(1)	477.68	n.a.	n.a.	n.a.	n.a.	0.65
6	96.71	3.29	5.5139(3)	5.5680(3)	15.550(1)	477.42	3.974(5)	5.72(1)	5.69(1)	129.52	1.01
8	94.87	5.13	5.5137(4)	5.5685(4)	15.550(1)	477.44	3.963(4)	5.70(6)	5.70(6)	129.34	0.68
10	45.97	54.03	5.5158(4)	5.5696(4)	15.550(1)	477.71	3.9817(2)	5.7136(4)	5.6934(4)	128.85	1.07

The average values of the refined cell volumes of $NaNbO_3$ and $KNbO_3$ (477.5 $Å^3$ and 129 $Å^3$ respectively) are found to be about 1-2 $Å^3$ larger than the bulk $NaNbO_3$ [177] and $KNbO_3$ [117] values. This amount of lattice expansion is typical for hydrothermally synthesized powders, due to known proton incorporation in the lattice [190]. Therefore, the lack of significant cell parameter variation indicates that an intercalation reaction is unlikely and that the conversion of $NaNbO_3$ to $KNbO_3$ occurs by a dissolution-reprecipitation reaction.

The dissolution-reprecipitation reaction in the conversion of $NaNbO_3$ to $KNbO_3$ is also supported by the evolution of the particle morphology's electron micrographs (Figure 47). After 1 and 3 hours when XRD reveals only $NaNbO_3$ in the powder, SEM micrographs in Figure 47(a-b) reveal majority particle sizes in excess of 500nm although smaller particles are also present. The smaller particle sizes are a result of the ongoing dissolution by KOH to form potassium hexaniobate as indicated by powder yield calculations in Figure 46(a). When XRD indicate that $KNbO_3$ is present, much smaller particles about 100nm in size begin to appear, with their numbers increasing as the reaction proceeds, as shown from Figure 47 (c–e). These smaller particles are not just newly precipitated $KNbO_3$ but also dissolving $NaNbO_3$ particles. Finally, mainly large particles are present when XRD indicates only the presence of $KNbO_3$ (Figure 47(f)). Obviously grain growth has caused the initial $KNbO_3$ nanosize particles to become larger and also agglomerate with neighboring particles. Therefore, a dissolution-reprecipitation process is confirmed since an intercalation reaction would not see such drastic changes in particle sizes.

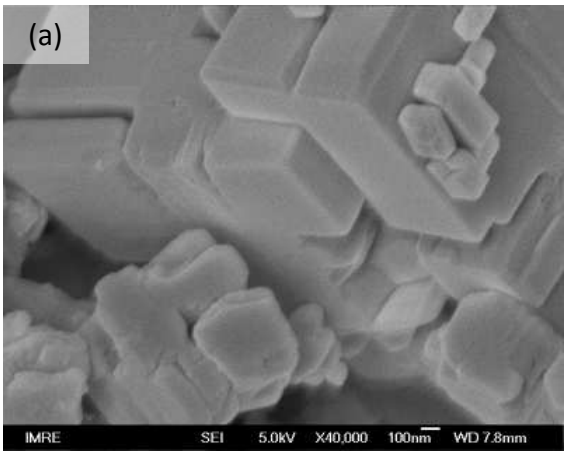

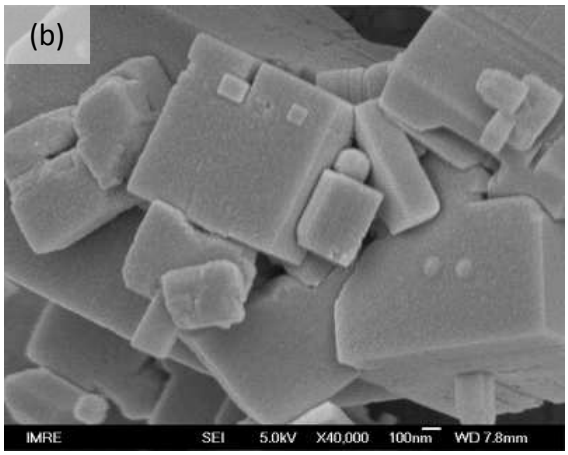

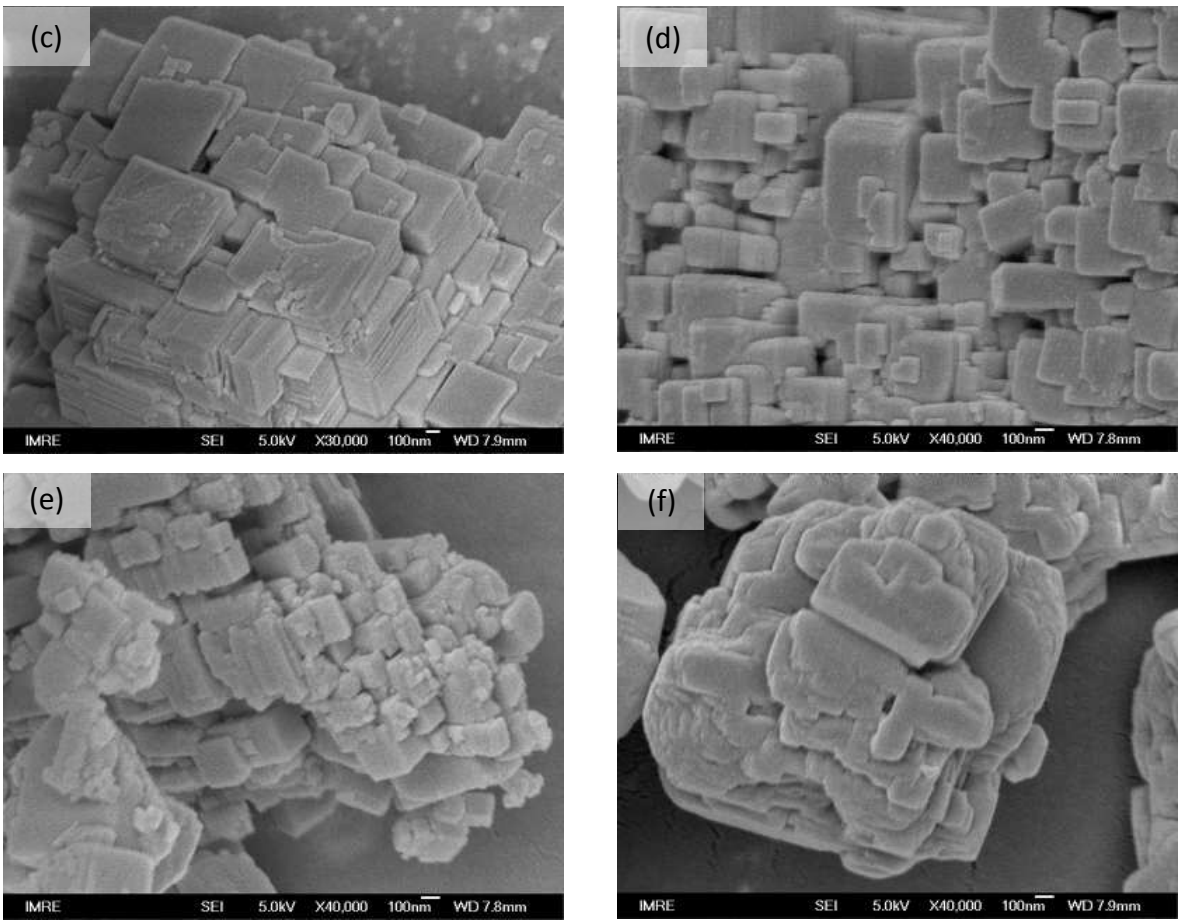

Figure 47: Evolution of particle morphology for $NaNbO_3$ to $KNbO_3$ conversion after (a) 1, (b) 3, (c) 6, (d) 8, (e) 10, and (f) 24 hours.

5.3 Achieving single phase NKN powders via short heat treatment

Although single phase $(Na_xK_{1-x})NbO_3$ solid solution powders were not obtained from either synthesis using oxide or perovskite precursors, significantly smaller particle sizes of mixed $KNbO_3$-$NaNbO_3$ powders can be obtained using the perovskite precursor approach. For such mixtures, physisorption measurements also indicated increased specific surface areas. For example, after 10 hours reacting $NaNbO_3$ in KOH (Figure 47 (e)), a BET surface area of 3.2 m^2/g was attained which is about 3.5 times larger than that of either the $KNbO_3$ or $NaNbO_3$

precursor powder (≈0.9 m^2/g). Large surface areas are useful for increasing the catalytic activity and also lowering calcination temperatures, which during solid state synthesis is normally done in the 800 to 1000°C range due to the need of converting carbonate precursors to the desired perovskite phase in several steps [141, 247, 248].

To demonstrate this advantage, a $KNbO_3$-$NaNbO_3$ powder mixture obtained after reacting $NaNbO_3$ in KOH for 10 hours (Table 10) was heated to 800^oC[††] and immediately furnace cooled once the temperature was reached. XRD (Figure 48) indicated that the resultant powder was a single phase perovskite $(Na_xK_{1-x})NbO_3$ solid solution powder while Rietveld refinement showed that it had a cell volume of 126.12 $Å^3$, smaller than the original and bulk $KNbO_3$ cell volume, an indication of lattice contraction due to incorporation of sodium atoms in the lattice (Table 11). Sodium occupancy refinement also revealed that 50% of the sodium atoms had replaced the potassium atoms, giving the $(Na_{0.5}K_{0.5})NbO_3$ solid solution powder a composition very close to the morphotropic phase transition boundary (MPB) which is at 51% Na [28], a requirement to display good piezoelectric performance.

[††] Determination of the optimum heat treatment temperature of 800°C is not shown here but can be referred to in the Appendix A.

Table 11: Cell volume, sodium occupancy and phase composition after 2 hours at 800°C.

R ratio (%)	NKN Pseudo cubic cell vol. (refined, Å^3)		Sodium occupancy (*x*)			NN 2nd phase (refined wt%)	
	Initial	After HT	Initial (from vol.)	After HT (from vol.)	After HT (EDS)	Initial	After HT
11.7	64.27	64.19	0.196	0.199	0.22	0	0
13.3	64.21	63.71	0.217	0.365	0.37	22.02	0
13.8	64.19	63.45	0.222	0.491	0.45	26.69	0
14.2	64.15	63.09	0.237	0.495	‡‡	47.65	10.16
15	64.11	62.78	0.251	0.626	‡‡	52.3	12.72
16.7	62.03	61.19	0.717	0.844	‡‡	78.44	26.26
Base-line §§	n.a.	63.28	n.a.	0.414	‡‡	56.52§§	38.10

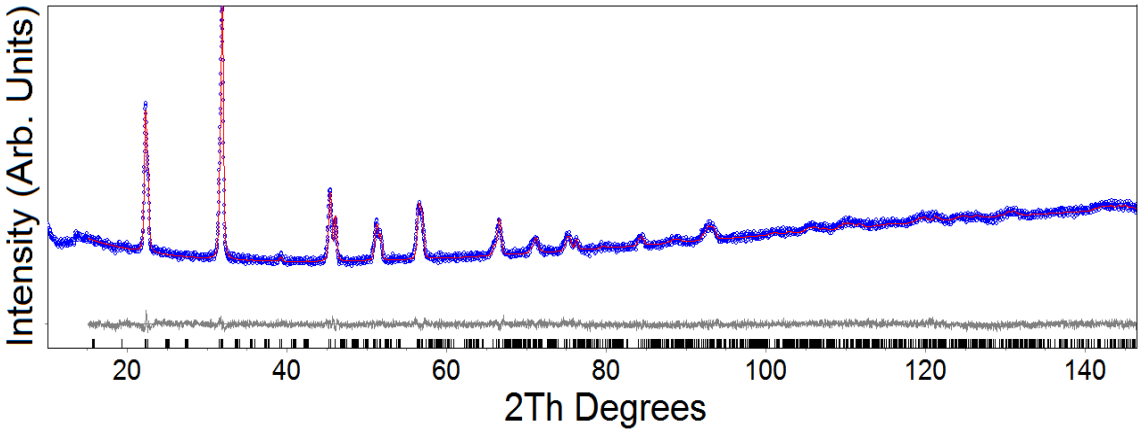

Figure 48: Rietveld refinement of XRD data ($Na_{0.5}K0_{0.5}$)NbO_3 powder obtained after heating to 800°C.

In contrast, heat treatment of a 1:1 (mole ratio) mixture of separately hydrothermally synthesized $KNbO_3$ and $NaNbO_3$ powders at 800°C after 3 hours could not form a single phase NKN powder. Instead, a mixture of $(Na_{0.4}K_{0.6})NbO_3$ and $NaNbO_3$ was obtained, indicating that the reaction was incomplete (Table 11).

‡‡ Reliable EDS data was unavailable due to presence of NN phase.

§§ Baseline sample is a mixture of individually synthesized KN and NN powder with approximately 1:1 KN to NN mol ratio, translating into 56.52wt% NN 2nd phase (calculated).

5.4 Summary

Attempts to form $(Na_xK_{1-x})NbO_3$ solid solution powders via intercalation by hydrothermally treating $NaNbO_3$ in 6M KOH or $KNbO_3$ in 6M NaOH at 200°C instead yielded the conjugate perovskite phase due to a dissolution-reprecipitation process. The $NaNbO_3$ to $KNbO_3$ conversion occurred by dissolution of $NaNbO_3$ to form potassium hexaniobate which then converted to $KNbO_3$. The $KNbO_3$ to $NaNbO_3$ conversion proceeded first by dissolution of $KNbO_3$ to form potassium hexaniobate which converted to sodium hexaniobate and finally $NaNbO_3$.

$Na_{0.5}K_{0.5}NbO_3$ was synthesized by heating a powder mixture of $KNbO_3$ and $NaNbO_3$ to 800°C and cooling immediately, significantly faster than the conventional all solid state route. The $KNbO_3$-$NaNbO_3$ powder mixture was obtained 10 hours into the conversion of $NaNbO_3$ to $KNbO_3$. The dissolution-reprecipitation nature of the conversion process led to an intimate mixture of $KNbO_3$ and $NaNbO_3$ powders with much smaller particle sizes than the initial $KNbO_3$ and $NaNbO_3$ powders that were used in their respective reactions. The smaller particle sizes led to a specific surface area that was 3.5 times greater than the separately hydrothermally synthesized perovskite powders. The increased surface area, smaller grain sizes and intimate mixing of the powders were responsible for the much faster conversion to a $Na_{0.5}K_{0.5}NbO_3$ solid solution powder with a composition close to the morphotropic phase boundary.

6. Hydrothermal epitaxy of $Na_xK_{(1-x)}NbO_3$ and $(Na_xK_{(1-x)})_yLi_{1-y}(Nb_zTa_{1-z})O_3$ solid solution thin films

6.1 Introduction

Despite proven [3] detrimental effects leading to recent expulsion of lead from many commercial applications and materials (e.g. from solder, glass, and electonic components [5]), $Pb(Zr,Ti)O_3$ (PZT) based ceramics are still used extensively in sensors, actuators and other piezoelectric devices because a similarly high performance material has yet to be established. PZT's best performance is achieved near the morphotropic phase boundary (MPB), a discontinuous change in the crystal structure when the tetragonal unit cell changes to a rhombohedral one as Zr increasingly substitutes for Ti [1, 2], containing 60 wt% lead [249]. Furthermore, high temperature steps required to synthesize PZT makes a valid concern for lead poisoning due to the ease of PbO volatility [4].

A fact is a simple statement that everyone believes. It is innocent, unless found guilty. A hypothesis is a novel suggestion that no one wants to believe. It is guilty, until found effective.
Edward Teller (1908 – 2003).

$(Na_xK_{1-x})NbO_3$ (NKN), a sodium-substituted potassium niobate is one possible candidate to replace PZT. This is because, like PZT, a morphotrophic phase boundary (MPB) exists when the sodium replaces ≈50% of the potassium sites [28, 119] in NKN, causing an abrupt change from an orthorhombic unit cell

(A*mm2*, 2 formula units/cell) to monoclinic (P*1m1*, 8 formula units/cell), while still maintaining a reasonably high Curie temperature (T_c) [141]. It was recently demonstrated [18, 19] that a new lead-free combination of NKN and hexagonal pseudo-ilmenite-type $LiTaO_3$ (LT thereafter) can exhibit an electric field induced strain comparable to typical actuator-grade PZT (d_{33} = 373 pCN^{-1}) for textured ceramics with an (empirical[***]) composition of $(K_{0.5}Na_{0.5})_{0.97}Li_{0.03}(Nb_{0.8}Ta_{0.2})O_3$ due to the formation of a new MPB between NKN and LT phases and a possible hybridization of covalency (Ta is more electronegative than Nb) onto the perovskite system that could lead in further improvement in piezoelectricity [90].

However, the process employed to get an NKN-LT film (or rather thick, textured ceramics via tape casting) with the correct composition requires multiple high temperature steps close to the composition's melting temperature (up to 1135°C) [18, 19]. The need for high temperature process is not attractive to existing industries that uses PZT based thin films as most miniaturized devices are prone to heat-induced damage. The extreme temperatures required to synthesize NKN-LT also prohibits the possible direct integration to micro/nano electro mechanical systems (M/NEMS) or polymeric substrates (e.g. polyimide epoxy, a widely used printed circuit board material, has a glass transition of 250 – 260°C [250]). This chapter reports an alternative route to synthesize epitaxial NKN-LT via hydrothermal synthesis at significantly lower temperatures of 130-200°C in water. Problems and difficulties faced during the epitaxial film growth via hydrothermal method and ways to

[***] The composition stated is empirical, based on the ratio of precursors added in the reference [19]

overcome the difficulties by understanding the reaction and different precursors' solubility will also be discussed.

6.2 Results and Discussion

6.2.1 Direct NKN film growth

Phase content of as-synthesized NKN films is first analyzed using a quick-scanning XRD equipped with a general area detector (Figure 49 (a)). Similar to the observation in hydrothermally epitaxied $KNbO_3$ films [37, 41], the as-synthesized NKN films display (0*l*) out-of-plane orientation. However, it is noticed that samples synthesized in higher R-ratio appear to have broader (022) peak and asymmetric shoulder near the (002) STO substrate peak (Figure 49 (a), circled). It is suspected that the unusually broad (022) peak is due to the presence of extra peaks. To confirm what causes the (022) peak broadening, short-range HRXRD scans around 46° 2θ were done on selected films (Figure 49 (b)). It is also revealed that the wide peak shoulders seen at high R-ratio samples are actually an array of extra peaks (Figure 49 (b), arrows) that is likely to originate from a second phase.

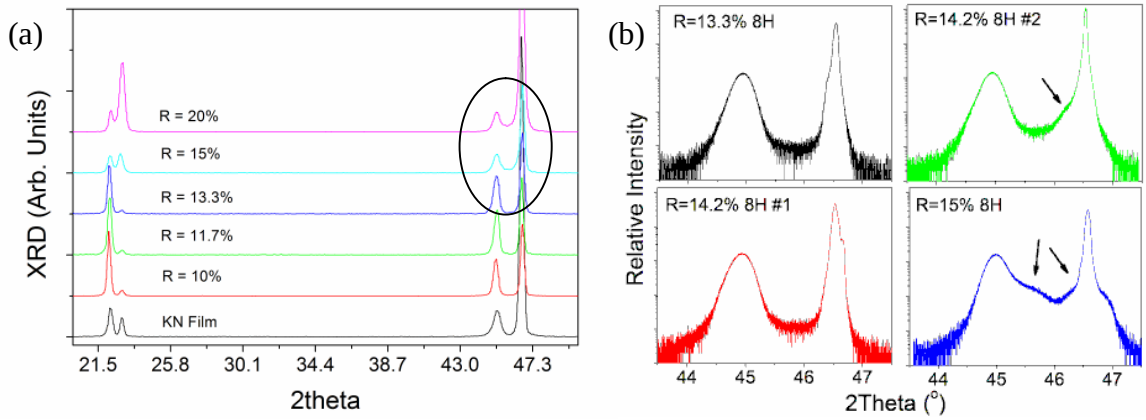

Figure 49: XRD of as-synthesized NKN as seen by (a) Fast-scanning XRD with area detector and (b) HRXRD of selected samples synthesized at different R ratios near NKN (022) peak. Data from hydrothermally synthesized epitaxial $KNbO_3$ is added in (a) (black line, bottom) as a reference.

Unlike XRD data obtained from single crystal or powder samples, quantitative analysis of epitaxial film XRD data is difficult because the out-of-plane reflexions are insufficient to accurately determine the symmetry, lattice parameters and estimated atomic positions, etc.

Bearing the possibility of impurity phase formation in the as-grown NKN film in mind, we proceed with caution in using an EDS-equipped electron microscope to determine the NKN films' composition. The EDS elemental analysis results together with estimated thickness of the NKN films with different R-ratio are listed in Table 12. Here it is observed that the Na content in the as-synthesized NKN films is increasing steadily with increased R-ratio, up to 13.3%. However, the steady increase is broken when the R-ratio reaches 14.2% (the "borderline" composition). Five different samples with similar R-ratio ≈14.2% show significant variation of their EDS results: three of them show a more reliable (low standard

deviation value) EDS reading of 37% Na fraction and two others show a significant jump in the Na fraction reading to ≈50% with significant standard deviation.

In our previous work on hydrothermal synthesis of NKN powder [251], the extra XRD peaks and fluctuating EDS readings are signs of a second, unwanted Na-rich perovskite phase formation. It is now proposed that the second phase formation may also happen during the epitaxial NKN film growth.

Table 12: EDS and thickness data of the as-synthesized epitaxial NKN films. The thickness values shown here are the average of 3-4 cross section measurements done using FESEM at randomly selected points. R-ratio 0% sample is a hydrothermally synthesized KN reference. Numbers in brackets represent the standard deviation value.

	R-ratio (200°C 8H)							
Elements	**0%**	**10%**	**11.7%**	**13.3%**	**14.2% #1**	**14.2% #2**	**15%**	**20%**
Na	0.002(2)	0.12(2)	0.16(1)	0.21(1)	0.37(1)	0.5(1)#	0.6(2)#	1.011(4)#
K	1.014(4)	0.87(1)	0.82(1)	0.77(1)	0.72(1)	0.5(1)#	0.5(2)#	0.05(1)#
Nb	0.9967(5)	1.003(3)	1.005(2)	1.004(2)	0.982(3)	0.986(1)	0.98(1)	0.987(2)
Thickness (μm)	0.229(6)	0.98(7)	1.11(2)	1.29(8)	1.14(4)	1.00(5)	1.52(2)	1.86(7)

#Possible EDS inaccuracy due to uneven phase composition. #1 and #2 are examples of borderline samples at R-ratio 14.2% showing different EDS results.

It is also apparent that the as-grown NKN films gradually become thicker as the R-ratio increases. Note that the thicknesses of NKN films are approximately 4-8 times thicker than KN film grown at similar condition without any sodium (Table 12). Hydrothermal epitaxy of NKN is likely to follow similar island growth mechanism reported for various types of perovskite oxides that is initiated by the "A" cation (of ABO_3 perovskite) adsorption on the substrate imperfections (steps/ledges) and followed by BO_6^{m-} monomer attachment [30, 37,

252, 253]. As the BO_6^{m-} monomer needs to be obtained (read: broken down) from the oxide precursor (in this case, Nb_2O_5), this means that the film growth rate will be limited by the slowest of these perovskite formation reactions reported in growth of $KNbO_3$ [32]: (a) Nb_2O_5 (oxide) precursor dissolution to form intermediate (variants of $Nb_6O_{19}^{8-}$) phase, (b) breaking down of intermediate $Nb_6O_{19}^{8-}$ phase to form NbO_6^{7-}monomer, and (c) monomer attachment and integration to the final perovskite phase. While it is known that $NaNbO_3$ formation in NaOH is faster than $KNbO_3$ under similar conditions in KOH [32, 242], more recent in-situ hydrothermal synthesis of $NaNbO_3$ results shed light that 1 g Nb_2O_5 can be dissolved in 1 M NaOH solution under hydrothermal conditions within 15 minutes [241]. Rapid dissolution of Nb_2O_5 precursor will in turn create supersaturation, as also reported in the hydrothermal synthesis of NKN powder [251], which are subsequently relieved by the precipitation Na-rich perovskites (also, refer to related section 5.1.3).

It is also noticed that the extreme film growth rate also worsens the film roughness, resulting in large and uneven island blocks that become more and more obvious with increasing R-ratio (e.g. Figure 50 (m) for R-ratio = 20%). Apart from the possible second Na-rich phase top layer formation suggested by XRD and EDS results, blocky island-like surface observed at higher R-ratio samples will lead to poor electrical contact that could prevent proper electrical measurements.

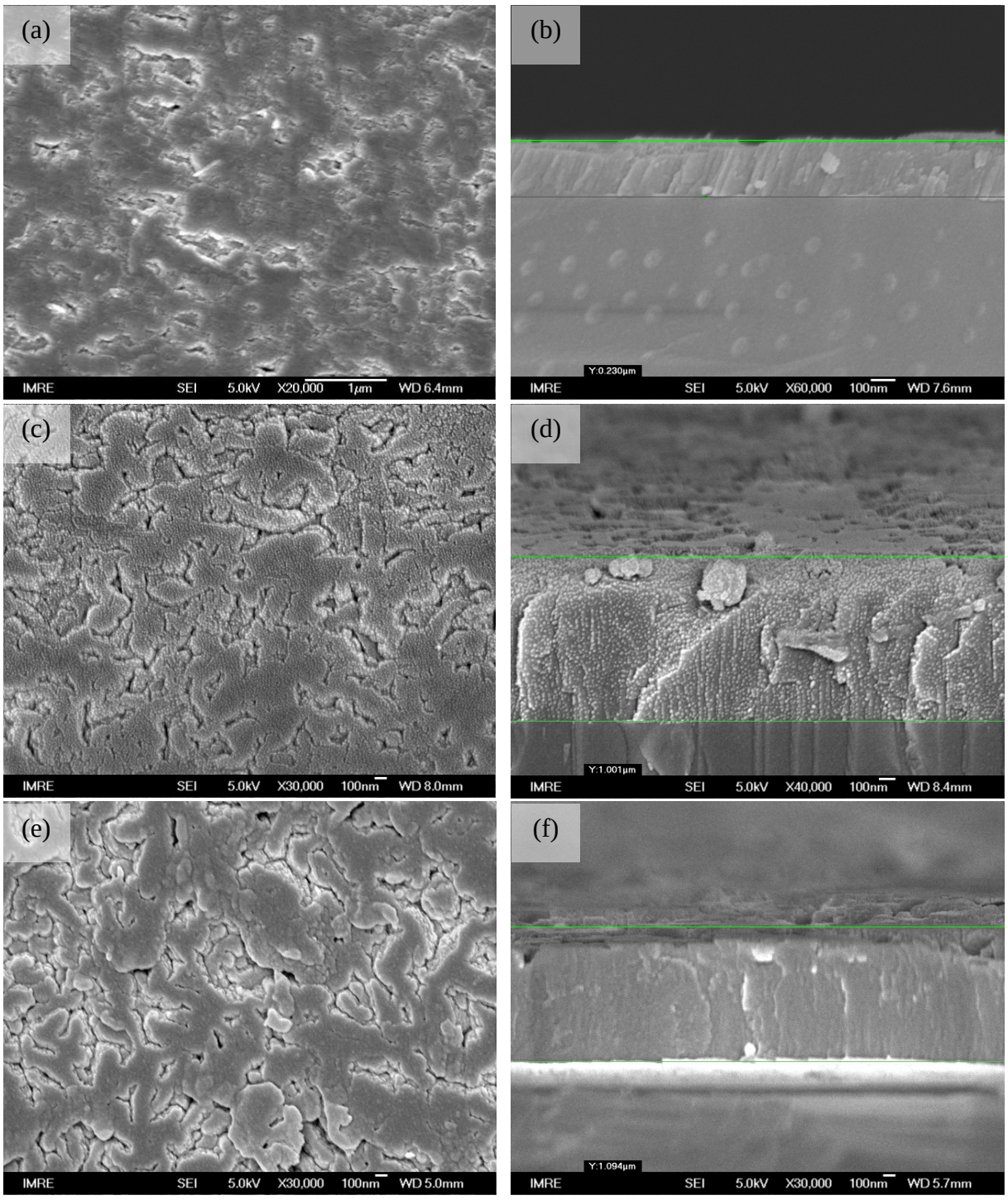
(a)
IMRE SEI 5.0kV X20,000 1μm WD 6.4mm
(b)
Y:0.230μm
IMRE SEI 5.0kV X60,000 100nm WD 7.6mm
(c)
IMRE SEI 5.0kV X30,000 100nm WD 8.0mm
(d)
Y:1.001μm
IMRE SEI 5.0kV X40,000 100nm WD 8.4mm
(e)
IMRE SEI 5.0kV X30,000 100nm WD 5.0mm
(f)
Y:1.094μm
IMRE SEI 5.0kV X30,000 100nm WD 5.7mm

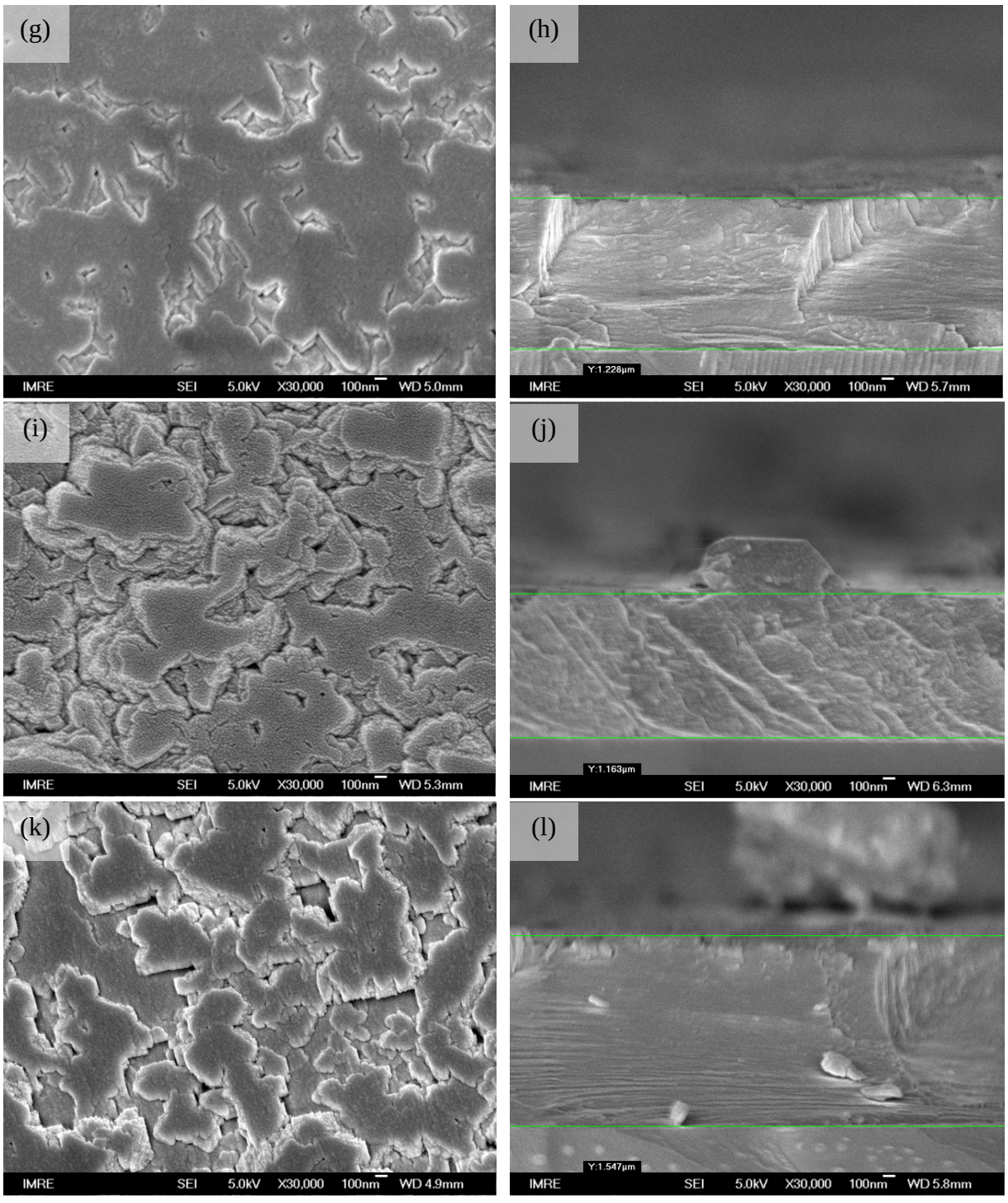
(g)
IMRE SEI 5.0kV X30,000 100nm WD 5.0mm
(h)
Y:1.228µm
IMRE SEI 5.0kV X30,000 100nm WD 5.7mm
(i)
IMRE SEI 5.0kV X30,000 100nm WD 5.3mm
(j)
Y:1.163µm
IMRE SEI 5.0kV X30,000 100nm WD 6.3mm
(k)
IMRE SEI 5.0kV X30,000 100nm WD 4.9mm
(l)
Y:1.547µm
IMRE SEI 5.0kV X30,000 100nm WD 5.8mm

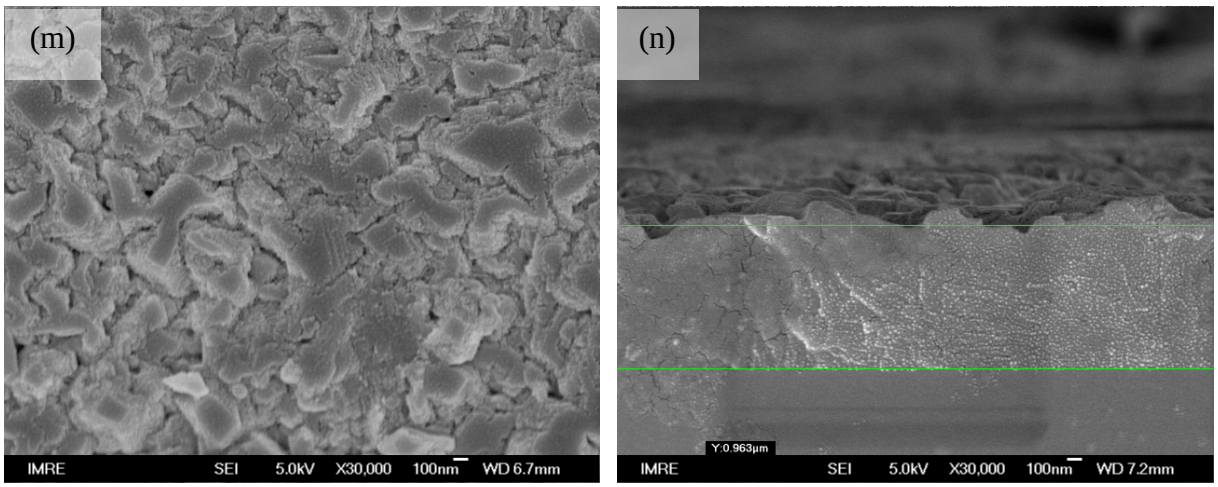

Figure 50: Top and cross sectional electron micrograph of epitaxial (a-b) KN film reference and various NKN film on STO (100) grown with increasing R ratio of: (c-d) 10%, (e-f) 11.7%, (g-h) 13.3%, (i-j) 14.2%, (k-l) 15%, and (m-n) 20% hydrothermally epitaxied at 200°C for 8 hours.

While it is not possible to observe the NKN film growth directly during synthesis using our current setup and capability, one possible ex-situ analysis can be done by TOF-SIMS by comparing spectrum of films grown at different R-ratio. TOF-SIMS is capable in providing elemental depth profile analysis of a film and, to some extent, compares the depth profile with other films or a standard sample analyzed at similar beam conditions.

The elemental depth profiles of selected as-grown NKN films with R = 10% to 15% obtained from TOF-SIMS are presented in Figure 51. Here “humps” (marked with broken circles) in Na signal near the film surface could be observed in samples synthesized in R ≥ 11.7% (Figure 51 (b-d), filled square symbol), indicating a sodium-rich layer near the surface. When Na signal intensity data from samples with different R-ratios are compared side by side (Figure 51 (d)), it is also observed that the Na signal (and also the humps near the surface) increases with increasing R-ratio. Similar to our experience with the NKN powder

direct synthesis (Chapter 5), extra peaks observed in HRXRD data, uneven composition detected by EDS and TOF-SIMS analysis indicate that the hydrothermally synthesized NKN films contain additional sodium-rich layer near the film surface when the R-ratio is 11.7% and above. Post-growth treatments are therefore necessary to attain usable, single phase NKN films with compositions near the MPB.

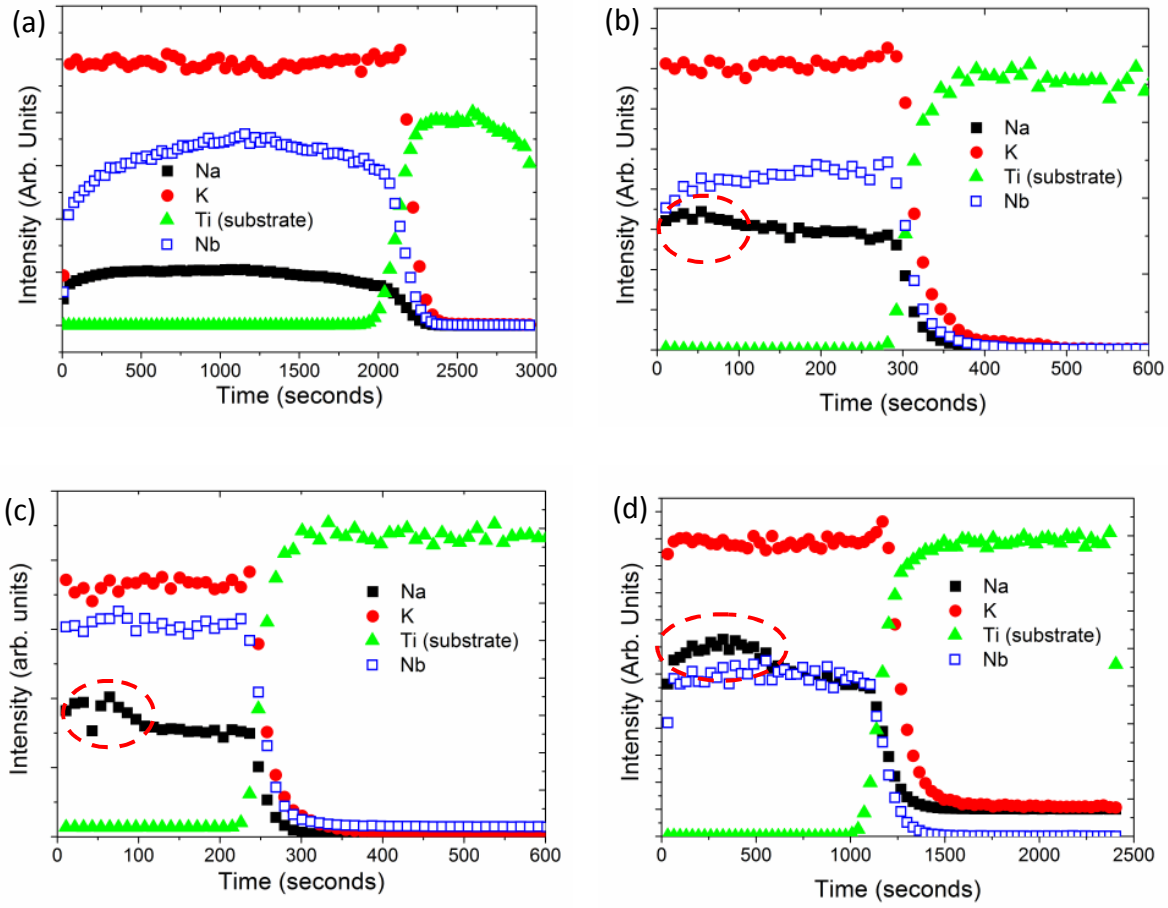

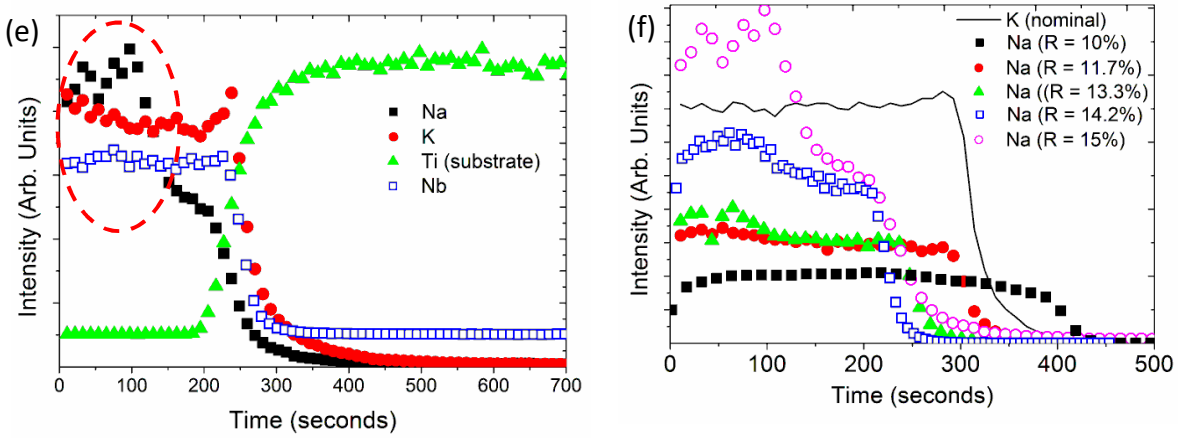

Figure 51: SIMS depth profile of samples with R ratio of (a) 10%, (b) 11.7%, (c) 13.3%, (d) 14.2%, and (e) 15%. (f) The difference in Na profile for samples with R-ratio of 10-15% with similar K level.

Note: data shown in (a) and (d) were measured at much lower sputtering rate, thus their longer sputtering time in the x-axis scale. The sputtering time axis has been adjusted to reflect the film thickness in (f) for presentation purpose.

6.2.2 Achieving single phase NKN film via heat treatment

So far, the epitaxial NKN films obtained via hydrothermal synthesis are always mixed with the unwanted Na-rich phase near the surface. The delocalized presence of Na-rich phase presents an opportunity to achieve single-phase epitaxial NKN film by a two-pronged approach of controlling the growth rate of the Na-rich top layer and removing the residues via post-growth treatments.

First, we explored different ways to retard the Na-rich top layer, and one of the simplest ways is by altering the growth parameters. The Na-rich phase growth location near the surface gives us a clue that it may not the favorable phase to nucleate at the substrate, either due to crystallographic (e.g. larger lattice mismatch) or reaction kinetic (e.g. solubility in the reaction condition) constraints, and, most importantly, it appears on the latter stage

of the reaction. The hydrothermal reaction time was then halved to approximately 4 hours, and the resulting film morphology, HRXRD and SIMS data is presented in Figure 52, vis-à-vis the original film grown for 8 hours. The Na-rich phase growth retardation can be easily observed from HRXRD data around NKN (022) reflexion, showing near absence of extra peak shoulders near 45.5° and 47° 2θ. Elemental analysis results using EDS (Table 13) also indicate a more uniform Na/K ratio (indicated by the low standard deviation value) across the film.

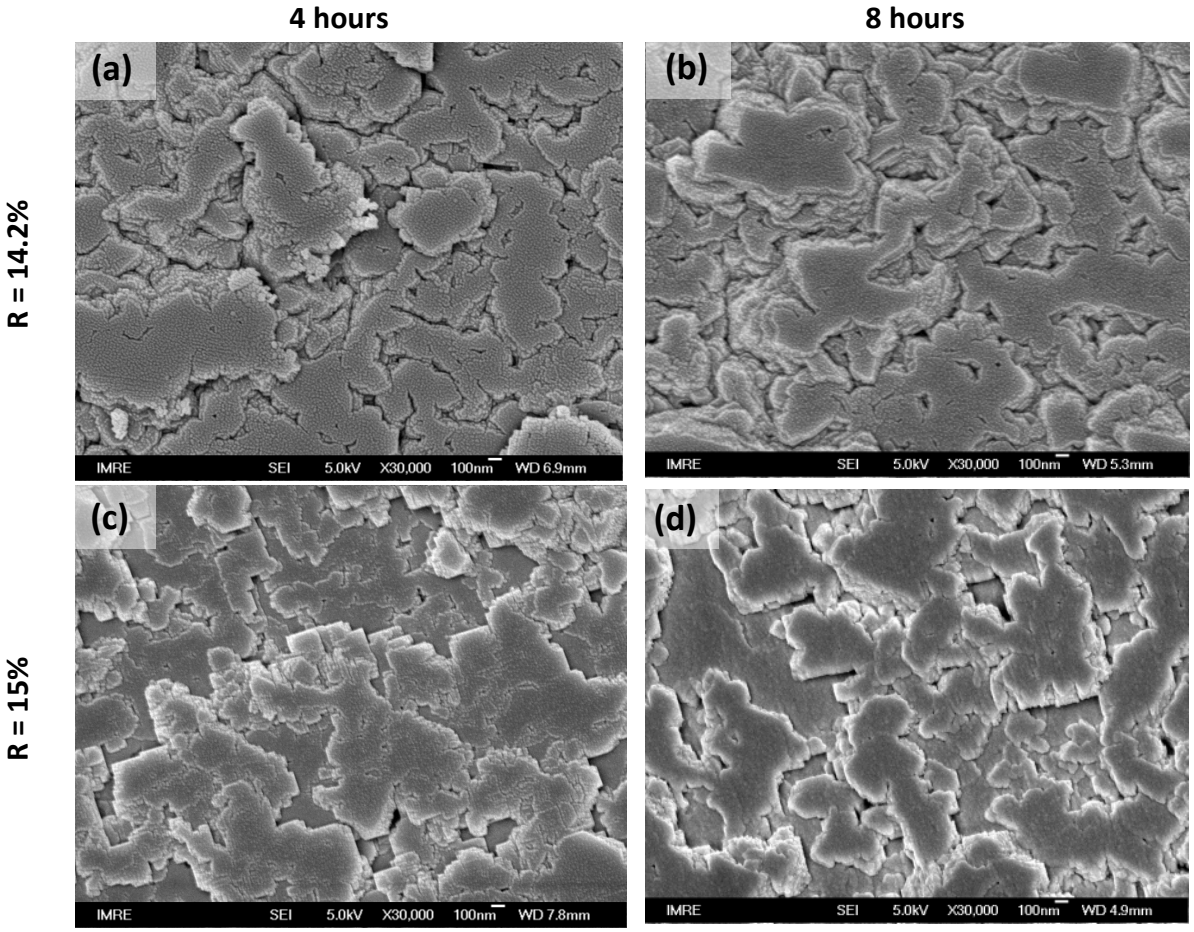

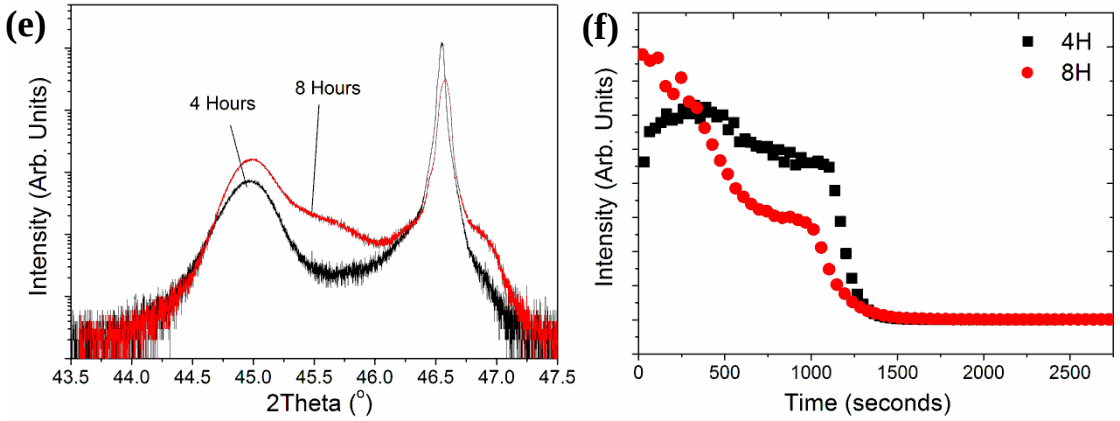

Figure 52: Top-view morphology of samples synthesized at R = (a-b) 14.2% and (c-d) 15% grown for 4 and 8 hours. (e) HRXRD around NKN (022) of samples with R=15% indicates that the extra reflexions /shoulders do not appear in samples synthesized for four hours. However, careful examination using SIMS depth profiling still indicates a Na-rich surface layer, as seen in (f).

Table 13: EDS and thickness data of selected samples grown at R = 14.2% and 15% for 4 and 8 hours, before and after post-growth treatment (PT). Bracketed numbers represent standard deviation values

Elements	R-ratio and process time						
	14.20%				15%		
	8 hrs #1	8 hrs #2	4 hrs	4 hrs + PT	8 hrs	4 hrs	4 hrs + PT
Na	0.36(2)	0.5(1)#	0.41(4)	0.37(1)	0.6(2)	0.62(1)	0.55(5)
K	0.73(1)	0.5(1)#	0.67(3)	0.72(1)	0.5(2)	0.45(1)	0.59(2)
Nb	0.982(5)	0.986(1)	0.984(5)	0.983(4)	0.99(1)	0.985(1)	0.97(1)
Thickness (μm)	1.14(4)	1.00(5)	0.84(2)	N.A.	1.52(2)	1.0(1)	N.A.

Although XRD and EDS results of films synthesized in shorter reaction time suggests a more uniform phase composition, closer investigation using SIMS (Figure 52 (f)) indicates that there are still some residues of uneven sodium levels. A second approach to achieve single phase NKN film via post-growth heat treatments is therefore implemented. As demonstrated with the mixed NKN+NN powders result in section 5.3, it is possible to achieve a single phase NKN by heat treating the mixed NKN+NN perovskite phases at a

sufficient temperature and time. In this section, we want to apply the knowledge obtained from the powder work to get a single phase NKN film via a short heat treatment process. To determine the optimum heat treatment parameters, NKN film with R = 15% were broken into three parts, and subjected to heat treatments at different temperatures of 600, 700 and 800°C for two hours. The film's HRXRD profile around <022> reflexions before and after heat treatments are presented in Figure 53. It is apparent that the extra peak/shoulders start disappearing only after treatments at 700°C onwards. Temperatures above 800°C was not explored due to start of potassium oxide volatility near 900°C [197].

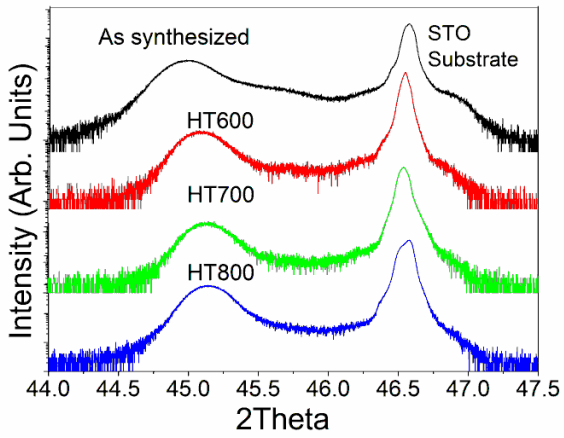

Figure 53: Effect of different heat treatment temperatures to NKN film (R = 15%)

The results of a combined shorter reaction period and post-growth treatments can be seen in Figure 54. Here it is observed that the Na depth profile variations (humps) are greatly reduced after heat treatment at 800°C. Samples with R = 14.2% shows nearly flat Na profile (empty squares), indicating a single phase NKN with x = 0.37, near the phase boundary, has been reached.

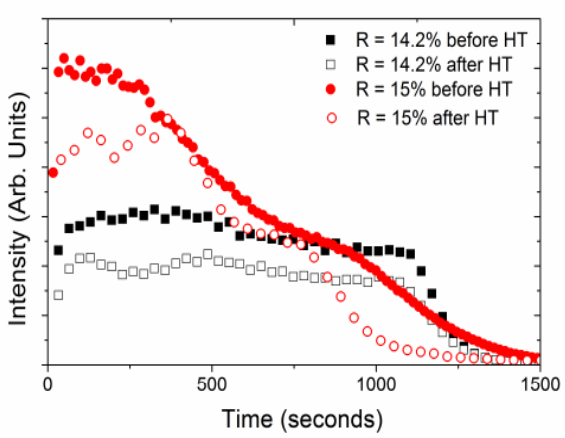

Figure 54: Na depth profile obtained from SIMS analysis of NKN films with R=14.2 and 15% before and after heat treatment at 800°C for 2 hours.

6.2.3 Achieving single phase NKN film via the addition of a complexing agent

While the combination of lowered growth time and a short post-growth heat treatment has been shown to be successful in achieving a single phase epitaxial NKN film up to *x* (the sodium fraction in NKN) = 0.37, there is a strong need to skip the heat treatment assisted removal of the Na-rich unwanted phase. The new strategy described here is by introducing some complexing agents into the starting precursor solution to selectively promote the growth of NKN phase and retard the formation of Na-rich phase (NN). The cause of selective growth promotion is proposed due to selective stabilization of sodium intermediate compounds in the solution which subsequently followed by the retardation of unwanted Na-rich phase growth.

Although the usage of complexing agents in hydrothermal synthesis of various crystals is not new (various examples including sodium citrate [189, 254], diethylene amine (DEA)

[255], and ethylene diamine (EDA) [256, 257] or ethylene diamine tetra acetic acid (EDTA) or EDTA variations [258, 259] are available), the usage of complexing agent is mainly limited in controlling the crystallite shapes and/or sizes. EDTA was chosen among different types of complexing agents available due to its high solubility with water (up to 1 g in 25 ml of water), easy handling (stays dry in air), and its stability on synthesis temperature (it does not melt or degrade at temperatures up to 250°C).

Before applying the EDTA to assist NKN film epitaxial growth, we first conduct a preliminary evaluation to determine the effect of different concentration of EDTA to the NKN powder growth. We choose the starting condition of R = 20% and 1 g of Nb_2O_5, as described in section 5.1.2 Table 8, that is known to yield >93% of $NaNbO_3$ (NN) phase when grown without complexing agent. The XRD data of as synthesized NKN powders with and without EDTA is described in Figure 55. The samples synthesized without EDTA (Figure 55 (a)) is expectedly dominated by NN phase, which forms approx. 96% (refined) of the entire powder weight. Gradual change in the powder XRD pattern can be observed after the addition of 0.2 g (Figure 55 (b)) and 0.5 g (Figure 55 (c)) of EDTA respectively. It is noticed that the unwanted NN phase content is suppressed with the increasing amount of EDTA addition, down to as low as 40 wt% (refined) when 0.5 g of EDTA is added.

How exactly the EDTA slows down the NN phase formation is still unknown at this point, but a hint can be taken from the persistence of the sodium hexaniobate intermediate phase and (traces of) Nb_2O_5 starting precursor even after 24 hours reaction at 200°C when 0.5 g of

EDTA is added (Figure 55 (c)). We believe that the EDTA may have increased the stability of the sodium hexaniobate intermediate phase such that the Na-rich NN phase formation is significantly hampered. The retarded NN phase growth may present an opportunity window to grow a pure NKN film where the desired NKN phase is dominant.

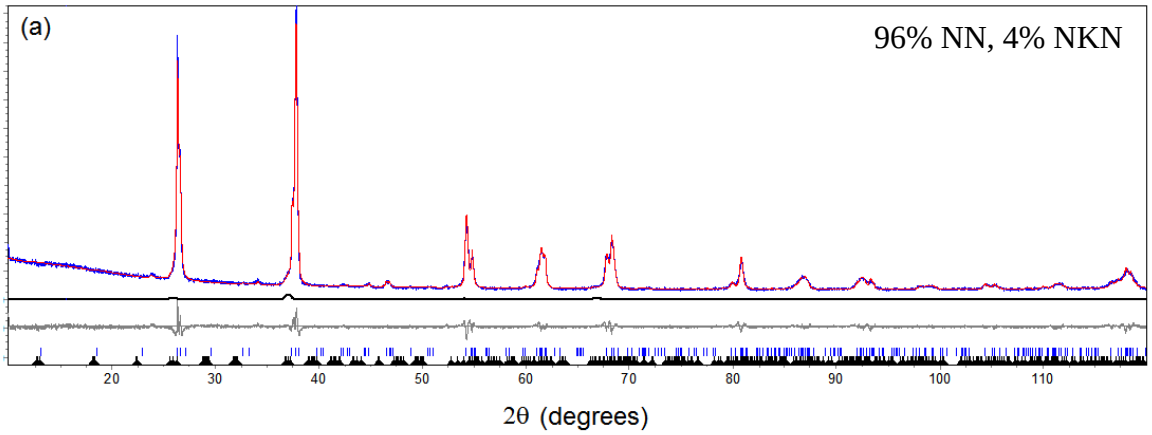

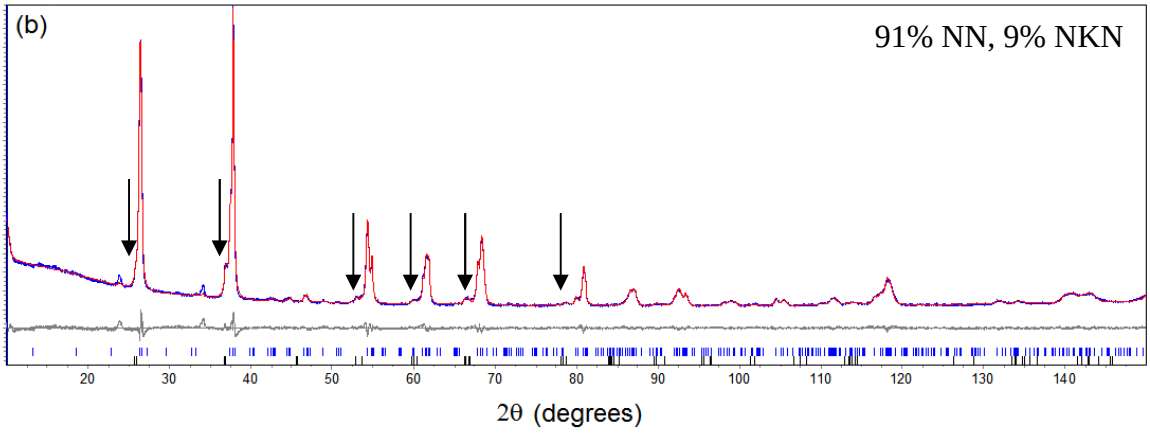

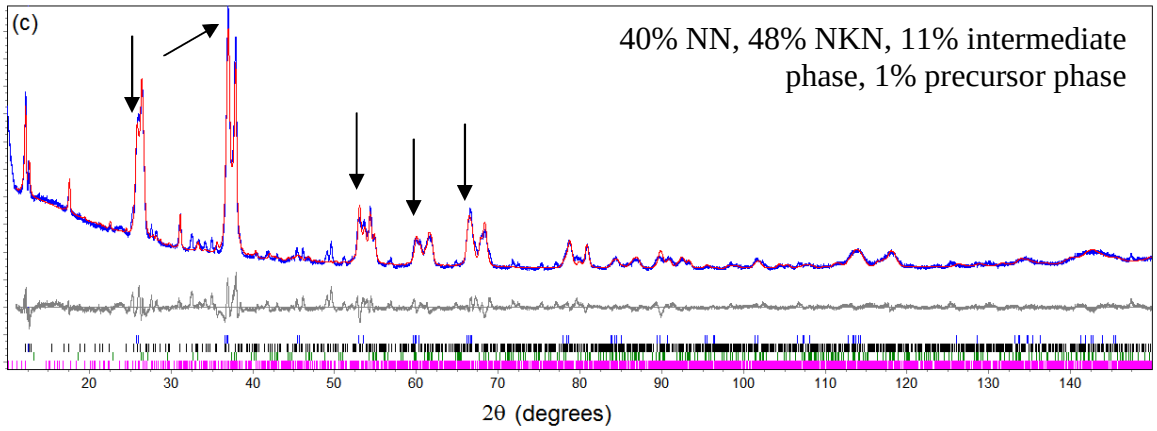

Figure 55: Experimental and fitted XRD data of NKN powders (R = 20%) synthesized by adding (a) 0, (b) 0.2 and (c) 0.5gr of EDTA into the KOH-Nb_2O_5-water solution. Phase content(s) on the top right hand corner are refined from the powder XRD data. The addition of EDTA results in slower unwanted NN phase growth and increase of desired NKN phase amount (arrows). All samples shown here were grown at 200°C for 24 hours.

Next, we proceed with NKN film growth with EDTA addition. The effect of EDTA addition to the epitaxial NKN film growth on a [100] STO single crystal substrate can be examined in Figure 56[†††]. It is noticed that the addition of EDTA in the starting solution alters the film morphology to smaller island blocks with more undefined edges (Figure 56 (b)), and consistently increases the film thickness by approx. 30–40% (Table 14). The addition of EDTA also results in the disappearance of humps around [022] NKN diffraction peak, as shown in the HRXRD data (Figure 56 (c)), suggesting that the presence of the unwanted Na-rich phase on the surface has been reduced.

[†††] R = 15% film samples were used to demonstrate the effect of EDTA addition in Figure 56 R = 20% samples display excessive growth rates, resulting in a very rough film that is not suitable for electrical testing. Refer to Appendix B for details.

Sodium and potassium elemental depth profile of the samples (Figure 56 (d)) supports the observation from the HRXRD data. Although a jump in sodium concentration near the film surface can still be observed in the samples synthesized with EDTA, the portion of the film that possesses a relatively constant sodium level has been increased (Figure 56 (d), light blue arrow). This is in line with the findings from NKN powder that EDTA only promotes the growth of NKN phase until the time when the second Na-rich nucleates and grows. The jump in sodium concentration can be addressed by shortening the reaction time, as discussed in section 6.2.2. When the EDTA addition approach and the shortened time strategy are combined together, the result is a pure NKN film with more or less level sodium content throughout the film thickness (Figure 56 (e)).

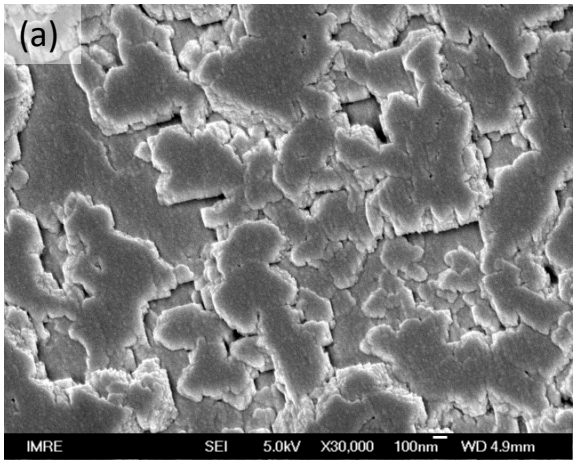

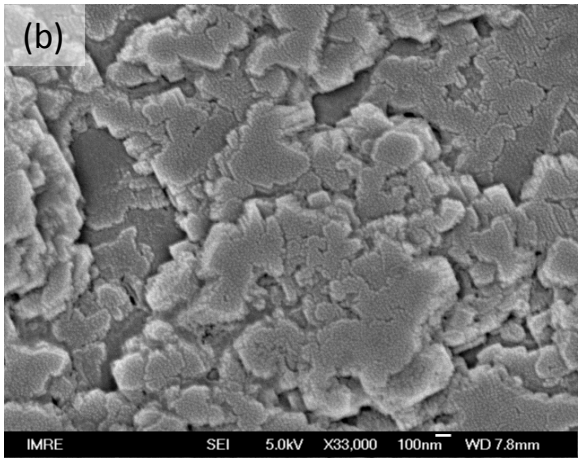

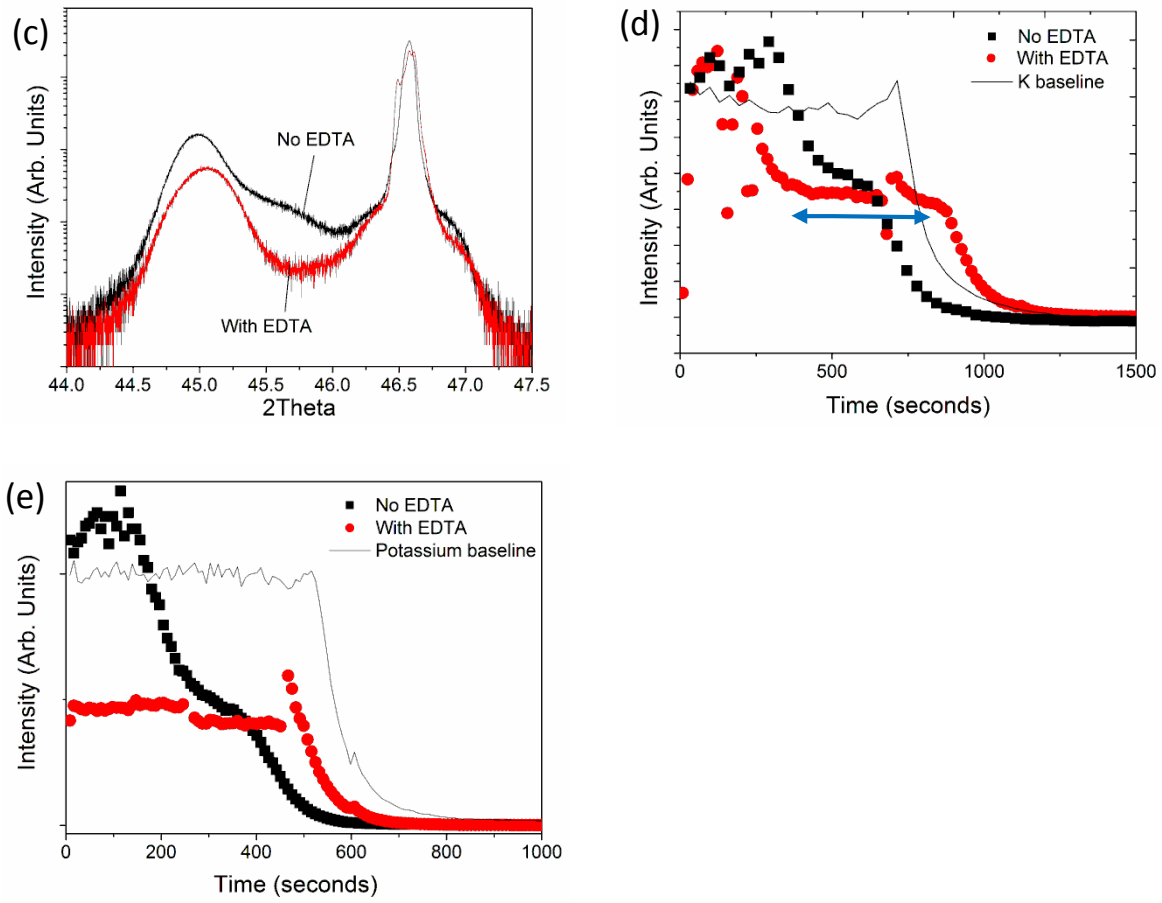

Figure 56: Surface morphology of films grown at 200°C for 8 hours, with an initial R = 15%: (a) without and (b) with 0.1gr EDTA added into the precursor solution. (c) HRXRD data around NKN (022) peak comparing film grown with and without EDTA. (d-e) Sodium depth profile of samples with and without EDTA synthesized for (d) 8 hours and (e) 4 hours as obtained by TOF-SIMS experiment. The solid black lines represent the nominal potassium baseline taken from the sample synthesized without EDTA.

Although the pure NKN film synthesized with EDTA at shortened 4 hours growth time appears to have a lower sodium content than the NKN film achieved after heat treatment at 800°C (described earlier in section 6.2.2), it is actually within the range of NKN powder synthesized at similar R ratio (refer to Table 8 section 5.1). The extra sodium content in the NKN film achieved after heat treatment comes from the second Na-rich layer that has been homogenized after the heat treatment.

Table 14: EDS analysis and thickness data of film with and without EDTA, R = 15%. Numbers in brackets represent standard deviation values.

Elements	R = 15%, 8 Hours		R = 15%, 4 Hours	
	no EDTA	with EDTA	no EDTA	with EDTA
Na	0.6(2)	0.67(2)	0.62(1)	0.23(1)
K	0.5(2)	0.39(2)	0.45(1)	0.76(2)
Nb	0.98(1)	0.988(3)	0.985(1)	1.00(1)
Thickness (μm)	1.52(2)	2.15(4)	0.9(1)	1.13(3)

6.2.4 Electrical results of NKN films

The film grown with EDTA at a shortened 4 hours reaction time (R = 15%) was split into two parts, and one of them was treated with the combined post-growth combination treatments of O_2 plasma followed by heat treatment (refer to section 4.3.2) to optimize its ferro/piezoelectric properties. As seen in Figure 57, it is found that the combination treatments of O_2 plasma followed by heat treatment improve the NKN film's ferroelectric and piezoelectric polarization response. It should be noted that judging from the shape of the P-E loop in Figure 57 (a), the contribution of leakage current to the polarization response is still significant. In line with what has been observed in KN films (section 4.3.2), the improvement after the combined post-growth treatment is due to oxygen-compensated removal of –OH hydroxyls, dense, and highly epitaxial film.

Post-growth treated NKN film was then scanned with the laser scanning vibrometry technique to probe its piezoelectric response. The d_{33} value of treated NKN film was estimated to be about of 8 pm/V based on 1 V voltage applied to the film (Figure 57 (b)). It should be noted that in the laser scanning vibrometry measurement, a linear displacement-

voltage relationship was assumed, and the film was measured under the in-plane clamping effect of the substrate, therefore underestimating the actual d_{33} value. Although the measured polarization response of NKN film is still very small compared to PZT based materials, possibly due to the film composition is still far away from the MPB, it was a clear demonstration that a hydrothermally grown lead-free NKN-based film can display an out-of-plane displacement.

The next few sections are dedicated to increase the ferro/piezoelectric response of NKN-based lead-free films by adding alloying elements to form complex solid solutions. Complex solid solution formation is known to improve the ferro/piezoelectric response of NKN in the bulk/thick film form [18, 19], but none so far has been reported for thin, epitaxial film.

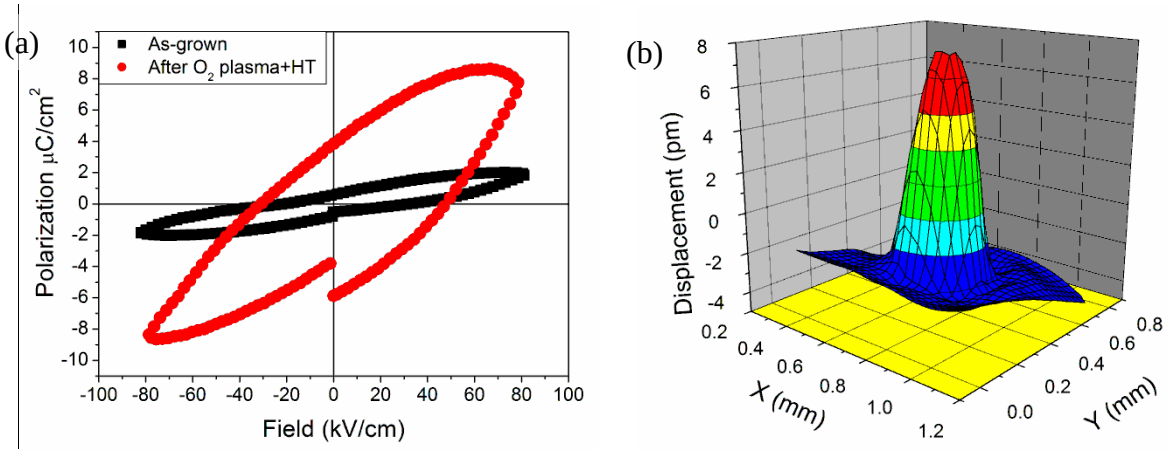

Figure 57: (a) Ferroelectric response of as-grown (red circles) and treated (green triangles) NKN films (R = 15%, grown with EDTA at a shortened time of 4 hours). As-grown KN ferroelectric response is also inserted as a reference (black squares). (b) Piezoelectric response of treated NKN film at 1 V.

6.2.5 Achieving single phase NKN-LT film with the addition of complexing agent

In this section, the knowledge obtained from the previous sections to synthesize a single phase NKN is applied to achieve a more complex epitaxial Li and Ta substituted NKN film [$(Na_xK_{1-x})_{1-y}Li_y(Nb_zTa_{1-z})O_3$ or NKN-LT for short]. The purpose of Li and Ta addition (substitution) to the NKN lattice is to create an additional phase boundary between NKN (*x* = 0.51) and $LiTaO_3$ [18, 19] that increases the net polarization response. Here, it is found that by applying three-pronged approach of controlling the reaction time, reducing processing temperature and addition of a complexing agent we were able to synthesize single phase NKN-LT close to the MPB composition.

Before going forward to discuss the NKN-LT film growth, we start with observing the growth of NKN-LT powders and the complications faced in synthesizing such a complex composition using hydrothermal method. The increased number of precursor types required to synthesize NKN-LT is predicted to make it exceptionally difficult to grow via hydrothermal route, particularly due to the additional group I anion – lithium. Lithium may complicate the solubilities of the intermediate phase(s), like in the case of sodium that is known to reduce the solubility of the hexaniobate-type intermediate phase in the hydrothermal snythesis of NKN [251]. Already complicated with three different types of group I anions present in the solution, growth of NKN-LT films/powder could be worsened by the different dissolution rates of Nb_2O_5 and Ta_2O_5 in basic solutions [30, 36, 252] and

difficulties of conducting precise elemental analysis (therefore controlling the composition) of lithium [260].

To investigate the growth of NKN-LT powders, three different precursor sets were then prepared to illustrate the effect of tantalum (as Ta_2O_5), lithium (as LiCl) and EDTA addition to the growth of NKN-LT powder. To minimize variations, the total concentration of $[Ta_2O_5]+[Nb_2O_5]$ is kept constant at approx. 0.15M and a new precursor ratio called the T ratio that represents $\frac{[Ta_2O_5]}{[Ta_2O_5]+[Nb_2O_5]}\times 100\%$ is introduced as a tool to control the Ta/Nb ratio in the final NKN-LT product (film or powder).

A list of the refined weight fraction (obtained from the powder XRD data) of phases found after 24 hours reactions at 200°C in different precursor sets can be found in Table 15. Here it is observed that the addition of small amounts of lithium and tantalum significantly change the end powder composition observed in pure NKN growth. A small 5 mol% Ta_2O_5 addition to the NKN precursor (R = 10%) resulted in a NKN-LT and NN phase separation, instead of pure phase NKN when no Ta_2O_5 is added (refer to Table 8, section 5.1). A small amount 2.5 mol% (of the total $[Na^+]+[K^+]$) of lithium results in a complicated mixture of intermediate hexaniobate phase(s) (majority phase) and at least three different perovskite phases (Table 15).

A mixture of hexaniobate and perovskite phases in the end product usually indicates that the reaction is incomplete; probably due to the different solubilities of intermediate

phases, similar to those observed in the hydrothermal growth of NKN powder (Table 9, section 5.1.3). To observe the phases present in the completed reaction (free of intermediate phases) that involves added lithium and tantalum elements, the growth temperature is raised to 240°C. The powders collected after 24 hours at 240°C is a mixture of different perovskites: NKN-LT (majority phase), $KTaO_3$, and NN (Table 15), indicating that a similar problem of perovskite phase separation observed in the NKN powder/film grown hydrothermally may also be seen in NKN-LT powder/film growth.

The effect of adding EDTA to the NKN-LT precursor solution is also examined and it is found that the composition of the powders collected after 24 hours of reaction at 200°C with EDTA is similar to the one synthesized *without* EDTA (Table 15). This time however, the desired NKN-LT perovskite phase is the majority, followed by a mixture of intermediate and other perovskite phases. The increased NKN-LT phase fraction in the synthesis using EDTA suggests the growth preference towards NKN-LT compared to other perovskite types.

Table 15: The phases present in the resulting powder with addition of Ta_2O_5, LiCl and EDTA to the NKN precursor in attempt to synthesize NKN-LT powders. All reactions were done at 200°C for 24 hours unless otherwise stated.

	Reaction parameters				
Phases detected	R = 10%, T = 0%, No LiCl	R = 10%, T = 5%, No LiCl	R = 10%, T = 10%, 0.15M LiCl	R = 10%, T = 10%, 0.15M LiCl (240°C 24H)	R = 10%, T = 10%, 0.15M LiCl, and 0.1gr EDTA
NKN-LT	-	83.4(2)%	5.1(4)%	80.9(3)%	53.9(6)%
NKN	100%	-	-	-	-
NN	-	16.6(2)%	12.0(4)%	2.4(1)%	6.9(3)%
$LiNbO_3$	-	-	8.9(4)%	-	2.0(3)%
$KTaO_3$	-	-	2.7(2)%	16.7(3)%	7.1(6)%
Hexaniobates	-	-	71.4(8)%	-	30.2(5)%

While continual process optimization and exploration of post-growth treatments may eventually result in a single phase NKN-LT powder, it is not pursued in this work because the synthesis–characterization–optimization cycles required to remove unwanted second phase(s) will be tedious. The results from the powder works are used to guide the NKN-LT film growth and testing, which is the main objective of this work.

Figure 58 shows the morphology and cross section of as-grown epitaxial NKN-LT films on niobium doped $SrTiO_3$ (Nb:STO) single crystal substrates. Direct growth of NKN-LT (by introducing Nb:STO substrate in the solution) results in a 120 µm thick film just after 24 hrs of growth at 200°C (Figure 58 (a-b)). The extremely thick film is unusual at 6M total hydroxide concentration ($[OH^-]$), because rapid film growth rate usually occurs only when the [OH-] is extremely high (>10M) [30]. Our repeated attempts to grow NKN-LT film using direct hydrothermal method often leads in failure, only to be discovered later that the extremely rapid growth rate causes the film to spall off from the substrate. Careful examinations using XRD (Figure 59, green line) and EDS elemental analysis (Table 16) indicate that the extremely thick film obtained by direct hydrothermal growth is actually made (almost[‡‡‡]) entirely of sodium niobate ($NaNbO_3$, NN).

Implementing the knowledge obtained from NKN film growth with EDTA (section 6.2.3) and preliminary NKN-LT powder work, EDTA complexing agent is then added to the starting

[‡‡‡] With respect to the extremely thick film, the XRD and EDS results should be taken with caution because the limited X-ray depth of penetration may not reach deeper layer(s) of the film that may have different composition.

precursor to retard the NN phase formation and promote the desired NKN-LT phase. Indeed, the EDTA addition improves the NKN-LT film growth: (1) it reduces overall film growth rate, resulting in a thinner, more manageable film (approx. 4 µm after 24 hours at 200°C, Figure 58 (c-d)). (2) XRD and elemental analysis revealed that the EDTA may specifically hamper unwanted NN phase growth or improve the growth of NKN-LT phase: film grown with EDTA shows increased potassium and tantalum fraction in the elemental analysis (Table 16) the appearance of NKN-LT peak in film XRD data (Figure 59 (b), red line, arrow on the left near 45.6° 2θ).

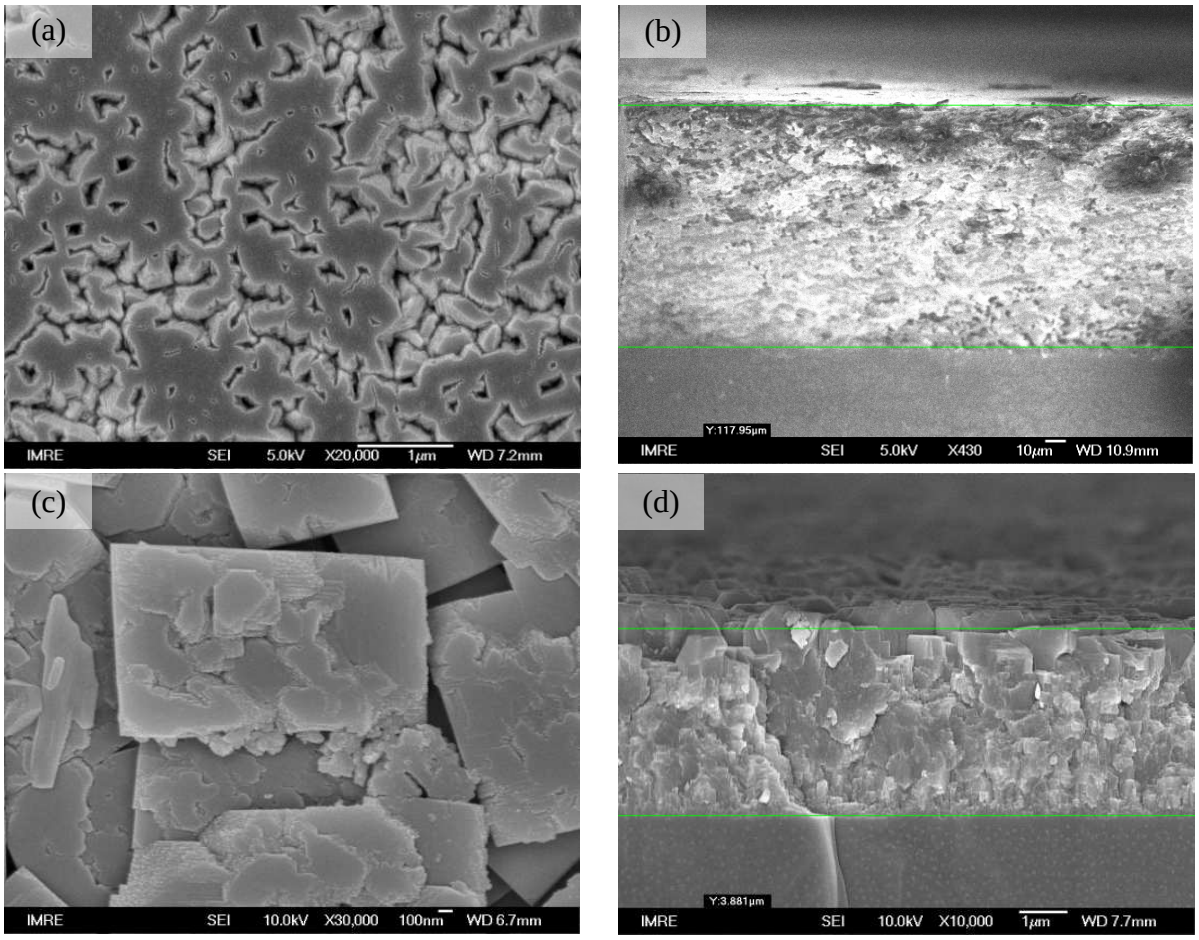

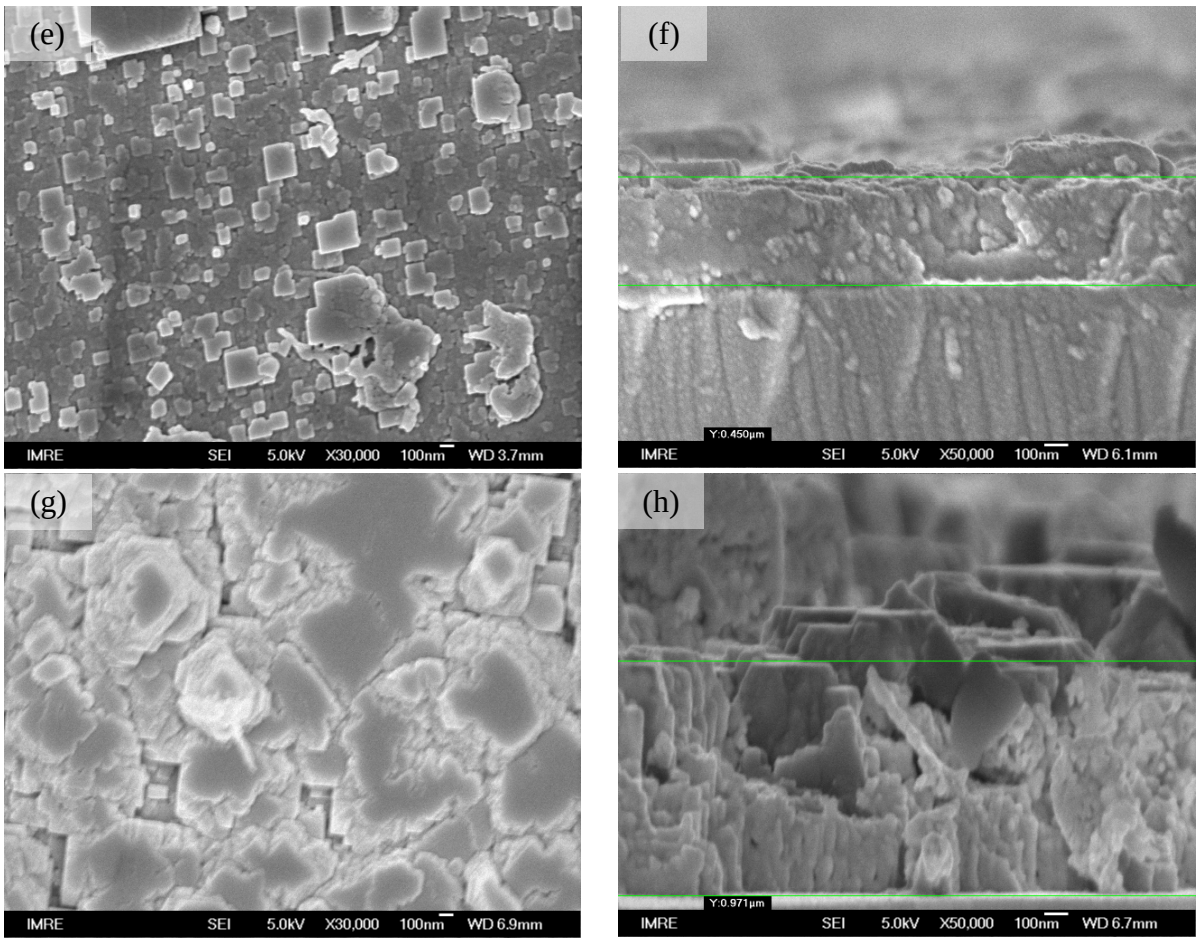

Figure 58: Effect of EDTA to the NKN-LT film growth. Films are grown with R = 16.7%, T = 20%, 0.15M LiCl at 200°C for 24 hours: (a-b) without EDTA and (c-d) with EDTA. (e-f) Films grown at similar conditions, with EDTA, at 130°C for 120 hours and (g-h) 168 hours.

Table 16: The average EDS data of films R = 16.7%, T = 20% with and without EDTA. Numbers in the brackets represents standard deviations.

	No EDTA (200°C 24H)	0.1gr EDTA (200°C 24H)	0.1gr EDTA (130°C 120H)	0.1gr EDTA (130°C 168H)
Na	1.034(4)	0.90(1)	0.50(1)	0.90(1)
K	0.10(1)	0.105(3)	0.42(1)	0.105(3)
Nb	1.082(3)	0.885(3)	0.64(1)	0.885(3)
Ta	0.029(3)	0.114(3)	0.38(1)	0.114(3)
Thickness (µm)	119(1)	3.9(1)	0.48(3)	1.00(3)

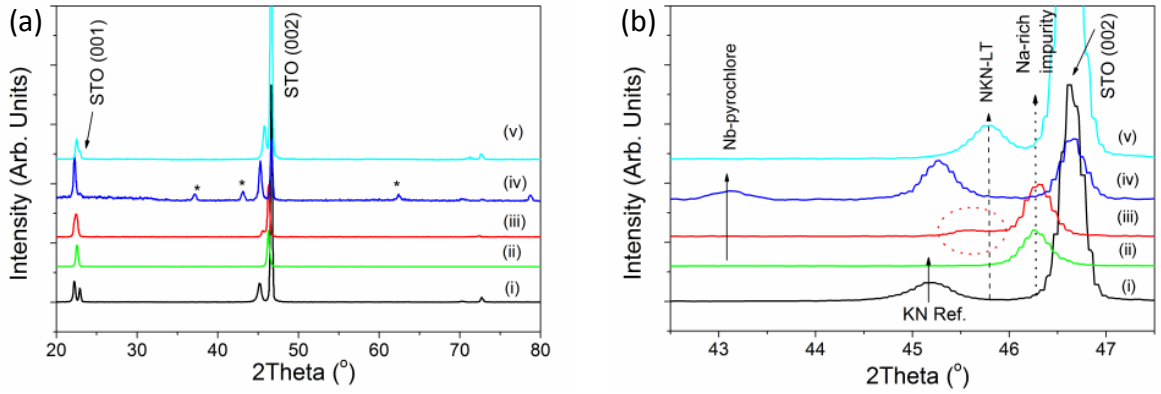

Figure 59: (a) XRD data of NKN-LT film with slightly different reaction conditions: (i) Pure $KNbO_3$ film reference, (ii) Sample 0, (iii) Sample 1, (iv) Sample 2, and (v) Sample 7. (b) The same XRD data zoomed in around 46° 2θ to observe different perovskite formation. Asterisk symbols represent Nb-Pyrochlore peak position according to reference [261]

Although the addition of EDTA has significantly reduce NN phase growth, the film obtained is still very thick, rough, and dominated by NN phase. The next step forward is therefore to achieve thinner, smoother films that are absent of Na-rich layer, presumably near the surface like the NKN film described in the previous section[§§§].

Several approaches have been attempted to achieve a pure NKN-LT films, such as shortening the total reaction time and delaying the introduction of sodium precursor (i.e. NaOH) to the solution – both of which are not shown in this thesis for brevity – but it was discovered that the best film can be achieved by lowering the reaction temperature to about 130-140°C. While it is easy to guess that lowering the growth temperature reduces the reaction kinetics, such that it took ≈120 hours just to grow 0.45 µm film at 130°C (Figure

[§§§] Although actual SIMS measurements were not carried out on the films grown without EDTA because of its extreme thickness, it is believed that Na-rich layer resides near the surface, as seen in the previous NKN film section.

58 (e-f)), the real advantage of using a lower reaction temperature is the wide (≈40 hours) time window for us to stop the reaction before the unwanted Na-rich layer starts growing after 160 hours, resulting in a rough, 1 µm thick film (Figure 58 (g-h).

As examined by XRD (Figure 59, blue line), the film grown at 130°C for 120 hours is a single phase NKN-LT film, with no signs of composition variations as determined by TOF-SIMS measurements (Figure 60). It should be noted that the TOF-SIMS data also serves as the only qualitative confirmation of lithium incorporation to the NKN-LT lattice, as lithium is too light to be detected using EDS analysis and its concentration is too low to be quantitatively analyzed using XPS.

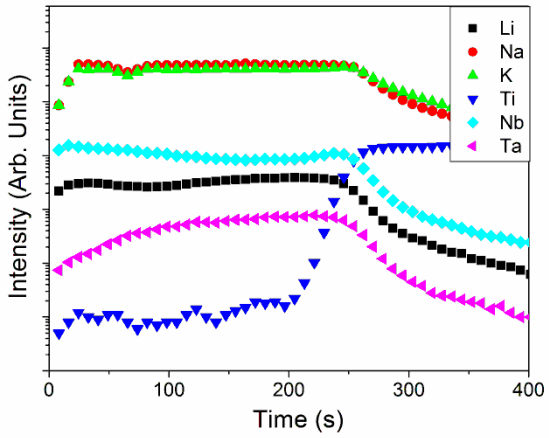

Figure 60: TOF-SIMS data of hydrothermally grown NKN-LT film at 130°C for 120 hours showing an even composition throughout the film thickness.

The next crucial experiments are then directed to achieve a single phase NKN-LT with the composition close to the morphotropic phase boundary (with a target empirical formula

of $(K_{0.5}Na_{0.5})_{0.97}Li_{0.03}(Ta_{0.2}Nb_{0.8})O_3$, as proposed by Saito et al. [18, 19]). Table 17 displays experiment details and analysis results of selected samples that summarize the effort to achieve such composition. The first target to tackle is to increase the sodium incorporation without forming a second Na-rich layer. The R-ratio optimization work is not described here for brevity, but the optimum condition is achieved at R ratio to 16.7%.

The lithium precursor concentration in this study was also kept constant at about 2.5 mol% because of the low solubility of lithium in the NKN-LT (about 7 mol%), above which $LiNbO_3$ phase tends to precipitate [10]. It was also observed that another impurity phase grew out of the NKN-LT film when we attempted to increase the lithium precursor concentration to about 5 mol% (Sample 2, Figure 61 (a-b)). This huge octahedral-shaped impurity was identified as niobium pyrochlore phase by comparing its XRD data (Figure 59 (a-iv)) to the references on niobate and/or tantalate pyrochlores [190, 261, 262].

Samples 3 – 7 illustrate the efforts done to obtain sufficiently thick and continuous film without the Na-rich layer for the purpose of electrical measurements. It was found that lower growth temperatures are necessary to control the film growth rate and thicker (approx. 0.4 μm) film can be achieved by prolonging the hydrothermal growth time to 5 or 6 days (sample 7, Figure 61 (c-d)).

Another challenge faced was to find a way to suppress the Ta incorporation from 0.38 to a MPB target concentration level of ≈0.2 (sample 7-9). It is found that a reduction of the T

ratio also affects the Na incorporation level. The optimum condition was obtained when the T ratio is cut to 7.5%, with Ta incorporation around 0.3 and Na incorporation approx 0.4 (sample 9). In the next section it will be demonstrated that sample 7 (T = 20%) actually gives the best electrical performance due to its higher Na incorporation.

Table 17: Selected sample details and characterization results of NKN-LT film synthesized at different conditions with EDTA

	Experiment details					EDS data					Thick-ness (μm)	Notes
No.	*R* ratio (%)	*T* ratio (%)	LiCl (M)	Temp (°C)	Time (hrs)	Li	Na	K	Nb	Ta		
1	16.7	20.0	0.15	200	24	#	0.90(1)	0.105(3)	0.885(3)	0.114(3)	3.9(1)	Very rough
2	16.7	20.0	0.3	200	24	#	0.32(2)	0.64(2)	0.95(1)	0.06(1)	3.4(3)	Pyro-chlores detected
3	16.7	20.0	0.15	140	24	#	0.62(2)	0.48(2)	0.77(1)	0.21(1)	0.31(1)	Porous, not coalesced
4	16.7	20.0	0.15	140	72	#	0.70(1)	0.38(1)	0.787(2)	0.196(2)	0.41(4)	Rough
5	16.7	20.0	0.15	130	72	#	0.44(2)	0.59(2)	0.70(1)	0.30(1)	0.27(1)	
6	16.7	20.0	0.15	130	168	#	0.90(1)	0.11(1)	0.885(3)	0.114(3)	0.99(3)	Very rough
7	16.7	20.0	0.15	130	120	#	0.50(2)	0.42(1)	0.64(1)	0.38(1)	0.48(4)	OK
8	16.7	10.0	0.15	130	120	#	0.37(1)	0.53(2)	0.67(1)	0.35(1)	0.26(2)	OK
9	16.7	7.5	0.15	130	144	#	0.37(2)	0.54(2)	0.70(2)	0.32(2)	0.31(3)	OK

Qualitative lithium detection using SIMS, but no quantitative analysis can be done.

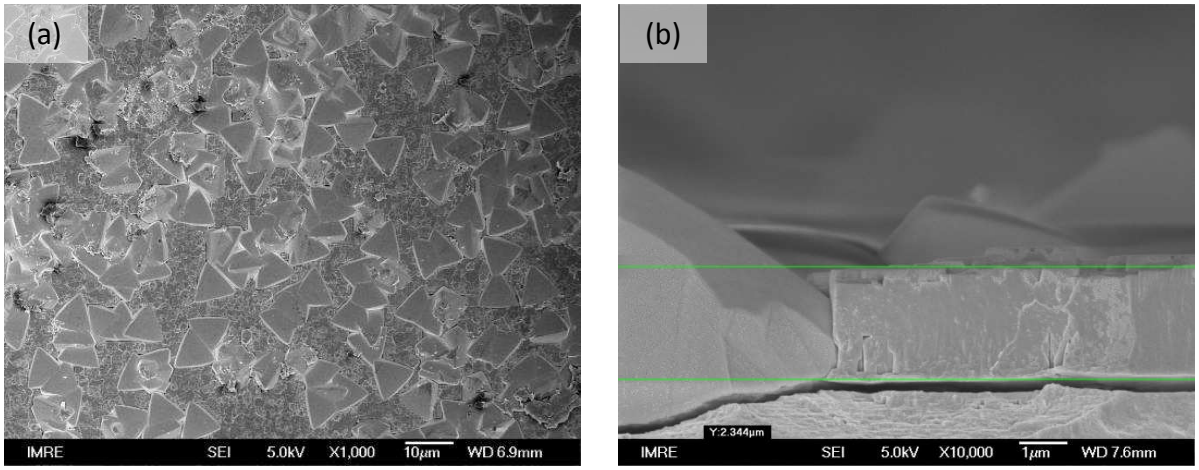

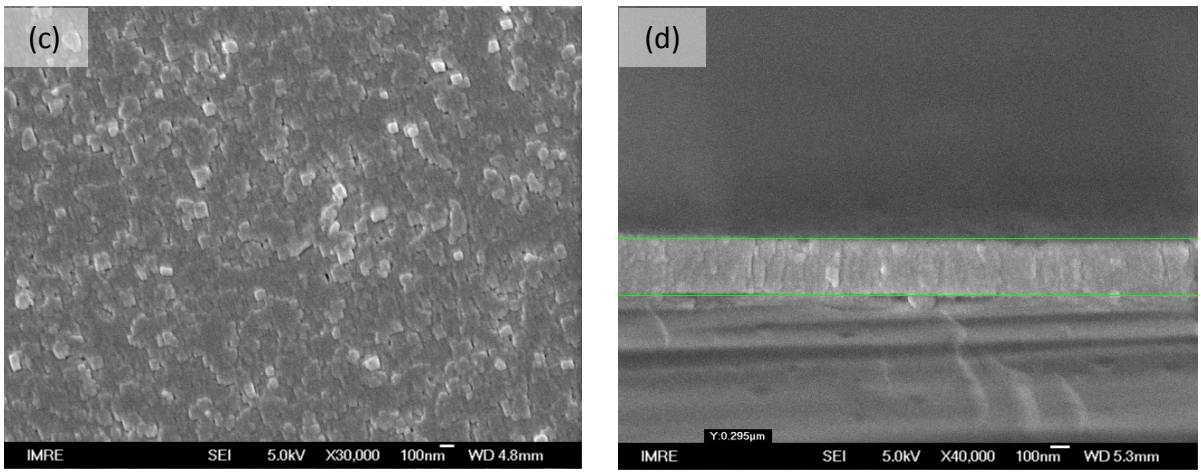

Figure 61: Morphology of As-synthesized NKN-LT shown in Table 17 as samples 2 and 7. (a-b) Pyrochlore filled morphology and cross section of sample 2 showing massive octahedra-shaped pyrochlore grown from inside the film out. (c-d) Flat and homogeneous surface of sample 7 after 5 days of reaction at 130°C.

6.2.6 Electrical results of NKN-LT films

Similar to the hydrothermally grown KN films [191], the dielectric constant and loss of NKN and NKN-LT films still show a frequency dependant characteristics (Figure 62 (a-b)). Increased values of dielectric constant and loss at lower frequency are normally attributed to mobile ionic species in the dielectric material, which would be trapped –OH defects in hydrothermally grown NKN and NKN-LT films.

It is observed that the dielectric constant value of the NKN-LT film gradually becomes higher with increasing amount of Ta incorporation (Figure 62 (a)). This phenomena has also been seen in previous works of NKN-LT bulk and connected to the NKN-LT's Curie temperature reduction as the fraction of Ta substitution of Nb increases [18]. In tandem, the NKN-LT dielectric loss value decrease with increasing Ta incorporation (Figure 62 (b)). The reason of the dielectric loss reduction with Ta is not clearly known, but Saito et al.

connected their similar finding to the larger atomic mass of Ta that dampens atomic vibrations that contributes to the dielectric losses [18, 19].

Although from section 3.4 we know that hydrothermally grown films generally have problems with incorporated –OH related defects, the as-synthesized NKN-LT films are actually able to display a higher than average ferroelectric response compared to some other NKN-LT thin films synthesized with other chemical solution deposition methods [263-265] (Figure 62 (c)). The good ferroelectric response measured here could be attributed to the dense and highly directional (epitaxial) NKN-LT film grown in this study.

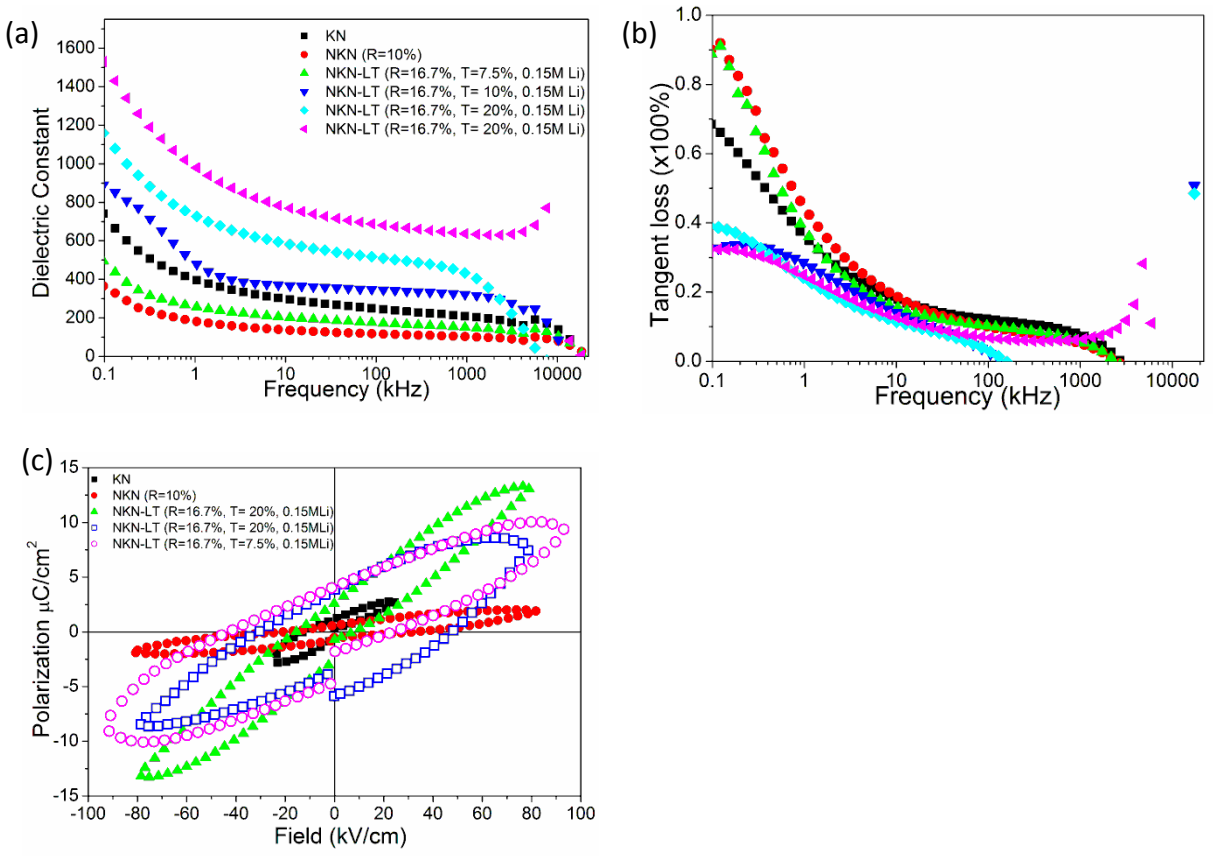

Figure 62: Properties of as-synthesized NKN-LT films grown hydrothermally. (a) Dielectric constant and (b) dielectric loss properties. (c) Ferroelectric properties.

The problem of proton incorporation and surface roughness were dealt with the combined post growth treatments developed previously for improving KN film properties (refer to section 4.3.2). Figure 63 demonstrates that the combined treatment of O_2 plasma and heat treatment at 600°C can also bring out the best ferroelectric response of hydrothermally synthesized NKN-LT film.

Figure 63 (a-b) compares the ferroelectric response of the films with different T ratio: (a) T = 7.5% (sample 9 in Table 17, measured Na = 0.37, Ta = 0.32), and (b) T = 20% (sample 7, measured Na = 0.5, Ta = 0.38). It is found that sample 7's ferroelectric response is actually higher than sample 9's. The higher ferroelectric response of sample 7 indicates that a closer Na content to the NKN MPB composition plays a more important role than the actual Ta composition's closeness to the NKN – $LiTaO_3$ phase boundary composition. This is because the dielectric and ferroelectric properties change more abruptly in the NKN phase boundary (Na/(Na+K) = 0.51) compared to the NKN – $LiTaO_3$ phase boundary (a linear, composite boundary of Ta/(Ta+Nb) = 0 - 0.4 and Li/(Li+Na+K) between 0 and 0.05), as reported in previous works involving bulk NKN and NKN-LT ceramics [18, 20, 266].

The performance of post-growth treated NKN-LT films shown in this report are within the same range of PZT, which response range from 20-56 $\mu C/cm^2$ depending on the composition and other enhancements made [267-271].

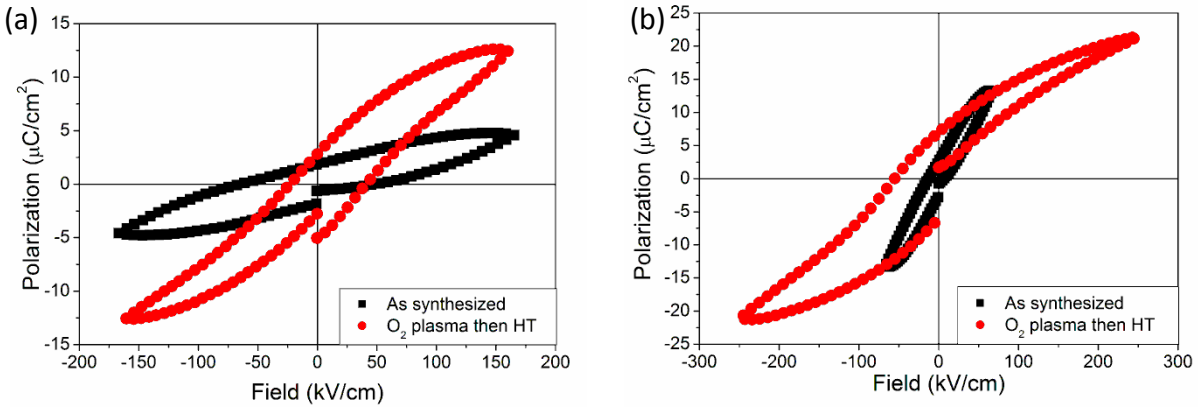

Figure 63: Ferroelectric response of NKN-LT film before and after a two-step post-growth treatment. (a) R = 16.7%, T = 7.5%, 0.15M LiCl (sample 9 in Table 17). (b) R = 16.7%, T = 20%, 0.15M LiCl (sample 7).

The best performing NKN-LT film (sample 7 in Table 17 after O_2 plasma and heat treatment) are then brought to the laser scanning vibrometry testing station to gauge their piezoelectric response. Again, the advantage of using a laser scanning vibrometry compared to conventional interferometer system is that it can measure displacement over a large area of the film, and take into account both the region under bias and movement of the substrate simultaneously, resulting in a more reliable and quantifiable measurements [183]. However it should be noted that the films measured are under in-plane constraint by the substrate and linear displacement-voltage relation is assumed, resulting in underestimation of the actual d_{33} value. The results shown in Figure 64 clearly demonstrate that treated NKN-LT film displays significant piezoelectric response, with a d_{33} value of 25 pm/V based on the 2 V applied to the sample. Although the NKN-LT measured d_{33} value is still very small compared to those of PZT (approx. 180-200 pm/V [267, 272]), it's a good starting value considering the films are still not exactly at the MPB composition.

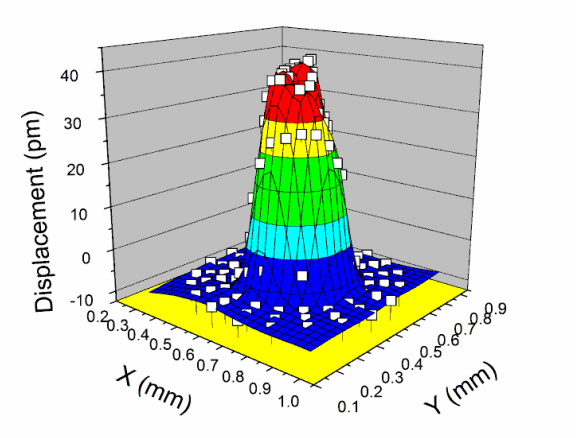

Figure 64: NKN-LT piezoelectric properties from vibrometry NKN-LT films. Result shown is after treatments.

6.3 Summary

We have carefully investigated the growth mechanism of epitaxial NKN and NKN-LT films via the hydrothermal route. Similar to the previous finding with NKN powder synthesis via hydrothermal method, it is found that hydrothermally epitaxied NKN film grows contains a second Na-rich layer near the film surface. This Na-rich layer grows rapidly, and at higher reaction temperature it results in an extremely thick and rough film.

A single phase NKN film can be obtained by applying multiple pronged approaches by shortening the growth period, reduction of reaction temperature and the introduction of complexing agent. As a last resort, we found that subjecting the film to a modest post growth heat treatment at 800°C for 2 hours is also effective to merge the two layers of different compositions into one with even composition.

With an increased number of precursors involved in the synthesis, NKN-LT film growth is understandably more complicated than KN or NKN film growth. The complication mainly rise due to the different solubilities of three different alkali ions (Li^+, Na^+, and K^+) and different dissolution behavior of Ta with respect to the usual niobium oxide. Controlling the exact composition of the NKN-LT proves to be a challenge, one of the reason is that quantitative analysis of Li, being a light element, is not possible to be done using conventional elemental analysis like EDX. Another factor is because the final powder composition may not be the same with the compositions of the precursor.

The electrical response of NKN and NKN-LT is predictably larger than pure KN film. The increased dielectric and ferroelectric response of NKN and NKN-LT film are the results of Ta and Na incorporation, which lowers the original KN its Curie temperature and pushing the composition towards the phase boundary. Although the absolute ferroelectric and piezoelectric response is still very small compared to the more established PZT based ferro/piezoelectric thin films, we have proven the concept that good performing lead-free piezoelectric thin films based on I-V perovskites can actually be synthesized at low temperatures of 200°C and below in water.

7. Current status and suggestions for future works

What is really missing in this study (and many others that relies on the precise composition of light elements) is the exact measurement of the Li incorporation amount in the NKN-LT film lattice. Lithium's low atomic number makes it particularly challenging to detect even with a windowless energy dispersive X-ray spectroscopy (EDS) technique [260]. The small amount of incorporation in NKN-LT (typically <5 at%) also makes quantitative XPS difficult. Alternatively, an inductively coupled plasma mass spectroscopy (ICP-MS) study can be done, but the difficulties in completely dissolving NKN-LT powders/films in ICP-MS compatible solvents remain a challenge.

We offer two possible techniques to improve the detection and quantification of lithium. The first technique is by using electron energy loss spectroscopy (EELS) that reportedly has improved detection for low atomic number elements like carbon and lithium [273, 274]. Another, less direct technique is to do semi-quantitative analysis based on the elemental depth profile generated by TOF-SIMS measurements. This can be done by comparing the unknown sample's analysis results with an NKN-LT standard with known composition and density.

> *...great difficulties are felt at first and these cannot be overcome except by starting from experiments .. and then be conceiving certain hypotheses ... But even so, very much hard work remains to be done and one needs not only great perspicacity but often a degree of good fortune.*
> ***Christiaan Huygens (1629-1695).***

Figure 65 illustrates the lithium and tantalum depth profile obtained by SIMS across different samples to highlight that the resolution of SIMS measurement is sufficient to do such studies.

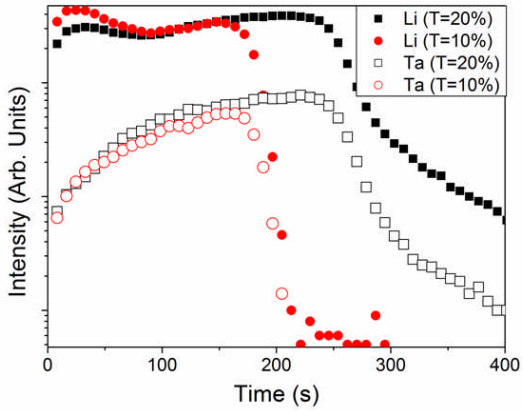

Figure 65: Comparison of lithium and tantalum depth profile of samples with different T ratio.

When the quantitative (or semi-quantitative) analysis of lithium can be established, the next logical step would be controlling the precise amounts of Li, Na and Ta to get the NKN-LT composition as close as possible to the MPB to get optimum ferro/piezoelectric properties. When optimum composition is achieved, further studies on hydrothermally grown NKN-LT can be thoroughly examined, including fatigue studies for possible ferroelectric memory devices etc.

The second development idea is to conduct in situ measurement during hydrothermal synthesis of powders, and if possible, films. Our current approach relies on stopping the reaction by quenching and then collecting the powder that precipitated – with problems of poor time resolution and possibilities of loosing (dissolving) intermediate phases as the solution cools down to room temperature. An excellent example would be the works of

Modeshia et al. [241], which successfully captures different polymorphs of sodium niobate ($NaNbO_3$) grown hydrothermally as the reaction progresses. In-situ measurements will give true insights of what is developing during hydrothermal synthesis without excessive disturbance to the actual reaction.

The third opportunity for future research is the development of a continuous flow reactor, to scale up the reaction (possible commercialization) use $NbCl_5$ salt as precursor, minimize wastage and amount of oxide precursor/powder. Focus on the film growth. Successful epitaxial film formation on conductive substrate opens possibility of incorporating NKN based piezoelectric materials in devices, which will have impact on efforts replacing PZT as the major piezoelectric materials used today.

Appendixes

Appendix A: Determination of optimum powder heat treatment conditions

To determine the optimum heat treatment scheme, we selected a particular sample containing mixed NKN and NN phase that were obtained during $NaNbO_3$ to $KNbO_3$ hydrothermal conversion experiment (in section 5.2, Table 10, referred here as "the 10 hours sample") to be heat treated at three different temperatures of 600, 700 and 800°C. This sample was selected because it has approx. 1:1 ratio of NN (impurity) to NKN phase.

Only a small quantity (about 0.3 g) of the "10 hours sample powder" was used for preliminary experiments due to limited availability of samples. Quick XRD scan results of heat treated "10 hours sample" (Figure A) reveals that the intensity of unwanted NN phase reflections starts decreasing when the samples are subjected to heat treatment at 700°C, and is completely absent after 800°C. The finding suggests that the optimum heat treatment condition is at 800°C for 2 hours.

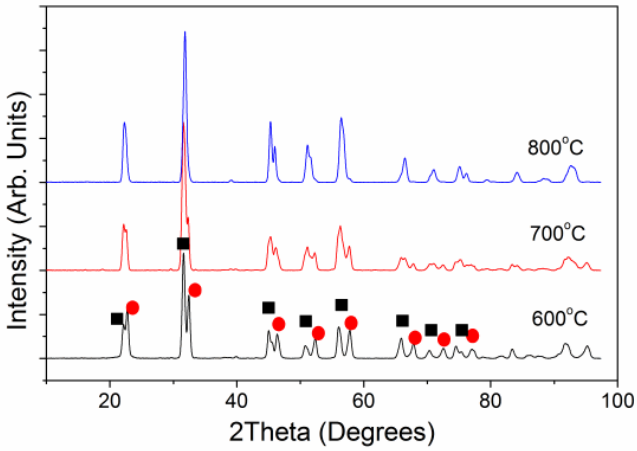

Figure A: XRD data of samples obtained during $NaNbO_3$ to $KNbO_3$ hydrothermal conversion experiment (refer to Table 10, 10 hours sample) after heat treatment at different temperatures.

Appendix B: NKN film (R = 20%) grown with EDTA

In section 6.2.3, the samples with R = 20% grown with EDTA were not tested and discussed in detail because it has a very rough surface (Figure B (1-2)), which makes it not suitable for electrical properties testing. The film grown at R = 20% with EDTA however has similar structural properties and sodium layer on top as seen by TOF SIMS measurements (Figure B (3)).

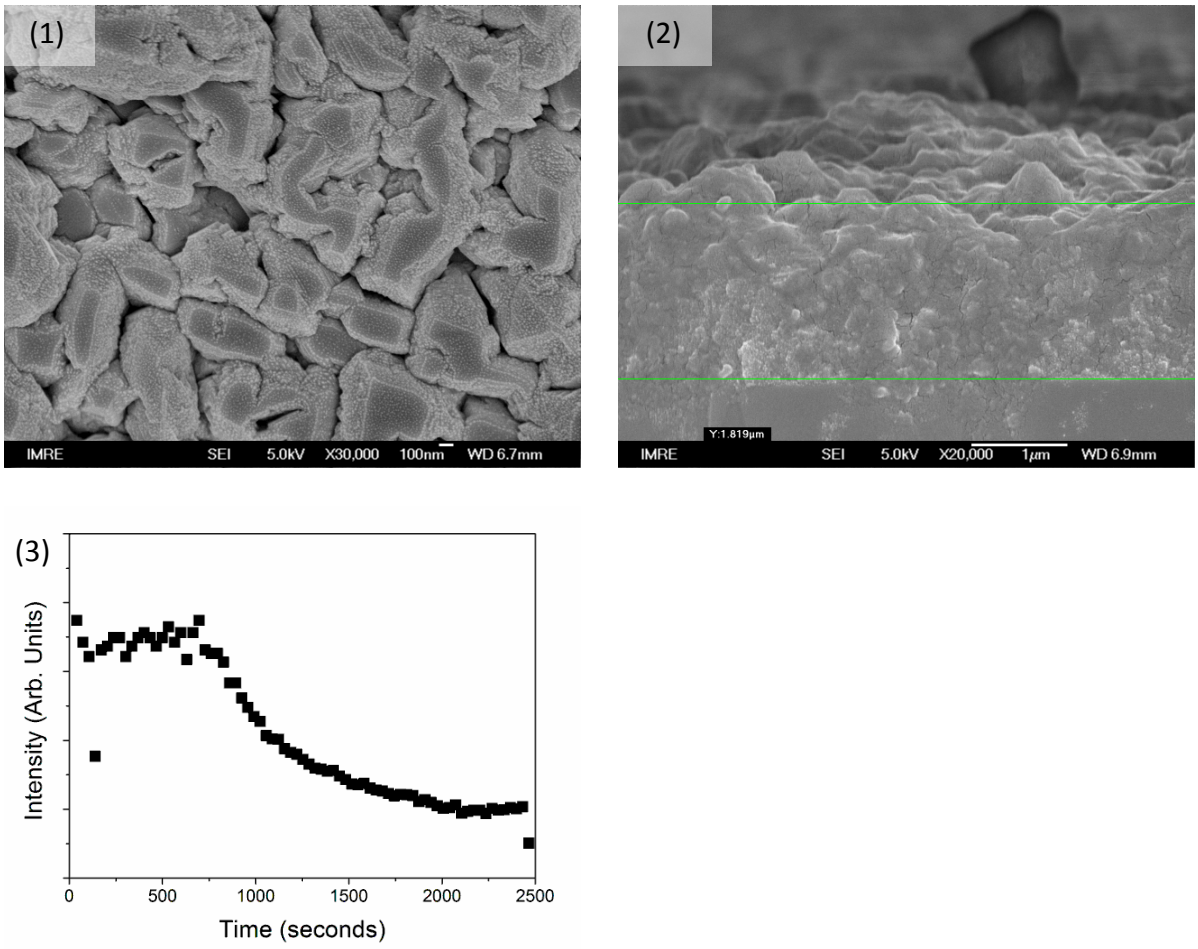

Figure B: (1) surface morphology and (2) cross section FESEM of NKN film (R = 20%) grown with EDTA at 200 for 24 hours. (3) Sodium depth profile taken from TOF-SIMS, indicating a sodium rich top layer.

Appendix C: Off-axis gonio scan of epitaxial KN film

Prior conducting off-axis phi (ϕ) scan to determine the orientation of KN film with respect to STO substrate, it is ensured that the KN (002) peak is well separated from STO (110) peak in the off-axis θ-2θ scan (Figure C). The purpose of the additional off-axis θ-2θ scan is to ensure that the phi scans signals of KN films do not originate from the STO substrate.

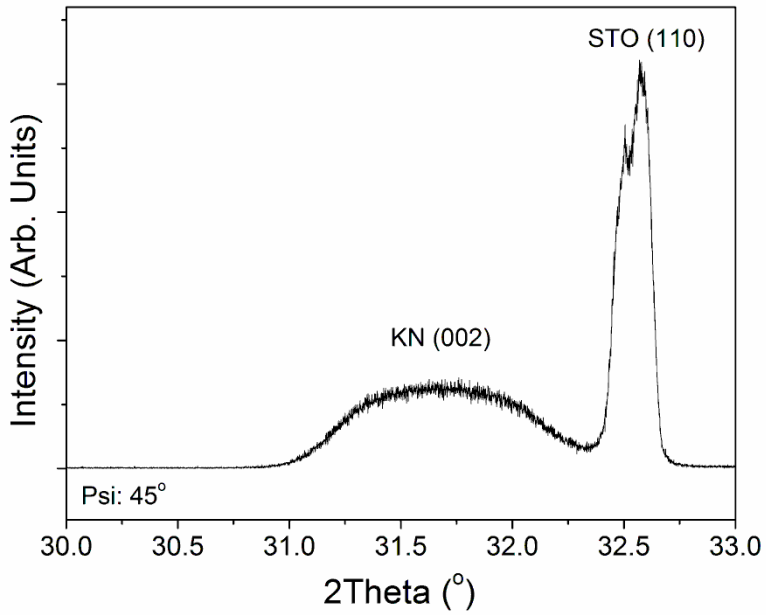

Figure C: Off-axis gonio scan showing distinguishable KN (002) and STO (110) peaks.

References and notes

1. Goldschmidt, V.M., *Crystal structure and chemical constitution.* Trans. Faraday Soc., 1929. **25**: p. 253 - 283.
2. Jaffe, B., R.S. Roth, and S. Marzullo, *Piezoelectric Properties of Lead Zirconate-Lead Titanate Solid-Solution Ceramics.* Journal of Applied Physics, 1954. **25**(6): p. 809-810.
3. Needleman, H., *Lead Poisoning.* Annual Review of Medicine, 2004. **55**(1): p. 209-222.
4. Olaf, A., *The Volatilization of Lead Oxide from Lead Silicate Melts.* Journal of the American Ceramic Society, 1919. **2**(10): p. 784-789.
5. Wicks, M., *The Restriction of the Use of Certain Hazardous Substances in Electrical and Electronic Equipment Regulations 2006*, 2006, UK Ministry of Trade and Industry, The Stationery Office Limited.
6. Hasegawa, T., et al. *Basic study on lead free BNT piezoelectric film deposited by hydrothermal method*. 2005. Rotterdam, Netherlands: Institute of Electrical and Electronics Engineers Inc., Piscataway, NJ 08855-1331, United States.
7. Huang, X., et al., *Influence of composition on properties of BNT-BT lead-free piezoceramics.* Journal of Rare Earths, 2006. **24**(SUPPL 2): p. 321-324.
8. Zhiwu, C. and L. Zhenya, *Piezoelectric and dielectric properties of* $(Bi_{0.5}Na_{0.5})TiO_3$-$(Bi_{0.5}K_{0.5})TiO_3$-$BaTiO_3$ *lead-free piezoelectric ceramics.* Key Engineering Materials, 2007: p. 54-7.
9. Chang, Y., Z. Yang, and L. Wei, *Microstructure, Density, and Dielectric Properties of Lead-Free* $(K_{0.44}Na_{0.52}Li_{0.04})(Nb_{0.96-x}Ta_xSb_{0.04})O_3$ *Piezoelectric Ceramics.* Journal of the American Ceramic Society, 2007. **90**(5): p. 1656-1658.
10. Guo, Y., K.-I. Kakimoto, and H. Ohsato, $(Na_{0.5}K_{0.5})NbO_3$-$LiTaO_3$ *lead-free piezoelectric ceramics.* Materials Letters, 2005. **59**(2-3): p. 241-244.
11. Zang, G.-Z., et al., *Perovskite* $(Na_{0.5}K_{0.5})_{1-x}(LiSb)_xNb_{1-x}O_3$ *lead-free piezoceramics.* Applied Physics Letters, 2006. **88**(21): p. 212908-3.
12. Yun, L., et al. *Ferroelectric lead zirconate titanate and barium titanate nanoshell tubes*. 2004. Boston, MA, USA: Mater. Res. Soc.

13. Chu, R.-Q., et al., *Ultrahigh piezoelectric response along some special cleavage plane in $BaTiO_3$ single-crystals.* Acta Physica Sinica, 2005. **54**(2): p. 935-8.
14. Karaki, T., et al., *Lead-free piezoelectric ceramics with large dielectric and piezoelectric constants manufactured from $BaTiO_3$ nano-powder.* Japanese Journal of Applied Physics, Part 2 (Letters), 2007. **46**(4-7): p. 97-8.
15. Megaw, H., *Ferroelectricity and crystal structure. II.* Acta Crystallographica, 1954. **7**(2): p. 187-194.
16. Cross, L.E., *Electric Double Hysteresis in $(K_xNa_{1-x})NbO_3$ Single Crystals.* Nature, 1958. **181**(4603): p. 178-179.
17. Wong, L.C.K. and W.L. Downs, *Renal effects of potassium niobate.* Toxicology and Applied Pharmacology, 1966. **9**(3): p. 561-570.
18. Saito, Y. and H. Takao, *High Performance Lead-free Piezoelectric Ceramics in the $(K,Na)NbO_3$-$LiTaO_3$ Solid Solution System.* Ferroelectrics, 2006. **338**(1): p. 17 - 32.
19. Saito, Y., et al., *Lead-free piezoceramics.* Nature, 2004. **432**(7013): p. 84-87.
20. Saito, T., et al., *Pulsed Laser Deposition of High-Quality $(K,Na)NbO_3$ Thin Films on $SrTiO_3$ Substrate Using High-Density Ceramic Targets.* Japanese Journal of Applied Physics, 2004. **43**(9B): p. 6627-6631.
21. Saito, Y. and H. Takao, *Synthesis of polycrystalline platelike $KNbO_3$ particles by the topochemical micro-crystal conversion method and fabrication of grain-oriented $(K_{0.5}Na_{0.5})NbO_3$ ceramics.* Journal of the European Ceramic Society, 2007. **27**(13-15): p. 4085-4092.
22. Li, J.-F., et al., *Ferroelectric and Piezoelectric Properties of Fine-Grained $Na_{0.5}K_{0.5}NbO_3$ Lead-Free Piezoelectric Ceramics Prepared by Spark Plasma Sintering.* Journal of the American Ceramic Society, 2006. **89**(2): p. 706-709.
23. Wang, Y., et al., *Hydrothermal synthesis of potassium niobate powders.* Ceramics International, 2007. **33**(8): p. 1611-1615.
24. Maeder, M.D., D. Damjanovic, and N. Setter, *Lead Free Piezoelectric Materials.* Journal of Electroceramics, 2004. **13**(1): p. 385-392.
25. Kodaira, K., et al., *Sintering and dielectric properties of $KNbO_3$.* Journal of Materials Science Letters, 1982. **1**(7): p. 277-278.

26. Matsubara, M., et al., *Processing and Piezoelectric Properties of Lead-Free (K,Na)(Nb,Ta)O_3 Ceramics.* Journal of the American Ceramic Society, 2005. **88**(5): p. 1190-1196.
27. Sigman, J., et al., *Dielectric response of K(Ta,Nb)O_3 thin films.* Applied Physics A: Materials Science & Processing, 2005. **V81**(2): p. 289-293.
28. Tennery, V.J. and K.W. Hang, *Thermal and X-Ray Diffraction Studies of the $NaNbO_3$-$KNbO_3$ System.* Journal of Applied Physics, 1968. **39**(10): p. 4749-4753.
29. Lange, F.F., *Chemical Solution Routes to Single-Crystal Thin Films.* Science, 1996. **273**(5277): p. 903-909.
30. Goh, G.K.L., et al., *Hydrothermal epitaxy of $KNbO_3$ thin films and nanostructures.* Journal of Crystal Growth, 2006. **286**(2): p. 457-464.
31. Komarneni, S., R. Roy, and Q.H. Li, *Microwave - Hydrothermal Synthesis of Ceramic Powders.* Materials Research Bulletin, 1992. **27**: p. 1393-1405.
32. Goh, G.K.L., et al., *Hydrothermal synthesis of $KNbO_3$ and $NaNbO_3$ powders.* Journal of Materials Research, 2003. **18**(2): p. 338-345.
33. Lange, F.F. and G.K.L. Goh, *Hydrothermal epitaxial growth of perovskite films.* Journal of Ceramic Processing Research, 2001. **2**(1): p. 4-8.
34. Lv, J.-H., et al., *Hydrothermal Synthesis and Characterization of $K_xNa_{(1-x)}NbO_3$ Powders.* International Journal of Applied Ceramic Technology, 2007. **4**: p. 571-577.
35. Sun, C., et al., *Hydrothermal Synthesis of Single Crystalline (K,Na)NbO_3 Powders.* European Journal of Inorganic Chemistry, 2007. **2007**(13): p. 1884-1888.
36. Goh, G.K.L., et al., *Low-Temperature Epitaxy of $KTaO_3$ and $KNbO_3$ Films.* Journal of The Electrochemical Society, 2008. **155**(1): p. D52-D56.
37. Suchanek, W.L., *Synthesis of Potassium Niobiate ($KNbO_3$) Thin Films by Low-Temperature Hydrothermal Epitaxy.* Chemistry of Materials, 2004. **16**(6): p. 1083-1090.
38. Yu, J. and X. Liu, *Hydrothermal synthesis and characterization of LiNbO3 crystal.* Materials Letters, 2007. **61**(2): p. 355-358.
39. Kennedy, J.H., *Sodium-Potassium Niobates and Tantalates.* Journal of Inorganic and Nuclear Chemistry, 1961. **1961**(20): p. 53-57.

40. Zhou, H.-M., et al., *The dissolution behavior of Nb_2O_5, Ta_2O_5 and their mixture in highly concentrated KOH solution.* Hydrometallurgy, 2005. **80**(1-2): p. 126-131.
41. Goh, G.K.L. and S.K. Donthu, *Hydrothermal Epitaxy of I:V Perovskite Thin Films.* Materials Research Society Symposium Proceedings, 2002. **718**: p. 201-206.
42. Howard, C.J. and H.T. Stokes, *Structures and phase transitions in perovskites - a group-theoretical approach.* Acta Crystallographica, Section A (Foundations of Crystallography), 2005. **A61**: p. 93-111.
43. Mitchell, R.H., *Perovskites : modern and ancient*2002, Thunder Bay, Ontario: Almaz Press. 318.
44. ISI, *ISI Web of Knowledge*, 2007, The Thomson Corporation.
45. Mitchell, R.H., *Perovskites : modern and ancient*2002, Thunder Bay, Ont.: Almaz Press. vii, 318.
46. Thurnauer, H. and J. Deaderick, *Insulating material*, 1947, American Lava Corp.: United States.
47. Ahart, M., et al., *Origin of morphotropic phase boundaries in ferroelectrics.* Nature, 2008. **451**(7178): p. 545-548.
48. Goldschmidt, V.M., Skrifer Norske Videnskaps-Akad. Oslo, I. Mat.-Nat., 1926. **8**.
49. Yamanaka, S., et al., *Thermophysical Properties of Perovskite-Type Strontium Cerate and Zirconate.* Journal of the American Ceramic Society, 2005. **88**(6): p. 1496-1499.
50. Li, C., K.C.K. Soh, and P. Wu, *Formability of ABO_3 perovskites.* Journal of Alloys and Compounds, 2004. **372**(1-2): p. 40-48.
51. Megaw, H., *Origin of ferroelectricity in barium titanate and other perovskite-type crystals.* Acta Crystallographica, 1952. **5**(6): p. 739-749.
52. Howard, C.J. and H.T. Stokes, *Structures and phase transitions in perovskites - a group-theoretical approach.* Acta Crystallographica Section A, 2005. **61**(1): p. 93-111.
53. Guo, R., et al., *Origin of the High Piezoelectric Response in $PbZr_{1-x}Ti_xO_3$.* Physical Review Letters, 2000. **84**(23): p. 5423.
54. Jaffe, B., R.S. Roth, and S. Marzullo, *Properties of piezoelectric ceramics in the solid-solution series lead titanate zirconate-lead oxide: tin oxide and lead titanate-lead hafnate.* J. Res. Natl Bur. Stand., 1955. **55**: p. 239-254.

55. Homes, C.C., et al., *Optical Response of High-Dielectric-Constant Perovskite-Related Oxide.* Science, 2001. **293**(5530): p. 673-676.

56. Fukunaga, M., Y. Uesu, and G. Li, *$CaCu_3Ti_4O_{12}$-type Colossal Dielectric Relaxation in Complex Perovskite $(Ba_{1-x}La_x)(Ti_{1-x}Cr_x)O3$* Ferroelectrics, 2007. **354**(1): p. 106 - 114.

57. Bednorz, J.G. and K.A. Müller, *Possible highTc superconductivity in the Ba–La–Cu–O system.* Zeitschrift für Physik B Condensed Matter, 1986. **64**(2): p. 189-193.

58. Maeno, Y., et al., *Superconductivity in a layered perovskite without copper.* Nature, 1994. **372**(6506): p. 532-534.

59. Choi, T., et al., *Switchable Ferroelectric Diode and Photovoltaic effect in BiFeO3.* Science, 2009: p. 1168636.

60. Lee, K.H., et al., *Thermoelectric properties of layered perovskite-type $(Sr_{1-x}Ca_x)_3(Ti_{1-y}Nb_y)_2O_7$.* Journal of Applied Physics, 2007. **101**(8): p. 083707-6.

61. Mathews, S., et al., *Ferroelectric Field Effect Transistor Based on Epitaxial Perovskite Heterostructures.* Science, 1997. **276**(5310): p. 238-240.

62. Keqin Huang, R.T.J.B.G.C.M., *Superior Perovskite Oxide-Ion Conductor; Strontium- and Magnesium-Doped $LaGaO_3$: III, Performance Tests of Single Ceramic Fuel Cells.* Journal of the American Ceramic Society, 1998. **81**(10): p. 2581-2585.

63. Ruzmetov, D., et al., *Epitaxial Magnetic Perovskite Nanostructures.* Advanced Materials, 2005. **17**(23): p. 2869-2872.

64. Berry, F.J., et al., *Magnetic order in perovskite-related $SrFeO_2F$.* Journal of Physics: Condensed Matter, 2008. **20**(21): p. 215207.

65. Fukuda, T. and Y. Uematsu, *Preparation of $KNbO_3$ Single Crystal for Optical Applications.* Japanese Journal of Applied Physics, 1972. **11**(2): p. 163.

66. Hoerman, B.H., et al., *Dynamic response of the electro-optic effect in epitaxial $KNbO_3$.* Applied Physics Letters, 1999. **75**(18): p. 2707-2709.

67. Dalakoti, A., A. Bandyopadhyay, and S. Bose, *Effect of Zn, Sr, and Y Addition on Electrical Properties of PZT Thin Films.* Journal of the American Ceramic Society, 2006. **89**(3): p. 1140-1143.

68. Hung, L.S. and L.A. Bosworth, *Multilayer structure for epitaxial growth of oxide films on Si with an underlying electrode.* Applied Physics Letters, 1993. **62**(21): p. 2625-2627.

69. Martín, M.J., et al., *Pulsed laser deposition of $KNbO_3$ thin films.* Journal of Materials Research, 1997. **12**(10): p. 2699-2706

70. Rae, A.D., J.G. Thompson, and R.L. Withers, *Structure refinement of commensurately modulated bismuth strontium tantalate, $Bi_2SrTa_2O_9$.* Acta Crystallographica Section B, 1992. **48**(4): p. 418-428.

71. Stachiotti, M.G., et al., *Electronic structure and ferroelectricity in $SrBi_2Ta_2O_9$.* Physical Review B, 2000. **61**(21): p. 14434.

72. Glazer, A., *The classification of tilted octahedra in perovskites.* Acta Crystallographica Section B, 1972. **28**(11): p. 3384-3392.

73. Wilson, T., *Dielectric Model*, 2007, Wikipedia.

74. Urusov, V. and T. Nadezhina, *Frequency distribution and selection of space groups in inorganic crystal chemistry.* Journal of Structural Chemistry, 2009. **50**(0): p. 22-37.

75. Jaffe, B., W.R. Cook, and H. Jaffe, *Piezoelectric Ceramics*. Non-Metallic Solids, ed. J.P. Roberts and P. Popper1971, London and New York: Academic Press. 317.

76. Scott, J.F., *Ferroelectric Memories*. Springer Series in Advanced Microelectronics, ed. K. Itoh and T. Sakurai. Vol. 3. 2000, Berlin: Springer-Verlag.

77. Barsoum, M.W., *Fundamental of Ceramics*. 2 ed. Series in Materials Science and Engineering, ed. B. Cantor and M.J. Goringe2003, Bristol: Institute of Physics Publishing.

78. Evans, J.T., *Characterizing Non-linear Materials*, 2011, Radiant Technologies, Inc.

79. Devonshire, A.F., *Theory of ferroelectrics.* Advances in Physics, 1954. **3**(10): p. 85 - 130.

80. Merz, W.J., *Domain Formation and Domain Wall Motions in Ferroelectric $BaTiO_3$ Single Crystals.* Physical Review, 1954. **95**(3): p. 690.

81. Hlinka, J. and P. Márton, *Phenomenological model of a 90^o domain wall in $BaTiO_3$-type ferroelectrics.* Physical Review B, 2006. **74**(10): p. 104104.

82. Lü, T. and W. Cao, *Generalized continuum theory for ferroelectric thin films.* Physical Review B, 2002. **66**(2): p. 024102.

83. Damjanovic, D., *Ferroelectric, dielectric and piezoelectric properties of ferroelectric thin films and ceramics.* Reports on Progress in Physics, 1998. **61**(9): p. 1267.

84. Arlt, G., *Twinning in ferroelectric and ferroelastic ceramics: stress relief.* Journal of Materials Science, 1990. **25**(6): p. 2655-2666.

85. Muralt, P., *Ferroelectric thin-films: The emancipation of ferroelectricity.* Nat Mater, 2007. **6**(1): p. 8-9.

86. Cochran, W., *Crystal Stability and the Theory of Ferroelectricity.* Physical Review Letters, 1959. **3**(9): p. 412.

87. Cochran, W., *Crystal stability and the theory of ferroelectricity.* Advances in Physics, 1960. **9**(36): p. 387 - 423.

88. Fontana, M.D., et al., *Infrared spectroscopy in $KNbO_3$ through the successive ferroelectric phase transitions.* Journal of Physics C: Solid State Physics, 1984(3): p. 483.

89. Boyer, L.L., et al., *First principles calculations for polarized crystals.* Ferroelectrics, 1991. **117**(1): p. 233 - 243.

90. Cohen, R.E., *Origin of ferroelectricity in perovskite oxides.* Nature, 1992. **358**(6382): p. 136-138.

91. Cohen, R.E., *Theory of ferroelectrics: a vision for the next decade and beyond.* Journal of Physics and Chemistry of Solids, 2000. **61**(2): p. 139-146.

92. Foster, C.M., et al., *Anharmonicity of the lowest-frequency $A_1(TO)$ phonon in $PbTiO_3$.* Physical Review B, 1993. **48**(14): p. 10160.

93. Pérez, J.A., et al., *Ferroelectric Domain Structure of PZT Tetragonal Single Crystals Analysed by Scanning Probe Microscopy.* Microscopy and Microanalysis, 2009. **15**(SupplementS3): p. 83-84.

94. Ontalus, V., et al., *Crystallization behaviour and phase coexistence at morphotrophic phase boundaries in PZT thin films prepared by sol-gel processing.* Journal of Materials Science, 1996. **31**(14): p. 3639-3642.

95. Li, L., et al., *Gradient stress induced coexistence of tetragonal and rhombohedral phases in Pb(Zr,Ti)O_3 films.* Physica B: Condensed Matter, 2009. **404**(8-11): p. 1362-1364.

96. Noheda, B., et al., *The monoclinic phase in PZT: New light on morphotropic phase boundaries.* AIP Conference Proceedings, 2000. **535**(1): p. 304-313.

97. Yokota, H., et al., *Crystal structure of the rhombohedral phase of $PbZr_{1-x}Ti_xO_3$ ceramics at room temperature.* Physical Review B, 2009. **80**(10): p. 104109.

98. Kakegawa, K., et al., *A compositional fluctuation and properties of Pb(Zr, Ti)O_3.* Solid State Communications, 1977. **24**(11): p. 769-772.

99. Glazer, A.M., et al., *Influence of short-range and long-range order on the evolution of the morphotropic phase boundary in $Pb(Zr_{1-x}Ti_x)O_3$.* Physical Review B, 2004. **70**(18): p. 184123.

100. Soares, M.R., A.M.R. Senos, and P.Q. Mantas, *Phase coexistence in PZT ceramics.* Journal of the European Ceramic Society, 1999. **19**(10): p. 1865-1871.

101. Noheda, B. and D.E. Cox, *Bridging phases at the morphotropic boundaries of lead oxide solid solutions.* Phase Transitions: A Multinational Journal, 2006. **79**(1): p. 5 - 20.

102. Noheda, B., et al., *A monoclinic ferroelectric phase in the $Pb(Zr_{1-x}Ti_x)O_3$] solid solution.* Applied Physics Letters, 1999. **74**(14): p. 2059-2061.

103. Araújo, E.B., et al., *Monoclinic-tetragonal phase transition in $Pb(Zr_{1-x}Ti_x)O_3$ studied by infrared spectroscopy.* Journal of Physics: Condensed Matter, 2002. **14**(20): p. 5195.

104. Araújo, E.B., et al., *Evidence for the monoclinic–tetragonal phase coexistence in $Pb(Zr_{0.53}Ti_{0.47})O_3$ thin films.* Journal of Physics: Condensed Matter, 2008. **20**(41): p. 415203.

105. Ragini, R.R., S.K. Mishra, and D. Pandey, *Room temperature structure of $Pb(Zr_xTi_{1-x})O_3$ around the morphotropic phase boundary region: A Rietveld study.* Journal of Applied Physics, 2002. **92**(6): p. 3266-3274.

106. Glazer, A.M., et al., *First single-crystal neutron diffraction results on PZT structure.* Acta Crystallographica Section A, 2010. **66**(a1): p. s167.

107. Fu, H. and R.E. Cohen, *Polarization rotation mechanism for ultrahigh electromechanical response in single-crystal piezoelectrics.* Nature, 2000. **403**(6767): p. 281-283.

108. Park, S.-E. and T.R. Shrout, *Ultrahigh strain and piezoelectric behavior in relaxor based ferroelectric single crystals.* Journal of Applied Physics, 1997. **82**(4): p. 1804-1811.

109. Bellaiche, L., et al., *Finite-Temperature Properties of $Pb(Zr_{1-x}Ti_x)O_3$ Alloys from First Principles.* Physical Review Letters, 2000. **84**(23): p. 5427.

110. Singh, A.K., et al., *Origin of high piezoelectric response of $Pb(Zr_xTi_{1-x})O_3$ at the morphotropic phase boundary: Role of elastic instability.* Applied Physics Letters, 2008. **92**(2): p. 022910-3.

111. Li, J.Y., et al., *Domain switching in polycrystalline ferroelectric ceramics.* Nat Mater, 2005. **4**(10): p. 776-781.

112. Matthias, B.T., *New Ferroelectric Crystals.* Physics Review, 1949. **75**(11): p. 1771.

113. Matthias, B.T. and J.P. Remeika, *Dielectric Properties of Sodium and Potassium Niobates.* Physics Review, 1951. **82**(5): p. 727-729.

114. Gunter, P., *Potassium Niobate Crystal*, in *Canadian Intellectual Property Office*, C.I.P. Office, Editor 1989: Canada.

115. Zgonik, M., et al., *Materials constants of $KNbO_3$ relevant for electro- and acousto-optics.* Journal of Applied Physics, 1993. **74**(2): p. 1287-1297.

116. Herzog, C., et al., *Epitaxial $K_{1-x}Na_xTa_{0.66}Nb_{0.34}O_3$ thin films for optical waveguiding applications.* Journal of the Optical Society of America B, 2007. **24**(4): p. 829-832.

117. Shuvaeva, V.A. and M.Y. Antipin, *Structural disorder in $KNbO_3$ crystal from X-ray diffraction and EXAFS spectroscopy.* Crystallography Reports, 1995. **40**(3): p. 466-471.

118. Egerton, L. and S.S. Flaschen, *Method of Manufacture of Potassium-Sodium-Niobate Ceramics*, in *Canadian Intellectual Property Office*, C.I.P. Office, Editor 1963: Canada.

119. Shirane, G., R. Newnham, and R. Pepinsky, *Dielectric Properties and Phase Transitions of $NaNbO_3$ and $(Na,K)NbO_3$.* Physics Review, 1954. **96**(3): p. 581-588.

120. Nichols, B.M., et al., *$KTa_xNb_{1-x}O_3$ thin films deposited by metalorganic chemical vapor deposition.* Journal of Materials Research 2003. **18**(1): p. 106-110.

121. de Andrade, J.S., et al., *Structural studies of KNbO3 in niobate glass-ceramics.* Journal of Physics and Chemistry of Solids, 2000. **61**(6): p. 899-906.

122. Kimura, H., et al., *Deviation from stoichiometry of $KNbO_3$ crystal in fiber shape grown using pulling down technique.* Optical Materials, 2007. **30**(1): p. 198-200.

123. Reisman, A. and F. Holtzberg, *Phase Equilibria in the System K_2CO_3-Nb_2O_5 by the Method of Differential Thermal Analysis.* Journal of the American Chemical Society, 1955. **77**(8): p. 2115-2119.

124. Flückiger, U. and H. Arend, *On the preparation of pure, doped and reduced $KNbO_3$ single crystals.* Journal of Crystal Growth, 1978. **43**(4): p. 406-416.

125. Hewat, A.W., *Cubic-tetragonal-orthorhombic-rhombohedral ferroelectric transitions in perovskite potassium niobate: neutron powder profile refinement of the structures.* Journal of Physics C: Solid State Physics, 1973. **6**(16): p. 2559-2572.

126. Katz, L. and H.D. Megaw, *The structure of potassium niobate at room temperature: the solution of a pseudosymmetric structure by Fourier methods.* Acta Crystallographica, 1967. **22**(5): p. 639-648.

127. Vousden, P., *The structure of ferroelectric sodium niobate at room temperature.* Acta Crystallographica, 1951. **4**(6): p. 545-551.

128. Ahtee, M. and A.M. Glazer, *Lattice parameters and tilted octahedra in sodium-potassium niobate solid solutions.* Acta Crystallographica Section A, 1976. **32**(3): p. 434-446.

129. Ke, T.-Y., et al., *Sodium Niobate Nanowire and Its Piezoelectricity.* The Journal of Physical Chemistry C, 2008. **112**(24): p. 8827-8831.

130. Yuzyuk, Y.I., et al., *Ferroelectric Q-phase in a $NaNbO_3$ epitaxial thin film.* Applied Physics Letters, 2010. **96**(22): p. 222904-3.

131. Ayyub, P., et al., *Ferroelectric behavior in thin films of antiferroelectric materials.* Physical Review B, 1998. **57**(10): p. R5559.

132. Wada, T., et al., *Ferroelectric $NaNbO_3$ Ceramics Fabricated by Spark Plasma Sintering.* Japanese Journal of Applied Physics, 2003. **42**(Copyright (C) 2003 The Japan Society of Applied Physics): p. 6110.

133. Oda, S., et al., *Preparation of ferroelectric $NaNbO_3$ thin films on MgO substrate by pulsed laser deposition.* IEEE Transactions on Ultrasonics, Ferroelectrics and Frequency Control, 2008. **55**(5): p. 1017-1022.

134. Wood, E., *Polymorphism in potassium niobate, sodium niobate, and other ABO3 compounds.* Acta Crystallographica, 1951. **4**(4): p. 353-362.

135. Egerton, L. and D.M. Dillon, *Piezoelectric and Dielectric Properties of Ceramics in the System Potassium Sodium Niobate.* Journal of the American Ceramic Society, 1959. **42**(9): p. 438-442.

136. Jaeger, R.E. and L. Egerton, *Hot Pressing of Potassium-Sodium Niobates.* Journal of the American Ceramic Society, 1962. **45**(5): p. 209-213.

137. Haertling, G.H., *Properties of Hot-Pressed Ferroelectric Alkali Niobate Ceramics.* Journal of the American Ceramic Society, 1967. **50**(6): p. 329-330.

138. Ahtee, M. and A.W. Hewat, *The structures of $Na_{0.98}K_{0.02}NbO_3$ and $Na_{0.90}K_{0.10}NbO_3$ (phase Q) at room temperature by neutron powder diffraction.* Acta Crystallographica Section A, 1975. **31**(6): p. 846-850.

139. Ahtee, M. and A.W. Hewat, *Structural phase transitions in sodium-potassium niobate solid solutions by neutron powder diffraction.* Acta Crystallographica Section A, 1978. **34**(2): p. 309-317.

140. Soderlind, F., P.-O. Kall, and U. Helmersson, *Sol-gel synthesis and characterization of $Na_{0.5}K_{0.5}NbO_3$ thin films.* Journal of Crystal Growth, 2005. **281**(2-4): p. 468-474.

141. Zuo, R., et al., *Sintering and Electrical Properties of Lead-Free $Na_{0.5}K_{0.5}NbO_3$ Piezoelectric Ceramics.* Journal of the American Ceramic Society, 2006. **89**: p. 2010-2015.

142. Ryu, K., et al., *Microstructure and Piezoelectric Properties of Lead-Free Niobate Ceramics.* Ferroelectrics, 2006. **338**: p. 57-63.

143. Lingwal, V. and N.S. Panwar, *Morphotropic Phase Transitions in Mixed Sodium-Potassium Niobate System.* Ferroelectrics, 2004. **300**(1): p. 3 - 14.

144. Lingwal, V., B.S. Semwal, and N.S. Panwar, *Relaxational Behavior of Mixed $NaNbO_3$-$KNbO_3$ System.* Ferroelectrics, 2006. **332**(1): p. 219 - 225.

145. Hungria, T., M. Alguero, and A. Castro, *Grain Growth Control in NaNbO3-SrTiO3 Ceramics by Mechanosynthesis and Spark Plasma Sintering.* Journal of the American Ceramic Society, 2007. **90**(7): p. 2122-2127.

146. Yamanouchi, K., et al., *Single crystal growth of $KNbO_3$ and application to surface acoustic wave devices.* Journal of the European Ceramic Society, 2001. **21**(15): p. 2791-2795.

147. Ikeda, S., et al., *Photocatalytic activity of hydrothermally synthesized tantalate pyrochlores for overall water splitting.* Applied Catalysis A: General, 2006. **300**(2): p. 186-190.

148. Lu, C.-H., S.-Y. Lo, and Y.-L. Wang, *Glycothermal preparation of potassium niobate ceramic particles under supercritical conditions.* Materials Letters, 2002. **55**: p. 121-125.

149. Wei, N., et al., *Synthesis and Mechanism of Ferroelectric Potassium Tantalate Niobate Nanoparticles by the Solvothermal and Hydrothermal Processes.* Journal of the American Ceramic Society, 2007. **90**(5): p. 1434-1437.

150. Byrappa, K. and M. Yoshimura, *Handbook of Hydrothermal Technology - Technology for Crystal Growth and Materials Processing*. Materials Science and Processing Technology Series, ed. G.E. Mcguire, S.M. Rossnagel, and R.F. Bunshah2001, Norwich, NY: Jointly published by Noyes Publications and William Andrew Publishing. 870.

151. Schafhalt, K.F.E., Galehrte Angeigen Bayer Academie, 1845. **20**: p. 557.

152. *4744 General Purpose Acid Digestion Bomb*, 2004, Parr Instrument Company: Moline. p. Detailed drawing of 4744 acid digestion bomb.

153. Lencka, M.M. and R.E. Riman, *Thermodynamic modeling of hydrothermal synthesis of ceramic powders.* Chemistry of Materials, 1993. **5**(1): p. 61-70.

154. Lencka, M.M. and R.E. Riman, *Hydrothermal synthesis of perovskite materials: Thermodynamic modeling and experimental verification.* Ferroelectrics, 1994. **151**(1): p. 159 - 164.

155. Nyman, M., et al., *A General Synthetic Procedure for Heteropolyniobates.* Science, 2002. **297**(5583): p. 996-998.

156. Xu, H., et al., *Prototype Sandia Octahedral Molecular Sieve (SOMS) Na2Nb2O6.H2O: Synthesis, Structure and Thermodynamic Stability.* Chemistry of Materials, 2004. **16**(10): p. 2034-2040.

157. Eckert, J.O., et al., *Kinetics and Mechanisms of Hydrothermal Synthesis of Barium Titanate.* Journal of the American Ceramic Society, 1996. **79**(11): p. 2929-2939.

158. Seo, J.-w., et al., *Development of Water-Soluble Single-Crystalline TiO_2 Nanoparticles for Photocatalytic Cancer-Cell Treatment.* Small, 2007. **3**(5): p. 850-853.

159. Hertl, W., *Kinetics of Barium Titanate Synthesis.* Journal of the American Ceramic Society, 1988. **71**(10): p. 879-883.

160. Ovramenko, N.A., et al., *Kinetics of hydrothermal synthesis of barium metatitanate.* Neorganicheskie Materialy, 1979. **15**: p. 1982–1984.

161. Kutty, T.R.N., R. Vivekanandan, and P. Murugaraj, *Precipitation of rutile and anatase (TiO_2) fine powders and their conversion to $MTiO_3$ (M = Ba, Sr, Ca) by the hydrothermal method.* Materials Chemistry and Physics, 1988. **19**(6): p. 533-546.

162. Zhou, K.-G. and M. Tokuda, *Study on solubility of Nb_2O_5 in KOH solution and alkali leaching of niobite.* Journal of Central South University of Technology, 2000. **7**(4): p. 171-174.

163. Chien, A.T., et al., *Synthesis and characterization of PbTiO3 powders and heteroepitaxial thin films by hydrothermal synthesis.* Journal of Materials Research, 1999. **14**(8): p. 3303-3311.

164. Tan, C.K., G.K.L. Goh, and G.K. Lau, *Growth and dielectric properties of $BaTiO_3$ thin films prepared by the microwave-hydrothermal method.* Thin Solid Films, 2008. **516**(16): p. 5545-5550.

165. Tan, C., et al., *Hydrothermal growth of $BaTiO_3$ thin films on printed circuit boards for integral capacitor applications.* Journal of Electroceramics, 2006. **16**(4): p. 581-585.

166. Chien, A.T., J.S. Speck, and F.F. Lange, *Hydrothermal synthesis of heteroepitaxial $Pb(Zr_xTi_{1-x})O_3$ thin films at 90–150°C.* Journal of Materials Research, 1997. **12**(5): p. 1176-1178.

167. Andeen, D., et al., *Lateral Epitaxial Overgrowth of ZnO in Water at 90 °C.* Advanced Functional Materials, 2006. **16**(6): p. 799-804.

168. Chien, A.T., et al., *Low temperature/low pressure hydrothermal synthesis of barium titanate: Powder and heteroepitaxial thin films.* Journal of Materials Research, 1995. **10**(7): p. 1784.

169. Kato, K., *Structure refinement of H-Nb2O$_5$.* Acta Crystallographica Section B, 1976. **32**(3): p. 764-767.

170. Kato, K. and S. Tamura, *Die Kristallstruktur von T-Nb2O$_5$.* Acta Crystallographica Section B, 1975. **31**(3): p. 673-677.

171. Santos, I.C.M.S., et al., *Studies on the hydrothermal synthesis of niobium oxides.* Polyhedron, 2002. **21**(20): p. 2009-2015.

172. Pawley, G., *Unit-cell refinement from powder diffraction scans.* Journal of Applied Crystallography, 1981. **14**(6): p. 357-361.

173. LeBail, A., H. Duroy, and J.L. Fourquet, *Ab-initio structure determination of LiSbWO$_6$ by X-ray powder diffraction.* Materials Research Bulletin, 1988. **23**: p. 447-452.

174. Toraya, H., *Whole-Powder-Pattern Decomposition Method.* The Rigaku Journal, 1989. **6**(2): p. 28-34.

175. Lin, C.H., et al., *A simple preparation procedure for the synthesis of sodium hexaniobate nanorods.* Materials Chemistry and Physics, 2005. **92**(1): p. 128-133.

176. Goiffon, A., E. Philippot, and M. Maurin, *Structure cristalline du niobate 7/6 de sodium (Na$_7$) (H$_3$O) Nb$_6$O$_{19}$, (H$_2$O)$_{14}$.* Revue de Chimie Minerale, 1980. **17**: p. 466-476.

177. Sakowski-Cowley, A.C., K. Lukaszewicz, and H.D. Megaw, *The structure of sodium niobate at room temperature, and the problem of reliability in pseudosymmetric structures.* Acta Crystallographica Section B, 1969. **25**(5): p. 851-865.

178. Krane, H.-G., S. Kek, and K.F. Fischer, *Schwingungsparameter im Perowskit K Ta O3 bei RT und 7 K gemessen mit Synchrotronstrahlung von 0.4 A.* Zeitschrift fuer Kristallographie, 1997. **12**: p. 129.

179. Abrahams, S.C., H.J. Levinstein, and J.M. Reddy, *Ferroelectric lithium niobate. 5. Polycrystal X-ray diffraction study between 24° and 1200°C.* Journal of Physics and Chemistry of Solids, 1966. **27**(6-7): p. 1019-1026.

180. Hummel, H.U., R. Fackler, and P. Remmert, *Tantaloxide durch Gasphasenhydrolyse, Druckhydrolyse und Transportreaktion aus 2H-Ta S2: Synthesen von TT-Ta2 O5 und T-Ta2 O5 und Kristallstruktur von T-Ta2 O5.* Chemische Berichte, 1992. **125**: p. 551-556.

181. Hewat, P., *Inorganic Crystal Structure Database for WWW*, 2007, Fachinformationszentrum Karlsruhe and National Institute of Standards and Technology.

182. Yao, K., S. Shannigrahi, and F.E.H. Tay, *Characterisation of piezoelectric thin films by areal laser scanning.* Sensors and Actuators A: Physical, 2004. **112**(1): p. 127-133.

183. Goh, P.C., K. Yao, and Z. Chen, *Lead-free piezoelectric ($K_{0.5}Na_{0.5}$)NbO_3 thin films derived from chemical solution modified with stabilizing agents.* Applied Physics Letters, 2010. **97**(10): p. 102901-3.

184. Rietveld, H., *A profile refinement method for nuclear and magnetic structures.* Journal of Applied Crystallography, 1969. **2**(2): p. 65-71.

185. Rodriguez-Carvajal, J., *FullProf.2k*, 2010. p. Crystallographic tools for Rietveld, profile matching and integrated intensity refinements of X-ray and/or neutron data.

186. Gonzalez-Platas, J. and J. Rodriguez-Carvajal, *GFourier Program*, 2007. p. A graphical tool for Fourier Maps.

187. Whipps, P.W., *Growth of high-quality crystals of KTN.* Journal of Crystal Growth, 1972. **12**(2): p. 120-124.

188. Hewat, A.W., *Soft modes and the structure, spontaneous polarization and Curie constants of perovskite ferroelectrics: tetragonal potassium niobate.* Journal of Physics C: Solid State Physics, 1973. **6**(6): p. 1074-1084.

189. Andeen, D., et al., *Lateral Epitaxial Overgrowth of ZnO in Water at 90°C.* Advanced Functional Materials, 2006. **16**(6): p. 799-804.

190. Goh, G.K.L., et al., *Hydrothermal synthesis of perovskite and pyrochlore powders of potassium tantalate.* Journal of Materials Research, 2002. **17**(12): p. 3168-3176.

191. Tan, C.K., G.K.L. Goh, and W.L. Cheah, *Dielectric properties of hydrothermally epitaxied I-V perovskite thin films.* Thin Solid Films, 2007. **515**(16): p. 6577-6581.

192. Chien, A.T., et al., *Electrical characterization of $BaTiO_3$ heteroepitaxial thin films by hydrothermal synthesis.* Journal of Materials Research, 1999. **14**(8): p. 3330-3339.

193. Balaraman, D., et al. *Low temperature (<100^oC) hydrothermal synthesis of high K-low loss $BaTiO_3$ films for integral capacitors*. in *4th Electronics Packaging Technology Conference, 2002*. 2002.

194. Fuyuki, S., *Ab initio study of proton dynamics on perovskite oxide surfaces.* Science and Technology of Advanced Materials, 2007. **8**(6): p. 504.

195. Viviani, M., et al., *Barium perovskites as humidity sensing materials.* Journal of the European Ceramic Society, 2001. **21**(10-11): p. 1981-1984.

196. Hennings, D. and S. Schreinemacher, *Characterization of hydrothermal barium titanate.* Journal of the European Ceramic Society, 1992. **9**(1): p. 41-46.

197. Hicks, W.T., *Evaluation of Vapor-Pressure Data for Mercury, Lithium, Sodium, and Potassium.* The Journal of Chemical Physics, 1963. **38**(8): p. 1873-1880.

198. *DOE Handbook of Design Consideration*, U.S.D.o. Energy, Editor 1999, National Technical Information Service: Washington. p. I-89.

199. Griffin, J.M., et al., *Dynamics on the microsecond timescale in hydrous silicates studied by solid-state ^2H NMR spectroscopy.* Physical Chemistry Chemical Physics, 2010. **12**(12): p. 2989-2998.

200. Brown, S.P. and L. Emsley, *Solid-State NMR*, in *Handbook of Spectroscopy*, G. Gauglitz and T. Vo-Dinh, Editors. 2003, WILEY-VCH Verlag GmbH & Co.: Weinheim. p. 269-326.

201. Fasquelle, D., et al., *Dielectric and structural characterization of $KNbO_3$ ferroelectric thin films epitaxially grown by pulsed laser deposition on Nb doped $SrTiO_3$.* Thin Solid Films, 2010. **518**(12): p. 3432-3438.

202. Romanov, M.V., et al., *MOCVD of $KNbO_3$ Ferroelectric Films and their Characterization.* Chemical Vapor Deposition, 2004. **10**(6): p. 318-324.

203. Xu, Y., et al., *Epitaxial ferroelectric thin films prepared by the Sol-Gel technique.* Ferroelectrics, 1997. **195**: p. 283-288.

204. Srikant, V., J.S. Speck, and D.R. Clarke, *Mosaic structure in epitaxial thin films having large lattice mismatch.* Journal of Applied Physics, 1997. **82**(9): p. 4286-4295.

205. Ishikawa, M., et al., *Growth of Epitaxial $KNbO_3$ Thick Films by Hydrothermal Method and Their Characterization.* Japanese Journal of Applied Physics, 2009. **48**(9): p. 09KA14.

206. Ang, C., Z. Yu, and L.E. Cross, *Oxygen-vacancy-related low-frequency dielectric relaxation and electrical conduction in Bi:$SrTiO_3$.* Physical Review B, 2000. **62**(1): p. 228.

207. Sundarakannan, B., K. Kakimoto, and H. Ohsato, *Frequency and temperature dependent dielectric and conductivity behavior of $KNbO_3$ ceramics.* Journal of Applied Physics, 2003. **94**(8): p. 5182-5187.

208. Tien, T.Y. and L.E. Cross, *Dielectric Relaxation in Strontium Titanate Solid Solutions Containing Lanthania.* Japanese Journal of Applied Physics, 1966. **6**: p. 459-468.

209. Hennings, D.F.K., C. Metzmacher, and B.S. Schreinemacher, *Defect Chemistry and Microstructure of Hydrothermal Barium Titanate.* Journal of the American Ceramic Society, 2001. **84**(1): p. 179-182.

210. Nakano, H., et al., *Characterization of Internal Pores in Hydrothermally Synthesized $BaTiO_3$ Particle by Transmission Electron Microscopy.* Journal of the American Ceramic Society, 2004. **87**(8): p. 1594-1597.

211. Hung, M.-y.H.-C., TW), Yu, Janet (Chang-hua, TW), Fang, Weng-liang (Hsin-Chu, TW), Kin, Chang-ching (Hsin-chu Hsien, TW), *Method for removal of photoresist residue after dry metal etch*, 1998, Taiwan Semiconductor Manufacturing Company, Ltd. (Hsin-Chu, TW): United States.

212. Cvelbar, U., M. Mozetic, and M. Klanjsek-Gunde, *Selective oxygen plasma etching of coatings.* Plasma Science, IEEE Transactions on, 2005. **33**(2): p. 236-237.

213. Chantarat, N., et al., *Selective Oxygen-Plasma-Etching Technique for the Formation of ZnO−FTO Heterostructure Nanotubes and Their Rectified Photocatalytic Properties.* Inorganic Chemistry, 2010. **49**(23): p. 11077-11083.

214. Lee, J.K., et al., *Characterization and elimination of dry etching damaged layer in Pt/Pb(Zr[sub 0.53]Ti[sub 0.47])O[sub 3]/Pt ferroelectric capacitor.* Applied Physics Letters, 1999. **75**(3): p. 334-336.

215. Wilkinson, C.D.W. and M. Rahman, *Dry etching and sputtering.* Philosophical Transactions of the Royal Society of London. Series A: Mathematical, Physical and Engineering Sciences, 2004. **362**(1814): p. 125-138.

216. Jiang, J.C., K. Lian, and E.I. Meletis, *Influence of oxygen plasma treatment on the microstructure of SnO_x thin films.* Thin Solid Films, 2002. **411**(2): p. 203-210.

217. Phan, B.T., et al., *Trap-Controlled Space-Charge-Limited Current Conduction in the Cr-Doped $SrTiO_3$ Thin Films Deposited by Using Pulsed Laser Deposition.* Journal of the Korean Physical Society, 2007. **51**(2): p. 664-668.

218. Matsushita, E., *Tunneling mechanism on proton conduction in perovskite oxides.* Solid State Ionics, 2001. **145**(1-4): p. 445-450.

219. Matsushita, E. and T. Sasaki, *Theoretical approach for protonic conduction in perovskite-type oxides.* Solid State Ionics, 1999. **125**(1-4): p. 31-37.

220. Wada, S., T. Suzuki, and T. Noma, *The Effect of the Particle Sizes and the Correlational Sizes of Dipoles Introduced by the Lattice Defects on the Crystal Structure of Barium Titanate Fine Particles.* Japanese Journal of Applied Physics, 1995. **34**: p. 5368-5379.

221. McCormick, M.A. and E.B. Slamovich, *Microstructure development and dielectric properties of hydrothermal $BaTiO_3$ thin films.* Journal of the European Ceramic Society, 2003. **23**(12): p. 2143-2152.

222. Kajiyoshi, K., Y. Sakabe, and M. Yoshimura, *Electrical Properties of $BaTiO_3$ Thin Film Grown by the Hydrothermal-Electrochemical Method.* Japanese Journal of Applied Physics, 1997. **36**: p. 1209-1215.

223. Li, P. and T.M. Lu, *Conduction mechanisms in $BaTiO_3$ thin films.* Physical Review B, 1991. **43**(17): p. 14261.

224. Bahl, S.K. and K.L. Chopra, *Electrical and Optical Properties of Amorphous vs Crystalline GeTe Films.* Journal of Vacuum Science and Technology, 1969. **6**(4): p. 561-565.

225. Walley, P.A., *Electrical conduction in amorphous silicon and germanium.* Thin Solid Films, 1968. **2**(4): p. 327-336.

226. Hickmott, T.W., *Formation of Ohmic contacts: A breakdown mechanism in metal-insulator-metal structures.* Journal of Applied Physics, 2006. **100**(8): p. 083712-7.

227. Zhang, M.-S., et al., *Study of structural and photoluminescent properties in barium titanate nanocrystals synthesized by hydrothermal process.* Solid State Communications, 2001. **119**(12): p. 659-663.

228. Nakano, Y., *Characterization of interface states in (Sr, Ca)TiO_{3-x} based ceramics by ICTS analysis.* Journal of Materials Research, 1991. **6**(6): p. 1346-1349.

229. Waser, R., T. Baiatu, and K.-H. Härdtl, *dc Electrical Degradation of Perovskite-Type Titanates: I, Ceramics.* Journal of the American Ceramic Society, 1990. **73**(6): p. 1645-1653.

230. Baiatu, T., R. Waser, and K.-H. Härdtl, *dc Electrical Degradation of Perovskite-Type Titanates: III, A Model of the Mechanism.* Journal of the American Ceramic Society, 1990. **73**(6): p. 1663-1673.

231. Kreuer, K.D., *Mechanisms of Proton Conduction in Perovskite-Type Oxides*, in *Perovskite Oxide for Solid Oxide Fuel Cells*2009. p. 261-272.

232. Hempelmann, R., et al., *Muon diffusion and trapping in proton conducting oxides.* Solid State Ionics, 1998. **107**(3-4): p. 269-280.

233. Cordero, F., et al., *Anelastic spectroscopy for studying O vacancies in perovskites.* Journal of the European Ceramic Society, 2006. **26**(14): p. 2923-2929.

234. Garcia-Belmonte, G., J. Bisquert, and F. Fabregat-Santiago, *Effect of trap density on the dielectric response of varistor ceramics.* Solid-State Electronics, 1999. **43**(12): p. 2123-2127.

235. Rick, U., *Revised Method for the Prediction of Lattice Constants in Cubic and Pseudocubic Perovskites.* Journal of the American Ceramic Society, 2007. **90**(10): p. 3326-3330.

236. Nagata, H., et al., *Fabrication and Electrical Properties of Potassium Niobate Ferroelectric Ceramics.* Japanese Journal of Applied Physics, 2007. **46**: p. 7084-7088.

237. Toby, B., *CMPR - a powder diffraction toolkit.* Journal of Applied Crystallography, 2005. **38**(6): p. 1040-1041.

238. Werner, P.E., L. Eriksson, and M. Westdahl, *TREOR, a semi-exhaustive trial-and-error powder indexing program for all symmetries.* Journal of Applied Crystallography, 1985. **18**(5): p. 367-370.

239. Howard, C.J., et al., *Neutron Diffraction Studies of Phase Transformations between Tetragonal and Orthorhombic Zirconia in Magnesia-Partially-Stabilized Zirconia.* Journal of the American Ceramic Society, 1990. **73**(10): p. 2828-2833.

240. Denton, A.R. and N.W. Ashcroft, *Vegard's law.* Physical Review A, 1991. **43**(6): p. 3161.

241. Modeshia, D.R., et al., *Control of polymorphism in $NaNbO_3$ by hydrothermal synthesis.* Chemical Communications, 2009. **7**(1): p. 68-70.

242. Zhu, H., et al., *Structural Evolution in a Hydrothermal Reaction between Nb_2O_5 and NaOH Solution: From Nb_2O_5 Grains to Microporous $Na_2Nb_2O_{6.2}/3H_2O$ Fibers and $NaNbO_3$ Cubes.* Journal of the American Chemical Society, 2006. **128**(7): p. 2373-2384.

243. Gasperin, M. and M.T. Le Bihan, *Mecanisme d'hydratation des niobates alcalins lamellaires de formule $A_4Nb_4O_{17}$ (A = K, Rb, Cs).* Journal of Solid State Chemistry, 1982. **43**(3): p. 346-353.

244. Hegetschweiler, K., et al., *Surface complexation of $[Nb_6O_{19}]^{8-}$ with Ni^{II}: solvothermal synthesis and X-ray structural characterization of two novel heterometallic Ni-Nb-polyoxometalates.* Inorganica Chimica Acta, 2002. **337**: p. 39-47.

245. Wu, G., et al., *Factors Affecting the Interlayer Arrangement of Transition Metal-Ethylenediaminetetraacetate Complexes Intercalated in Mg/Al Layered Double Hydroxides.* European Journal of Inorganic Chemistry, 2007. **2007**(6): p. 799-808.

246. Nagai, I., et al., *Electrochemical intercalation of lithium in layered niobates $AB_2Nb_3O_{10}$ (A=K, Rb, Cs; B=Ca, Sr) and their superconductivity.* Physica C: Superconductivity, 2001. **357-360**(Part 1): p. 393-396.

247. Ichiki, M., et al., *Electrical properties of piezoelectric sodium-potassium niobate.* Journal of the European Ceramic Society, 2004. **24**(6): p. 1693-1697.

248. Lin, D., K.W. Kwok, and H.L.W. Chan, *Piezoelectric and ferroelectric properties of $K_xNa_{1-x}NbO_3$ lead-free ceramics with MnO_2 and CuO doping.* Journal of Alloys and Compounds, 2008. **461**(1-2): p. 273-278.

249. Izyumskaya, N., et al., *Processing, structure, properties, and applications of PZT thin films.* Critical Reviews in Solid State and Materials Sciences, 2007. **32**(3-4): p. 111-202.

250. Olson, L.D., *Conventional Plastic Composite Boards: Resins and Reinforcements.*, in *Electronic Materials Handbook: Packaging*, M.L. Minges, Editor 1989, ASM International: Boca Raton. p. 537.

251. Handoko, A.D. and G.K.L. Goh, *Hydrothermal Synthesis of Sodium Potassium Niobate Solid Solutions at 200°C.* Green Chemistry, 2010. **12**(4): p. 680-687.

252. Goh, G.K.L., C.G. Levi, and F.F. Lange, *Hydrothermal epitaxy of $KTaO_3$ thin films.* Journal of Materials Research, 2002. **17**(11): p. 2852-2858.

253. Chien, A.T., et al., *Microstructural development of $BaTiO_3$ heteroepitaxial thin films by hydrothermal synthesis.* Journal of Materials Research, 1998. **13**(3): p. 649-659.

254. Kim, J.H., D. Andeen, and F.F. Lange, *Hydrothermal Growth of Periodic, Single-Crystal ZnO Microrods and Microtunnels.* Advanced Materials, 2006. **18**(18): p. 2453-2457.

255. Lu, C.-H., Y.-C. Lai, and R.B. Kale, *Influence of alkaline sources on the structural and morphological properties of hydrothermally derived zinc oxide powders.* Journal of Alloys and Compounds, 2009. **477**(1-2): p. 523-528.

256. Trejo, M.n., et al., *Synthesis and Growth Mechanism of One-Dimensional Zn/ZnO Core-Shell Nanostructures in Low-Temperature Hydrothermal Process.* Crystal Growth & Design. **0**(0).

257. Zhao, Q., et al., *Surfactant-assisted growth and characterization of CdS nanorods.* Inorganic Chemistry Communications, 2003. **6**(12): p. 1459-1462.

258. Nishizawa, H., T. Tani, and K. Matsuoka, *Crystal Growth of ZnO by Hydrothermal Decomposition of Zn-EDTA.* Journal of the American Ceramic Society, 1984. **67**(6): p. C-98-C-100.

259. Zhuang, et al., *Controlled Hydrothermal Growth and Up-Conversion Emission of $NaLnF_4$ (Ln = Y, Dy−Yb).* Inorganic Chemistry, 2007. **46**(13): p. 5404-5410.

260. Watt, I.M., *The analytical electron microscope.* Journal of Physics E: Scientific Instruments, 1986. **19**(9): p. 668.

261. Britvin, S.N., et al., *Niobate and Tantalate Pyrochlores: Soft Synthesis by the Fluoride Route.* European Journal of Inorganic Chemistry, 2010. **2010**(7): p. 1082-1088.

262. Wu, J., et al., *A one-pot method to grow pyrochlore $H_4Nb_2O_7$-octahedron-based photocatalyst.* Journal of Materials Chemistry, 2010. **20**(10): p. 1942-1946.

263. Suzuki, K., et al., *Processing of Oriented $K(Ta,Nb)O_3$ Films Using Chemical Solution Deposition.* Journal of the American Ceramic Society, 1999. **82**(6): p. 1463-1466.

264. Tanaka, K., et al., *Effect of (Na,K)-Excess Precursor Solutions on Alkoxy-Derived $(Na,K)NbO_3$ Powders and Thin Films.* Japanese Journal of Applied Physics, 2007. **46**(10B): p. 6964-6970.

265. Lai, F. and J.-F. Li, *Sol-gel processing of lead-free $(Na,K)NbO_3$ ferroelectric films.* Journal of Sol-Gel Science and Technology, 2007. **42**(3): p. 287-292.

266. Chu, S.-Y., et al., *Properties of $(Na, K)NbO_3$ and $(Li, Na, K)NbO_3$ Ceramic Mixed Systems.* Ferroelectrics, 2003. **287**: p. 23-33.

267. Chen, H.D., et al., *Electrical properties' maxima in thin films of the lead zirconate--lead titanate solid solution system.* Applied Physics Letters, 1995. **67**(23): p. 3411-3413.

268. Yang, C., et al., *Structure and Ferroelectric Properties of PZT Thin Film Deposited on LaNiO3 Bottom Electrodes.* Integrated Ferroelectrics, 2008. **98**(1): p. 69-76.

269. Zhang, S., J. Liu, and C. Yang, *Growth and characterization of PZT films with different grain sizes.* Integrated Ferroelectrics: An International Journal, 2006. **84**(1): p. 99 - 105.

270. Fukushima, J., K. Kodaira, and T. Matsushita, *Preparation of ferroelectric PZT films by thermal decomposition of organometallic compounds.* Journal of Materials Science, 1984. **19**(2): p. 595-598.

271. Park, C.-H., Y.-G. Son, and M.-S. Won, *Microstructure and ferroelectric properties of r.f. magnetron sputtering derived PZT thin films deposited on interlayer (PbO/TiO2).* Microchemical Journal, 2005. **80**(2): p. 201-206.

272. Cho, C.R. and L.F. Francis, *Electromechanical properties and acoustic response of integrated PZT thin films.* Journal of Materials Science Letters, 2000. **19**(16): p. 1477-1479.

273. von Bradsky, G. and R.A. Ricks, *Solidification microstructures in rapidly solidified, gas atomized aluminium-lithium alloy powders.* Journal of Materials Science, 1987. **22**(4): p. 1469-1476.

274. Liu, D.R. and D.B. Williams, *Accurate Quantification of Lithium in Aluminium-Lithium Alloys with Electron Energy-Loss Spectrometry.* Proceedings of the Royal Society of London. A. Mathematical and Physical Sciences, 1989. **425**(1868): p. 91-111.